Modeling and Position Control of Piezoelectric Motors

Mouhanned Brahim

To cite this version:

Mouhanned Brahim. Modeling and Position Control of Piezoelectric Motors. Automatic. Université Paris Saclay (COmUE), 2017. English. NNT : 2017SACLS296 . tel-01689921

HAL Id: tel-01689921
https://theses.hal.science/tel-01689921
Submitted on 22 Jan 2018

université
PARIS-SACLAY

UNIVERSITÉ
PARIS
SUD
Comprendre le monde,
construire l'avenir

NNT : 2017SACLS296

Modeling and Position Control of Piezoelectric Motors

Thèse de doctorat de l'Université Paris-Saclay
préparée à l'Université Paris-Sud

École doctorale n°575: Electrical, Optical, Bio-physics and Engineering (EOBE)
Spécialité de doctorat: Génie électrique

Thèse présentée et soutenue à Gif sur Yvette, le 10 Octobre 2017, par

M. Mouhanned BRAHIM

Composition du Jury:

M. Mickaël HILAIRET	
Professeur des universités, Université de Franche-Comté (FEMTO-ST)	Rapporteur
M. Fréderic GIRAUD	
Maître de conférences HDR, Université de Lille (L2EP)	Rapporteur
M. Yves BERNARD	
Professeur des universités, Université Paris-Sud (GeePs)	Directeur de thèse
M. Demba DIALLO	
Professeur des universités, Université Paris-Sud (GeePs)	Président
M. Emanuele GRASSO	
Maître de conférences, Université de la Sarre (LAT)	Examinateur
Mme Imen BAHRI	
Maître de conférences, Université Paris-Sud (GeePs)	Examinatrice

Thèse de doctorat

Acknowledgments

This thesis is submitted in partial fulfillment of the requirements for the Doctor of Philosophy in electrical engineering at the Group of Electrical Engineering of Paris (GeePs), University of Paris-Sud, France. The work has been carried out in the period from October 2014 to October 2017 under the supervision of Professor Yves BERNARD.

First and foremost, I would like to express my sincere gratitude to my supervisor Prof. Yves BERNARD for the continuous support of my PhD study and related research, for his patience, motivation, and immense knowledge. His guidance helped me in all the time of research and writing of this thesis. I could not have imagined having a better advisor and mentor for my PhD study.

Besides my advisor, special thanks go also to my co-supervisor, Associate Professor Imen BAHRI, for his help and advice during this PhD project.

I am gratefully indebted to the staff of GeePs for their assistance and support, who provided me an opportunity to join their team as PhD student. GeePs team have contributed immensely to my personal and professional time at Pari-Sud. The group has been a source of friendships as well as good advice and collaboration.
My sincere thanks go to the team of the Laboratory of Actuation Technology (LAT), at the University of Saarland, Saarbrucken in Germany, and especially to Professor Matthias NIENHAUS and Associate Professor Emanuele GRASSO for having permitted me to stay at his laboratory, for a period of two months.

For this dissertation I would like to thank my reading committee members, Prof. Mickaël HILAIRET, and Dr. Fréderic GIRAUD for their time, interest, and helpful comments. I would like to thank the other two members of my oral defense committee, Prof. Demba DIALLO, and Dr. Emanuele GRASSO for their time and insightful questions.

Lastly, I am indebted to my parents, without them I would not be around, and also to my sisters for their unconditional love and encouragement.

October 2017,
Gif sur Yvette, France.
Mouhanned BRAHIM

Contents

List of figures

List of tables

Nomenclature

Abbreviations

PZM	Piezoelectric Motor
PZA	Piezoelectric Actuator
USM	Ultrasonic Motor
TWUSM	Traveling Wave Ultrasonic Motor
SWUSM	Standing Wave Ultrasonic Motor
TW	Traveling Wave
SW	Standing Wave
WPZM	Walking Piezoelectric Motor
LSPA	Linear Stepping Piezoelectric Actuator
RSPA	Rotary Stepping Piezoelectric Actuator
PMA	Piezoelectric Multilayer Actuator
PAD	Piezoelectric Actuator Drive
MRI	Magnetic Resonance Imagery
ECM	Equivalent Circuit Model
FEM	Finite Element Method
TF	Transfer Function
PID	Proportional Integrator Derivative
FLC	Fuzzy Logic Control
NN	Neural Network
FNN	Fuzzy Neural Network
RC	Repetitive Control
BMC	Behavior Model Control
COG	Causal Ordering Graph
DOF	Degree Of Freedom
MRAC	Model Reference Adapting Control
PZL	Piezoelectric Legs
PI	Physik Instrumente
GS	Gain Scheduling

Remaining notations

f_r	Resonance frequency
V_{max}	Maximum voltage
V_{rms}	Root mean square voltage
φ	Phase shift
f	Frequency
ω	Angular frequency
w	Traveling wave amplitude
w_{max}	Maximum amplitude of traveling wave
w_1, w_2	Amplitude of the standing waves
δ_1, δ_2	Vibration amplitudes of the mechanical orthogonal modes
λ	Wave length
x_0	Half contact length of the traveling wave
x_s	Stick point location
m_{eff}	Effective mass of the stator of USR60
$Cs_{1,2}$	Damping factors of USR60 stator
$Ks_{1,2}$	Spring coefficients of the USR60 stator
ρ	Piezoelectric force factor
k	Wave number
F_{v1}, F_{v2}	Forces generated by the USR60 stator
$F_{f1,T}$, $F_{f2,T}$	Tangential feedback forces
$F_{f1,N}$, $F_{f2,N}$	Normal feedback forces
μ	Coulomb friction coefficient
b	Inner radius of the stator
h	Half thickness of the stator
R_0	Middle radius of the contact surface
R_r	Radial shape constant of the travelling wave
x_r	Rotor stiffness per unit area
M_r	Rotor mass
z(t)	Vertical distance between the rotor and the un-deformed stator surface
z_0	Initial vertical position of the rotor
F_N	Generated normal force
F_{ext}	External force

Ω	Angular velocity
θ	Angular position
$\upsilon_{h,rotor}$, $\upsilon_{h,stator}$	Horizontal velocities of the rotor and stator
T_{usm}	USM generated torque
T_L	Load torque
J_r	Rotor inertia
$G_{USM}(s)$	Transfer function model of USR60 motor
k_m	Gain constant of USR60
τ_m	Time constant of USR60
d_{ring}	Diameter of the PAD stator ring
d_{shaft}	Diameter of the PAD rotor shaft
x_a, y_a	Elongations of orthogonal stacks
r_x, r_y	Cartesian coordinates of the PAD stator ring
Δ x	Actuator displacement
d_{33}	Piezoelectric constant
C	Equivalent capacitance of the stack
F	Stack generated force
Q	Electrical charge
U	Applied voltage
$k_{x,y}$	Actuators stiffness in x-y directions
$d_{x,\ y}$	Actuators damping factors in x-y directions
$m_{eff\ x,y}$	Actuators effective mass in x-y directions
m_R	Ring mass
m_{tk}	Top cap mass
m_{res}	Tubular spring mass
$F_{gx,y,}$ $F_{ax,y}$	Actuators generated and applied forces in x-y directions
a	diameter of ring circular trajectory
θ_s	Angular position of the stator
x_s,Y_s	Circular coordinates of the stator
T_{act}	Actuator torque
T_s	Stator torque
T_r	Rotor torque
Ω_r	Rotor angular velocity
Ω_s	Stator angular velocity

J_{trans}	Transmission inertia
J_r	Shaft inertia
d_r	Shaft damping factor
i_{trans}	Transmission ratio
x_{adjust}, y_{adjust}	Shaft deviations in x-y directions
$G_{PAD}(s)$	Transfer function model of the PAD
A	Maximum voltage amplitude
$U_{1,2,3,4}$	Driven voltages
$G_{WPZM}(s)$	Transfer function model of the WPZM
k_w	Gain constant of WPZM
τ_w	Time constant of WPZM
H_∞	H-infinity controller
t_r	Response time
W_i	Weighting filter number i
γ	Optimal gamma value
K(s)	Controller transfer function
$K_{red}(s)$	Reduced controller transfer function

Thesis outcomes

➢ Publications

❖ International journals

- M. Brahim, I. Bahri, Y. Bernard, "Real time implementation of H-infinity and RST motion control of rotary traveling wave ultrasonic motor", Mechatronics, vol.44, pp.14-23, 2017
- M. Brahim, I. Bahri, Y.Bernard, " H-Infinity and RST Position Controllers of Rotary Traveling Wave Ultrasonic Motor", International Journal of Mechanical, Aerospace, Industrial, Mechatronic and Manufacturing Engineering, vol: 11, no: 2, pp 323-330, 2017.
- M. Brahim, I. Bahri, Y. Bernard, "Design and Implementation of Robust Position Control of Piezoelectric Actuator Drive (PAD)", Accepted for publication in International Journal of Mechatronics and Automation.
- M. Brahim, I. Bahri, Y. Bernard "Design and Real Time Implementation of Robust Position Controller of Walking Piezoelectric Motor'', submitted to IEEE Trans on Mechatronics

❖ International conferences

- **M. Brahim**, I. Bahri, Y. Bernard, "Piezoelectric Motors in Mechatronic Systems: Electromechanical Performances and Positioning Potentials", Accepted for presentation in International Conference on Mechatronic and Smart Materials, Paris, November 2017.
- M. Brahim, I. Bahri, Y.Bernard, "Modeling and Robust Closed Loop Position Controllers of Piezoelectric Actuator Drive (PAD)", IEEE International Conference on Systems, Automation & Control (SAC), Marrakech, March 2017.
- M. Brahim, I. Bahri, Y.Bernard, "H-Infinity and RST Position Controllers of Rotary Traveling Wave Ultrasonic Motor", 19th International Conference on Control Applications, Amsterdam, February 2017.
- M. Brahim, I. Bahri, Y.Bernard, "Modeling and RST Position Controller of Rotary Traveling Wave Ultrasonic Motor", IEEE Conference on Systems, Process and Control (ICSPC), Malaysia, 2015.

➢ International mobility

- 2 months (10-11/2016) in the Laboratory of Actuation Technology (LAT), University of Saarland, Saarbrucken, Germany.

  Mission: Design and real time validation of positioning experimental platform for linear walking piezoelectric motor

Résumé en français

I. Introduction générale

Les moteurs électromagnétiques ont été largement utilisés dans de nombreuses applications d'ingénierie comme actionneurs. Les méthodes de conception, d'optimisation et de fabrication de ces moteurs ont été développées afin d'améliorer leurs performances. Toutefois, en raison des progrès rapides des technologies d'ingénierie, y compris les produits de haute technologie, l'aérospatiale, les équipements médicaux, l'automobile, les robots d'Imagerie par Résonance Magnétique (IRM), des nouvelles exigences des moteurs électriques sont apparues comme la taille réduite, la haute précision, un temps de réponse rapide, une forte densité massique et volumique, et l'insensibilité aux champs magnétiques.

Dans ce contexte où la réponse rapide et silencieuse, l'encombrement réduit, et les bonnes performances dynamiques des actionneurs sont appréciées, les moteurs piézoélectriques trouvent leurs places. Ces moteurs se caractérisent en effet par un couple massique important, des forts couples à basse vitesse sans réducteur, une discrétion acoustique dans le cas des moteurs ultrasonores, et ne sont pas affectés par les interférences magnétiques.

Cependant, les phénomènes non linéaires (hystérésis, creep, vibration, dérive thermique…) qui caractérisent leur fonctionnement et les exigences spécifiques de leurs circuits de commande, mettent un frein à leur utilisation et à leur développement. L'alimentation et le contrôle de ces moteurs soulèvent des problèmes liés au comportement capacitif de leur impédance et à la précision des modèles et aux techniques de contrôle qui leurs sont associées.

Pour faire face à ces problèmes de contrôle des moteurs piézoélectriques, deux démarches sont généralement abordées. La première consiste à utiliser des modèles simples tels que les circuits équivalents pour développer des techniques de contrôle non linéaires comme les réseaux de neurones et la logique floue. La deuxième repose sur la connaissance approfondie des comportements réels des moteurs et de leurs principes de fonctionnement, qui débouche sur l'obtention de modèles non linéaires reflétant leur comportement. Cependant la complexité des modèles ou des techniques de contrôle risque d'aboutir à l'élaboration de lois de commande non- implantables en temps réel.

Dans cette thèse, on traite le problème de contrôle en position des Moteurs Piézoélectriques (MPEs) dans des applications à haute précision, et on vise spécialement la robotique, dans le but d'évaluer la faisabilité de réalisation des systèmes de positionnement précis et robustes à base des MPEs dans des applications robotiques, et de dégager les limites de ces actionneurs dans tels applications. Les contributions de cette thèse peuvent être résumées de la manière suivante :

- L'établissement de modèles fidèles aux comportements des trois MPEs qui puissent être utilisés pour implémenter des lois de contrôle de position. Les trois moteurs étudiés sont :
    - Un moteur rotatif ultrasonique à ondes progressives de type USR60 de chez Shinsei.Co.
    - Un moteur rotatif quasi-statique de type PAD7220 de chez Noliac.
    - Un moteur linéaire pas à pas de type N-310.13 de chez Physik Instrumente (PI) GmbH.

- La synthèse des contrôleurs de position précis et robustes des PMEs qui répondent aux exigences d'applications spécifiques des trois moteurs étudiés. Deux contrôleurs sont proposés:
    - Un contrôleur de type H-infini (H_∞) basé sur des filtres de pondérations.
    - Un contrôleur en temps discret de type RST basé sur le placement des pôles.

- La garantie des critères de précision, stabilité, et robustesse dans un contrôleur efficace et simple à implémenter en temps réel quelle que soit la topologie du moteur.

- La validation des performances de précision et de robustesse des contrôleurs de position proposés sans faire appel ni à des systèmes de compensation supplémentaires des comportements non linéaires, et ni à des techniques d'adaptation des paramètres des contrôleurs pour surmonter le problème d'incertitude des modèles.

- La conception de bancs de positionnements expérimentaux basés sur les trois PMEs et l'implantation en temps réel des techniques de contrôle développées. Ces techniques sont comparées expérimentalement à un contrôleur PID conventionnel pour mettre en évidence les avantages des méthodes proposées.

- L'évaluation des atouts et des limites des trois moteurs par rapport aux applications robotiques. Les critères d'évaluation sont liés aux topologies des moteurs, aux caractéristiques électromécaniques, aux techniques d'entraînement et aux capacités de positionnement en boucle fermée.

Pour arriver à ces objectifs, une démarche de synthèse des contrôleurs de type H_∞ et RST est d'abord mise en place pour un système généralisé dans le second chapitre. Cette démarche est appliquée aux trois MPEs à travers leurs modèles et en respectant les performances des boucles fermées. Les travaux de modélisation et de contrôle en position des moteurs sont présentés dans les chapitres trois à cinq. Des conclusions générales ainsi que des recommandations liées à la modélisation, au contrôle/commande, et aux performances des moteurs étudiés sont présentées à la fin de cette thèse.

II. Modélisation et Contrôle en position de l'USR60

Le moteur ultrasonique à ondes progressives de type USR60 (Fig.1) est commercialisé par le constructeur japonais Shinsei.Co. Son stator est constitué d'un disque de bronze sur lequel est collé un anneau de céramique piézoélectrique. L'anneau piézoélectrique est divisé en deux phases A et B. Chacune de ces phases est divisée en petits secteurs avec des polarisations opposées. Le principe de fonctionnement est basé sur la superposition des ondes stationnaires générées par chaque phase pour créer une onde progressive qui se propage tout le long de la surface du stator. Les vibrations du stator vont suivre des trajectoires elliptiques (Fig.1.c). Ces micro-vibrations du stator sont transformées en mouvement rotatif du rotor par le biais du principe d'entrainement par frottement.

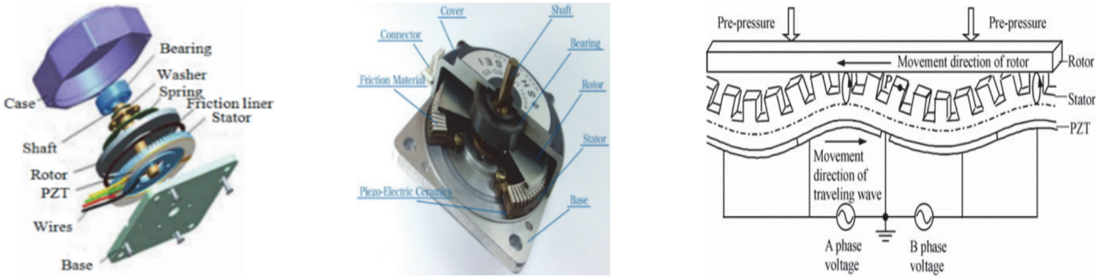

(a) (b) (c)

Fig.1. (a) Structure de USR60, (b) USR60 en vue de coupe, (c) mécanisme de contacte stator-rotor

Le modèle proposé de l'USR60 décrit le principe de génération de l'onde progressive, et la surface de contact entre stator et rotor. Celui-ci donne la possibilité d'évaluer la variation des grandeurs de sortie du moteur (vitesse, couple, position) en fonction des paramètres de commande, et les effets de variation des paramètres du stator et de la surface de contact sur les performances du moteur. Ce modèle permet aussi de simuler facilement des lois de contrôles (position, vitesse) en utilisant les amplitudes des tensions d'alimentation, la fréquence, et le déphasage comme grandeurs de contrôle.

Le modèle de l'USR60 est principalement composé des trois sous-systèmes montrés dans la Fig.2 :

- **Stator :** Dans cette partie on modélise les processus de vibration de l'anneau et la génération de l'onde progressive (W, W_{max}).
- **Mouvement vertical de rotor :** l'évolution temporelle de la position verticale du rotor est déterminée dans cette partie ainsi que la longueur de surface de contact entre le stator et rotor (x_0). Ce dernier paramètre va être utilisé pour le calcul du couple généré par le moteur (T).
- **Mouvement angulaire de rotor :** Le mouvement angulaire ainsi que la vitesse de rotation (Ω) sont analysés dans ce sous-ensemble.

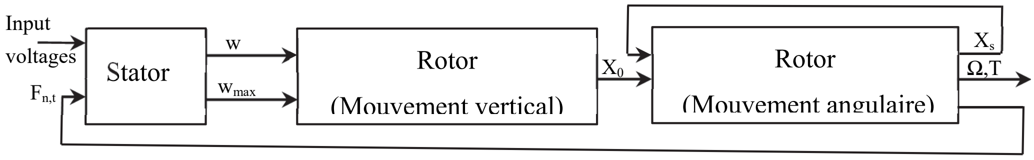

Fig.2. Synoptique du modèle de l'USR60

Le modèle de l'USR60 est développé sur MATLAB/Simulink comme le montre la Fig.3.

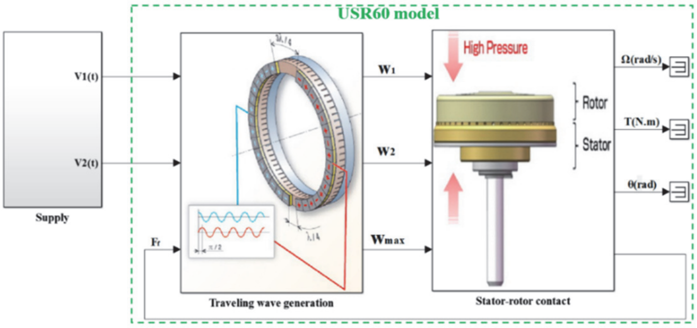

Fig.3. Architecture du modèle de l'USR60 sur MATLAB/Simulink

La variation de la vitesse de rotation (Ω) en fonction des paramètres de commande (amplitude de tension, fréquence, déphasage) est simulée afin de choisir la meilleure grandeur de contrôle pour notre système de positionnement. Comme illustré dans la Fig.4, le déphasage entre les deux tensions d'alimentation (φ) est le seul paramètre qui permette de faire tourner le moteur dans le deux sens. Cette grandeur (φ) va être donc utilisée comme signal de control de position de l'USR60 bien que la caractéristique vitesse-déphasage présente une zone morte autour du déphasage nul quand un couple de charge est appliqué.

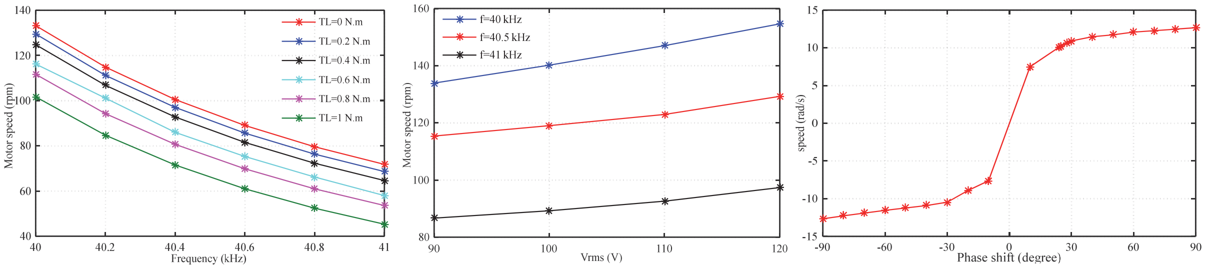

(a) (b) (c)

Fig. 4. (a) Caractéristique vitesse-fréquence**,** (b) Caractéristique vitesse-tension, (c) Caractéristique vitesse-déphasage

Un banc de positionnement expérimental est mis en place pour déterminer les caractéristiques de l'USR60 en boucle ouverte et identifier la fonction de transfert entre la position angulaire du moteur (θ) et le déphasage (φ). Ce banc (Fig.5) va être utilisé aussi pour implémenter en temps réel les lois de contrôle développées à travers la maquette dSPACE.

La Fonction de Transfert (FT) du moteur est déterminée en boucle ouverte en intégrant la relation entre la vitesse angulaire du moteur et le déphasage identifié à partir de la Fig.6. On peut l'écrire sous la forme :

$$G_{USM}(s)=\frac{\theta(s)}{\varphi(s)}=\frac{k_m}{s(1+\tau_m s)} \tag{1}$$

Avec k_m= 11.5, et τ_m=4.25 ms

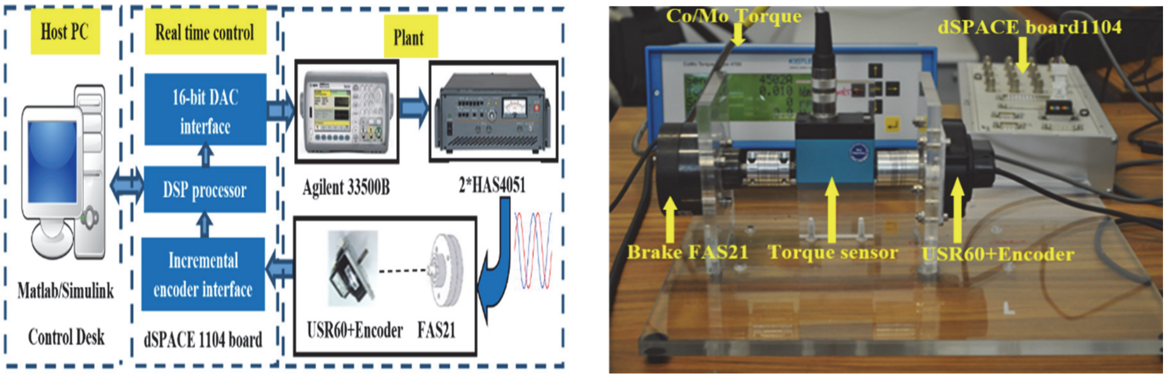

(a) (b)

Fig.5. (a) Synoptique de système de positionnement de l'USR60, (b) Plateforme expérimentale

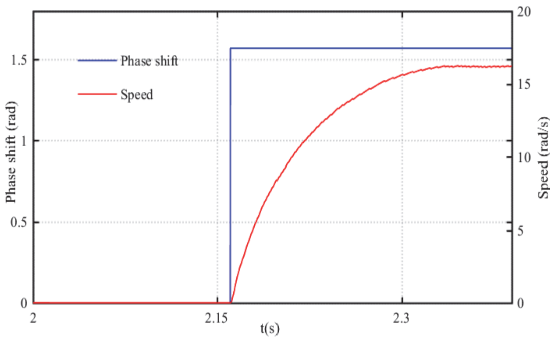

Fig.6. Variation de vitesse en boucle ouverte pour un échelon de déphasage de π/2

Cette FT est utilisée pour synthétiser un contrôle en temps continu de type H_∞, et un autre en temps discret de type RST comme illustré dans les Fig.7.a et b respectivement. Ces deux contrôleurs permettent l'introduction des performances de précision et de robustesse demandées à travers les filtres de pondérations pour le H_∞, et à travers le placement des pôles pour le RST.

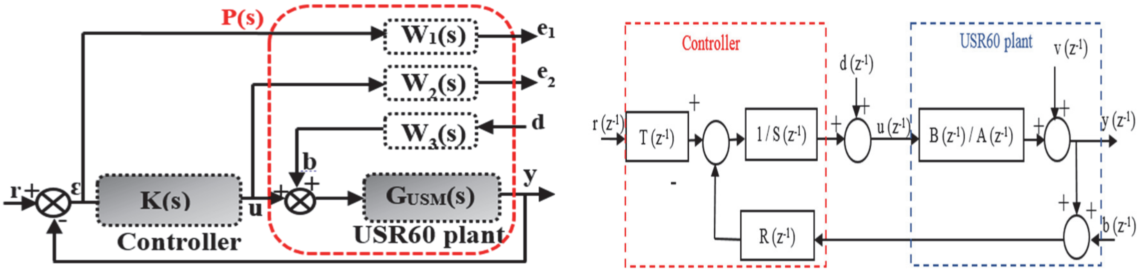

(a) (b)

Fig.7. (a) USR60 contrôlé en position par un H_∞, (b) USR60 contrôlé en position par un RST

Les contrôleurs H_∞ et RST sont implémentés en temps réel, et leurs résultats sont comparés avec un correcteur PID classique. Les performances du H_∞ en terme d'erreur statiques, en présence d'un couple de charge sont meilleures que celles du RST et du PID comme indiqué dans le tableau.1 et Fig.8. La robustesse de ces trois contrôleurs face aux perturbations au niveau des mesures ou au niveau des signaux de contrôle est aussi testée expérimentalement (Fig.9a et b). Ces figurent montrent bien l'avantage de H_∞ en terme de rejection des bruits injectés.

Tableau.1: Erreur statique en fonction de couple charge

TL(N.m)	H_∞	RST	PID
0.1	0.1%	0.3%	0.4%
0.3	0.25%	0.6%	1%
0.5	0.4%	1%	1.65%

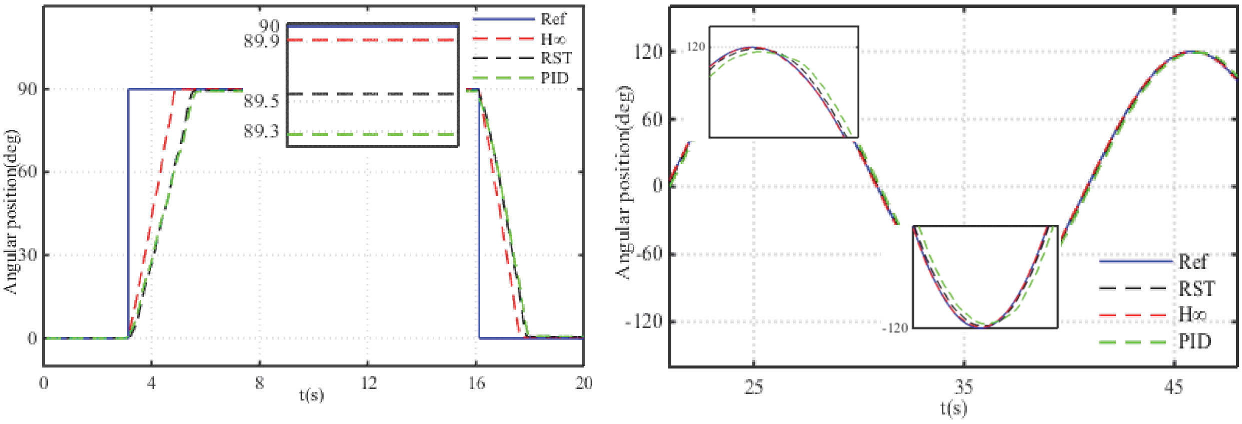

(a) (b)

Fig.8. Comparaison des résultats expérimentaux en présence de couple de charge : (a) Echelon de position, (b) Trajectoire sinusoïdale

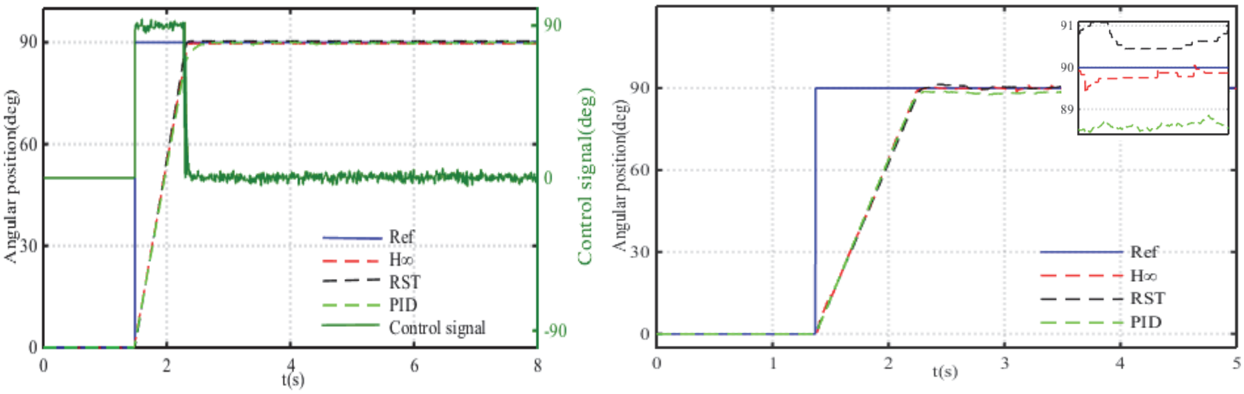

(a) (b)

Fig.9. Comparaison de la robustesse aux perturbations : (a) niveau signal de contrôle, (b) niveau capteur

III. Modélisation et Contrôle en position de PAD7220

Le deuxième moteur étudié est un moteur piézoélectrique rotatif commandé avec des fréquences quasi-statiques (loin de la résonance mécanique) de type « Piezelectric Actuator Drive (PAD) » commercialisé par la firme danoise Noliac. Son principe de fonctionnement (Fig.10) est principalement basé sur la conversion des élongations des actionneurs piézoélectriques multicouches en une rotation de rotor moyennant un système d'engrenage mécanique. Ce moteur est alimenté par deux tensions (entre -20 Vmin et 200 Vmax) en quadrature de phase avec une amplitude de 160 $V_{c\text{-}c}$.

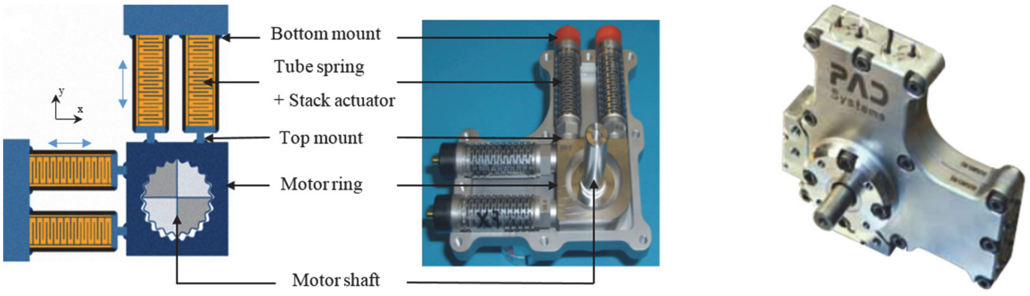

(a) (b)

Fig.10. (a) Principe de fonctionnement de PAD, (b) Prototype de PAD7220

Dans le modèle du PAD, on commence par la modélisation des actionneurs multicouches afin d'obtenir les déformations linéaires orthogonales dans les axes x, et y (Fig.11). La surface de contact entre les actionneurs et l'anneau du stator est ensuite prise en compte, et la transmission de mouvement par engrenage est introduite en dernière étape. Ce modèle permet la simulation d'évolution des grandeurs de sortie du moteur en boucle ouverte (Fig.12), et peut aussi servir pour tester des lois de contrôle en boucle fermée.

Un banc de positionnement expérimental (Fig.13) est mis en place pour déterminer les caractéristiques de PAD7220 en boucle ouverte et pour valider les techniques de contrôle en boucle fermée. Une FT entre la position angulaire du moteur et la fréquence de commande est aussi identifiée expérimentalement :

$$G_{PAD}(s) = \frac{\theta(rad)}{f(Hz)} = \frac{2\pi}{320}\frac{1}{s} \qquad (2)$$

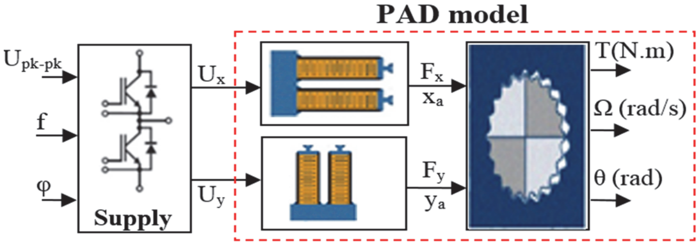

Fig.11. Topologie du modèle de PAD

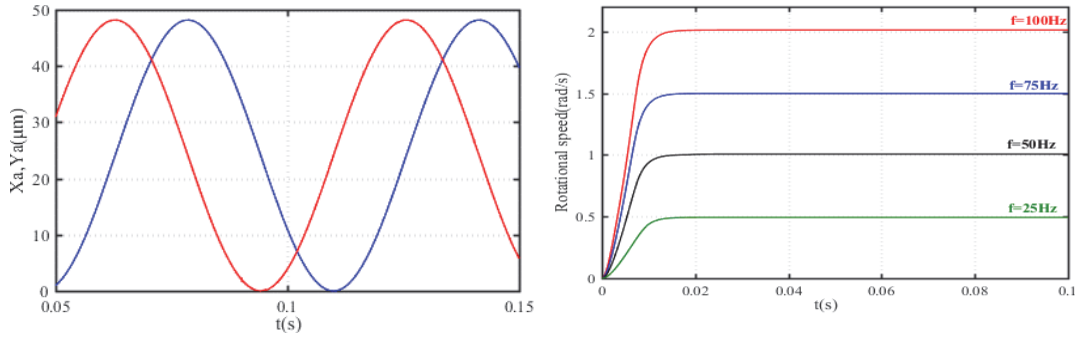

(a) (b)

Fig.12. (a) Déplacements linéaires des actionneurs, (b) Vitesse de rotation à différentes fréquences

Une étude de comparaison expérimentale entre les résultats de robustesse face aux perturbations (mesures et signal de contrôle) des contrôleurs H∞ et RST avec un correcteur PID est abordée. Les figures 14 et 15 confirment l'avantage du contrôleur H∞ par rapport aux deux autres en terme de rejection des bruits.

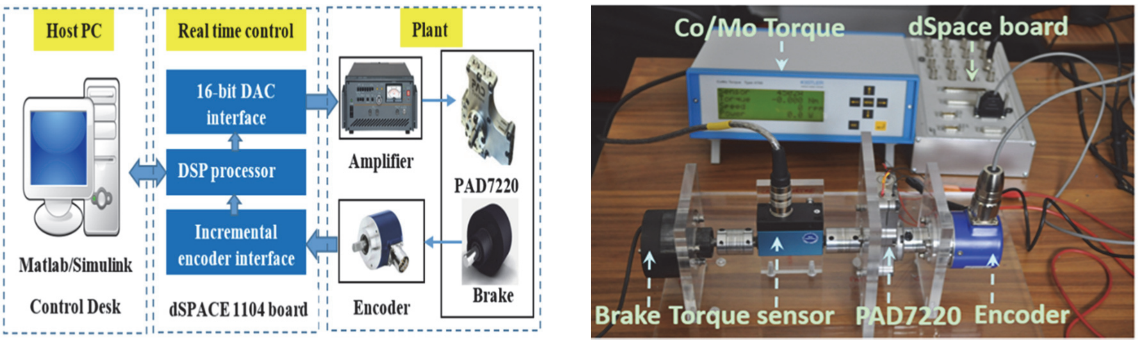

(a) (b)

Fig.13. (a) Synoptique de système de positionnement de pad7220, (b) Plateforme expérimentale

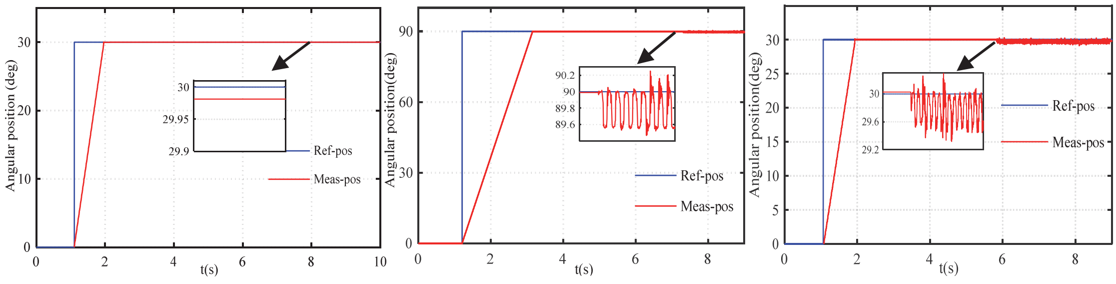

(a) (b) (c)

Fig.14. Robustesse face aux bruits de mesures :(a) H_∞, (b) RST, (c) PID

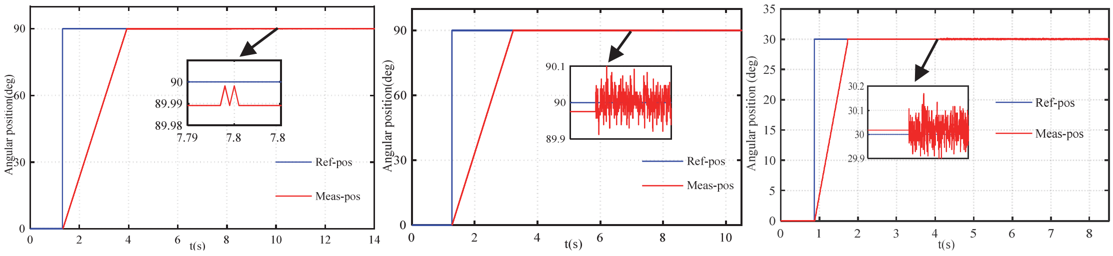

(a) (b) (c)

Fig.15. Robustesse face aux bruits au niveau du signal de contrôle:(a) H_∞, (b) RST, (c) PID

IV. Modélisation et Contrôle en position du N-3101.13

Le troisième moteur étudié dans cette thèse est un moteur piézoélectrique linéaire de chez Physik Instrumente (PI) GmbH, fonctionnant aussi à des fréquences faibles par rapport à la résonance mécanique. Sa topologie est montrée dans la Fig.16, son mouvement linéaire continu est créé par la succession des pas réalisés par les actionneurs piézoélectriques qu’on appelle « pieds piézoélectriques ». Ces pieds entrainent par frottement une tige linéaire pré-chargée avec une vitesse qui peut aller jusqu’à 10 mm/s. Ce moteur est alimenté par quatre tensions déphasées avec une amplitude entre 0 et 45 V, et peut être contrôlé en vitesse et position à travers la fréquence.

Un banc de positionnement expérimental pour le N-310.13 (Fig.17.a) est mis en place pour identifier tout d’abord la FT entre le signal de contrôle (V_c) et la position de la tige (Y). Ensuite, ce banc va servir pour valider expérimentalement les lois de contrôle. La FT est identifiée à partir de la courbe de variation de vitesse en boucle ouverte suite à un échelon de fréquence (Fig.17.b). Cette FT peut s’écrire sous la forme suivante :

$$G_{WPZM}(s) = \frac{Y}{V_c} = \frac{k_w}{s(1+\tau_w s)} \tag{3}$$

Avec k_w= 1.2 mm/V, et τ_w=0.15 s

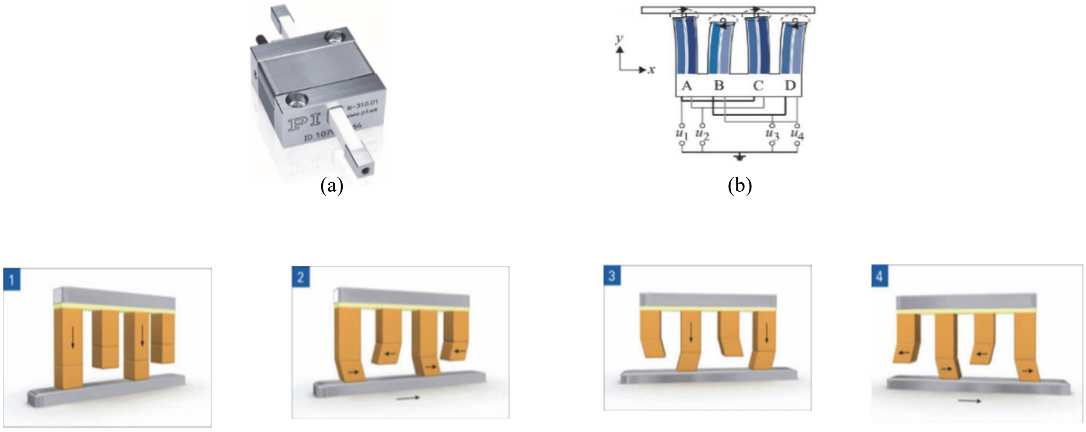

(a) (b)

1: One pair is in contact the rod, the second is lifted off

2: the first pair of the legs is lifted and bent in the right direction, keeping contact with the rod while the other pair retracts and moves in the left direction

3: The leg pair that was initially retracted now extends to push against the rod while the first pair retracts

4: The cycle is completed with the second pair bending to the right while the first pair is moved left

(c)

Fig.16. (a) N-310.13, (b) Mouvement elliptique des pieds, (c) Principe de fonctionnement de moteur

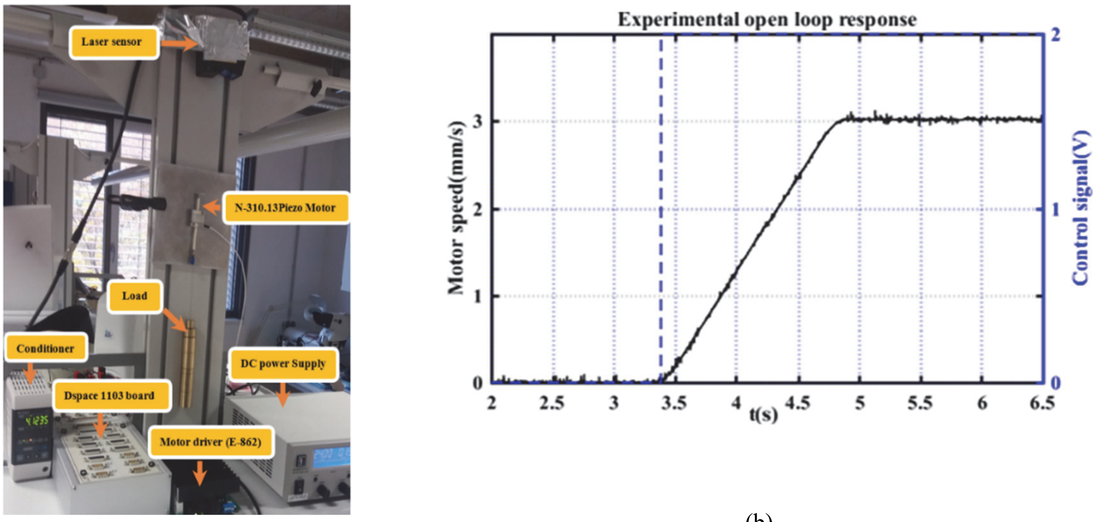

(a) (b)

Fig.17. (a) Plateforme expérimentale, (b) Variation de vitesse en boucle ouverte pour un échelon de tension de contrôle

Une comparaison expérimentale entre H_∞, RST, et PID est abordée pour le positionnement du moteur piézoélectrique linéaire. Les critères de comparaison sont, la précision en présence des diffèrents couples de charges, et à différentes vitesses de déplacements. La Fig.18 montre les résultats de trois contrôleurs quand le moteur est soumis à des forces allant jusqu'à 7.5N. Le H_∞ garantit la haute précision quelle que soit la force appliquée, alors que pour les deux autres, on remarque que la précision et le temps de réponse se dégradent en augmentant la force exercée. Le H_∞ présente aussi une forte robustesse face au changement de vitesse de déplacement par rapport aux deux autres contrôleurs (Fig.19).

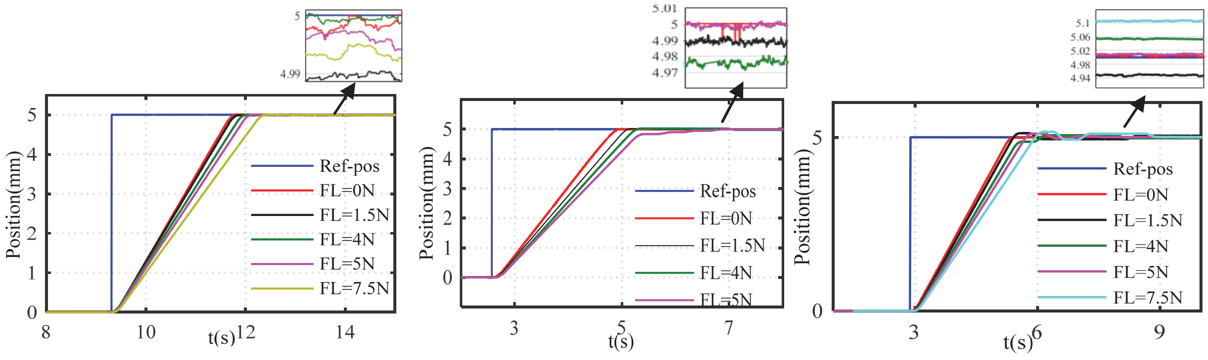

(a) (b) (c)

Fig.18. Comparaison des résultats expérimentaux avec différents couple de charges : (a) H_∞, (b) RST, (c) PID

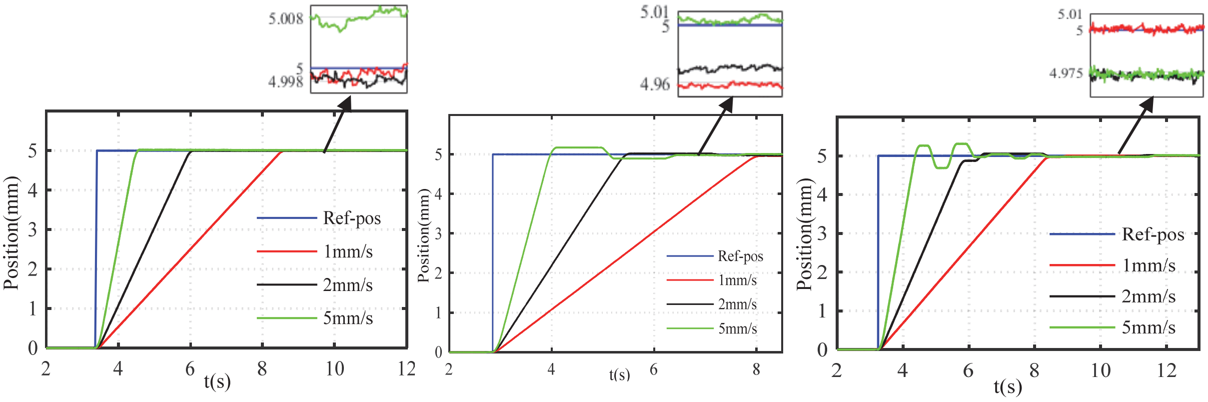

(a) (b) (c)

Fig.19. Comparaison des résultats expérimentaux avec différentes vitesses : (a) H_∞, (b) RST, (c) PID

V. Conclusion

Dans cette thèse, la problématique de contrôle en position des moteurs piézoélectriques est traitée, afin de valider la faisabilité de réalisation des applications robotiques à haute précision à base des MPEs. Pour arriver à ce but, trois moteurs avec différentes technologies sont testés.

Une démarche de modélisation de ces moteurs a été mise en place, ces modèles permettent à la fois la vérification des comportements des moteurs et l'implémentation des lois de contrôle.

Deux types de contrôles sont ensuite synthétisés, un en temps continu de type H_∞ avec des filtres de pondérations, et l'autre en temps discret de type RST.

Trois bancs expérimentaux à la base de ces trois moteurs sont mis en place afin d'implémenter en temps réel les lois de contrôle développées. Ces bancs ont tourné en boucle ouverte dans un premier temps pour évaluer les caractéristiques des moteurs et pour identifier les fonctions de transferts. Les contrôleurs synthétisés sont ensuite implantés en boucle fermée moyennant une carte dSPACE. La précision et la robustesse des systèmes de positionnements à base des MPEs ont été testées sous différentes conditions de fonctionnement.

Ces moteurs piézoélectriques contrôlés en position par le H_∞ ont montré une haute précision quelle que soit la charge appliquée (jusqu'à la valeur maximale) et la vitesse de mouvement, sans avoir besoin d'algorithmes d'adaptation des paramètres. La robustesse face au comportement non-linéaire des moteurs et aux bruits injectés est aussi confirmée sans faire appel à des systèmes de compensation supplémentaires.

Chapter I

Introduction

Traditional electrical motors based on electromagnetic principle have been widely used in many engineering applications as actuators and mechanical power sources. The design, optimization and manufacturing methods of these motors have been developed in order to improve their performances. However, due to the rapid progress of engineering technologies including the high-tech products, aerospace, medical equipment, automotive, semiconductor technologies, and smart robots, new requirements of electric motors appeared such as small size, light-weight, ultra-high precision, fast response, high torque density, and no electromagnetic interferences. Due to the structure and operating principle of electromagnetic motors, it becomes difficult to meet these requirements.

In parallel, the intensive worldwide research efforts in smart materials based actuators and related drive circuits promote the integration of new type motors. The piezoelectric motors are relatively mature among these innovative motor concepts. Where, since the discovery of the piezoelectric effect in 1880, the piezo-system technologies have made rapid progress in terms of reliability, efficiency, and compactness. The piezo-motors benefit from the direct drive principle using the converse piezoelectric effect to achieve interesting performances required in advanced engineering fields. They are well classified to actuate ultra-precision positioning system, where the quick response, small size, and self-locking criteria are important.

As an introduction, this chapter presents an initiation to the piezoelectric technology including the operating principles of piezo-actuators and motors, and the nonlinear behaviors of these devices. The piezo-motors are classified based on various criteria, and the motion generation principle of each category is explained. A survey of the industrial applications of piezo-motors is proposed in order to highlight the importance of these actuators in positioning applications. Finally, the thesis contributions and outlines are highlighted.

I.1 Objectives and scope of the research

In the recent decades, the piezoelectric motors (PZMs) are widely suggested for engineering applications where the high precision, fast response, and compact size requirements are very important. This is mainly due to the electromechanical characteristics of these motors such as the small size, fast response, theoretical unlimited resolution, self-locking, high torque density, and high torque at low speed without gear.

These features make the PZMs a very competitive candidate to the electromagnetic motors for industrial fields and especially robotic applications. In parallel to the precision and fast response potentials of PZMs, let us explain the advantage of high holding torque of PZM without supply. When actuating a robot arm by electromagnetic motor, to avoid the returning to initial position or laying down of the arm in case of off-power, a fail-safe brakes system is applied to stop and hold. These fail-safe brakes systems are generally based on permanent-magnetic and spring-set systems. This additional mechanism leads to an increase of system size and moment inertia, and in consequence slower response time. Due to the driving principles of PZMs, they benefit of their high holding torque without supply to maintain the final position without braking system. In other hand, the non-magnetic characteristic makes PZMs as a promising solution to actuate the Magnetic Resonant Imagery (MRI) robots for surgical operations.

Nevertheless, the insertion rate of PZMs into robotic applications do not reflect the real potentials of these motors. These integration difficulties are due to many factors that can be resumed in; the highly nonlinear behavior especially when operating close to the resonance, several sources of nonlinearities in different frequencies operations ranges (hysteresis and creep in low frequency, and vibration in high frequency), the requirement of specific drive system for high capacitive loads (PZMs), and the time-variant motor parameters due to the sensitivity to heating, load torque and electrical noises. Therefore, complexes, time consumption, and adaptive techniques are generally addressed to control the position of PZMs in closed loop operation mode, where an on-line parameters adaptation and additional compensation systems are required to overcome the motor nonlinear behaviors. The application of these methods in practical engineering applications remains difficult.

This thesis aims to study the feasibility of the design and implementation of robust position control of PZMs with different topologies. The control technique should meet the specific requirements of the PZMs robotic applications in terms of accuracy and robustness, and fulfill the simplicity criteria for practical implementation issues. This goal will be achieved through the establishment of electromechanical models of different topologies of PZMs for control purposes. Afterwards, the design and real time implementation of simple, precise, and robust position controllers of PZMs. The strengths and limitations of each piezo-positioning system in terms of control performance and the motor behaviors in open/closed loop operation conditions will be evaluated. This is in order to collect the most required data to design an "ideal" piezoelectric motor for robotic applications as perspective of this research work.

The piezoelectric motors that will be in the scope of this research are in the mechanical power range between 1 and 20 Watts. The output motion is in the range up to 100 mm for linear motors and bidirectional motion for rotary motors. These motors are mainly used to actuate MRI surgical robots, to adjust the driver's seat in automobiles, and for silent and smooth window operation of a car door. Therefore, in this thesis we will not be interested to the nano/micro-motors nor to the micro-robots based on PZMs.

I.2 Initiation to piezoelectric actuators and motors

I.2.1 Direct and converse piezoelectric effects

The origin of the world piezoelectric is derived from the Greek world "piezo" which means"press". The piezoelectric effect is the property of some materials to develop electric charge on their surface when a mechanical stress is exerted on them [1], and it was discovered in 1880 by the brother Pierre and Jacques Curie. There are many materials that exhibit a piezoelectric effect, and the lead zirconate titanate (PZT) is the most widely used material. The electrical response of these materials to the mechanicals effort is called direct piezoelectric effect and it is the principle of piezoelectric sensors. The same material can also generate a mechanical stress when an electric field is applied, and this mechanical response is called converse piezoelectric effect (Fig. I-1). The converse piezoelectric effect is at the origin of creation of the piezoelectric actuators.

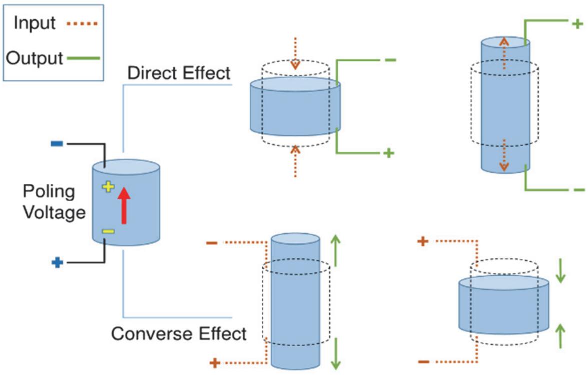

Fig. I-1. Direct and converse piezoelectric effects

I.2.2 Principle of piezoelectric actuator and motor

As aforementioned, the piezoelectric actuator (PZA) is based on the converse piezoelectric effect. The major drawbacks of PZAs is their small stroke, Amplified Piezoelectric Actuators (APA) [2] and multilayer bending actuators [3] are proposed to increase the actuators full stroke at the expense of stiffness and actuation force. However, the full stroke stills in the range of a few millimeters, even with such structures.

The piezoelectric motor (PZM) consists on the conversion of the limited displacements of PZA into unlimited linear or rotational motion using different mechanical structures and drive principles. The PZMs can be classified into many categories based on the motion type, operation principle, and frequency operation range. The classification and the operation principle of PZM categories will be discussed in the section I.3.

I.2.3 Nonlinearities of piezoelectric actuators

As aforementioned, the piezoelectric motor is mainly composed by one ore many piezoelectric actuators emerged into a mechanical structure to produce unlimited motion. Thus, the nonlinear characteristics of the PZA outputs will generally affect the PZM performances. In this section, an overview of the common nonlinearities of PZAs will be discussed.

The strain of PZA is not only determined by the driving parameters (voltage amplitude, frequency, and phase shift), but it depends on many factors. These factors include the mechanical boundary conditions, especially on the pre-stress of the actuator, thermal drift, and self-heating [4]. The PZA displacement shows also several nonlinear behaviors caused principally by the hysteresis, creep, and vibration phenomena.

I.2.3.1 Hysteresis

Hysteresis is a nonlinear behavior between the applied electric field (u) and the mechanical displacement of a piezoelectric actuator (x) as shown in Fig. I-2. This phenomenon is the cause of irreversible losses that occur when similarly oriented electric dipoles interact upon application of an electric field [5]. The hysteresis effect on the displacement of a piezoelectric actuator is more significant over large range motion. In general, the maximum error caused by the hysteresis can reach 15% of the travel range of the PZA. With the increase of driving frequency, the hysteresis caused errors may go beyond 35% [6].

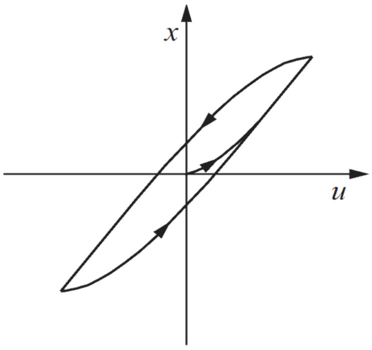

Fig. I-2. Hysteresis between the applied voltage (u) and the actuator displacement (x)

To treat the hysteresis, many efforts have been made in the literature. The proposed solutions can be classified into feedforward and feedback control techniques. The feedforward techniques (also called inversion-based controls) consist on the modeling of the hysteresis nonlinear behavior, and in second time to apply the inverse model in order to compensate the hysteresis effect (Fig. I-3). Good tracking results can be achieved if the plant model and its frequency response are known with high accuracy [7]. As a consequence several models are proposed to deal with the hysteresis phenomenon. Roughly speaking, the hysteresis model of piezo-actuated stages can be classified into physics-based and phenomenological models [6]. An overview of the hysteresis models of actuated piezo-stages is given in Fig. I-4, and the principle of each modeling approach can be found in [6-9]. However, it is demonstrated that, until now, there is no general reliable model to completely represent the hysteresis behaviors of piezo-actuated stages [6].

The second control approach of the hysteresis in piezo-stages is the feedback control method as illustrated in Fig. I-5. In this configuration, the hysteresis nonlinearity is treated as a nonlinear bounded disturbance or characterized by the aforementioned hysteresis models [6].Then, different feedback controllers can be applied to compensate the hysteresis effect [7].

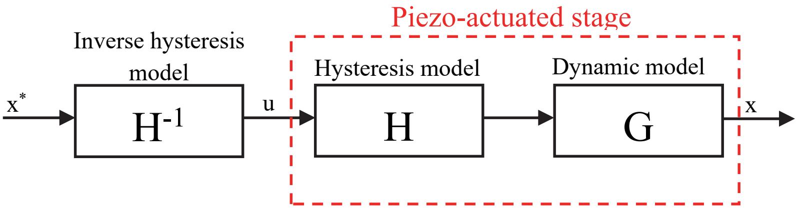

Fig. I-3. Feedforward control of Hysteresis effect

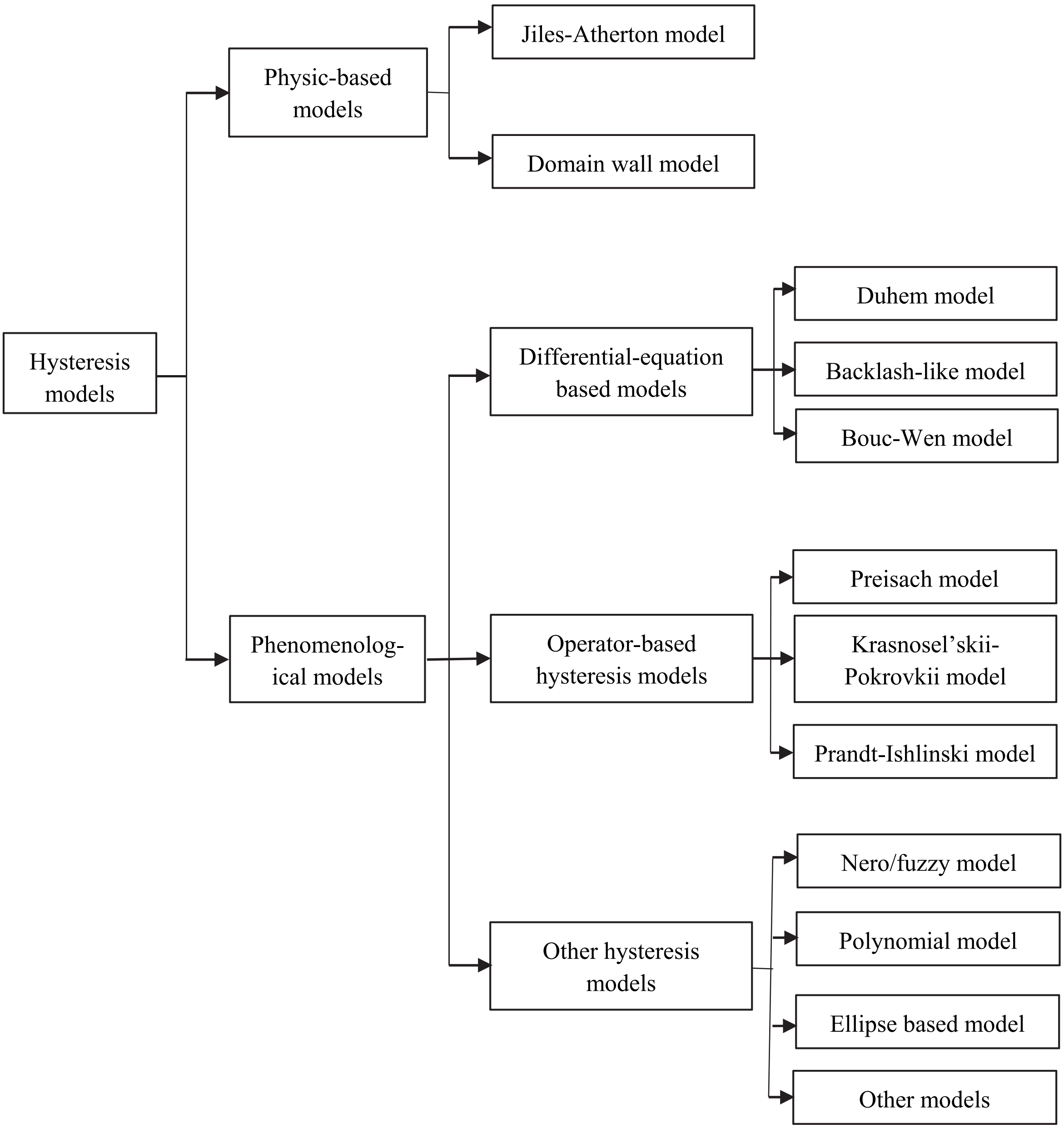

Fig. I-4. Classification of hysteresis models for piezo-actuated stages [6]

The major drawback of these techniques is the limitation of the closed loop bandwidth of the positioning system in presence of highly resonant modes.

The feedforward and feedback controllers can be combined to deal with the compensation of hysteresis nonlinearity in piezo-actuated stages as shown in Fig. I-6. With this methodology, the inverse compensators with different models are applied in the feedforward part and the feedback controllers are simultaneously designed in the feedback loop to mitigate the effect of the inversion errors and to handle the remaining dynamics of the systems [6].

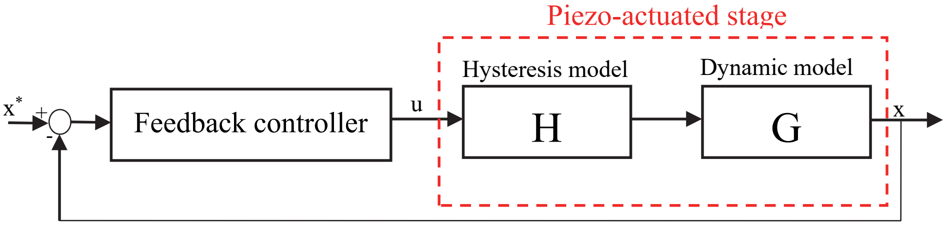

Fig. I-5. Feedback control of Hysteresis effect

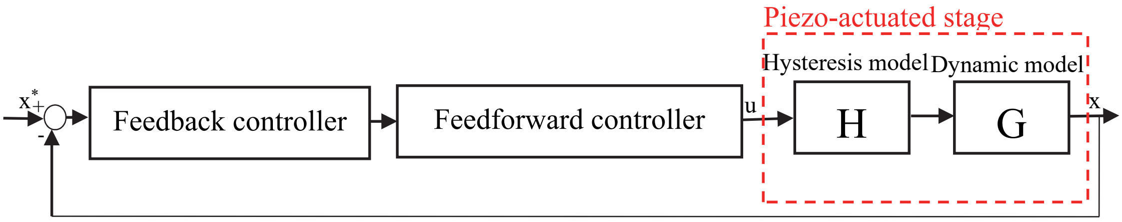

Fig. I-6. Feedback-feedforward control of Hysteresis effect

There is also a hardware solution to reduce the hysteresis nonlinear behavior of piezoelectric actuators which is the use of charge amplifier rather than voltage amplifier. By using charge drivers and through the regulation of the piezoelectric current or charge, significant reduction of hysteresis effect can be achieved [10-12]. However, the capacitive behavior of piezoelectric actuators complicates the design of charge driver due to the finite output impedance and dielectric leakage [7].

I.2.3.2 Creep

When a voltage step change is sent to drive a piezoelectric actuator, the response consists on a fast dynamic transient followed by low frequency drift (Δy) of the final position known as creep (Fig. I-7). As shown in Fig. I-7, the creep effect becomes noticeable over extended periods of time, where large position errors are produced with the increase of time. Therefore, the creep can particularly degrade the static positioning potential of piezoelectric actuators.

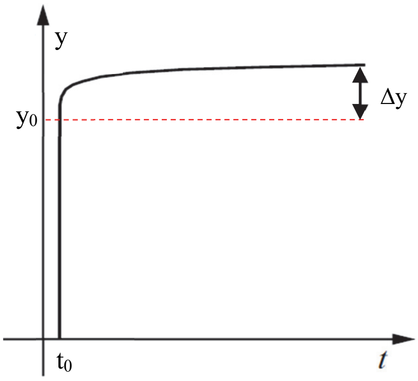

Fig. I-7. Effect of creep in piezoelectric actuator displacement

The creep effect can be avoided by driving the piezo-stage at high speed, but this operation limits the use of piezoelectric positioning systems in slow and static applications. As done with the other nonlinearities sources, feedback [13-15] and feedforward [16, 17] controllers are proposed to compensate the creep effect. To describe this phenomenon and to apply the compensation control methods, creep models are reported in the literature. One of them is usually called logarithmic model, and it can be expressed by the following equation [6]:

$$y\,(t) = y_0[1 + \,\gamma\, log_{10}\left(\frac{t}{t_0}\right)] \tag{I-1}$$

Where y(t) is the displacement of the piezo-actuator when subjected to a fixed input voltage, t_0 is the time at which the creep effect is obvious, y_0 is the displacement at the time of t_0 after applying the input voltage, and γ is a coefficient determining the rate of the logarithmic response. Generally, y_0, t_0, and γ are identified experimentally.

I.2.3.3 Vibrational dynamics

The dynamic vibration of piezoelectric devices is a relatively high frequency nonlinear behavior. The vibration effects are mainly caused by exciting the resonance modes of the piezo-actuated stage. Due to the high stiffness and low structural damping ratio of piezoelectric actuators [6], a sharp peak of the damped structure emerges in the frequency response of the piezo-actuated stages as shown in Fig. I-8.a. The vibrational dynamics have a low-gain margin problem because of the rapid phase drop associated with the small structural damping ratio and hysteresis nonlinearity [18, 19]. In consequence, the high frequency input signals can easily excite the motion vibration and tracking errors will be obtained as shown in Fig. I-8.c. Thus, the dynamic vibration is the main factor limiting the bandwidth of piezo-positioning stages. To overcome this problem, several vibrational dynamic models are proposed. The concept consists of neglecting the hysteresis effect, and linear dynamic equations are identified using the input and output data of the piezoelectric system [6].

The common feedforward control of vibration is the model-based control method by inverting the linear dynamic model of the piezo-actuated stage and without considering the hysteresis effect [18, 20, 21]. The input shaping method is alternatively proposed to deal with the dynamical vibrations problems [22, 23]. The notch filter [15], integral resonant [24], and positive feedback [25] controllers are also tested to compensate the dynamical vibration effects and to increase the piezo-stage bandwidth.

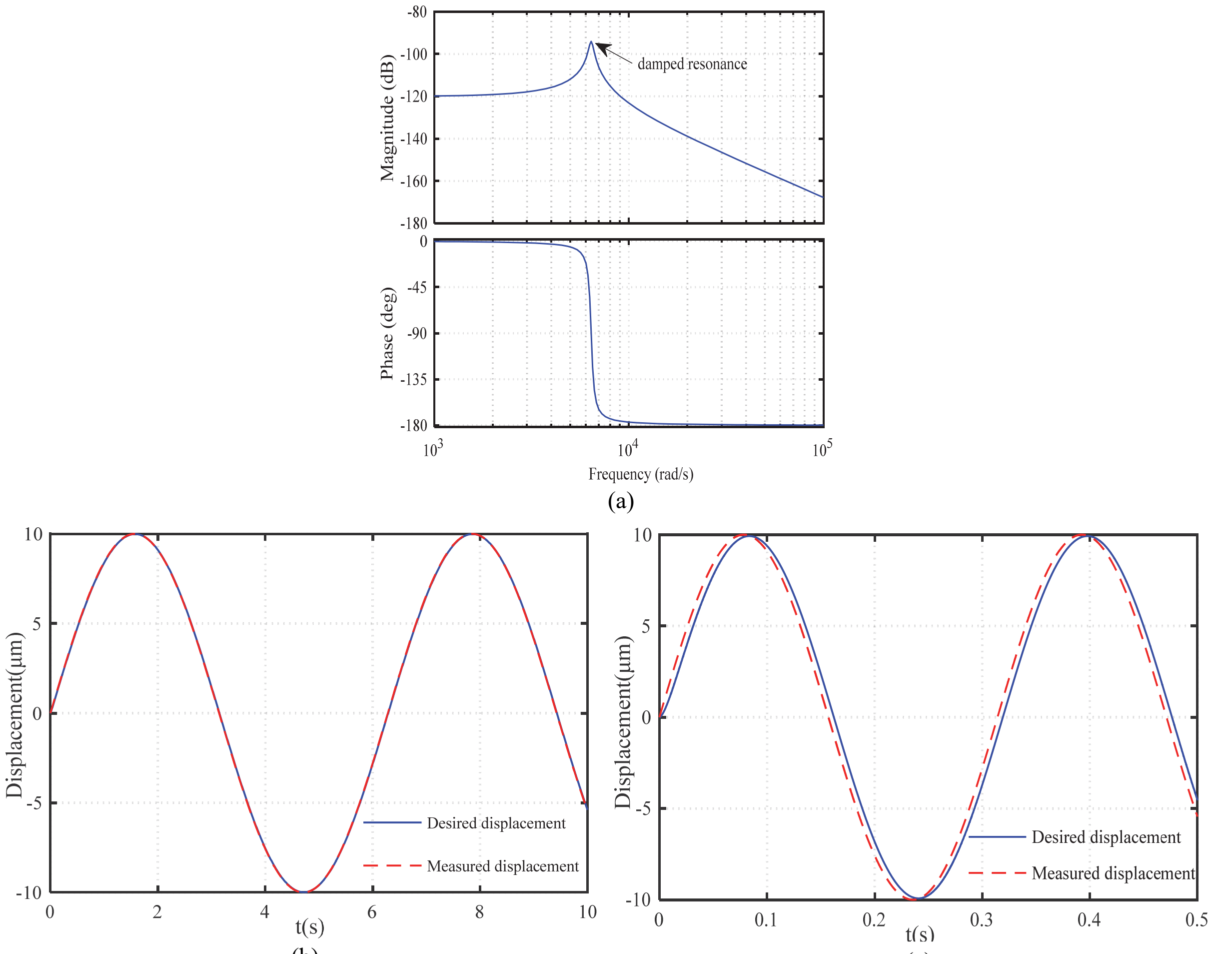

(a)

(b)

(c)

Fig. I-8. Vibration effect: (a) Frequency response, (b) Tracking results at 1 rad/s, (c) Tracking results at 20 rad/s

I.3 Classification of piezoelectric motors and operating principles

The piezoelectric motors can be classified according to different criteria including the motion type (linear, rotational), frequency operation range, stator geometric, and operating principle [4, 8, 26-28]. In this report, the PZMs are classified in sub-categories in order to integrate the most used criteria as shown in Fig. I-9. In the first level of Fig. I-9, the PZMs are classified based on the motion type into linear or rotary motors. These two types of PZMs can be classified according to the frequency operation range into quasi-static and ultrasonic motors. Two categories of quasi-static PZMs can be distinguished based on the driving method, which are the stepping and inertia motors.

The operating principle of the inertia motors is based on the stick-slip drive method, while the commercialized stepping PZMs can be devised into inchworm and walking principle motors. The ultrasonic motors (USM) are classified as function of the wave propagation method into traveling and standing waves USM.

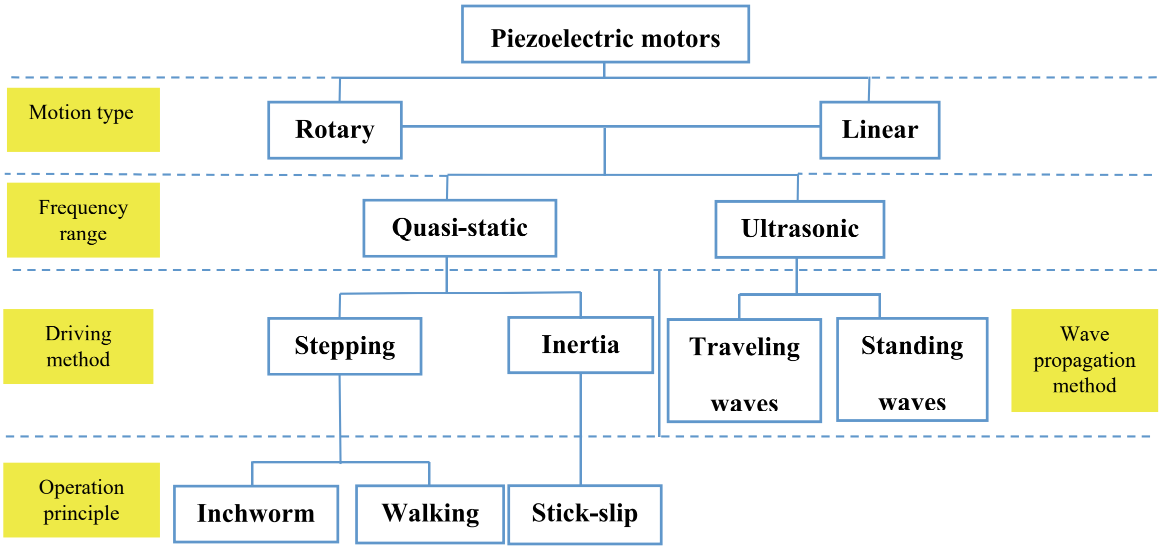

Fig. I-9. Classification of piezoelectric motors

I.3.1 Quasi-static piezoelectric motors

The quasi-static motors are the piezoelectric motors driven in a frequency range much lower than their mechanical resonance frequencies. These types of motors are principally characterized by the theoretically unlimited resolution at low speed without gear. The quasi-static PZMs are driven based on the inertia and steeping methods. In the following two sub-sections, the characteristics, and operating principles of the two PZM categories will be reviewed.

I.3.1.1 Inertia motors

Compared to the others PZMs, the inertia motors have a simply mechanical design, and are typically driven by one electrical voltage. These characteristics favorite the miniaturization of inertia motors for very compact positioning systems.

The inertia motors use the inertia of the driven part to drive it through an uninterrupted friction contact to generate motion [4]. These motors are driven by asymmetric voltages to create the transition between the static (stick) and sliding (slip) friction, which explains the name “stick-slip” given to inertia PZMs. There are two basic functional principles of inertia motors, one with fixed actuator, and the second with moving actuator (called also impact drive motor). The operating principles of the two types of inertia motors are illustrated in Fig. I-10.

In the inertia drive PZM incorporating fixed actuator two movement stages can be distinguished. As shown in Fig. I-10.a, the actuator expands slowly and the slider follows this movement due to static friction. Next, the actuator contracts rapidly so that the slider is unable to follow this movement and lets the actuator slip back due to its own inertia and the not sufficiently high dynamic friction. The motion direction is determined by the mode of the slow movement (expansion or contraction).

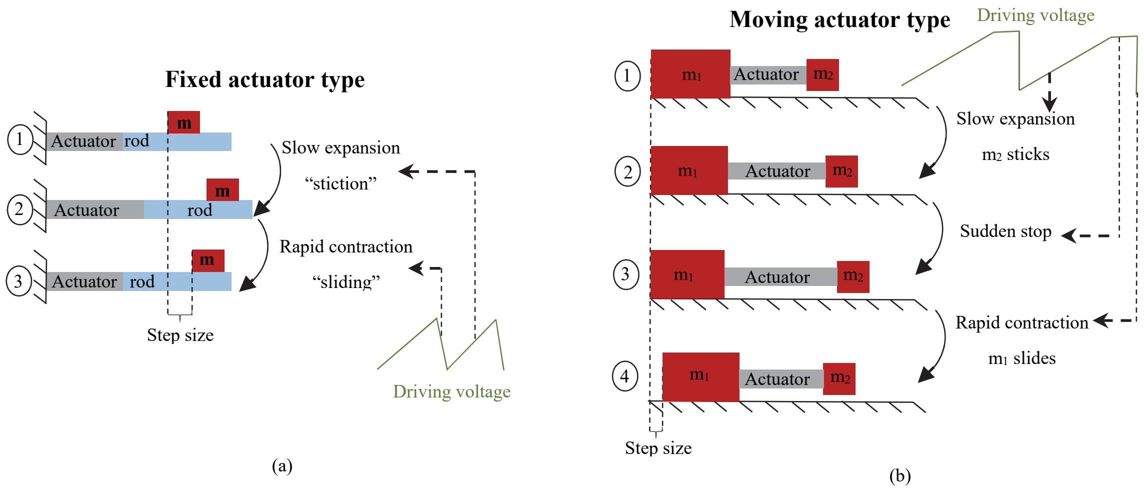

Fig. I-10. Description of inertia motor principles: (a) Fixed actuator type, (b) Moving actuator type

The inertia drive PZM based on moving actuator (impact drive motor) is typically composed by three main parts: the main body (m_2), the actuator, and the inertia weight (m_1). The main body is in frictional contact with a guiding surface, the actuator and the weight do not touch this surface (Fig. I-10.b). When the actuator expands (or contracts) slowly, the inertial weight moves with it, while the main body maintains its position due to the high friction force compared to the inertia force. This expansion is stopped suddenly to overpass the static friction, and immediately a rapid contraction of the actuator follows which causes impulsive inertia force to be exerted on the main body. As consequence, the main body follows the motion direction of the actuator. At the end of this cycle, one motor step motion is generated. In order to change the motion direction, the slope of the driving voltage will be inverted (rapid expansion and slow contraction). The first experimentally validated inertia PZMs are proposed firstly by Pohl in 1986 [29] and by Higuchi et al. [30]. There are others little different topologies of inertia motors derived from the two aforementioned principles, which are reported in the literature [4, 26, 31].

I.3.1.2 Stepping motors

The piezoelectric motors based on stepping mode are also called clamping-based motors. As the name reflects, these motors are based on the succession of clamping and unclamping movements. Depending on the operating principle and the employed moving parts, two categories of stepping PZMs can be distinguished, which are the inchworm and walking PZMs. This kind of motors are characterized by the unlimited resolution with high force capability, and it suffers from the low speeds.

➢ Inchworm PZMs

The first clamping-type PZM working with inchworm principle was developed and commercialized by Burleigh Instruments, Inc. in 1974 [32]. The basic structure of inchworm motor consists of three piezoelectric actuators; two are used for clamping and one for extension [33, 34]. In order to obtain continuous motion and higher forces, similar designs of clamping motors with five actuators are proposed [35, 36]. The topology and the clamping sequences of the inchworm motor are illustrated in Fig. I-11. The slider is initially clamped by one of the clamping actuators. In step 1, the extensional actuator expands allowing the slider to move away from the open clamp. In steps 2 and 3, the switching between the closed and open clamps is subsequently realized. When the extensional actuator contracts in step 4, the distance between the clamps reduces and the slider moves further in the same direction. The clamping actuators change their roles again and a new cycle starts in steps 5 and 6 respectively.

The step size of the inchworm motor depends on the maximum strain of the extensional actuator, and the no-load speed is determined directly by the frequency of the clamping movements. The motion direction of the motor can be reversed by inverting the clamping sequences.

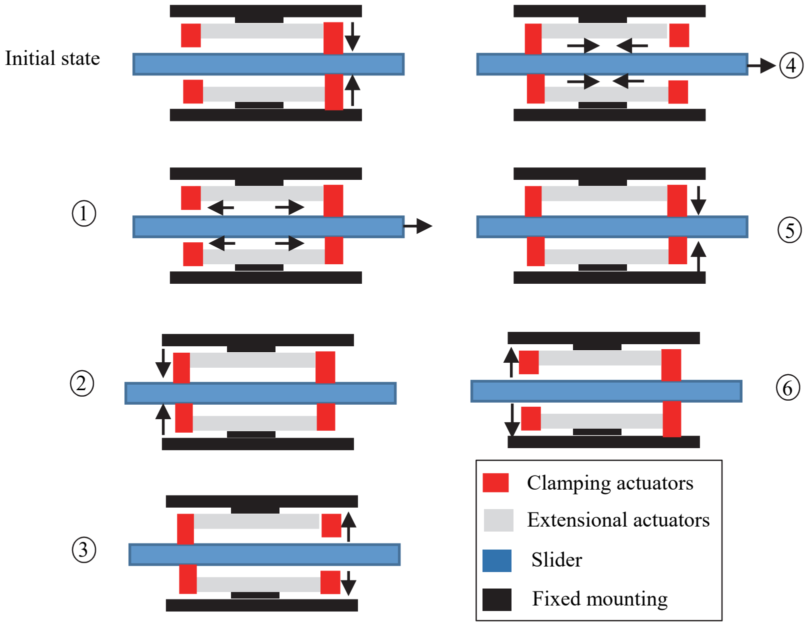

Fig. I-11. Schematic description of actuation stages in an inchworm motor

➢ Walking PZMs

The Walking Piezoelectric Motor (WPZM) is a modified clamping-type PZM. The WPZM was proposed for positioning in a large range of motion and with higher speeds than the inchworm motors. It consists of several piezoelectric drive elements (legs) engaging and disengaging in a frictional contact with a movable rod.

The motor proposed by Brisbane in 1965 [37] (Fig. I-12) is one of the earlier PZMs working with the walk drive principle. It consists of two piezoelectric disc shaped plates (4 and 5) acting as clamping actuators and attached to a moving part which is a hollow cylinder (6). Similar structure of WPZM employing multilayer piezoelectric actuators as clamping elements was presented by Galutva et al [38]. A detailed description of the working principles of the two aforementioned motors is highlighted in [26]. The design and the structure of the WPZMs are widely ameliorated through the research efforts. Actually, this kind of motors is commercialized by many piezoelectric devices companies, such as the Swedish company Piezo Motor Uppsala AB, and the German company Physik Instrumente (PI) GmbH.

A linear WPZM is studied in this thesis for modeling and position control purposes. Thus the operating principle and the motor topology will be explained in details in Chapter V.

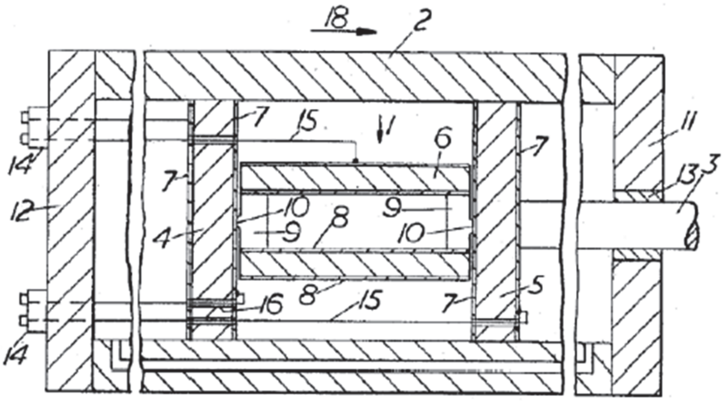

Fig. I-12. Walking piezoelectric motor proposed by Brisbane [37]

I.3.2 Ultrasonic piezoelectric motors

The Ultrasonic Motor (USM) is a piezoelectric motor driven by a high frequency (above 20 kHz) voltage at one of its mechanical resonant frequencies. As the working principle is based on the converse piezoelectric effect, the applied voltages will be converted by the piezoelectric ceramics into resonant vibrations. These vibrations are transmitted to a movable part (rotor) often through frictional contact, leading to a rotational or linear motion. The working principle of USM can be described by the process given in Fig. I-13:

- Step 1: The electrical energy is converted into ultrasonic vibrations by the piezoelectric materials mounted on the stator.
- Step 2: The resonant vibrations will be amplified and transmitted to the rotor through friction coupling to create motion.

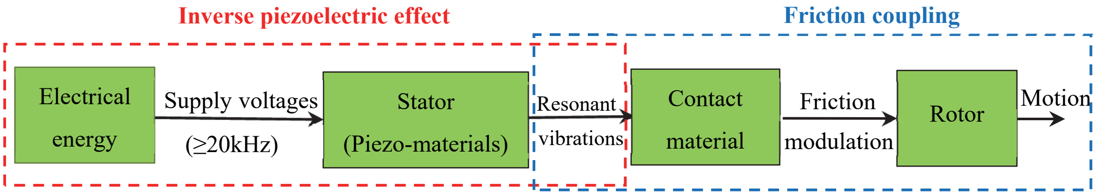

Fig. I-13. Synoptic of USM working principle

The first USM was introduced by Lavrinenko et al in 1965 [39], and it consisted of piezoelectric plate excited at the ultrasonic range and pressed against a smooth rotor (Fig. I-14.a). This invention marked the beginning of research works related to ultrasonic motors, and similar concept to Lavrinenko motor was developed in [40]. In 1973, a practical USM was proposed by H.V. Barth of HBM [41]. As shown in Fig. I-14.b, the rotor was pressed against two horns placed at different locations. By exciting one of the horns, the rotor was driven in one direction, and by exciting the other horn, the rotation direction was reversed [31]. The development of piezoelectric USM was significantly increased in the 1980s, due to the increase demand of more precise and sophisticated positioners which were not affected by magnetic fields, particularly by semiconductor industries.

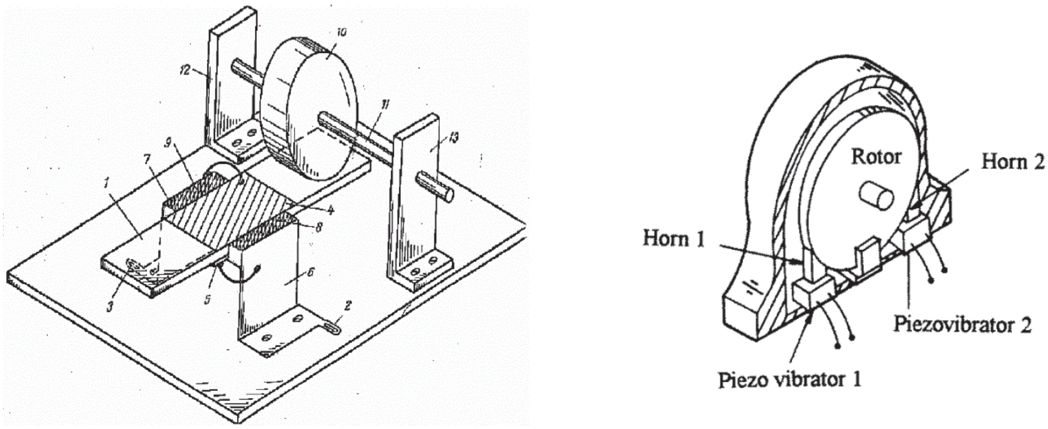

(a) (b)

Fig. I-14. Earlier structures of USMs proposed by : (a) Lavrinenko [40], (b) Bath [41]

The USMs can be classified depending on many criteria, such as the wave propagation method (traveling wave, standing wave), motion type (rotational, linear), geometric shape of the stator (Disk, Ring, Bar…), contact state (contact, non-contact), and rotor directions (unidirectional, bidirectional) [8, 26, 28, 42]. In this thesis report, the USMs will be classified based on the wave propagation method into traveling and standing waves.

I.3.2.1 Standing waves ultrasonic motors

The Standing Wave Ultrasonic Motor (SWUSM) is also called vibratory-coupler motor consists basically on a vibratory element driven close to its resonance frequency and generating elliptical motion of its tip portion. This motion is transferred to the rotor as a series of microscopic pushes. The SWUSM is generally a low cost motor (one vibration source) and has high efficiency, but its control in bidirectional motion is little complex [28]. In fact, the bidirectional motion of SWUSM can be obtained by employing two separate vibrating elements excited with a phase shift, or by superimposing two oscillations in a single resonator (bimodal motor).

Among the earlier structures of SWUSM, the simple design of unidirectional motor proposed by Sashida (Fig. I-15) [43]. It consists on a piezoelectric vibrator attached to a slider with a cant angle. When the piezoelectric element is excited, the vibrating piece will generate bending. If the bending deformation is sufficiently small compared to the piece length, elliptical motion of the piece tip will be created. This motion will be transmitted to the slider through friction contact.

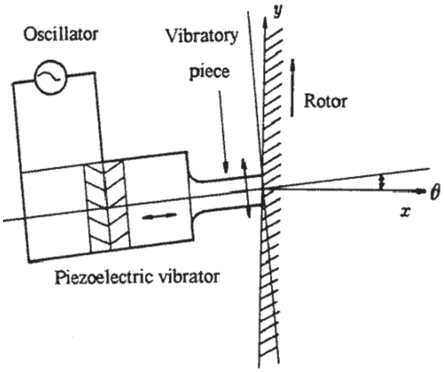

Fig. I-15. Vibratory-coupler type motor proposed by Sashida [43]

Endo et al [44] proposed a bidirectional SWUSM which employs two quadratic oscillations of piezoelectric elements in order to create elliptical motion of the common tip. The motion direction of the motor can be reversed by switching the driving voltages. An interesting design of bidirectional rotational SWUSM using two orthogonal bending modes of a hollow cylinder was developed by Uchino et al [45]. This design is at the origin of the development of the smallest worldwide linear PZM by New Scale Technology, Inc [46] in a series of squiggle motors, where the smallest version has a size of 1.5*1.5*6 mm. As shown in Fig. I-16, the squiggle motor is mainly composed by a threaded nut, screw, and four piezoelectric plates. The piezoelectric plates are excited by two phase shifted voltages (+/-90°), allowing the nut to vibrate in a fixed resonance frequency. The vibration sequences of the nut will cause the screw to rotate and translate with nanometer resolution.

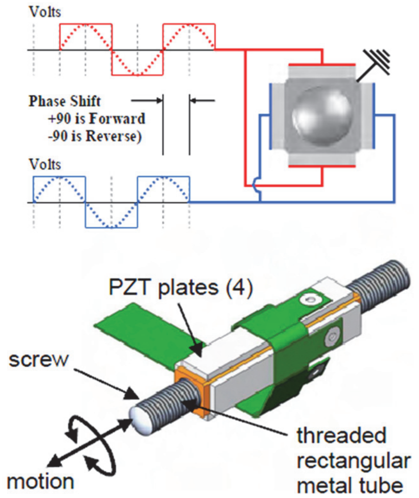

Fig. I-16. The squiggle motor from New Scale Technology [46]

An example of bimodal piezoelectric SWUSM was commercialized by Nanomotion Ltd in a series of HR motors [47]. Similar structure is also developed and commercialized by Physik Instrumente GmbH in a series of PIline ultrasonic motors [48]. The operation of these motors is based upon resonant asymmetric excitation of a two standing waves in a piezo-ceramic plate element. The elliptical motion of the piezo-ceramic plate is transmitted into linear movement of the bar through friction (rotational version is also commercialized). The basic design of this motor and the motion sequences of the piezo-element are shown in Fig. I-17.

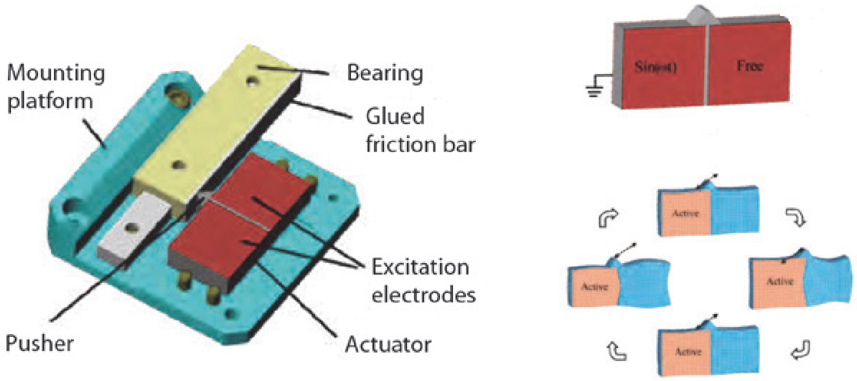

Fig. I-17. Concept of PIline ultrasonic motor series from Physik Instrumente GmbH [48]

I.3.2.2 Traveling waves ultrasonic motors

The Traveling Waves Ultrasonic Motor (TWUSM) was invented by Sashida in 1982 [49] and commercialized one year later by Shinsei Corporation [50] in a serie of USR motors. In this type of motor, the elliptical trajectory of the contact point between the stator and rotor results from a traveling wave. This Traveling Wave (TW) is formed by the superposition of two standing waves with a phase shift of 90° both in time and space. The TWUSM can be easily driven in bidirectional motion by switching the driving voltages phase shift between +/-90°. The original invention of TWUSM was a rotary motor and it has had a great success in the lenses drive of autofocus camera and watches. The structure of rotary TWUSM and its working principle will be explained in details in Chapter III, where an example of TWUSM motor will be studied for modeling and position control purposes.

Linear TWUSM was also proposed by Sashida in 1985 in two configurations; straight beam and ring beam types [51]. The prototype of straight beam TWUSM is shown in Fig. I-18.a, it consists of two langevin vibrators fixed on both ends of the beam. When the vibrators are exited, one will act as vibrator and the second as absorber to prevent the reflection of the TW [42]. The generated TW will transmit through friction contact in order to move the slider pressed against the beam. TWUSM with ring-type stator was proposed by Hermann et al. [52] as shown in Fig. I-18.b. In this case, the TW is generated by the piezoelectric ceramics bonded inside the ring beam. The slider will perform linear motion when it is pressed against the linear portion of the beam. Many attempts to create linear TWUSM are also reported in [53, 54].

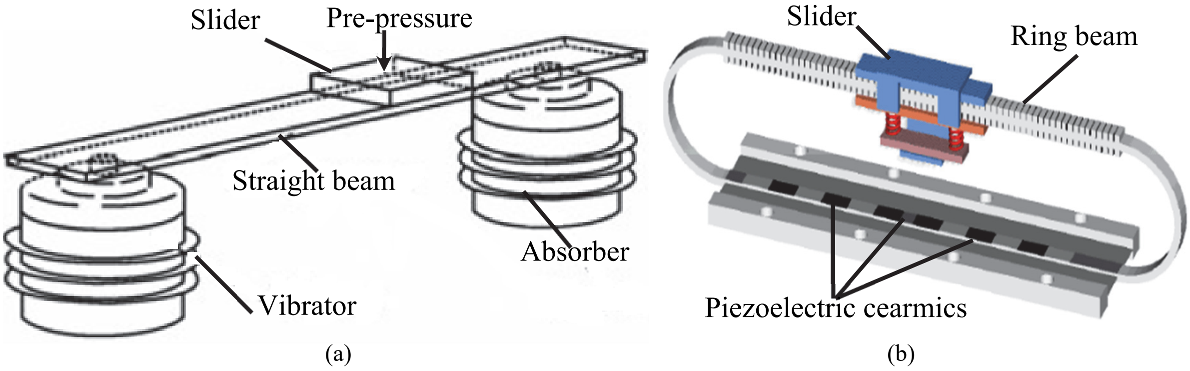

(a) (b)

Fig. I-18. Prototype of straight beam TWUSM [42] , (b) Linear ring-type TWUSM [52]

I.4 Piezoelectric motor applications

Piezoelectric motors are increasingly used in various engineering applications where the accuracy, efficiency, miniaturization, and multi degrees of motion are required. In this section, a brief review of the PZMs applications in different engineering fields will be highlighted. Before starting this review, let us summarize the merits and demerits of PZMs in the table below:

Table I-1: Characteristics of PZMs

Merits of PZMs	Demerits of PZMs
• Ultra-high precision (nanometer scale) • Fast response • Compact and flexible design • Miniaturization • Silent drive • High torque/size ratio • High torque at low speed without gear • High holding torque without supply • No-backlash • Vacuum compatible • Insensitive to high magnetic fields	• Nonlinear variation of the output characteristics as function of driving parameters • Nonlinear behaviors when operating close to the resonance • Specific drive circuits • Less life time due to frictional drive

➢ Optics and autofocus camera:

The compact size, fast response time, and self-locking at rest position make PZMs an attractive solution for focusing, zooming, and image stabilization in cameras. These features make also PZMs suitable candidate for the adjustment of lens mirrors of optical equipment. Actually, all major cameras, cellular phones, and lens manufacturers use PZMs especially the inertia and ultrasonic motors [55]. Canon realized the world's first practical application of an USM in auto focus lenses and fast zoom drive of digital camera [56] (Fig. I-19.a). Olympus is using multi-mode excitation type motor which employs multilayer vibrating element [55]. Samsung electro-mechanics in collaboration with the Penn State University developed in 2003 a zoom and focus mechanism for cellular phone using two rotary USMs [57]. Another camera model is also proposed by Samsung electro-mechanics employing linear multilayer USM. The Korean manufacturer designed also various miniature PZMs for lens positioning applications [55]. The New Scale Technology developed many solutions for optical and autofocus camera based on compact USMs (squiggle motor). This motor is employed also in an optical zoom module for higher resolution in smaller devices (Fig. I-19.b) [46]. The same company presents an Ultra-Thin Auto Focus (UTAF) for the new generation of phone camera [58]. Konica Minolta is using inertia PZMs for autofocus, zooming, and image stabilizations [59].

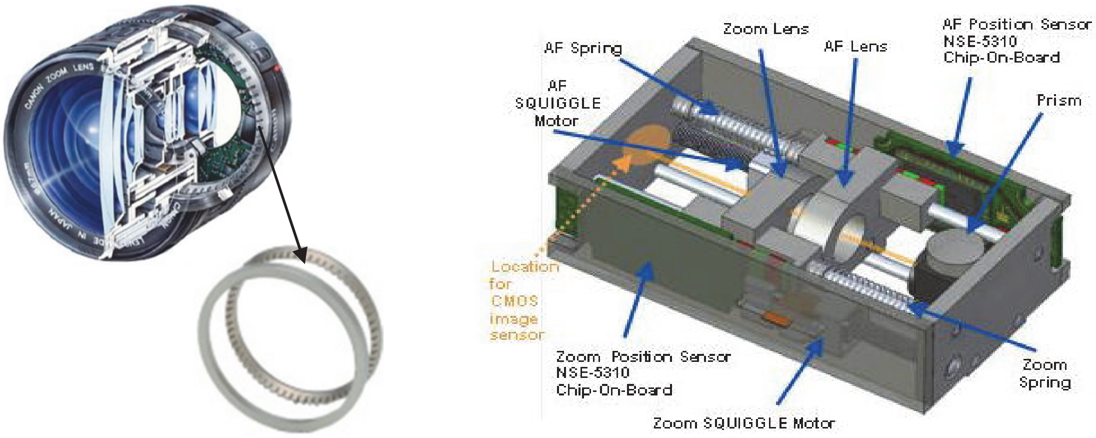

(a) (b)

Fig. I-19 . (a) Ring-type USM used in camera [56], (b) Optical zoom module using squiggle motor [46]

- Robotic applications

In addition to the precision and force capabilities, the high holding torque without supply and non-magnetic features make PZMs to be a suitable candidate for robotic application and especially to actuate Magnetic Resonance Imagery (MRI) and surgical robots. The ultrasonic and walking piezoelectric motors are the major type of PZMs used in such applications. It should be mentioned that this survey do not focuses on the micro and nano-robots based PZMs.

The Piezo LEGS developed by the Swedish company Piezo Motor Uppsala AB, which works with the walking principle are integrated to actuate medical robots for MRI and surgical operations. This motor is used by the Automation and Interventional Medicine (AIM) laboratory of the Worcester Polytechnic Institute (WPI) to design a various types of medical application robots. The robot shown in Fig. I-20 is guided by piezoelectric motors to capture ultra-high resolution images of the tumor using MRI and to actuate ultra-precise surgical tools to remove the tumor [60]. It consists on one module with X, Y, Z translations and two rotational modules. Four Linear Piezo LEGS are used to generate the linear motion to move the robot in the three directions and to insert the needle, while two rotary Piezo LEGS motors serve to drive aluminum lead screws. The AIM is very invested on PZMs powered MRI robots, the applications include stereotactic neurosurgery for deep brain stimulation, lead placement for Parkinson's disease, and brachytherapy seed implantation for prostate cancer therapy [60, 61]. The linear Piezo

LEGS with maximum stroke up to 80 mm and forces up to 40 N [62] are used for the linear motion of the robots, while the rotary versions of these motors are employed for rotational degrees of freedom.

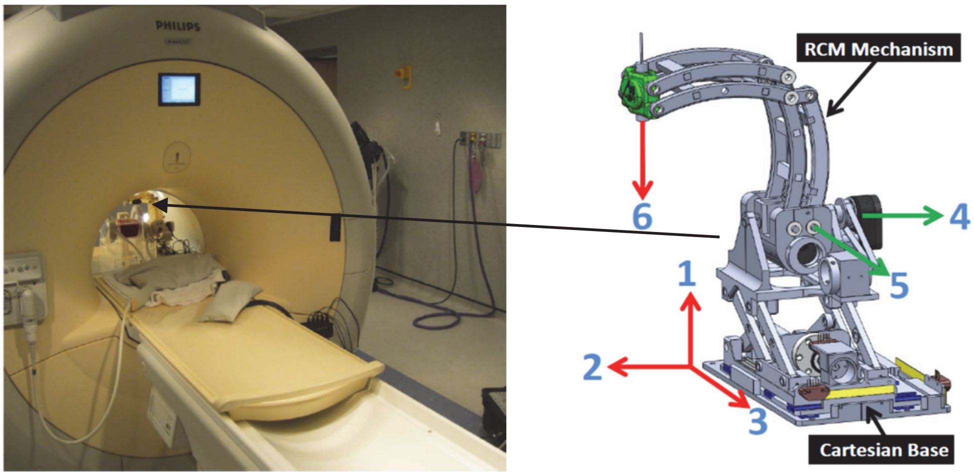

Fig. I-20. Piezoelectric motor powered MRI robots [60]

Robots based on USMs are reported in many research and industrial projects in the literature. One of the famous project of USM powered robot is the NeuroArm project, where a medical robot for neurological operations was developed. The latest version of the NeuroArm robot (Fig. I-21.a) employs sixteen ultrasonic motors from Nanomotion Ltd for multi-degrees of freedom motion [63]. Keio university of Japan team was developed a five-fingered robot hand (Fig. I-21.b) which has totally 20 Degrees Of Freedom (DOFs) [42]. Each DOF is driven by an USR30-B4 motor from Shinsei.Co, the hand has approximately the same size of human hand and weighs 853 g. Referring to the designer documents [64], the weight of the lightest hand driven by the traditional motor is 1400 g, and due to the fast response of USM, the hand response speed is faster than the human hand.

The PZMs are also a suitable candidate to actuate the production and assembling robots and for the pick and place automation. An example of these robot types, the prototype of Delta-3 robot proposed by Noliac (Fig. I-22.a). It is based on Clavel 's Delta robot [65], but without rotational degree of freedom. The Delta-3 robot can handle up to 4 kg within an area with a diameter of 20 cm and a height of 14 cm [66]. Physik Instrumente (PI) GmbH developed hexapod driver for robotic applications in production and assembling (Fig. I-22.b) [67]. The hexapod is driven by NEXLINE motors which are quasi-static stepping PZMs.

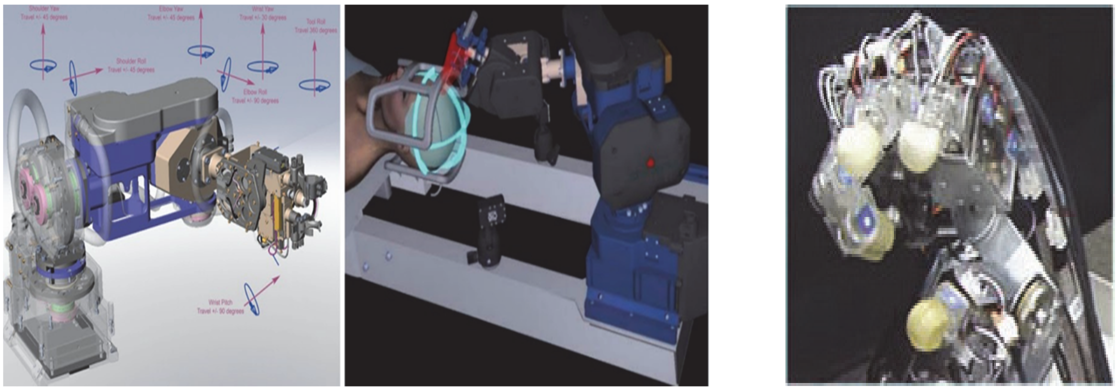

(a) (b)

Fig. I-21. (a) NeuroArm robot based on USMs [63], (b) five-fingered robot hand based on USMs [42]


(a) (b)

Fig. I-22. (a) Delta-3 robot based on PAD [66] , (b) Robotic arms equipped with hexapod [67]

- Automotive applications

The PZMs are promising actuators for automotive applications when silent, fast response, and efficient motors in high temperature are needed. Due to the smaller size, low speed without gear, and high torque density of USMs, they have been integrated in some automobiles. USMs have been used to adjust the rearview mirror, as shown in Fig. I-23.a [42]. Since there is no gearbox between the USM and the mirror, the output shaft of the USM can be directly connected with the mirror frame and the USM itself is fixed with the car body. The integration of the motor with the rearview mirror, which makes it lightweight, compact, and convenient for adjustment.

The USMs are employed also to adjust the driver's seat in automobiles. Fig.I-23.b shows an example of the USM adjustment mechanism of headrest attached to top of the seat [42]. The needed motor for such applications should be silent, small in size, fast in response, and delivering high torque with self-locking. The features of USMs make it suitable to meet the application requirements. The ultrasonic motors are also tested for the steering wheel adjustment mechanism. The proposition of USMs allows the avoiding of the slow response of the control system due to the considerable moment of inertia of motor associated to the gear system [42].

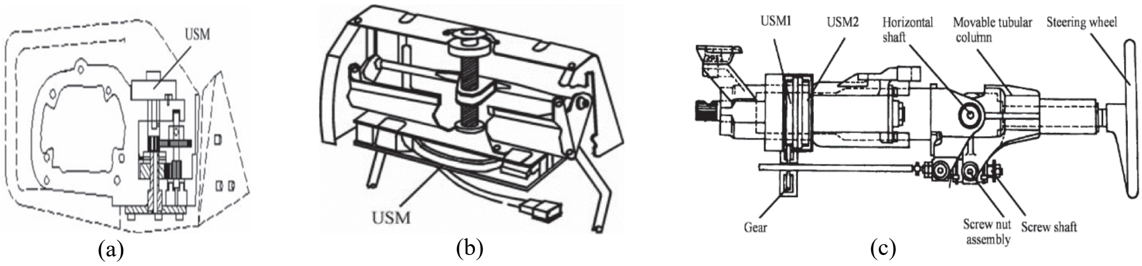

(a) (b) (c)

Fig. I-23. Automotive applications of USMs [42]: (a) rearview mirror, (b) headrest, (c) steering wheel

Quasi-static PZM of type Piezoelectric Actuator Drive (PAD) is used for silent and smooth window operation of a car door (Fig. I-24) [68]. Due to the PAD sensorless potentials, it offers a sensitive and intelligent pinch detection without additional sensors.

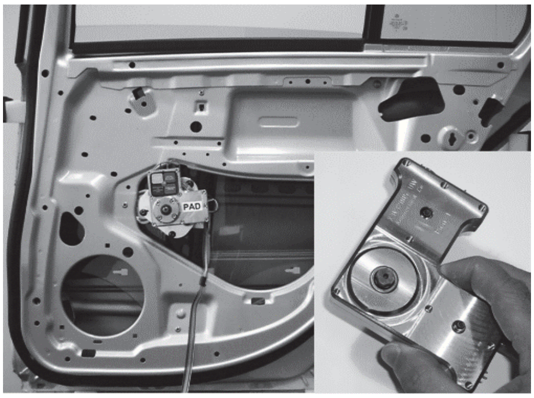

Fig. I-24. PAD application in car door [68]

- Aircraft and aerospace applications

Compact, efficient, precise, and fast response actuators are generally needed to meet the aircraft and aerospace application requirements. These conditions facilitate the integration of PZMs into the space engineering fields. PZMs are mostly used for the flap actuation for noise cancellation, flight control surface actuation, and active flutter suppression, and scanning and image stabilization. The linear and rotary stepping piezo motors (LSPA and RSPA) developed by Cedrat Technologies [69] are integrated into space telescopes mainly to actuate high dynamic and high precise scan mechanism, and to control a laser fiber extension. In [42] two dimensional airfoil control system prototype was presented, in which the USM is used in wind tunnel model test.

The DARPA /AFRL/NASA Smart Wing program conducted by Northrop Grumman Corporation (NGC) team, aimed to develop novel and smart technologies and demonstration of relevant concepts to improve the aerodynamic performance of military aircraft [70]. In one of the project phases, the team addressed a comparative study between smart materials based motors, USMs, and conventional electromagnetic motors, which are tested for an adaptive control of the aileron. The results show that the USMs have higher power density than the other motors, and enable simpler integration into the limited available space.

- Other applications

The ultra-precise PZMs positioning systems commercialized by the worldwide piezo-devices manufacturers [46, 47, 62, 67, 69, 71], are used in several applications where the precision , fast response, and small size criteria are important. These positioning systems are generally multi DOFs platforms. There are very interesting solutions for biotechnology and biomedical engineering applications, especially the cells manipulation and optical microscope actuation. The PZMs are highly requested to actuate medical equipment. Quasi-static and USM PZMs are used to drive high precision mechanism in ophthalmic surgery, adaptive diaphragm positioning, and compact piezoelectric micro-pumps.

Benefiting of the features mentioned above, the PZMs are integrated in many other applications including the semiconductor technology, surveillance camera platforms, and scientific instrumentation.

I.5 Thesis contributions

Despite the performances of piezoelectric motors listed above, their integration into the industrial fields does not reflecting the real motor potentials. This is due to many factors including the special structure and the specific driving circuit requirements, uncertain motor parameters, sensitivity to external perturbations (load, temperature, electrical noises, etc.), and the nonlinear variation of the motor output characteristics as function of the driving parameters. In consequence, the establishment of PZM models for control design and the synthesis and implementation of accurate and robust position controllers for practical engineering applications still in the heart of research efforts.

Thus, the contributions of this thesis can be summarized as following:

- The study of three different topologies of PZMs for modeling and position control purposes, the studied motors are:
  - Rotary traveling wave ultrasonic motor from the USR series of Shinsei.Co (USR60) [50].
  - Rotary Piezoelectric Actuator Drive (PAD) from Noliac [71].
  - Linear walking piezoelectric motor from Physik Instrumente (PI) GmbH [67].
- The establishment of electromechanical models of the rotary PZMs (USR60 and PAD) which describe the motor motion generation process, reflect the output motor characteristics variation function of driving parameters, and can be used for closed loop control validation.
- The synthesis of precise position controllers of PZMs that fulfill the specific application requirements of the three studied PZMs. Two controllers are proposed:
  - H-infinity control based on the mixed sensitivity approach.
  - Discrete time RST control based on pole placement technique.
- The guarantee of precision, stability, and robustness criteria in one simple and effective controller whatever the motor topology.
- The validation of the precision and robustness performances of the proposed position controllers without additional compensation systems of the nonlinear behaviors (especially the speed-phase shift dead zone of the USR60). These techniques do not require parameters adaptation approach to overcome the uncertain motor parameters as reported in almost research works related to the position control of PZMs.

  This is in order to prove the feasibility of positioning engineering applications based on PZMs and with simple, precise, and robust position controllers.
- The design of compact experimental platforms based on the three PZMs, and the experimental validation of the proposed positioning systems. Comparison of experimental positioning results with conventional PID control method is carried out to highlight the advantages of the proposed methods.
- The evaluation of strengths and limitations of the three PZMs regarding to the robotic applications. The evaluation criteria are related to the motor topologies, electromechanical characteristics, drive techniques, and closed loop positioning capabilities.

I.6 Thesis outlines

The thesis is organized as follows:

Chapter II deals with the synthesis approaches of robust position controllers dedicated to piezoelectric motors. The requirement specifications of piezoelectric motor applications are firstly introduced to justify the choice of H-infinity and discrete time RST controllers. The two controllers are synthesized for a generalized plant in order to be applied later to each studied motor as function of each motor model.

Chapter III focuses on the modeling and design of robust closed loop position controllers for rotary traveling wave ultrasonic motor. This chapter starts with the illustration of the structure and working principle of rotary TWUSM. Afterwards, a literature review about the modeling and position control of TWUSM is proposed to clarify the contributions of the proposed work. Then, the modeling of USR60, position controller synthesis, and simulation and experimental validations of the precision and robustness of the proposed methods will be respectively detailed. A comparative study of experimental results between the H-infinity, RST, and PID controllers will be proposed at the end of this chapter to prove the performance of the proposed methods.

Chapter IV presents the modeling and design of robust closed loop position controllers for Piezoelectric Actuator Drive (PAD). Rotary quasi-static piezoelectric motor with innovative topology is studied in this chapter for position control purposes. The state of the art of the modeling and position control method of PAD is detailed in the introduction of this chapter. The working principle, and the specific features of the PAD are then illustrated. Similarly to the other motor, the modeling, simulation, and experimental results of the PAD positioning system based on robust control methods will be discussed.

Chapter V is dedicated to the modeling and design of robust closed loop position controllers for linear Walking Piezoelectric Motor (WPZM). In this chapter, linear quasi-static piezoelectric motor based on walking drive method is studied. A survey of the position control techniques of WPZM and the advantages of the proposed method are firstly introduced. The working principle of this motor and the positioning platform are described. The model experimental identification process and the synthesis procedure of position controllers are explained in details. The simulation and experimental positioning results of WPZM are presented and discussed at the end of this chapter.

The suggestions, recommendations, and general conclusions related to the studied motors will be addressed in Chapter VI.

Chapter II

Synthesis of Robust Position Controllers of Piezoelectric Motors

II.1 Introduction

The position control of piezoelectric motors is in the heart of recent research topics related to these motors. This is principally due to the increase demand of high accurate positioning systems based on piezo-motors. In other hand, the special structure of the motor and the nonlinear behaviors of the used materials present a serious challenge for position control. To prove the performances of piezoelectric motors in closed loop positioning systems, the mostly developed techniques deal with the adaptive based model methods and the on-line learning methods which involve the fuzzy logics and neural networks. The time consumption and the industrial integration efforts of such techniques into engineering applications are real locks.

Thus, the contribution of the proposed control methods is to guarantee the high precision performances and robustness against motor nonlinear behaviors and external disturbances using simple and easy implemented controllers. Moreover, the developed controllers will fulfill the positioning performances with different technologies (ultrasonic, quasi-static) and topologies of piezoelectric motors.

In this chapter, the synthesis approaches of two position controllers for piezoelectric motors will be detailed. The first one is a H-infinity controller integrating sensitivity functions to prove the robustness issues. The second one is a discrete time RST control based on pole placement technique to achieve high performances in a specified frequency operation range. The controller concepts for generalized plants is presented in this chapter, then it will be applied to control the different studied piezoelectric motors.

II.2 H-infinity position controller

The shortcomings of classic feedback control methods motivate researchers to shift to H_∞ optimization methods to achieve the desired performances with high robustness levels [72]. The significant development of the H_∞ control methods in an engineering context are started with Helton [73] and Zames [74]. This technique was then developed and applied to many process [72] . In this section, we will begin with a general control problem formulation into which we can cast the H_∞ optimization method. The selection of the controller parameters as function of the closed loop performances of generalized plant will be then explained. The generalized plant will be replaced by each motor plant to deal with the different studied systems. It is not our intention to explain in details the mathematical analysis of H_∞ optimization method since it can be easily found in the literature [72, 75-77] and many softwares for solving such problems are available.

In the current research, the control system design is made as follow: defining the closed loop performances of the positioning system, then synthesis and parameters selection of the robust controller in order to achieve the desired performance. In comparison with the other feedback control approaches, the robust H_∞ control exhibits the advantage of combining the performance, robustness, and easy implementation requirements in one controller design procedure.

The H_∞ optimization problem can be posed in the standard formulation as shown in Fig. II-1 [77]. In this figure, P(s) is the generalized plant, K(s) is the controller, u and y are respectively the control and measured signals, e are the error signals, and w are the exogenous signals such as the reference signal and the external perturbations.

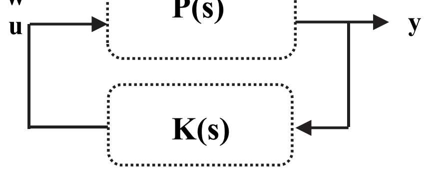

Fig. II-1. Generalized plant [77]

H_∞ optimization problem appears to be formulated as the task of designing a stabilizing controller K(s), which minimizes the H-infinity norm of the closed loop transfer matrix T_{ew} from w to e for a given plant P(s) (see Fig. II-1), defined by state space equations [77] :

$$\begin{aligned} \dot{x} &= Ax + B_1 w + B_2 u \\ e &= C_1 x + D_{11} w + D_{12} u \\ y &= C_2 x + D_{21} w + D_{22} u \end{aligned} \qquad \text{II-1}$$

Therefore, the state-space realization of the generalized plant P(s) can be written as:

$$\begin{pmatrix} \dot{x}(t) \\ e \\ y \end{pmatrix} = \begin{pmatrix} A & B_1 & B_2 \\ C_1 & D_{11} & D_{12} \\ C_2 & D_{21} & D_{22} \end{pmatrix} \begin{pmatrix} x(t) \\ w(t) \\ u(t) \end{pmatrix} \qquad \text{II-2}$$

The algorithms used to solve the H_∞ optimization problem are generally based on the state-space solutions [72]. To guarantee the existence of the solution of H_∞ problem, the following assumptions should be taken into account:

(A1): (A, B_2, C_2) is stabilizable and detectable.

(A2): D_{12} and D_{21} have full rank.

(A3): $\begin{bmatrix} A - jwI & B_2 \\ C_1 & D_{12} \end{bmatrix}$ has full column rank for all ω.

(A4): $\begin{bmatrix} A - jwI & B_1 \\ C_2 & D_{21} \end{bmatrix}$ has full row rank for all ω.

Assumption A1 is required for the existence of stabilizing controllers K(s), and assumption A2 is sufficient to ensure that the controllers are proper and hence realizable, Assumptions A3 and A4 ensure that the optimal controller does not try to cancel poles or zeros on the imaginary axis which would result in closed loop instability [72]. Another assumption (A5) can simplify the resolution algorithm:

(A5): $D11 = 0$ and $D22 = 0$

The system presented in Fig. II-1 can be also described by the transfer matrix between the inputs and the outputs as:

$$\begin{pmatrix} e(s) \\ y(s) \end{pmatrix} = P(s) \begin{pmatrix} w(s) \\ u(s) \end{pmatrix} = \begin{pmatrix} P_{11}(s) & P_{12}(s) \\ P_{21}(s) & P_{22}(s) \end{pmatrix} \begin{pmatrix} w(s) \\ u(s) \end{pmatrix} \qquad \text{II-3}$$

$$u(s) = k(s)\, y(s)$$

The closed loop transfer function from w to e is given by the Linear Fractional Transformation (LFT):

$$e(s) = F_l\big(P(s), K(s)\big) w(s) \qquad \text{II-4}$$

where

$$F_l\big(P(s),K(s)\big) = P_{11}(s) + P_{12}(s)K(s)(I - P_{22}(s)K(s))^{-1}P_{21}(s) \qquad \text{II-5}$$

With reference to the generalized system plant (Fig. II-1), the optimal H∞ control consists on finding all stabilizing controllers K(s) which minimize the following standard value [72]:

$$\|F_l(P,K)\|_\infty = \max \sigma(F_l\,(P,K)) \qquad \text{II-6}$$

Therefore, the H∞ control approach consists on finding all stabilizing controllers K which for a given γ, it satisfy the following inequality:

$$\|F_l(P,K)\|_\infty < \gamma \qquad \text{II-7}$$

This problem can be solved using the resolution of Ricatti equations [77, 78], and by updating γ iteratively.

To deal with the motor position control, the motor plant is represented now by G(s) and controlled by K(s) as shown in Fig. II-2.a. In this figure, b is an input perturbation, r and y are respectively the reference and measured positions, u is the control signal, and ε is the tracking error. The transfer matrix of the system given in Fig. II-2.a, can be written as [77]:

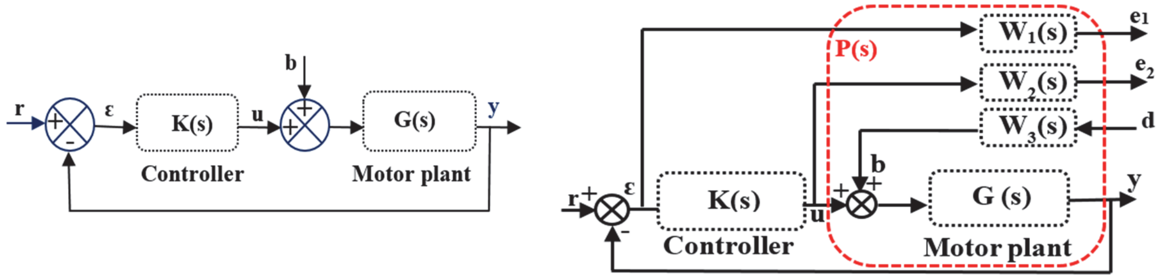

(a) (b)

Fig. II-2. (a) Closed loop configuration [77], (b) Closed loop augmented by weighting filters [77]

$$\begin{pmatrix}\varepsilon\\u\end{pmatrix} = \begin{pmatrix}S & -SG\\KS & -KSG\end{pmatrix}\begin{pmatrix}r\\b\end{pmatrix};\, S = \frac{1}{(1+KG)} \qquad \text{II-8}$$

Where S is the sensitivity function and it can be defined as the transfer function between the reference signal r and the tracking error ε. The transfer function SG represents the effect of the system input perturbation (b) on the error (ε). KS represents the effect of the reference (r) on the control signal (u). KSG represents the effect of the input perturbation on the control signal.

In II-9, as it will be done in most of the following work , the Laplace term “s” will be omitted for the sake of simplicity. Referring to the standard formulation (Fig. II-1), the equivalent LFT (F_l (P(s), K(s))) can be identified for the system given in Fig. II-2.a. After that, finding γ>0 and the controller K which internally stabilize the closed loop and ensuring that its H∞ norm is lower than γ:

$$\|F_l(P(s)),K(s)\|_\infty = \left\|\begin{matrix}S & -SG\\KS & -KSG\end{matrix}\right\|_\infty < \gamma \qquad \text{II-9}$$

In order to achieve the closed loop performances and to prove the robustness potentials, the mixed sensitivity H∞ control method is often applied (Fig. II-2.b) [72, 77]. In Fig. II-2.b, the error ε is weighted by the filter W_1, the control signal u is weighted by W_2, and the input perturbation b is the output of the

weighting filter W_3. In fact, the mixed sensitivity can be defined as the transfer function shaping problems in which the sensitivity function S is shaped along with one or more other closed loop transfer functions such as KS or the complementary sensitivity function T=1-S. For typical industrial process, the low order plant models (first or second order) are employed. As a consequence, applying this approach generates excessive overshoot in the time responses [79]. The addition of weighting filters (Fig. II-2.b) to the mixed sensitivity approach will perform simultaneously the controller performances (response time, overshoot, and tracking) and robustness issues. Moreover, the weighting filter parameters will be selected in order to shape the closed loop transfer functions S and KS. The weighting filters are crucial to confirm the robustness of the H_∞, for example the disturbance d can be successfully rejected if the maximum singular value of S is made small at low frequencies. To do this, we should select W_1 as low pass filter with a bandwidth equal to that of the disturbance. The size of KS is also important to improve the robustness to modeling uncertainty as additional perturbation [72].
The transfer matrix of the system plant shown in Fig. II-2.b is given by:

$$\begin{pmatrix} e_1 \\ e_2 \end{pmatrix} = \begin{pmatrix} W_1 S & -W_1 S G W_3 \\ W_2 K S & -W_2 S G W_3 \end{pmatrix} \begin{pmatrix} r \\ d \end{pmatrix} \qquad \text{II-10}$$

Referring to II-9, the H_∞ problem consists now on finding $\gamma > 0$ and the controller K which internally stabilize the closed loop and ensuring that:

$$\left\| \begin{matrix} W_1 S & -W_2 S G W_3 \\ W_2 K S & -W_2 K S G W_3 \end{matrix} \right\| < \gamma \qquad \text{II-11}$$

If II-11 is satisfied, the following inequalities must be satisfied:

$$|S(j\omega)| < \frac{\gamma}{|W_1(j\omega)|} \qquad \text{II-12}$$

$$|S(j\omega)G(j\omega)| < \frac{\gamma}{|W_1(j\omega)W_3(j\omega)|} \qquad \text{II-13}$$

$$|K(j\omega)S(j\omega)| < \frac{\gamma}{|W_2(j\omega)|} \qquad \text{II-14}$$

$$|K(j\omega)S(j\omega)G(j\omega)| < \frac{\gamma}{|W_2(j\omega)W_3(j\omega)|} \qquad \text{II-15}$$

Therefore, the problem resolution topology can be resumed as given in the flowchart bellow:

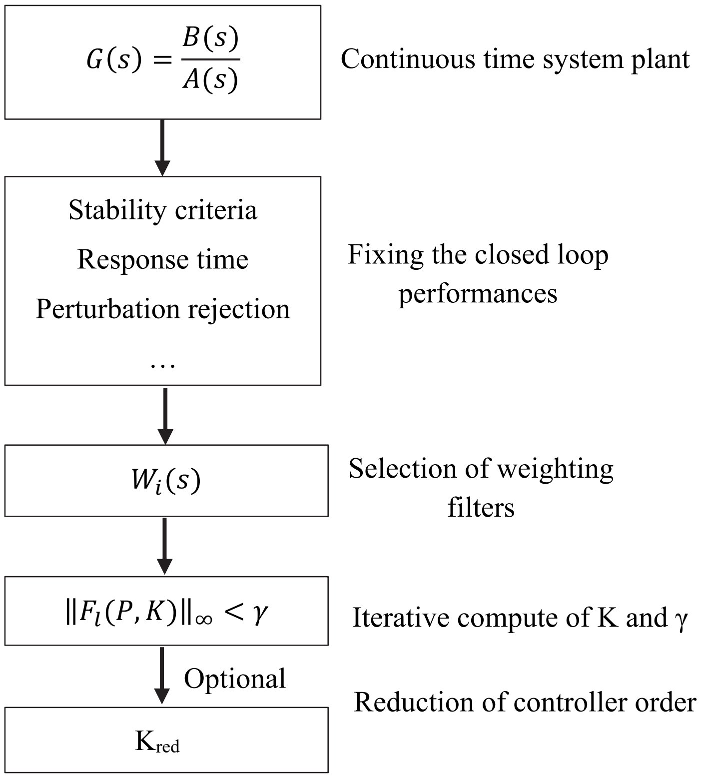

Fig. II-3. Flowchart of H_∞ control synthesis approach

The expression of the weighting filters is given by [79]:

$$W_i = \frac{(s \,/\, M + \omega_0)}{(S + A_1 \omega_0\,)} \qquad \text{II-16}$$

where ω_0 is the closed loop bandwidth, A_1 is the minimum steady state error, and M is the high frequency amplification gain.

The transfer $1/W_1$ should have a low gain at low frequency to prove the controller precision and perturbation rejection capability. Whereas the filter cut-off frequency can be interpreted as the minimal system bandwidth.

The most important parameter of W_2 is the cut-off frequency that will limit the maximum system bandwidth to avoid very fast system response and therefore excessive control signal values. As W_2 is used to shape the transfer function KS, the primordial goal of W_2 is to perform the robustness to model parameters uncertainty.

The weighting filter W_3 is a supplementary degree of freedom to improve the perturbation rejection capability of other types of external perturbations.

This robust H_∞ control concept will be applied to each studied piezoelectric motor (in the next chapters) in order to synthesis ultra-precision robust controllers.

II.3 RST position controller

The RST controller presented in Fig. II-4 is a two degree of freedom digital controller based on a robust pole placement method allowing one to impose different specifications in terms of tracking and regulation performances. This digital control approach consists on finding the polynomials R, S, and T which satisfies the desired performances with respect to the disturbances and reference signal.

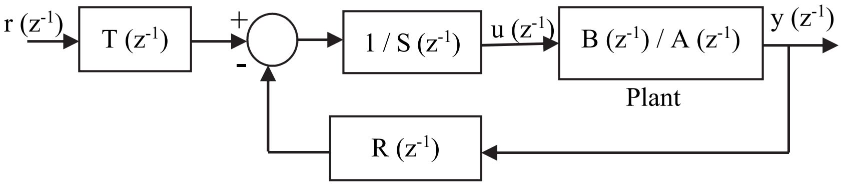

Fig. II-4. Discrete time RST control system

Let us assume that a discrete-time plant, or a continuous time plant sampled at a given period t_s can be described in terms of z-transforms as shown in in Fig. II-4. Where u is the control signal, and r and y are the reference and measured signals. The z-transform of the control signal $u(z^{-1})$ can be written as:

$$U(z^{-1}) = \frac{T(z^{-1})}{S(z^{-1})} r(z^{-1}) - \frac{R(z^{-1})}{S(z^{-1})} Y(z^{-1}) \qquad \text{II-17}$$

The discrete time closed loop transfer function can be written as following:

$$G_{CL}(z^{-1}) = \frac{B(z^{-1})T(z^{-1})}{A(z^{-1}).S(z^{-1}) + B(z^{-1})R(z^{-1})} = \frac{B(z^{-1})T(z^{-1})}{D(z^{-1})} \qquad \text{II-18}$$

where

$$D(z^{-1}) = A(z^{-1}).S(z^{-1}) + B(z^{-1})R(z^{-1}) = 1 + p_1 z^{-1} + p_2 z^{-2} + \cdots \qquad \text{II-19}$$

is the denominator of the closed loop system and it contains the system poles. It is also called as the characteristic polynomials of the closed loop system. This explain why the desired closed loop performances will be expressed in terms of closed loop poles and eventually in terms of desired zeros. The polynomial $S(z^{-1})$ and $R(z^{-1})$ perform respectively the regulation and tracking performances of the closed loop.

As can be seen in II-18, $T(z^{-1})$ appears only in the numerator giving the second degree of freedom to this controller, which allows the distinction between tracking and regulation performance specifications. In the presence of disturbances (Fig. II-5), there are other important sensitivity functions linking the disturbances to the outputs and inputs of the plant that should be considered in the synthesis approach.

The transfer function between the disturbance v(t) (such as loads) and the output y(t) (output sensitivity function) can be written as:

$$S_{yv}(z^{-1}) = \frac{A(z^{-1}).S(z^{-1})}{A(z^{-1}).S(z^{-1}) + B(z^{-1}).R(z^{-1})} \qquad \text{II-20}$$

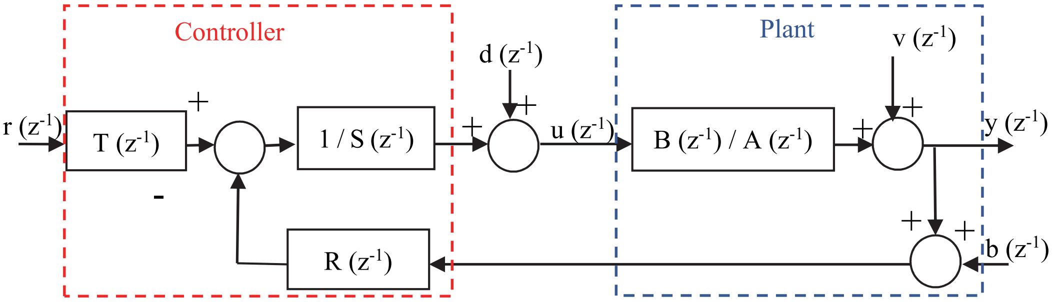

Fig. II-5. Discrete time RST control system in presence of disturbances

This sensitivity function allows the characterization of the perturbation rejection performances through the polynomial S(z^{-1}) coefficients. In fact, to prove the disturbance rejection of the digital controller in a specified frequency, S(z^{-1}) must contain a zero corresponding to this frequency [80].

The output measured signal can be noised (sensor + signal acquisition noises), the transfer function that relates the noises b(t) to the output signal y(t) can be used to improve the noises rejection potentials. This transfer function is given by:

$$S_{yb}(z^{-1}) = \frac{-B(z^{-1})R(z^{-1})}{A(z^{-1}).S(z^{-1}) + B(z^{-1})R(z^{-1})} \qquad \text{II-21}$$

The common noises in this side are generally a high frequency signals. Therefore, the idea is to achieve low gain of this transfer function in this frequency range in order to attenuate these noises.

The input sensitivity function is defined as the transfer function between u(t) and the disturbance v(t), and is given by:

$$S_{uv}(z^{-1}) = \frac{-A(z^{-1})R(z^{-1})}{A(z^{-1}).S(z^{-1}) + B(z^{-1})R(z^{-1})} \qquad \text{II-22}$$

This sensitivity function permits the evaluation of disturbance effects on the input signal. The control system robustness to such disturbances in a specific frequency range can be improved via the adjustment of polynomial R(z^{-1}) coefficients [80].

The fourth sensitivity function is the transfer function that relates the disturbances d(t) to the output signal y(t) which describes the influence of d(t) on the output signal of the plant. It is also called the input disturbance-output sensitivity function and it is given by:

$$S_{yd}(z^{-1}) = \frac{B(z^{-1})S(z^{-1})}{A(z^{-1}).S(z^{-1}) + B(z^{-1})R(z^{-1})} \qquad \text{II-23}$$

This sensitivity function serves to compensate the unstable poles of the plant by the zeros of R(z^{-1}).

It should be mentioned that the closed loop system of the plant presented in Fig. II-5 is asymptotically stable if and only if all the four sensitivity functions (S_{yv}, S_{yb}, S_{uv}, and S_{yd}) are asymptotically stable.

The first step of the digital RST pole placement method consists on defining the desired performances. These performances can be expressed by the reference transfer function model of the plant $G_m(z^{-1})$:

$$G_m(z^{-1}) = \frac{B_m(z^{-1})}{A_m(z^{-1})}$$

$$G_m(z^{-1}) = \frac{B_m(z^{-1})}{A_m(z^{-1})} \qquad \text{II-24}$$

The idea is then to carefully select the system poles in order to make equal the reference closed loop model and the actual input-output closed loop transfer function y/r:

$$\frac{y(z^{-1})}{r(z^{-1})}=\frac{B(z^{-1})T(z^{-1})}{A(z^{-1})S(z^{-1})+B(z^{-1})R(z^{-1})}=\frac{B_m(z^{-1})}{A_m(z^{-1})} \qquad \text{II-25}$$

In other hand, the closed loop transfer function can be written as:

$$G_{CL}(z^{-1})=\frac{B^{+}(z^{-1})\,B^{-}(z^{-1})}{A^{+}(z^{-1})\,A^{-}(z^{-1})} \qquad \text{II-26}$$

Where $B^{-}$and A^{-}contain all poles and zeros of $G_{CL}(z^{-1})$ that cannot be compensated. $B^{+}$and A^{+}contain all the other terms.

As mentioned above that $G_m(z^{-1})$ was chosen in order to impose the desired closed loop poles, with the only constraint that its numerator had to contain as a factor the plant pure delay and its un-compensable zeros (zeros lying outside of the unit circle) and zeros that one decides not to compensate, all regrouped in the polynomial $B^{-}(z^{-1})$:

$$B_m(z^{-1})=B^{-}(z^{-1})B'_m(z^{-1}) \qquad \text{II-27}$$

In order to ensure an unity gain in steady state $B_m(1)=1$, a constant factor (A_0) is introduced in the expression of $T(z^{-1})$:

$$T(z^{-1})=A_0B'_m(z^{-1}) \qquad \text{II-28}$$

The partial transfer function from the reference r to the true error signal $\varepsilon=y-r$, is given according to II-25 as:

$$\frac{\varepsilon(z^{-1})}{r(z^{-1})}=1-\frac{y(z^{-1})}{r(z^{-1})}=1-G_m(z^{-1}) \qquad \text{II-29}$$

To cancel the steady state errors in response to polynomial references ($r(t)=\alpha t^{m}$), which have a z-transform defined by:

$$r(z^{-1})=\frac{r_1(z^{-1})}{(1-z^{-1})^{m+1}} \qquad \text{II-30}$$

Where r_1 is a polynomial in z^{-1}, it should be also mentioned that $m=0$ in the case of step signal and equals to 1in the case of ramp.

It is necessary and sufficient that $(1-z^{-1})^{m+1}$ divides A_m-B_m, according to the final limit theorem of the z-transform. This condition can be expressed also by:

$$A_m-B_m=(1-z^{-1})^{m+1}L(z^{-1}) \qquad \text{II-31}$$

Where $L(z^{-1})$ is an unknown polynomial to be determined.

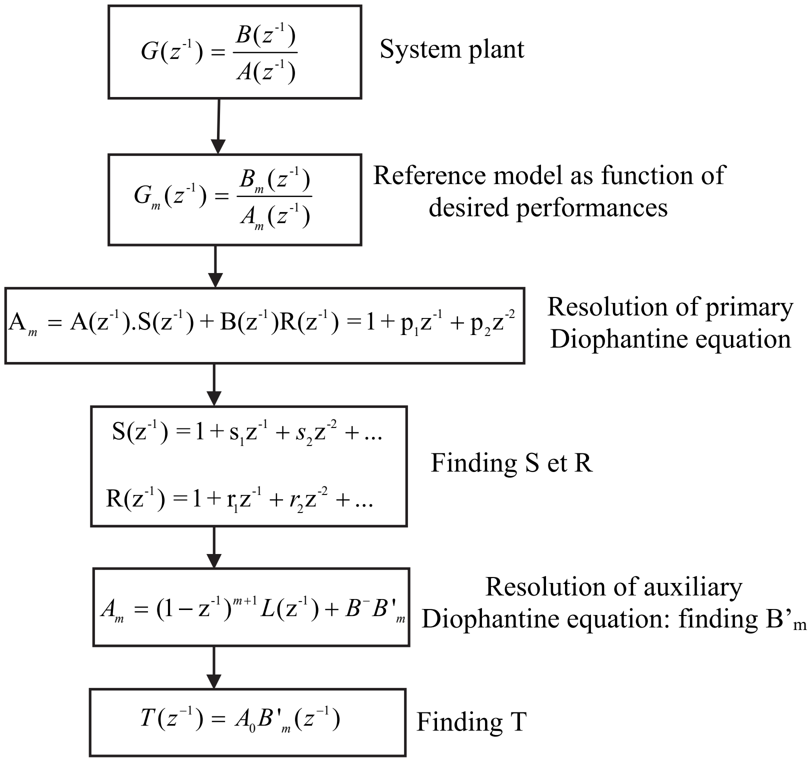

Fig. II-6. Flowchart of RST control synthesis approach

Referring to equations II-27 and II-31, the polynomial A_m can be given by:

$$A_m = (1 - z^{-1})^{m+1} L(Z^{-1}) + B^- B'_m \qquad \text{II-32}$$

The discrete time RST pole placement method can be resumed in the following given in Fig. II-6.

In the case of sine-wave reference signal, the final limit theorem cannot be applied. Thus, the magnitude of the transfer function from the reference r to the true error signal can be considered [81]:

$$\left|\frac{\varepsilon(z^{-1})}{r(z^{-1})}\right|_{z=e^{j\omega t_s}} = \left|\frac{A_m - B_m}{A_m}\right|_{z=e^{j\omega t_s}} \qquad \text{II-33}$$

In order to cancel the error at a given angular frequency ω_0, it is necessary to introduce a transmission zero into the transfer function (II-33) at this frequency. If we take the case of a complex conjugate pair of zeros, this is can be done by letting $(1 - e^{j\omega_0 t_s} z^{-1})\,(1 - e^{-j\omega_0 t_s} z^{-1})$ divide $A_m - B_m$. Therefore, the equation (II-31) will be rewritten as:

$$\begin{aligned} A_m - B_m &= \left(1 - e^{j\omega_0 t_s} z^{-1}\right)\left(1 - e^{-j\omega_0 t_s} z^{-1}\right) L(z^{-1}) \\ &= (1 - 2\cos(\omega_0 t_s)\, z^{-1} + z^{-2}) L(z^{-1}) \end{aligned} \qquad \text{II-34}$$

And the auxiliary Diophantine equation which must be solved is:

$$A_m = (1 + 2\cos(\omega_0 t_s)z^{-1} + z^{-2})L(z^{-1}) + B^- B'_m \qquad \text{II-35}$$

The synthesis approach for the sine-wave case can be applied to all polynomials reference by taking account the signal frequency. Moreover, the step signal can be tracked by using the auxiliary Diophantine equation.

The detailed digital poles placement concept based on RST method will be then applied to the studied piezoelectric motor plants. Therefore the discrete time plant model will identified in first time. Afterwards, the poles of the closed loop will be fixed as function of the desired performances and the R, S, and T polynomial coefficients will be deduced.

II.4 Conclusions

In this chapter, the synthesis approaches of two position controllers for accurate positioning systems based on piezoelectric motors are explained in details. The first control method consists on robust mixed sensitivity H_∞ controller, and the second one is a digital RST controller based on pole placement method. Many precautions are taken into account in the synthesis concept, in particular the ultra-precision under system parameters uncertainties and the robustness to additional disturbances.

The constraints of piezoelectric motor positioning systems and the real time implementation in engineering applications issues are considered during the selection and the design of the proposed methods.

To deal with the different studied piezoelectric motors, the H_∞ and RST position controllers are synthesized for a generalized plant. Then, for each motor, the control methods can be easily applied by introducing each specified plant model.

The challenge of the position controllers is to validate the precision performances and robustness requirements in a simple controller without additional parameters adaptation or nonlinearity compensation systems

Chapter III

Modeling and Design of Robust Closed Loop Position Controllers for Rotary Traveling Wave Ultrasonic Motor

III.1 Introduction

Rotary traveling wave ultrasonic motor is presently the most typical and widely used ultrasonic motor [42]. TWUSM presents a good compromise between a compact, silent, and efficient motor. The technology used remains relatively simple and the performances are among the most interesting in the mechanical power range up to 20W. It combines two standing waves with a 90° of phase difference both in time and space. This operation mode makes the clockwise and counterclockwise motion of the motor very simple (by switching between +/-90° of phase shift). The TWUSM is an attractive solution for compact positioning systems and it was integrated in many engineering fields as detailed in Chapter I. In order to improve the design efficiency of TWUSM and realize precise control, extensive research has been done on the models establishment and position controls synthesis.

In this chapter, the working principle of the rotary TWUSM will be explained, afterwards a literature review of the modeling and position control of such type of motors will be given. An electromechanical model of rotary TWUSM (USR60) is designed in the MATLAB/Simulink environment. It reflects the variation of the motor output characteristics as function of the driving parameters, and can be easily used for control purposes via the driving signals (voltage amplitude, frequency, and phase shift). The output characteristics of the USR60 will be verified via the open loop simulations of the proposed model. A compact experimental platform is setup in order to validate the USM characteristics, to identify the Transfer Function (TF) between the motor angular position and the control signal, and to implement the synthesized robust position controllers of USR60. The synthesized H-infinity and discrete time RST controllers are applied to the USR60 motor, and the controller parameters are determined based on the identified TF. The proposed positioning system must fulfill the accuracy and stability criteria needed for the most USR60 applications. Moreover, the challenge is to confirm the robustness of the closed loop system in case of loaded motor condition without additional compensation system, motor heating, and injected noises to the control signal or to the measured position. The proposed control methods are compared to a PID controller in order to confirm the advantage of the proposed methods. The closed loop positioning system is simulated and implemented in real time. The precision, stability and robustness of the proposed system are evaluated and compared through the simulation and experimental results.

III.2 Working principle of rotary TWUSM (USR60)

The studied motor is a commercialized rotary TWUSM (USR60) (Fig. III-1.a) from Shinsei.Co [50] .The exploded figure of the motor is shown in Fig. III-1.a.

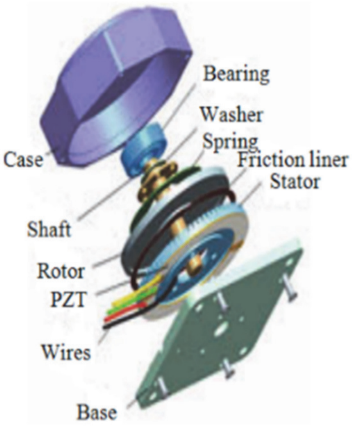

Fig. III-1. Structure diagram of USR60[42]

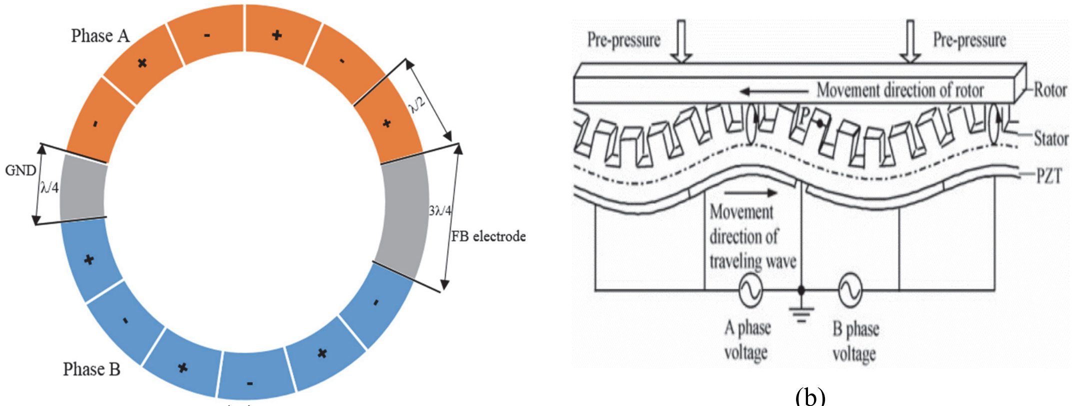

(a) (b)

Fig. III-2. (a) Polarization of the piezo-ceramic ring , (b) Driving mechanism of TWUSM [42]

The stator is made of an elastic body and its bottom side is bonded to a piezoelectric ceramic ring. The piezoceramic ring has the role of exciting transversal mechanical vibrations at the stator surface. Teeth are machined into the upper side of the stator (Fig. III-1.b) and have the role of increasing the horizontal deflection of the stator at the contact interface with the rotor. The rotor is made of a metallic disc and pressed against the stator by the case. Therefore, the stator is in permanent contact with the rotor [50].

The piezoelectric ring is divided into two semicircular sectors A and B, as shown in Fig. III-2.a. Each of these semicircular sectors is further divided into small sectors with opposite polarization. Therefore, when the motor is supplied by two sinusoidal voltages at a frequency range close to one of its mechanical resonance frequencies and with 90 degree of phase shift, one sector will contract while the other will expand. Two Standing Waves (SW) with equal amplitude and 90° of phase difference in time and space will be created based on the inverse piezoelectric effect. The traveling wave is formed by the superposition of the two SW. The surface points of the stator will follow an elliptical trajectory as shown in Fig. III-2.b. The micro-vibration of the piezoelectric ring will be transformed to rotary motion of the rotor through frictional forces. The traveling wave generation, the stator-rotor contact mechanism, and the motion of the rotor will be modeled in the USR60 modeling section.

III.3 Literature review

Since the invention of TWUSM, intensive research works have been done to establish an accurate model of such motor. Many control methods of TWUSM have been also developed based on the designed models. In this section, a literature review of the TWUSM models and position controllers will be proposed.

III.3.1 Modeling of rotary TWUSM

This section treats the modeling studies of TWUSM and its applications on the motor behavior analysis and parameters estimation. The TWUSM models can be classified into; Equivalent Circuit Models (ECM), Finite Element Method (FEM), and mathematical models.

A very good introduction to the construction and operating principle of TWUSM was undertaken by Sashida and Kenjo [82]. In this book, the motor is modeled by an equivalent electrical network of capacitors, resistors, inductors, and Zener diodes. This modeling approach is simple, however, the rotor-stator interface which is the origin of torque generation is missing. The Equivalent Circuit Model (ECM) have been presented in [83] to estimate the TWUSM speed and load characteristics. Elghouti and Helbo [84] highlight the importance of the electromechanical coupling factor in their proposed ECM, which is responsible for the electrical to mechanical energy conversion. The model is performed based on experimental approach combined with the electrical network method and some simplifying assumptions about the motor real behavior [85]. Similar ECM modeling approaches based on experimental tests have been also reported in [86, 87], to determine the stator parameters and vibrational behavior. When compared to other methods, the ECM has the advantages of simplicity and low computational efforts. However, the main drawback of this model is its inability to accurately model the contact mechanism between the motor stator and rotor.

The Finite Element Method (FEM) has been widely used for the analysis of the stator/rotor interaction and contact surface parameters. Maeno et al.[88] proposed FEM approach to model the TWUSM stator and the rotor/vibrator contact surface. Numerical calculation method is used to determine the load characteristics. FEM modeling of the TWUSM stator with comparison between closed and segmented ceramic ring has been presented by Krome and Wallaschek [89]. Three-dimensional FEM have been reported in many works for modeling of TWUSM. It was applied by Kagawa et al. [90] to simulate the dynamic behavior of USM including transient response. The performance of USM as a function of input parameters such as the driving frequency, voltage input and pre-load was evaluated using the three-dimensional FEM in [91]. The stator is simulated as a fully deformable elastic body, the interaction through contact between the stator and the rotor is accounted by assuming that the rotor behaves as a rigid surface. A three dimensional finite element model with cohesive zone elements embedded between friction material and rotor is developed by Shen et al. [92] to model the TWUSM contact mechanism. The traveling wave generation and the vibrational behavior of TWUSM have been also simulated through FEM in [93]. The time computation of FEM to analyze the motor parameters makes it not convenient for control implementation and fast evaluation.

Intensive research studies on the mathematical modeling of TWUSM have been reported in the literature. This modeling method is used to model the stator vibration, the rotor/stator interaction parameters, and the motor output characteristics. Working principle and mathematical modeling of the stator of TWUSM have been presented by Hagedorn and Wallaschek [94]. In this paper, the stator is modeled using the theory of Mindlin and Reissner for circular plates of non-constant thickness, and the eigenvalue problem is solved using numerical methods. The Rayleigh-Ritz approach is used by Hagood and McFarland [95] to model the distributed piezoceramics and the traveling wave dynamics of the stator. The purpose is to give a general framework for modeling TWUSM and predicting motor performances as a function of design parameters. Wallaschek [96] presented contact mechanics model of piezoelectric USMs to summarize the state of the art in the understanding of some fundamental processes governing the contact mechanics of piezoelectric USMs. Moregal et al. [97] presented mathematical modeling and numerical simulation of the TWUSM stator dynamics. In this study, modal analysis is provided for the structural Eigen frequencies of the stator. Mathematical model of USM for speed control is proposed by Senjyu et al. [98]. In this model the dead zone in control input effect is included, and the model parameters are derived by fitting the transfer function of dynamic speed response. Second order model for a rotary TWUSM was derived using Canudas-de-Witt method by Rochin et al. [99]. The model parameters are identified through experimental tests under different frequencies and load torques. This model take into account the dependency of the motor velocity on the driving frequency. Another analytical modeling approach for the ultrasonic motor is presented by Elgotti [100]. The author presents the derivation of a general framework for a simplified analytical model using the energy method based on Hamilton's principle with simplifying assumptions. An interesting hybrid model is also proposed by Elgotti [100], which has the strengths of both an equivalent circuit model and an analytical model. The idea is to overwhelm the simplified analytical model of the unloaded stator with the equivalent circuit model. Therefore, the parameters of the ECM can be substituted in the framework of the simplified model.

III.3.2 Position control of rotary TWUSM

In parallel with the modeling and design of TWUSMs, a variety of position control methods of such motors have been developed. The speed/position of the TWUSM was controlled using the driving voltage frequency, phase shift, and dual control by combined the two control signals. The PID with fixed and variable gains, adaptive model based, fuzzy logic, neural networks, and mixed controllers are the commonly used methods for TWUSM position control. In the following section, an overview of the developed position controls methods (but not all) for rotary TWUSMs is given. The fixed gain PID controller was tested in [101, 102], where the equivalent circuit model of USM is used to determine the system parameters. It is simple and easy to be implemented but it is difficult to set the controller parameters and to meet the performance requirements of USM while the motor parameters are time varying. Tuning PID is proposed to overcome the shortcoming mentioned above [103]. The tuning parameters technique requires the setting of related parameters according to the USM operating state, load conditions, and temperature. Therefore, it is not easy to be implemented in practical applications [42].

The Adaptive methods are widely reported in the literature for USM position control. The main idea of these techniques is to design a Model Reference Adapting Control (MRAC) and self-correcting controller. On-line control parameters identification will be then executed by comparing the output with reference model in order to compensate the position error. The MRAC is mainly used to compensate the control input dead zone in case of load conditions [104, 105]. The generated position errors remain relatively important for precise application due to the uncertainty of the reference model. Senjyu et al. [106] present a dual mode control by using both the driving frequency and voltages phase shift as control signals. This control scheme consists of a PI controller and an adaptive controller, which compensates the speed characteristic variations. However, as shown in the positioning experimental results of this paper, the oscillation of the final motor position increases significantly when operating close to the resonance frequency. Moreover, there is a weakness of sine-wave motion tracking for loaded motor.

Due to the fact that Fuzzy Logic Control (FLC) is preferred when the mathematical model of a control plant is difficult to obtain, this technique was proposed in several research works to achieve superior speed and position characteristics [107-110]. It is based on the knowledge of the USM state and experimental data to make up the fuzzy inference rules. But under certain conditions, the motor parameters are variable, and the output motion can be outside the inference rules [42]. Moreover, this control method uses an empirically derived motor model, which does not reflect the real behavior of the motor [85].

The Neural Network (NN) control is also investigated in the position control system of USM [111-114]. The output characteristics of the USM depend on the stator/rotor contact surface. The parameters of this contact surface are defined mainly by the amplitude of the traveling wave and the phase shift between the two standing waves. The dependency between the traveling wave and the motor output characteristics is at the origin of the design of NN control methods. The speed/torque-traveling wave characteristic curves are measured experimentally. Mapping function using neurons and connection weights are then investigated to model this dependency. With the NN better control accuracy can be obtained. However, USM behavior and parameter variation yields to the growth of the network's complexity for the NN controller which will increase the execution time and learning procedure [42].

The USM position control methods mentioned above have their advantages and disadvantages. In order to take advantage of each method, different types of mixed controllers have been developed such as fuzzy neural network (FNN) [115-117], fuzzy PID [118], NN-PID [119, 120], and fuzzy sliding mode control [121]. The key of the mixed controllers is to employ dual control via the voltages frequency and phase shift to handle system nonlinearities and parameters uncertainties. The FNN is adopted to determine a dead-zone compensation equivalent input and to construct a plant which does not have dead-zone. Afterwards, PI controller will be applied to perform the accurate positioning. The mixed controllers can make the control precision with some improvements. However, the fuzzy rules and neurons connections are empirically designed. That means, a new parameters identification is required each time a new motor has to be controlled. Moreover, the implementation of such methods for engineering applications is still complicated [42].

Several robust position controllers are also developed based on USM model. Among them, the Behavior Model Control (BMC) proposed by F.Giraud et al. [122]. Where the USM model is represented by a Causal Ordering Graph (COG), and the control law is then deduced by inversion of the COG. However, the model parameters are identified through the experimental characteristics of the studied motor. Therefore, a new identification is required for new motor or under other test conditions. The genetic algorithm method is also used for TWUSM position control [123], the control effectiveness and prospective for engineering applications still need to be improved.

III.4 Proposed Simulink model of USR60

In this thesis, the aim of the TWUSM modeling approach is to establish a simplified model of the rotary USM which reflects the motor behavior and makes the position control implementation easier. In fact, the characterization, parameters identification, and complex contact mechanism of the USR60 motor will not be detailed here. Since the dynamic characteristics of the real motor are difficult to capture in analytical models, and the parameters of the motor are time varying and highly nonlinear [105], then some assumption are required in order to design a suitable model for control purposes. The following section details the design, assembly, and simulation of electromechanical USR60 model in MATLAB Simulink. This model is mainly composed by three subsystems as shown in Fig. III-3, and the related parameters are illustrated in the equivalent stator/rotor contact mechanism in Fig. III-5.

- **Stator:** The piezo-ceramics vibration and traveling wave generation (w, w_{max}) based on the inverse piezoelectric effect and the stator/rotor interaction forces ($F_{n,t}$) are detailed in this subsystem.
- **Vertical motion of the rotor:** The rotor vertical position, half contact length of the traveling wave(x_0), will be determined and used to calculate the output torque (T) and the angular motion of the rotor.
- **Angular motion of the rotor:** The angular velocity (Ω) is analyzed to deduce the stick point (x_s) needed for the output torque calculation

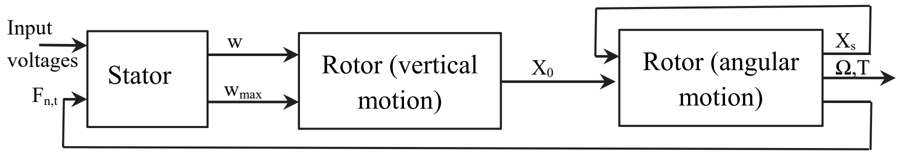

Fig. III-3. Block diagram of USR60 model subsystems

III.4.1 Stator

The stator is composed by two set of piezoelectric ceramics with opposite polarization (A, B) which will be supplied by two sinusoidal voltages (V_1 (t), V_2 (t)) with a phase shift of 90°:

$$V_1(t) = V_{max}\sin(\omega t)$$
$$V_2(t) = V_{max}\cos(\omega t) \qquad \text{III-1}$$

Where V_{max} and ω are respectively the maximum voltage amplitude and angular frequency

In order to simplify the motor model, it is assumed that only two orthogonal modes δ_1 and δ_2 with the same amplitude can be excited within the piezo-ceramic plate. These modes are given by [100]:

$$\delta_1 = R_r\sin(k\theta)$$
$$\delta_1 = R_r\cos(k\theta) \qquad \text{III-2}$$

where R_r is the shape constant of the traveling wave in radial direction, and k is the wave number. The orthogonal temporal amplitudes of the generated standing waves are denoted by $w_1(t)$ and $w_2(t)$ respectively

$$\begin{aligned} w_1(t) &= w_{max}\sin(\omega t) \\ w_2(t) &= w_{max}\cos(\omega t) \end{aligned} \qquad \text{III-3}$$

where w_{max} is the maximum temporal amplitude of the traveling wave (m),

The superposition of their corresponding standing waves (in case of 90° of phase shift) results in a traveling wave at the surface of the stator expressed by [124]:

$$w(r,\theta,t) = \delta_1 w_1(t) + \delta_2 w_2(t) = R_r\cos(\omega t - k\theta) \qquad \text{III-4}$$

$$w_{max} = \sqrt{{w_1}^2 + {w_2}^2} \qquad \text{III-5}$$

In the case of voltages phase shift different from 90°, the model will be developed based on two standing waves with phases different from 90°. The resulting simulated wave in this case is not a purely traveling wave.

The general state space model of the stator was also derived based on the hypothesis that it is composed by two orthogonal and symmetrical phases. It is possible to reduce the general state space model by decoupling the two orthogonal modes and thereby obtain a separate model for each phase of the stator [100]. The contact between the two orthogonal stator phases and the rotor is supposed symmetrical along the contact surface[100].

The performances of the two decoupled modes can be represented by two mass-spring-damper systems as shown in Fig. III-4. The motion equations are given by [124]

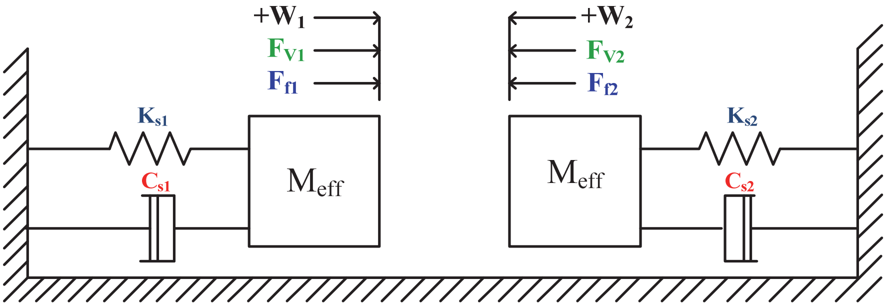

Fig. III-4. Spring-mass-damper representation of the USM stator

$$\begin{aligned} m_{eff}\ddot{w}_1 + C_{s1}\dot{w}_1 + K_{s1}w_1 &= F_{v1} + F_{f1} \\ m_{eff}\ddot{w}_2 + C_{s2}\dot{w}_2 + K_{s2}w_2 &= F_{v2} + F_{f2} \end{aligned} \qquad \text{III-6}$$

where m_{eff}, $C_{s1,2}$ and $K_{s1,2}$ are respectively the effective mass, damping, and spring coefficient of the stator. $F_{v1,2}$ and $F_{f1,2}$ are respectively the piezo-forces and feedback forces (The numerical values of the USR60 model parameters are given in Appendix A).

The piezo-forces F_{v1} and F_{v2} are the forces generated by the stator piezoelectric ceramics when excited by two phase shifted sinusoidal voltages (V_1, V_2). They can be written as following:

$$\begin{aligned} F_{v1} &= \rho V_{max}\sin(2\pi f t) \\ F_{v2} &= \rho V_{max}\cos(2\pi f t) \end{aligned} \qquad \text{III-7}$$

where ρ is the piezoelectric force factor (N/V).

The feedback forces $F_{f1,2}$ are composed of normal and tangential components and they serves as the coupling terms between the stator and rotor. They depend mainly on the half-contact length x_0 (will be defined later) and the wave amplitudes (w_1, w_2). The normal feedback forces can be calculated as in [125]:

$$F_{f1,N} = -kx_r b w_1 (\frac{R_0}{k} x_0 - \frac{1}{2} \sin\left(2\frac{R_0}{k} x_0\right))$$
$$F_{f2,N} = -kx_r b w_2 (\frac{R_0}{k} x_0 - \frac{1}{2} \sin\left(2\frac{R_0}{k} x_0\right)) \tag{III-8}$$

The tangential feedback forces for the ideal motor operating within its load carrying range are [125]:

$$F_{f1,T} = 2k\mu x_r bhw_2 (\frac{R_0}{k} x_0 + \frac{1}{4} \sin\left(2\frac{R_0}{k} x_0\right) - \sin\left(\frac{R_0}{k} x_0\right) \cos\left(\frac{R_0}{k} x_0\right))$$
$$F_{f2,T} = -2k\mu x_r bhw_1 (\frac{R_0}{k} x_0 + \frac{1}{4} \sin\left(2\frac{R_0}{k} x_0\right) - \sin\left(\frac{R_0}{k} x_0\right) \cos\left(\frac{R_0}{k} x_0\right)) \tag{III-9}$$

where: μ is the coulomb friction coefficient, b is the inner radius of the stator (m), h is the half thickness of the stator (m), R_0 is the middle radius of the contact surface (m), and x_r is the rotor stiffness per unit area ($N.m^{-3}$).

For a non-ideal model, additional terms would be added to equation III-1 accounting for unequal stick-point lengths (x_s) on either side of the traveling wave crest as done in [126]. However, following the ideal wave assumption, the stick-point lengths to the right and left of the wave crest are of equal length and the additional terms cancel each other in the feedback calculation.

The total feedback force experienced by each stator phase is determined by combining equations III-8 and III-9:

$$F_{f1} = F_{f1,N} - dir(R) F_{f1,T}$$
$$F_{f2} = F_{f2,N} - dir(R) F_{f2,T} \tag{III-10}$$

where dir(R)=+/-1 for clockwise/counterclockwise rotor motion directions .

III.4.2 Contact surface

The contact mechanism refers to the friction between the stator and rotor surfaces. The main approach for the modeling of the contact mechanic is shown in Fig. III-5. The stator is assumed as undeformable while the rotor is deformable with some uniform stiffness. We will interested on two variables of this contact surface which are the half-contact length (x_0) and the stick points (x_s). The two variables will be used to determine the motor characteristics such as the no-load speed, feedback forces, and generated torque.

III.4.2.1 Half-contact length, x_0

The half-contact length is defined as half of the horizontal length of the traveling wave crest of the stator submerged within the rotor from its point of entry to its exit [124]. The generated stator wave crest presses into the rotor contact material creating a normal force F_N. As w_{max} increases from zero, F_N increases towards the preload between the rotor and the stator F_{ext}. At a critical value of w_{max}, with the contact length set at its maximum of $\lambda / 4$, F_N becomes larger than F_{ext}, and the rotor accelerates away from the stator surface to a height z(t). By monitoring the rotor height, the half-contact length can be calculated as in [125]:

$$x_0 = \frac{1}{k}\cos(\frac{z(t) - h}{R_r w_{max}}) \qquad \text{III-11}$$

where z(t) is the vertical distance between the rotor's lowest surface and the top surface of the un-deformed stator and h is the half-thickness of the stator.

The created normal force F_N can be calculated as function of the half-contact length and the traveling wave amplitude w_{max} as [100]:

$$F_N = \frac{2x_r w_{max}}{k}(\sin(kx_0) - kx_0\cos(kx_0) \qquad \text{III-12}$$

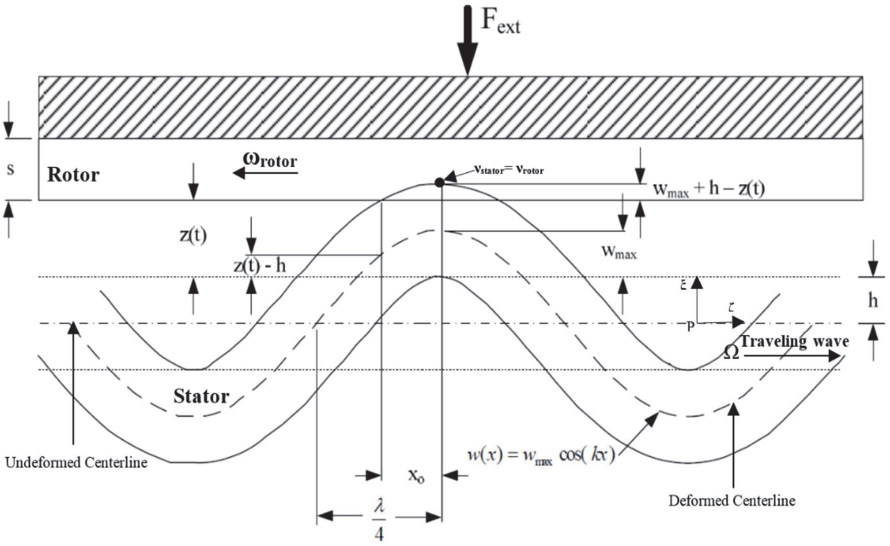

Fig. III-5. Drawing of stator rotor contact surface [100]

III.4.2.2 Stick points, x_s

The stick points, x_s, are defined as the location where the horizontal velocity component of the stator surface point matches the horizontal velocity of the rotor, and their magnitude represents the length from the traveling wave crest to that location [124]. If the rotor moves with an angular velocity Ω, then the horizontal velocity of the rotor is:

$$\upsilon_{h,rotor} = R_0\Omega \qquad \text{III-13}$$

The horizontal velocity of the stator surface point is given by [100]:

$$v_{h,stator} = \frac{k\omega h R_r}{R_0} w_{max} \qquad \text{III-14}$$

The stick point condition is achieved when the following equation is fulfilled; $|v_{h,stator}| = |v_{h,rotor}|$:

$$x_s = \frac{1}{k}\text{acos}(\frac{R_0^2}{k\omega h R_r w_{max}}) \qquad \text{III-15}$$

III.4.2.3 Torque generation

The USM generated torque depends on the preload between the rotor and the stator, the applied external load, the stator-rotor friction coefficient, and the stator-rotor contact surface. The output torque of USM in steady state was derived in [100] using a linear spring contact model as:

$$T_{USM} = 2\mu k x_r R_0{}^2 w_{max}(2\phi(x_s) - (\phi(x_0)) \qquad \text{III-16}$$

where

$$\phi(\mathrm{x}) = \sin(kx) - \mathrm{kx}\cos(kx_0) \qquad \text{III-17}$$

In steady state, the stick-point length is less than or equal to the half-contact length, and the horizontal stator surface-point velocity at the stick-point is equal to the rotor horizontal velocity. For the USM, the transient condition is defined as the period in time that the traveling wave amplitude has not yet reached its steady state value. As the motor speed increases from zero to its steady state value, in the simulation model, it is possible for the stick-point to fall outside of the contact length (x_s>x_0). In the proposed motor model, if the stick point (x_s) is calculated to be larger than the half-contact length (x_0), it will set equal to x_0:

$$x_s = \begin{cases} x_s \; if x_s \le x_0 \\ x_0 \; if x_s > x_0 \end{cases} \qquad \text{III-18}$$

III.4.3 Rotor (vertical motion)

The rotor of USR60 will be forced out of its initial vertical position (z_0) as shown in Fig. III-6.

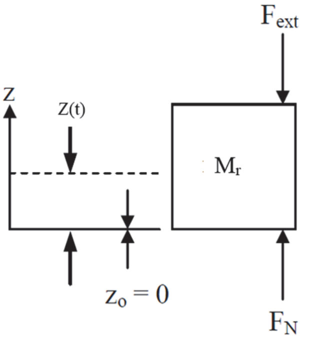

Fig. III-6. Diagram of the rotor vertical motion

The vertical motion of the rotor will be described by the following equation:

$$M_r \ddot{\mathrm{Z}} = F_N - F_{ext} \qquad \text{III-19}$$

where M_r is the rotor mass (kg), and F_{ext} is the applied external force

III.4.4 Rotor (angular motion)

The angular motion of the rotor can be represented as shown in Fig. III-7 , where T_{USM} and T_L are respectively the motor and load torques, and J_r is the rotor inertia. Then, the angular motion equation of the rotor is given by:

$$J_r \dot{\Omega} = T_{USM} - T_L \qquad \text{III-20}$$

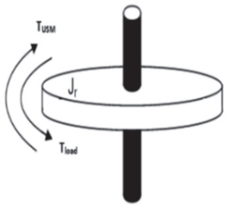

Fig. III-7. Description of rotor angular motion

III.5 Simulation of USR60 model

The detailed USR60 model is implemented in Matlab/Simulink environment (Fig. III-8) in order to validate in first time the motor behavior, and afterwards to design the closed loop position controllers. The motor is supplied by two phase shifted sinusoidal voltages (V_1, V_2) around one of its mechanical resonance frequencies (40 kHz). The voltage amplitude is of 110 V and the phase shift is of 90°. The vibration amplitudes of each phase are significant because they are used to calculate the Traveling Wave (TW) amplitude and to determine the feedback forces caused by the interaction between the stator and rotor. The stationary waves in the steady state are shown in Fig. III-9.a. The superposition of the two standing waves will create a TW propagating on the stator surface. The amplitude of the generated TW when the motor is driven at a frequency of 40 kHz is shown in Fig. III-9.b.

The TW amplitude plays a critical role in the operation mechanism of TWUSM, where it is used to determine the contact surface parameters (x_0, x_s), feedback forces, and generated torque. It should be mentioned that a minimal TW amplitude value must be reached before the stator normal force (F_N) matches the external pressing force (F_{ext}). During the period where the TW is less than the minimal value, F_N is less than F_{ext} and the rotor remains pressed into the stator with a height of zero. For the TWUSM, the maximum amplitude of the TW is generated at the mechanical resonance frequency (f_r). The USR60 motor is driven at different frequencies in order to identify the motor resonance frequency. Fig. III-10.a shows that the maximum TW amplitude is of 3.5 µm and corresponds to 39.95 kHz.

There is a non-linear relationship between the driving frequency and the TW amplitude. The evaluation of the rotor height is monitored during the motor operation as shown in Fig. III-10.b. The half-contact length is an output of the rotor vertical motion subsystem and is used in the rotor angular rotor motion subsystem to calculate the output motor torque (T_{USM}) as explained in equation III-16. During the motor operation the rotor horizontal velocity is compared to the horizontal velocity component of the stator in order to determine the stick point locations (x_s). In the transient time, the stick point length may be larger than the half-contact length. In this condition, x_s is taken equal to x_0 as mentioned in equation III-18. The simulated contact surface parameters (x_0, x_s) are shown in Fig. III-11.a. The generated torque in case of no-load condition is shown in Fig. III-11.b. The motor output torque matches to the applied load torque, that's why in this case it tends to zero in steady state. The time evaluation of the angular motor speed (Fig. III-12.a) confirms the quick response of the USR60 motor, where the steady state velocity is reached in approximately 7 ms. The USR60 model is simulated under different load torques (T_L) up to 1 N.m (driven frequency=40 kHz), the motor speed variation as function of T_L is shown in Fig. III-12.b.

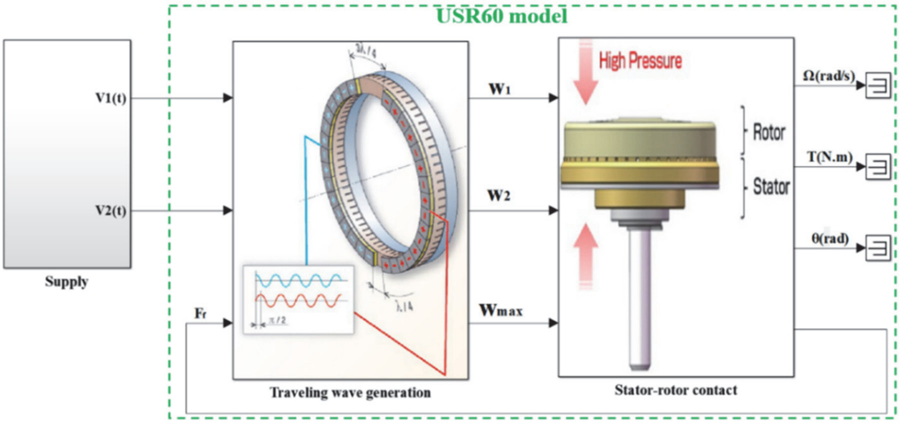

Fig. III-8. Block diagram of the Simulink model of USR60

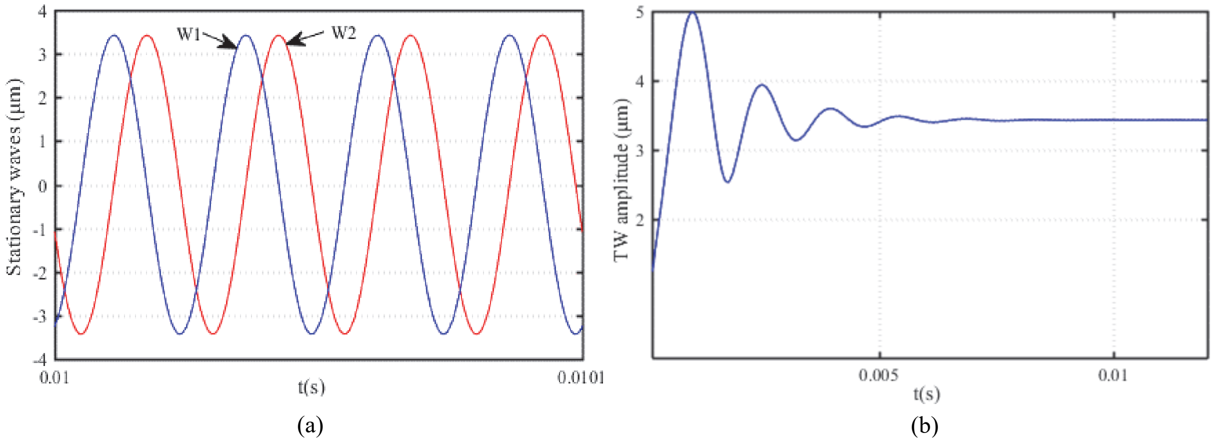

Fig. III-9. (a) Generated stationary waves, (b) Traveling wave amplitude at 40kHz

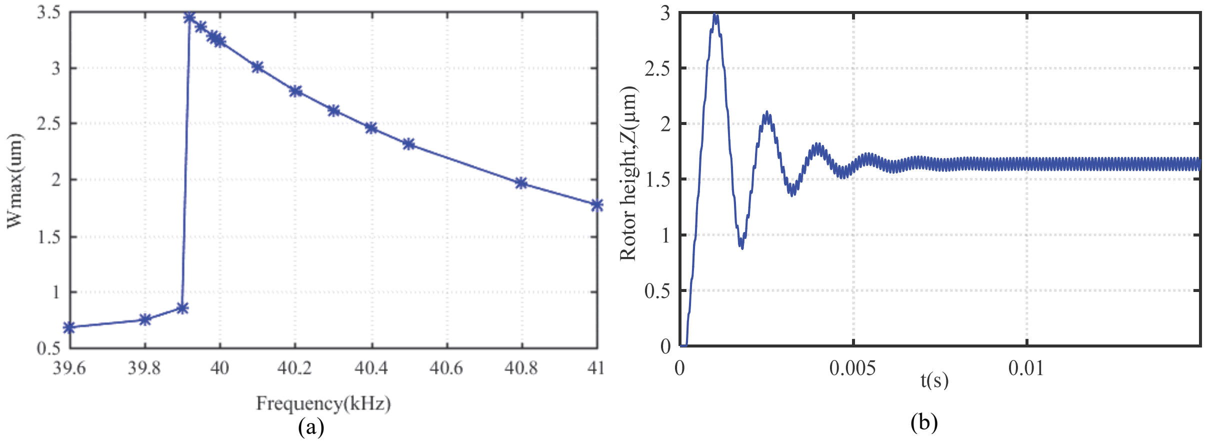

Fig. III-10. (a) TW amplitude as function of driving frequency, (b) Rotor height

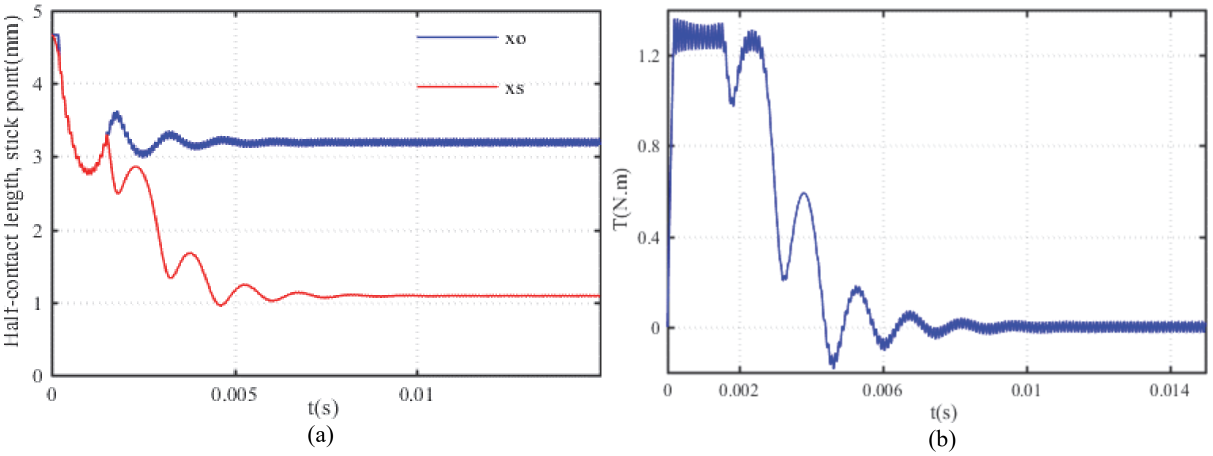

Fig. III-11. (a) Half-contact length and stick point locations, (b) Motor generated torque

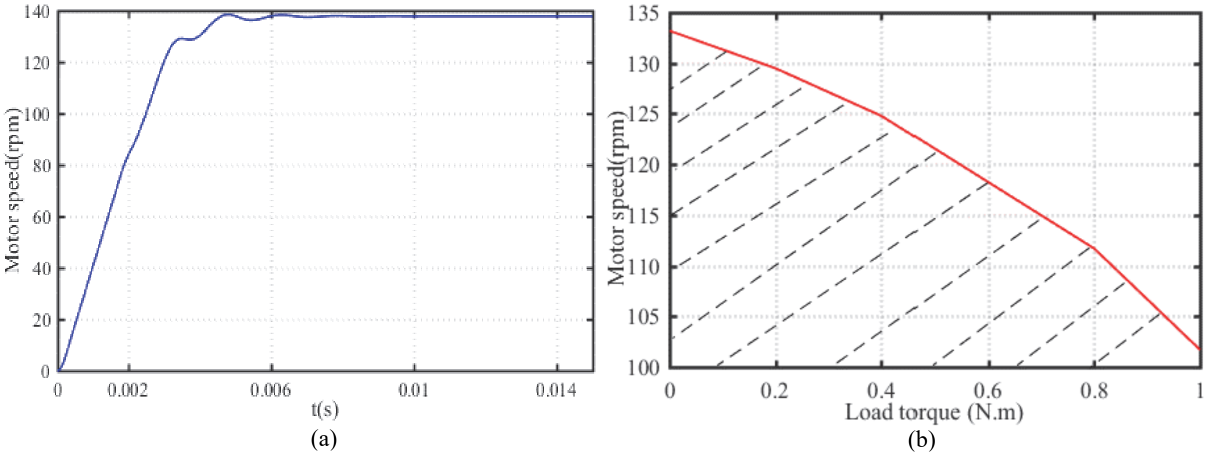

Fig. III-12. (a) Time analysis of motor velocity, (b) Speed-load characteristics

The speed-load characteristics are similar to that given by the manufacturer [50], and the dashed zone corresponds to the motor operation zone. The USM is simulated at the frequency range above the mechanical resonance frequency (f_r) and under different load torques, the steady state speed data are collected and the speed-frequency characteristic is plotted in Fig. III-13. When the driving frequency decreases below the mechanical resonance frequency, a breakdown appears and there is no motion at the rotor side (Ω=0). This breakdown is well known as the pull-out phenomenon of TWUSMs [3].

The effect of the driving voltage amplitude variation on the motor motion is also analyzed via the proposed USM model as shown in Fig. III-14. It should be mentioned that the supply voltage of the USR60 motor is recommended by the manufacturer to be in the range between 80 V_{rms} and 130 V_{rms}. There is a quasi-linear relationship between the driving voltage amplitude and the angular velocity but the positioning speed is limited, because a voltage amplitude increase of 30Vrms generates approximately a speed increase of 10 rpm as shown in Fig. III-14 (f=40.5 kHz).

The proposed model gives also the possibility to simulate the bidirectional motion of the USR60 via the voltages phase shift (φ). The motor speed (Ω) variation as function of φ in no-load condition is shown in Fig. III-15.

An electro-mechanical model of the rotary USR60 is successfully designed in Matlab/Simulink environment. The proposed model includes the TW generation process at the stator surface, the contact surfaces variables needed for the vertical rotor motion and torque generation, and the angular motion of the rotor. The simulation results reflect the behavior of the rotary TWUSM and the motor fast response is validated. The output characteristics variation as function of the driving parameters confirms that the model is suitable for closed loop control implementation via any control parameter (V_{rms}, f, φ). Therefore the USR60 Simulink model will be used to validate the synthesized position controllers.

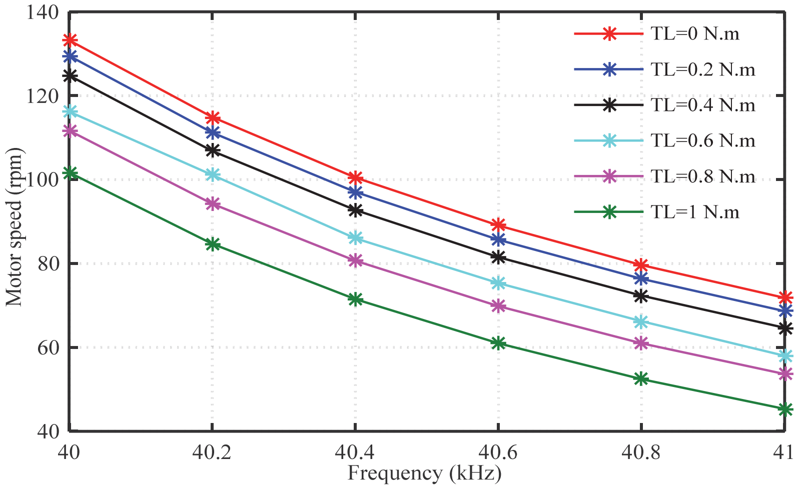

Fig. III-13. Speed-frequency characteristic under different load torques

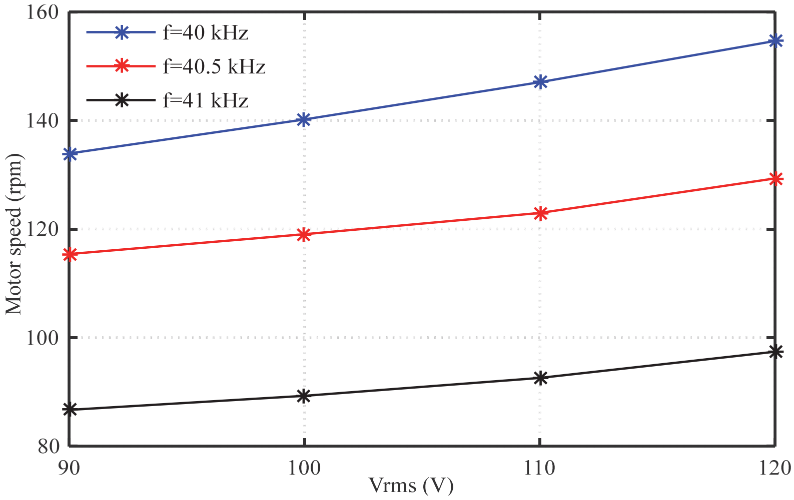

Fig. III-14. Speed-Vrms characteristic at different frequency (T_L=0 Nm)

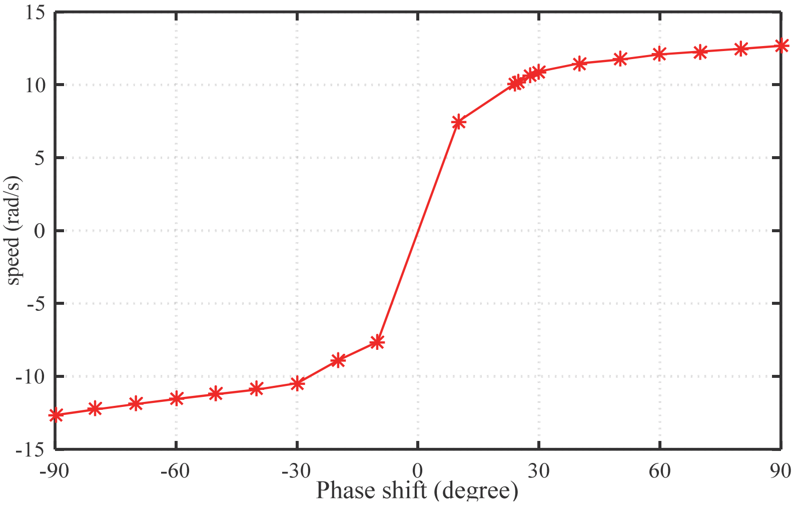

Fig. III-15. Speed variation as function of voltages phase shift (T_L=0 Nm)

III.6 Experimental test bench

This section describes the experimental test platform of the rotary TWUSM (USR60). The experimental setup is used in first time to evaluate the motor behavior via the open loop tests. Afterward, the designed closed loop positioning systems will be implemented. Therefore, the architecture of the experimental test bench is detailed, and the driving techniques of USR60 using the voltages amplitude, frequency and phase shift are discussed. The experimental open loop characteristics are presented in order to select the suitable position control parameter. Finally, an open loop TF between the motor position and the control parameter is experimentally identified.

III.6.1 Experimental platform description

The block diagram of the experimental test bench is shown in Fig. **III-16** and is comprised of the following components:

- Rotary TWUSM from Shinsei.Co (USR60-E3T) with incremental position encoder (HEM5540-B14, 1000 p/r).
- Dual channels waveform generator (Agilent 33500B)
- Two power amplifiers (HSA4051)
- Powder brake (FAS21)
- Mini-smart torque sensor from Kistler (4502A) with a control/monitoring board (4700B).
- Dspace control board (dS1104)
- Host PC

In the open loop test configurations, the two phase shifted sinusoidal voltages ($V_1(t)$, $V_2(t)$) are sent by the waveforms generator at the frequency range close to the mechanical resonance frequency of the USR60. The two voltages will be amplified using two switching power amplifiers type HSA4051 in order to obtain the adequate voltages range and power levels. The input voltage of the HSA4051 power amplifier is an analog signal between +/-10V (50 Ω/600 Ω) and its maximum output voltage is of 300 V_{p-p} with a maximum RMS current of 1 A (2.83 A_{p-p}). The frequency response of the amplifier is of 500 kHz with a slew rate of 450 V/µs. The load test conditions of the USM are realized by applying a load torque at the motor shaft side using a powder brake type FAS21 (Fabricated by Merobel). The nominal torque of the brake is 2 N.m with a nominal current of 0.45 A (Fig. III-18 (a)). The chosen brake produces a torque proportional to the low DC supply current as shown in Fig. III-18 (b). The torque is measured and conditioned via a mini-smart torque sensor type 4502A with a control/monitoring board type 4700B (Fabricated by Kistler). The measurement range of the torque sensor is 2 N.m with a linearity error <0.2%. The angular position of the USR60 motor is measured by the incremental encoder (1000 p/r) mounted at the rotor shaft as shown in Fig. III-17.

In the closed loop test configurations, the motor position is introduced to the control board via the incremental encoder interface of dSPACE microprocessor (type dS1104). The measured position is compared to a reference signal, and a position control algorithm will be executed in Matlab environment. The control signal parameter is then calculated and sent to the waveforms generator operating in external modulation mode. The driving voltages will be generated and connected to the two power amplifiers to drive the USR60. The synoptic of the driving diagram is illustrated in Fig. **III-16**.

III.6.2 Experimental characteristics of USR60

In this section, the open loop test results of the UR60 motor are carried out. These tests aim to validate the behavior of the USM discussed in section 3, and to analyze the motor output characteristics as function of the driving parameters in order to choose the suitable position control parameter. The motor is driven at first time in the frequency range between 30 and 45 kHz, which corresponds to the location of one its resonance frequencies. The RMS voltage amplitude is of 110 V and the phase shift is of 90°. The steady state motor speed values are collected for different frequency values as shown in Fig. III-19.

The arrows in Fig. III-19 indicate the frequency sweep direction. The motor rotates when the excitation frequency reaches 37.2 kHz.

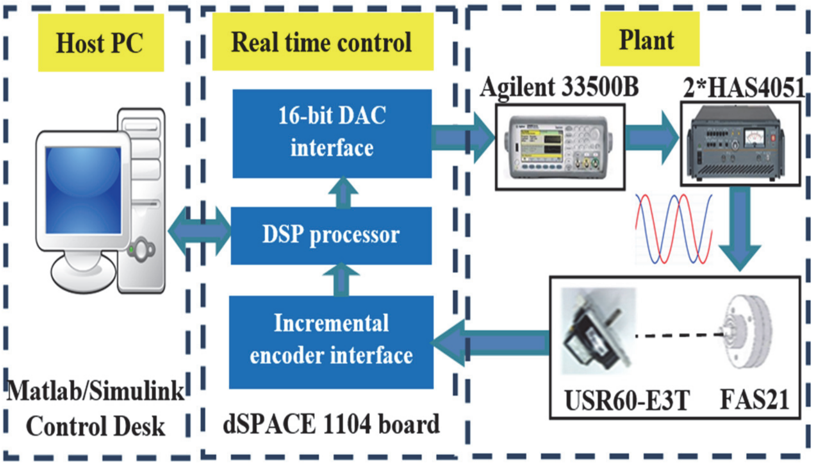

Fig. III-16. Block diagram of experimental setup

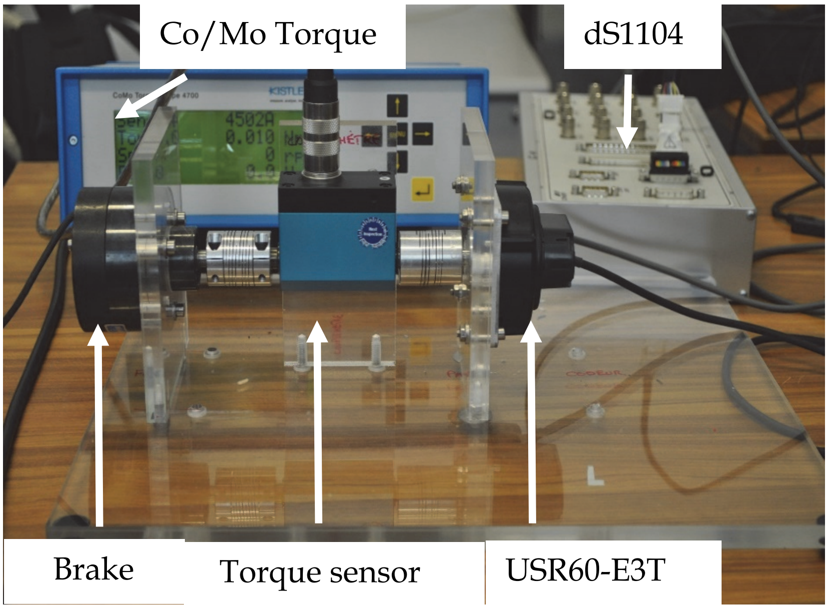

Fig. III-17. Experimental platform

Nominal torque (Nm)	2
Minimal torque (Nm)	0.04
Rated current DC (A)	0.45
Rotor inertia (Kg.m^2)	35.10^{-6}

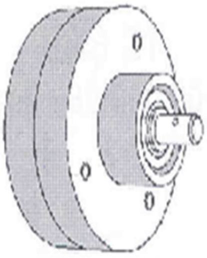

Fig. III-18. (a) The electromechanical specifications of FAS 21[127] ,

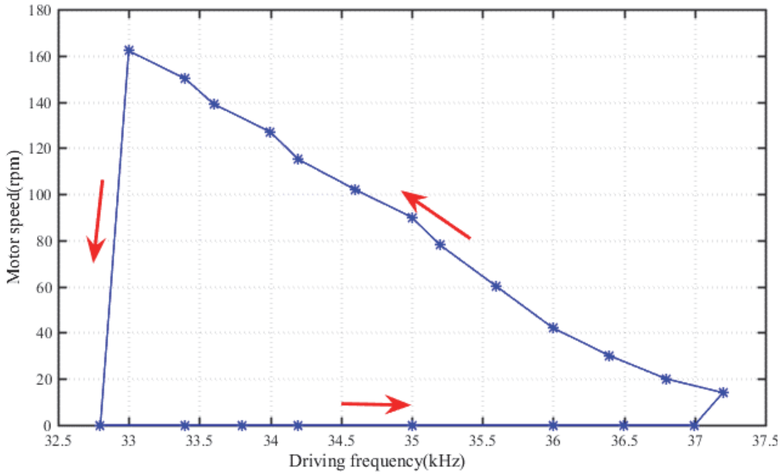

Fig. III-19. Experimental motor speed variation as function of the driving frequency (T_L=0 Nm)

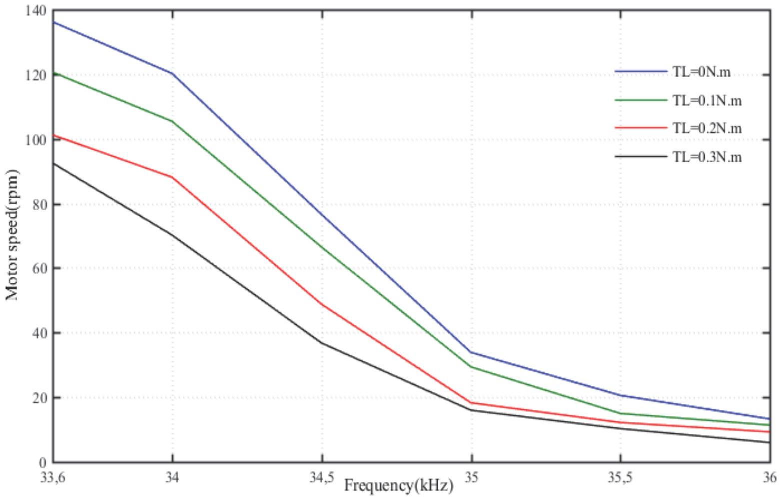

Fig. III-20. Experimental motor speed variation as function of the driving frequency under different load torques

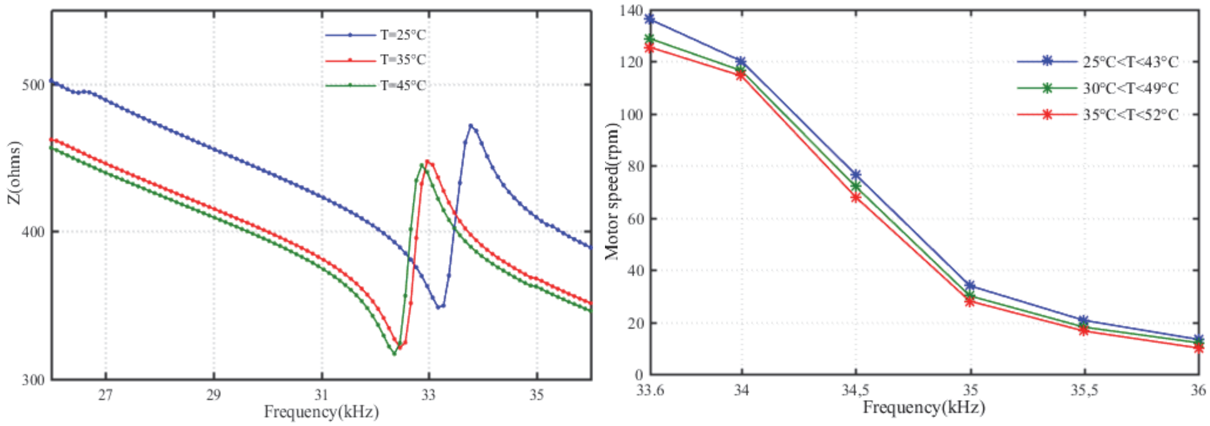

(a) (b)

Fig. III-21. Motor temperature effect on : (a) Resonance frequency, (b) Rotational speed

By decreasing the driving frequency, the motor speed increases until the resonance frequency (f_r=33 kHz). When the frequency decreases below f_r a breakdown appears and the motor shutdown immediately. This breakdown is well known as the pull-out phenomenon of TWUSMs [3]. The motor speed variation as function of the frequency is also evaluated in case of loaded motor (Fig. III-20), which confirms the behavior given by the model simulation results (Fig. III-13). The driving frequency variation gives a flexible control range but with a nonlinear relationship between the speed and frequency. Moreover, the resonance frequency depends on the motor temperature as shown in Fig. III-21.a. In consequence, the motor speed changes depending on the motor temperature range as illustrated in Fig. III-21.b. Therefore, avoiding the pull-out phenomenon is complicated when the motor speed/position is controlled through the excitation frequency. As it has been explained above in section III.2, the feedback electrode of the piezo-ceramic placed between the two excited phases provides a voltage signal (V_{fb}) according to the piezoelectric direct effect. The feedback voltage gives information about the traveling wave characteristics. Consequently, an intuitive understanding of the behavior of the motor is possible. From Fig. III-22 (a), it can be noticed that the feedback voltage characteristics exhibit a resonance behavior around the fundamental resonance frequency of the USR60. However, the speed-V_{fb} characteristics are almost linear for each load torque (Fig. III-22 (b)). Since the amplitude of standing waves depends on the voltage amplitude, speed and position can be controlled through adjusting the driving voltage amplitude.

From the open loop experimental tests of the studied motor (Fig. III-23), it can be seen that a large voltage amplitude variation (40 Vrms) generates a small speed variation. Thus, this drive technique permits only a smooth motor motion in one direction. The voltage phase shift (φ) can be also used to control the motor speed and position, and it is the only parameter that allows the inversion of motor rotation direction. This driving method also has the problem that the speed is not nicely linear with the voltage phase shift. Moreover, there is a dead zone around zero value of phase shift when load torque (T_L) is added (Fig. III-24). Therefore, the phase shift is more suitable for a position control than a speed control. Regarding the intended use of the USM in robotic applications and the obligation of precision and bidirectional operation mode, φ is chosen as the position control parameter. For these purposes, a transfer function between φ and the angular motor position (θ) must be identified to be used for the synthesis of the position controllers.

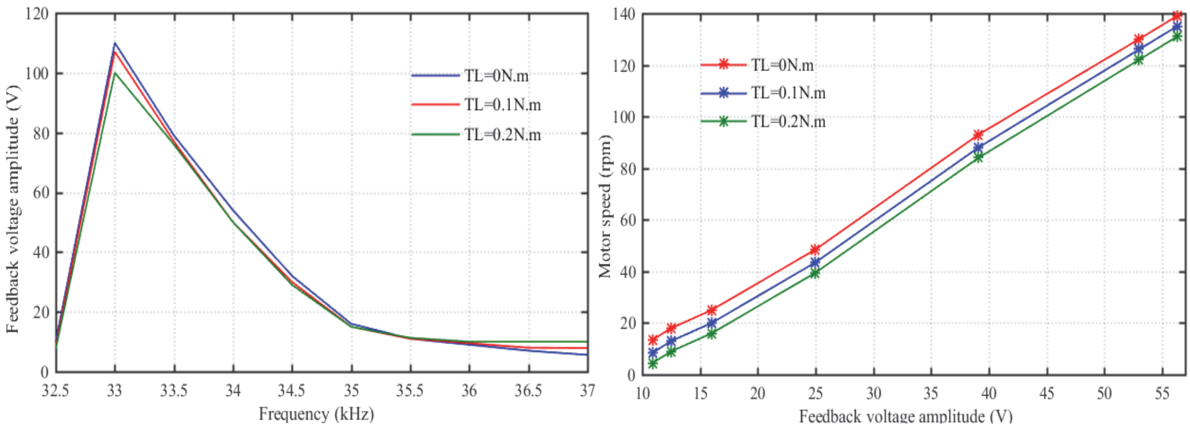

(a) (b)

Fig. III-22. (a) V_{fb} amplitude versus excitation frequency at various load torques, (b) The motor speed versus V_{fb} amplitude at various load torques

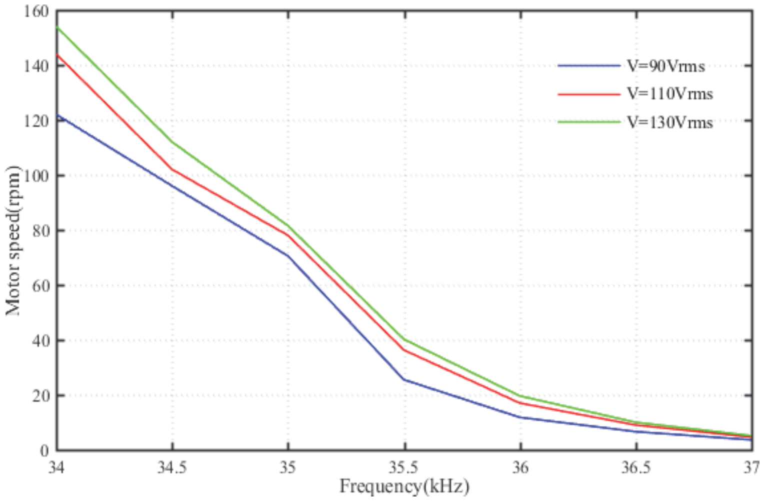

Fig. III-23. Voltage amplitude effect on the motor speed (T_L=0 Nm)

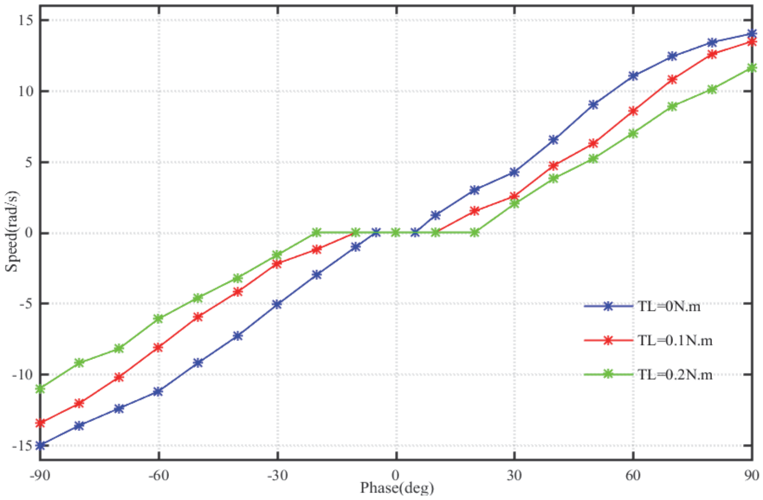

Fig. III-24. Experimental motor speed variation as function of the voltage phase shift under different load torques

III.6.3 Phase shift-position transfer function identification

An open loop experimental identification method will be used to determine the TF between the voltages phase shift (φ) and the angular position of the rotor (θ). A step change of the voltage phase shift (φ) is applied at the input of the function generator (Agilent3350B), two phase shifted voltages at the resonance frequency are then generated and amplified. The corresponding position variation (θ) is measured via the rotary position encoder. The motor velocity (**Ω**) is then derived from the position data as illustrated in Fig. III-25.a. (a). The TF between φ and **Ω** is estimated to a first order system using the Matlab identification toolbox from the introduced velocity and phase shift data with a sampling time of 100 µs. The TF between φ and θ is then deduced as a second order TF [9]:

$$G_{USM}(s) = \frac{\theta(s)}{\varphi(s)} = \frac{K_m}{s(1+\tau_m s)} \qquad \text{III-21}$$

where the gain constant K_m and the time constant τ_m are respectively equal to 11.5 and 4.25 ms.

As mentioned above, the dynamic behavior of the TWUSM is nonlinear. Firstly, because the mechanical resonance frequency of the TWUSM can change as function of the test conditions. The parameters of the motor TF are not the same if the open loop test was done at another driving frequency. For example the gain and time constants (k_m, τ_m) are respectively equal to 6.5 (instead of 11.5) and 9.3 ms (instead of 4.25 ms) when the motor is driving at a frequency of 35 kHz. Moreover, these parameters are for an unloaded motor (T_L=0 N.m), therefore when the motor is loaded the parameters will also change. The motor heating due to the contact mechanism between stator and rotor will affect the speed response (Fig. III-21) and therefore the TF parameters. For an operation temperature about 45°C the time constant (τ_m) reaches 6.5 ms due to the motor speed decrease. The minimum and maximum values of the TF parameters function of the drive frequency and the motor temperature are presented in table III.1. That is the reason why w rely on the robustness of the proposed controllers to overcome the model uncertainty problems and to ensure high precision levels at any operating temperature (<55°C) or under any loads (up to1 N.m).

Table III-1. Variation of the TF parameters

	k_m	τ_m (ms)
f_{min} = 33 kHz (T= 30° C, T_L= 0 Nm)	12.5	3.25
f_{max} = 37 kHz (T= 30° C, T_L= 0 Nm)	2.6	13.2
T_{min} = 25° C (f = 34 kHz, T_L= 0 Nm)	11.5	4
T_{max}= 50° C (f = 34 kHz, T_L= 0 Nm)	11.5	8.5

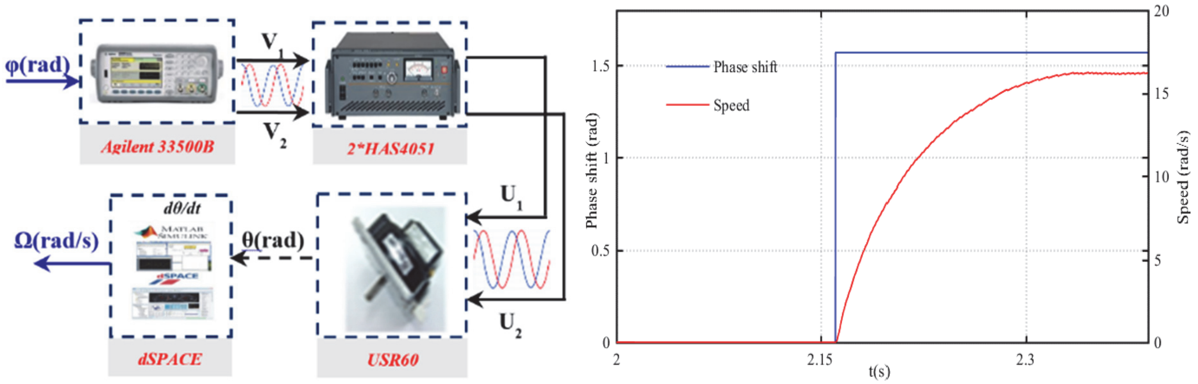

(a) (b)

Fig. III-25. (a) Synoptic of TF identification method, (b) Open loop speed response for π/2 phase shift step

III.7 Synthesis of robust position controllers of USR60

The identified TF model $G_{USM}(s)$ (Eq. III-21), is used for the controller synthesis. As for the rest of studied PZMs in this manuscript, robust H-infinity (H_∞) and discrete time RST position controllers are designed, evaluated, and compared in order to select the accurate closed loop positioning system. The synthesis approach of H_∞ and RST controllers for general plant is explained in details in chapter.II. In this section, the USR60 plant will be studied and the position controllers will be found as function of the desired closed loop performances. A proportional, integral, and derivative (PID) controller will be designed and experimentally implemented and compared to the proposed robust position controllers to prove the advantage of the proposed techniques.

III.7.1 H-infinity position controller of USR60

As detailed in chapter II, the mixed sensitivity H_∞ optimization method is used to synthesize the feedback controller K(s). To deal with the USR60, the closed loop configuration of the H-infinity optimization process (Fig. III-26.a) will be used to synthesize the position controller K(s). In Fig. III-26.a, the USR60 plant is represented by $G_{USM}(s)$, b represents the input system perturbation, r and y are respectively the reference and measured positions, and ε is the error between the reference and measured data. For the mixed sensitivity H_∞ optimization method, in order to shape respectively the sensitivity function S, the transfer G.S, and the complementary sensitivity function T (T=1-S), weighting filters (Wi) are introduced as shown in Fig. III-26.b. The W_1 filter parameters are chosen in order to reduce the error (ε) between the reference and measured position. W_2 is integrated to perform the control signal (u) quality which is the phase shift (φ) in this case, by overcoming the perturbation effects caused for example by the load torque. The input perturbation b is the output of the weighting filter W_3 which is addressed to reduce the effect of eventually electrical noises injected to the control signal.

As explained in chapter II, for the system configuration shown in Fig. III-26.b, the controller K(s) must satisfy the inequality given in II-11 by:

$$\left\| \begin{matrix} w_1 \mathrm{S} & -w_1 \mathrm{SG} w_3 \\ w_2 \mathrm{KS} & -w_2 \mathrm{KSG} w_3 \end{matrix} \right\|$$

For the USR60 plant, the desired closed loop performances are fixed in order to achieve a time response (t_r) lower than 10 ms with a gain and phase margins respectively of 10 dB and 45°. The steady state error ratio of the positioning system should be lower than 0.1% of the final position. The weighting filter parameters will be then determined to satisfy the performances listed above. The transfer $1/W_1$ should have a low gain at low frequency to satisfy the steady state error criteria while its cut-of frequency represents the system bandwidth.

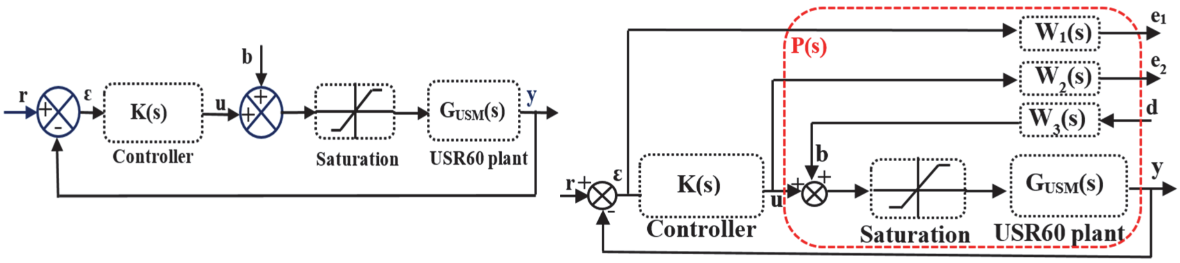

(a) (b)

Fig. III-26. (a) USR60 Closed loop configuration, (b) USR60 closed loop augmented by weighting filter

The cut-off frequency of W_2 will be chosen much higher than that of W_1 to limit the maximum system bandwidth and therefore to avoid very fast system responses and high control signal values. The W_3 will be chosen as constant and can be readjusted as function of the introduced noises. The obtained weighting filters for the USR60 plant are:

$$w_1 = \frac{(s+510)}{1.42(s+503)}\,;\; w_2 = \frac{(s+510)}{0.1(s+5.10^5)}\,;\; w_3 = 0.1 \tag{III-22}$$

Based on the filter parameters, the optimal controller and gamma constant can be found using the MATLAB function “hinfsyn”:

$$\mathrm{K(s)} = \frac{38.10s^3+1.9.10^{11}s^2+5.4.10^{13}s+5.6.10^{13}}{s^4+6.6.10^{13}s^3+1.9.10^{13}s^2+2.7.10^{12}s+6.10^{12}} \quad ; \quad \gamma = 1.05 \tag{III-23}$$

The controller order equal to the sum of system and filters order. Therefore, for the USR60 case, K(s) will be a fourth order controller. As given in Eq.III-23, the obtained controller contains zeros and poles outside the system operation frequency range. The useless zeros and poles can be reduced via the “reduce” MATLAB function. Finally, an optimal second order controller is obtained:

$$\mathrm{K}_{red}(\mathrm{s}) = \frac{3.8.10^5\mathrm{s} + 1.12.10^8}{\mathrm{S}^2 + 2.6.10^3\mathrm{s} + 3.3.10^6} \tag{III-24}$$

As explained above, the H_∞ feedback controller and the associated weighting filters must satisfy the inequalities given in II-11. Therefore, the filters and system transfer functions behavior are verified through the frequency analysis as shown in Fig. III-27. The behavior of S(jω) is fixed at low gain in low frequencies to ensure the precision requirements of the controller. The frequency ω_1 represents the desired bandwidth for the controller. The cut off frequency of the weighting filter W_2 is fixed at high value to perform the rejection of high frequency noises of the control signal.

As can be seen, that the desired performances of the closed loop can be easily introduced in the frequency domain via the H_∞ control principle with the minimum controller degree. The robustness of this controller is also ensured and will be confirmed later by simulation and experimental results.

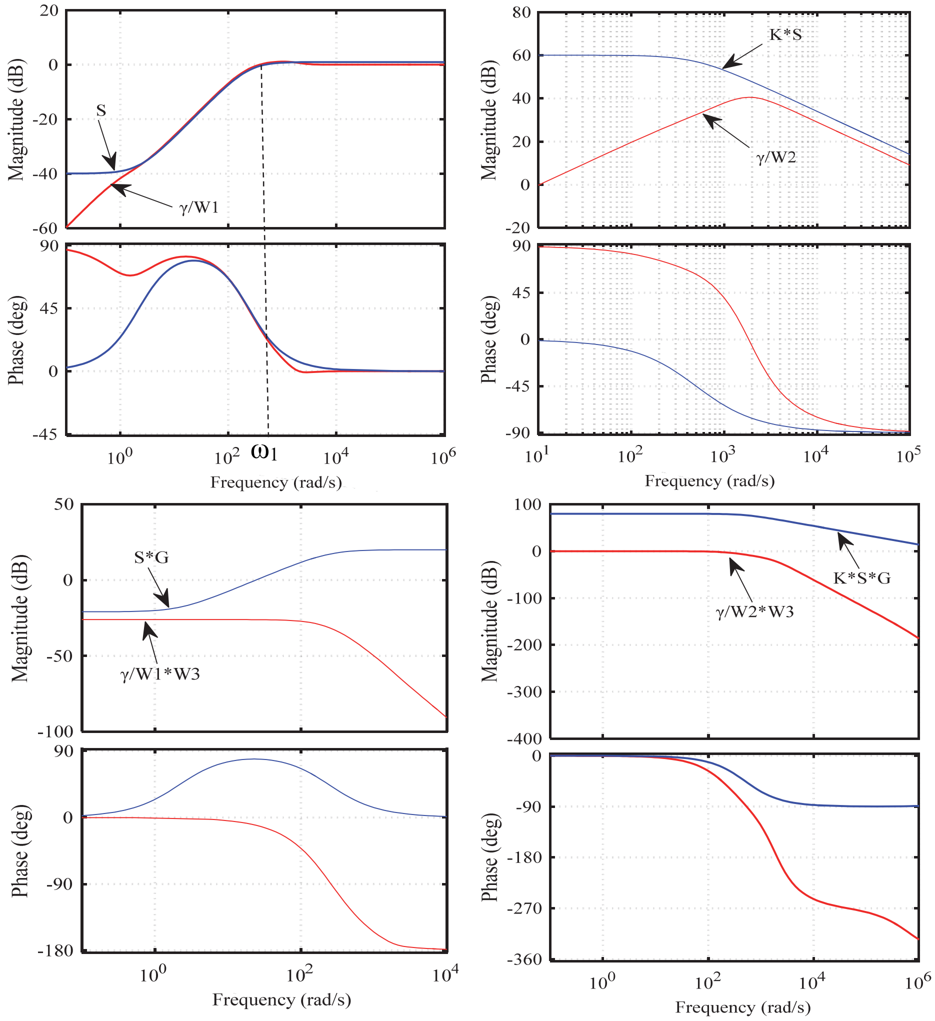

Fig. III-27. Frequency analysis of sensitivity transfer functions

III.7.2RST position controller of USR60

The second position controller synthesized for the USR60 is a discrete time RST control (Fig. III-28) based on pole placement method. Therefore, a discrete time motor plant ($G_{USM}(z^{-1}) = \frac{B(z^{-1})}{A(z^{-1})}$) is needed to synthesis the controller. It can be obtained by the discretization of the continuous model $G_{USM}(s)$. A zero-order hold method with a sampling time of 0.1ms is used for the discretization aproach and a discrete USR60 plant is obtained:

$$G_{USM}(z^{-1}) = \frac{B(z^{-1})}{A(z^{-1})} = \frac{10^{-5}(1.43z^{-2} + 1.45z^{-1})}{0.97z^{-2} - 1.97z^{-1} + 1} \tag{III-25}$$

This plant is designed to be controlled so that the closed loop will have a second order type with a damping factor of 0.6 and a bandwidth of 500 rad/s. Thus, a discrete characteristic polynomial $A_m(z^{-1})$ is given by:

$$A_m = 1 - 1.92z^{-1} + 0.932z^{-2} \qquad \text{III-26}$$

By the resolution of the primary Diophantine equation (ref), the polynomials $S(z^{-1})$ and $R(z^{-1})$ can be obtained:

$$s(z^{-1}) = 1 - 0.02z^{-1} \;\; ; \quad R(z^{-1}) = 1.47 - 1.38z^{-1} \qquad \text{III-27}$$

In order to track sine-wave position trajectories with angular frequency ω_0 =10rad/s, the auxilliary Diophantine equation (II-35) is rewritten as:

$$\begin{aligned}(1{-}2z^{-1} + +z^{-2})L(z^{-1}) + 10^{-5} &= 1 - 0.02z^{-1}(1.43z^{-2} + 1.45z^{-1})B'_m \\ &= 1 - 1.92z^{-1} + 0.932z^{-2}\end{aligned} \qquad \text{III-28}$$

The polynomials $T(z^{-1})$ is obtained by fixing unity gain in steady state and by resolving the auxiliary Diophantine equations (II-28, and II-35):

$$T(z^{-1}) = 2.46 - 2.38z^{-1} \qquad \text{III-29}$$

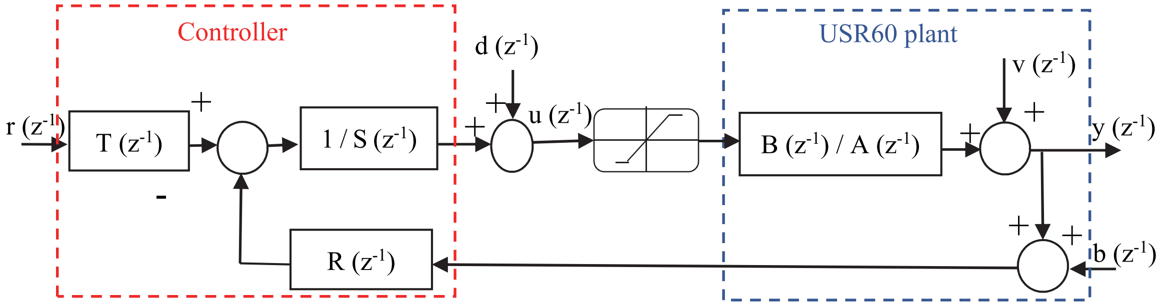

Fig. III-28. Discrete time USR60 plant controlled by RST regulator

The discrete time synthesis of the RST controller minimizes the delays introduced by the discretization stage of a continuous regulator. The robust pole placement method is effective for the tracking of polynomial reference signals. Moreover, the third degree of freedom which is the polynomial T, can be easily used to ameliorate the tracking performances.

III.7.3 Simulation of closed loop USR60 positionning system

The simulation results will be presented in this section to verify the performances of the proposed positioning system. The closed loop simulation results using the motor TF model ($G_{USM}(s)$) will be firstly discussed to prove the stability, time response, precision, and robustness of the proposed system. Afterwards, the simulation results with the developed electro-mechanical model of USR60 (section III.4) will be presented to confirm that the proposed model is suitable for control purposes. In order to prove the advantage of the proposed controllers, PID controller is compared to the H_∞ and RST for the robustness issues.

III.7.3.1 Transfer function model simulations

The simulation results of the closed loop system are presented to verify the controller performances in terms of stability, time response, precision, and robustness. The fixed response time and the stability of the closed loop system are guaranteed with the two proposed controllers as illustrated in Table III-2,

Fig. III-29, and Fig. III-30.a. It should be mentioned that the minimum margins to guarantee the stability of a closed loop system are around to 10 dB and 45° for the gain and the phase margins.

The phase shift (φ) between the two driven voltages of TWUSM is limited between +/-π/2 for practical use, because outside of this range the motor behavior will be highly nonlinear [9]. The control signal saturation between +/-π/2 will be taken into account in the simulation and experimental tests. The closed loop simulation results without and with control signal (φ) saturation are presented in Fig. III-30.a and b respectively. Fig. III-30.a is presented in order to verify the fixed performance criteria in terms of time bandwidth and overshoot. The time analysis of the closed loop system controlled by H_∞ and RST for different position trajectories is shown in Fig. III-30.c and d. The two proposed controllers show high precision levels with zero steady state error and no overshoot. The motor speed depends on the driving frequency, motor temperature, and load torque. Therefore, the identified motor transfer function parameters (k_m, τ_m) will change if the motor operation conditions change. The robustness of the position controllers in the case of motor parameter variation is also evaluated. The motor gain and time constant are changed without modifying the controller parameters in order to validate the system robustness. The two presented controllers are compared also to a PID controller to confirm the advantage of the proposed strategies. The PID parameters are determined based on the motor TF (Eq.III-21) and tuned by trial-and-error through intensive tests. The resulting PID parameters are finally; K_p=5, Ki=0.1, and K_d=1.15. Fig. III-31 presents the position responses respectively in case of gain constant (k_m) decreases by a ratio of 50% (5.75 instead of 11.5), and time constant (τ_m) increases by a ratio of 65% (7 ms instead of 4.25 ms). This is the case when the motor is driven with a frequency of 36 kHz. The simulation results show that the response of the three designed controllers is not much affected by the gain constant variation (Fig. III-31.a). Whereas, the time constant variation generates an overshoot of respectively 0.5%, 0.9%, and 3% for the RST, H_∞ and PID controllers as illustrated in Fig. III-31.b.

To simulate the effect of electrical noises injected the generated control signal (φ) or to the measured position (θ), external Gaussian random noises are injected to the closed loop system to examine the perturbation rejection capability of the position controllers.

Table III-2: Stability margins

	H_∞	RST
Phase margin(deg)	70.9	61.5
Gain margin(dB)	24.2	33.4

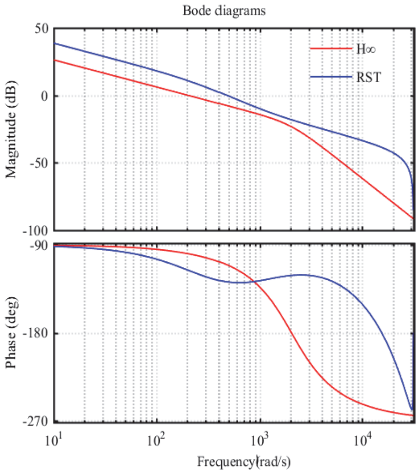

Fig. III-29. Bode diagrams of USR60 control systems

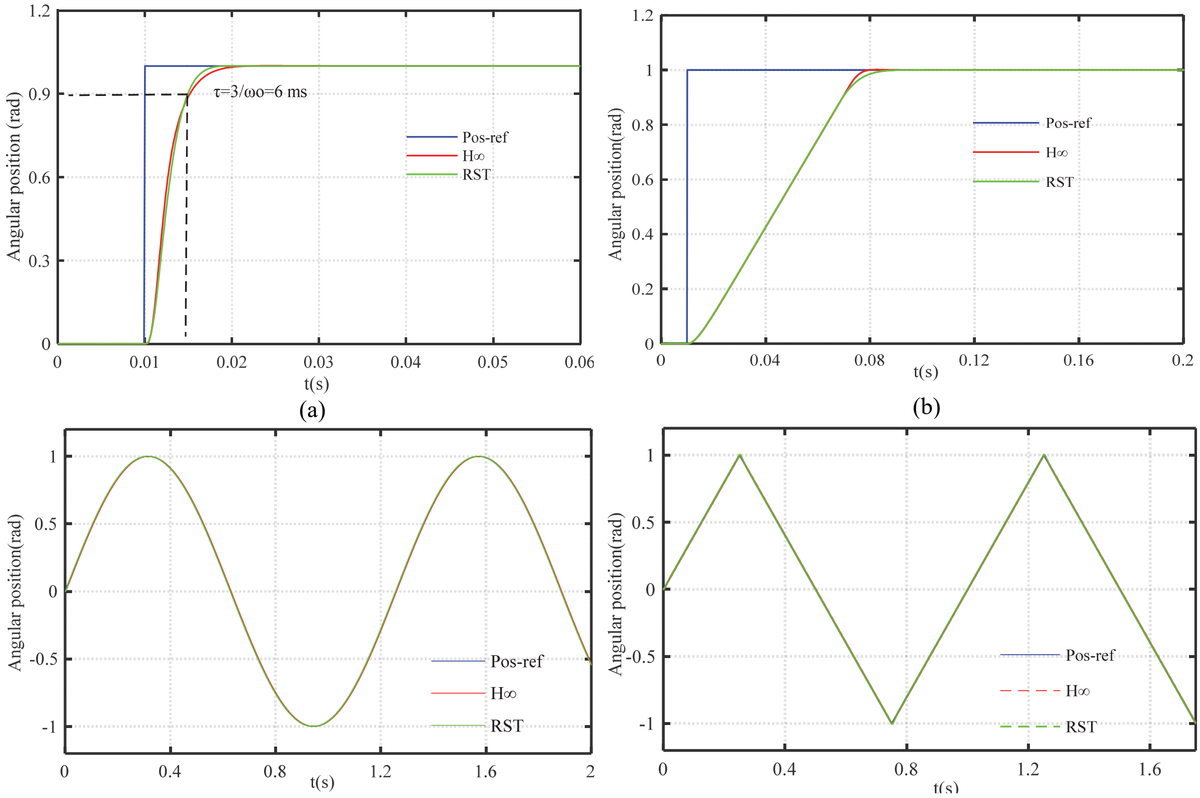

(a) (b)

(c) (d)

Fig. III-30. Comparison of closed loop position responses: (a) Step response , (b) Step response with limited phase shift, (c) Sine-wave motion,(d) Triangular motion

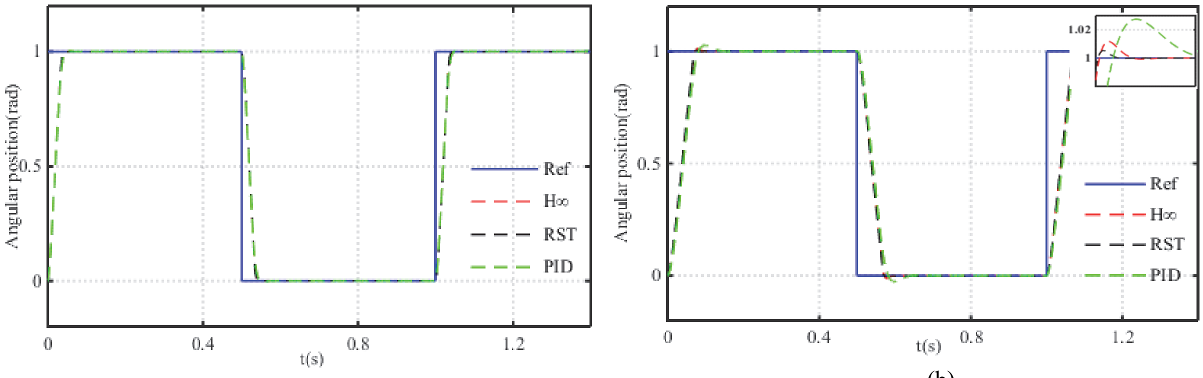

(a) (b)

Fig. III-31. Controller performances under motor parameters variation: (a) 50% k_m, (b) 65%τ_m

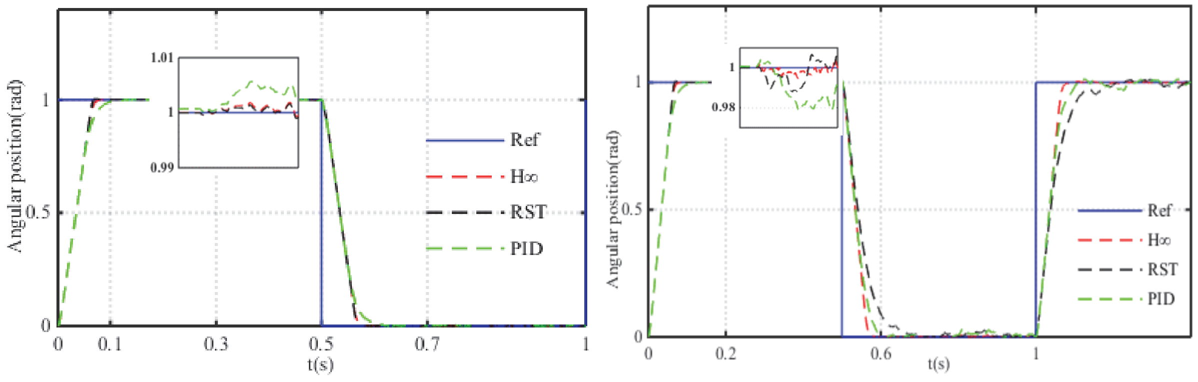

(a) (b)

Fig. III-32. Comparison of position step responses under: (a) Control signal noises, (b) Measurement noises

The difference between the three controllers in term of control signal noises rejection can be deduced from the amount of the output position distortion in Fig. III-32.a. For an injected control signal noises of +/- 0.1 rad, the output position distortion is +/- 0.001 rad for the RST and H_∞ and +/-0.005 rad for the PID controller. The measured position is perturbed, by a high frequency signal noises (+/-0.1 rad/10 kHz) equivalent to the noises that can be generated by the position sensing and ADC/DAC conversion stages. Fig. III-32.b shows that the motor position is much affected by the measurement noises. In this case, as illustrated in Fig. III-32.b, the robustness of the H_∞ can be easily distinguished compared to the rest of controllers. In fact with the H_∞ controller, we keep a maximum position distortion of +/- 0.007 rad for a step position of 1 rad. Moreover, the time responses of the positioning system based on PID and RST controllers is affected by these noises, and this is not the case with the H_∞ controller.

III.7.3.2 Simulation results based on electromechanical model

The established Simulink model of USR60 presented in section III.4 is used here to validate the closed loop position system based on H_∞ and RST controllers. As shown in Fig. III-33, the measured and reference positions are introduced to the position controller subsystem, and one of the synthesized control techniques will be then executed and generates the position control signal (voltages phase shift). This signal will be sent to the motor supply subsystem in order to generate the driving voltages. The voltages amplitude and frequency are constant and equal respectively to 130 V_{rms} and 40 kHz. The step position responses of the closed loop system shown in Fig. III-34.a confirm the accuracy and fast response of the positioning system without overshoot. The tracking of variable position trajectories is also validated with high precision levels as illustrated in Fig. III-34.b and c for respectively triangular and sine-wave motions. A brief comparison with PID controller in term of robustness to injected disturbances has been done in order to prove the advantage of the proposed method.

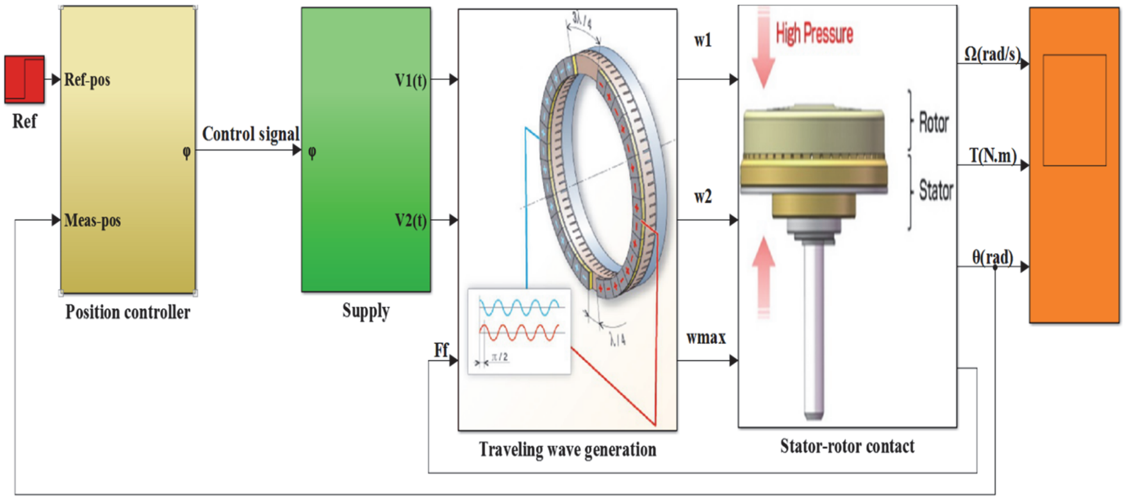

Fig. III-33. Block diagram of Simulink closed loop system

Therefore, Gaussian random noises (Fig. III-35.b) are injected to the control signal and the measured position (at t= 0.1s). The noises rejection capability of each control method is then evaluated. Fig. III-35.a and c show the comparison between the simulation results of the closed loop system in case of control signal and measurement noises. As clarified in the zoomed area, the H_∞ and RST controllers have a better noises rejection capability than the PID, the position error remains less than 0.1% for a step position of 30°.

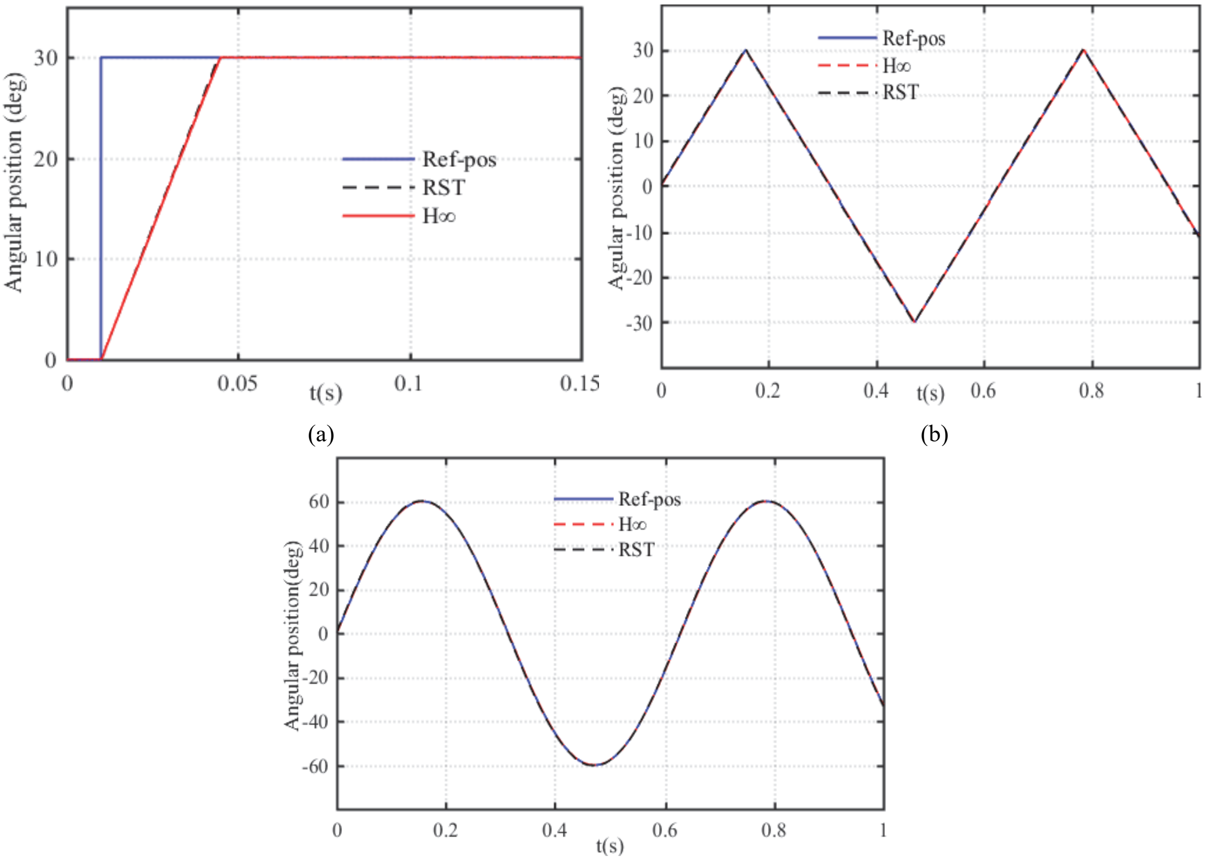

(a) (b)

(c)

Fig. III-34. Simulation of closed loop responses: (a) Step, (b) Triangular motion, (c) Sine-wave motion

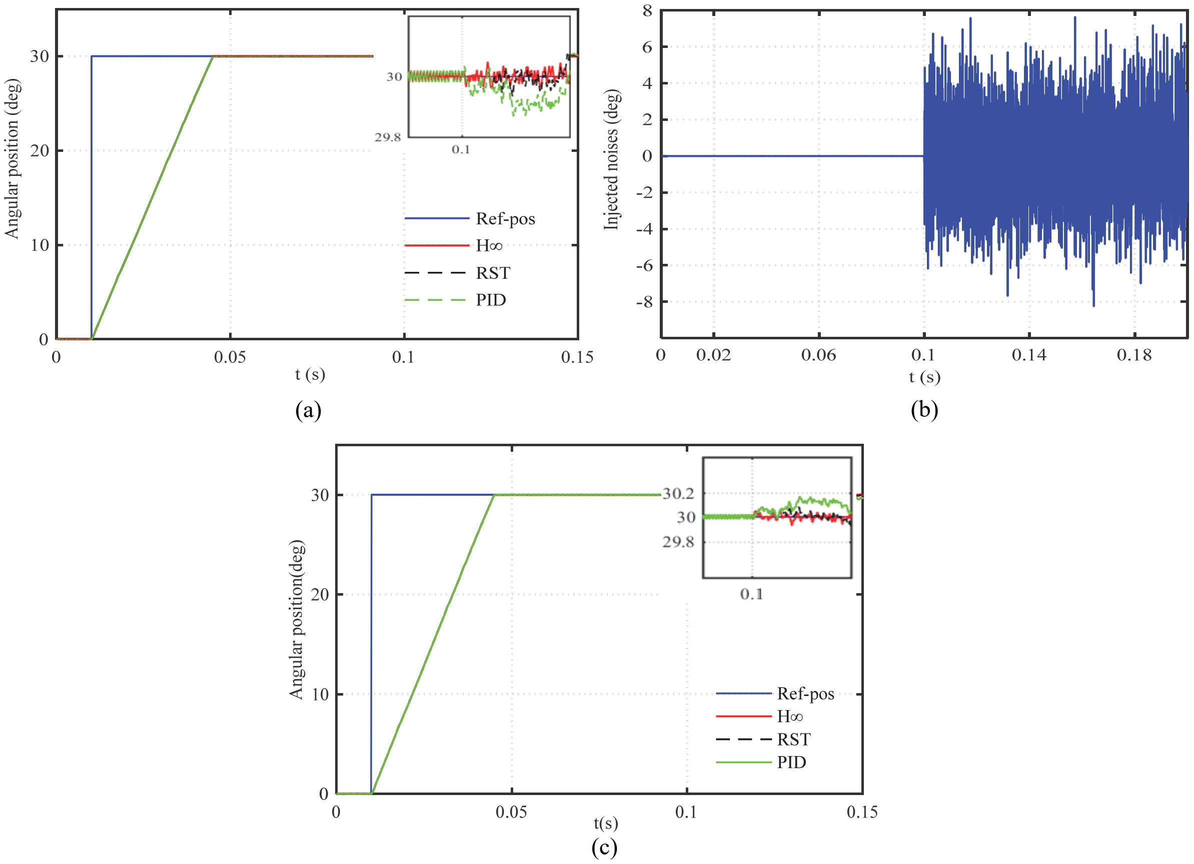

(a) (b)

(c)

Fig. III-35. (a) Comparison of control signal noises rejection capability, (b) Injected noises,(c) Comparison of measurement noises rejection capability

III.8 Real-time implementation of TWUSM closed loop positioning system

The compact experimental platform shown in Fig. III-17 is used for the real time implementation of the positioning system. As explained in section III.6.1, the proposed position controllers are implemented in the Matlab/Simulink environment and compiled via the dSPACE board (with a sampling time of 0.1 ms). In order to prove the advantage of the proposed method, the H_∞, RST, and conventional PID controllers are experimentally implemented. A graphical interface (Annex A) is also built to configure the motor operation mode, and to change the system parameters in order to evaluate the performances of the closed loop system. Via the graphical interface one can also switch between the open and closed loop operation mode, and choose the motor motion trajectory.

III.8.1 H-infinity test results

The motor tests show that the mechanical resonance frequency and consequently the motor speed changes as functions of the motor temperature. Because of this, the closed loop tests are done with a driving frequencies higher than f_r to avoid the instability around the resonance frequency. For this reason, the response time with the experimental tests is higher than obtained with the simulation results at the resonance frequency. The H_∞ controller is tested with different position trajectories, variable driving frequencies, and in the presence of load torque. In Fig. III-36, the control method is tested with a rotor velocity of 10 rpm (f_r=36 kHz) and without load. As can be seen, there is no overshoot with a static error of 0.09° (0.1% which is the maximum resolution of the encoder). The tracking performances of different position trajectories are tested at the driving frequency 35 kHz (30 rpm) showing similar results in terms of precision and response time (Fig. III-37). When a load torque is applied to the shaft of rotary TWUSM, a dead zone appears at the phase-speed characteristic (Fig. III-24). The reported solution is generally the addition of dead zone compensation system to the principal position controller [105, 128, 129].

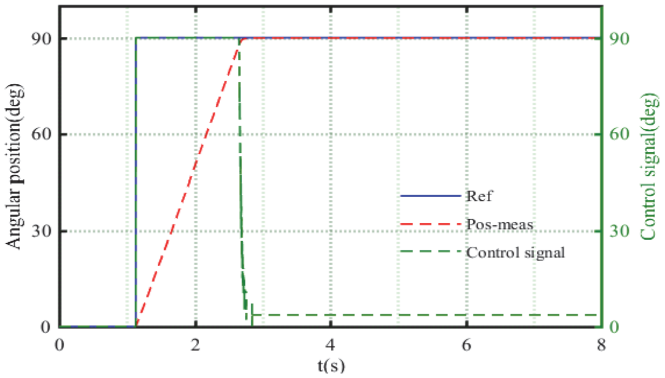

Fig. III-36. Step response of H_∞ position controller (T_L=0 Nm)

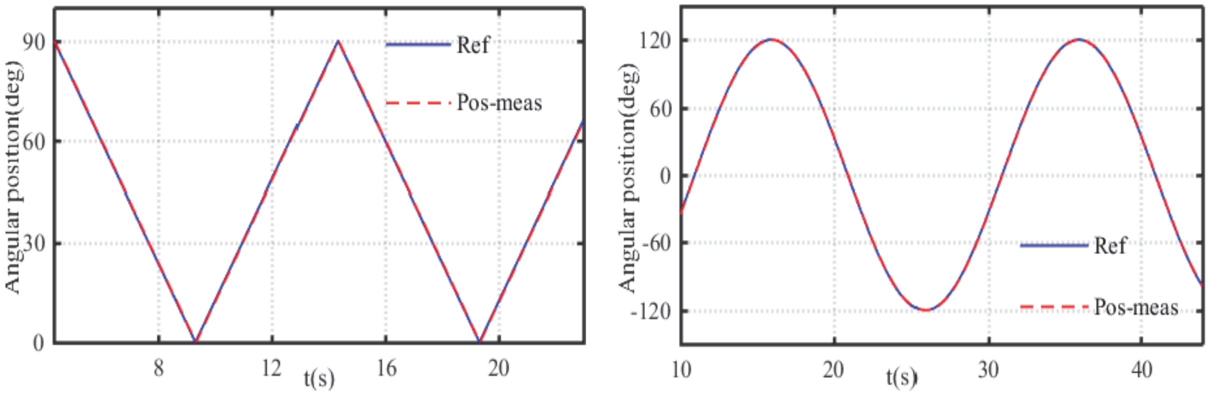

(a) (b)

Fig. III-37. H_∞ response for periodic position trajectory (T_L=0 Nm): (a) Triangular motion, (b) Sine-wave motion

In this work, the challenge is to validate the precision and the robustness of the positioning system based on TWUSM even in the presence of dead zone. While the motor speed is load-depending, it is an expected result that the motor response time increases with load increasing as shown in Fig. III-38.a. However the H_∞ closed loop system keeps a high precision level in case of loaded motor, where for example the steady state error is of 0.36° for a position step of 90° when a load torque of 0.35 N.m is applied (Fig. III-38.a). It should be mentioned also that for the case of 0.35 N.m the dead zone reaches +/-30°. Due to the friction system between the stator and rotor of the TWUSM, the motor temperature will increase if no cooling system is used. The motor parameters and performances of TWUSM are temperature-depending [130-132]. In order to validate the performances of the proposed system under any motor temperature (up to 55°C), the H_∞ is tested under different motor temperatures (Fig. III-38.b). The precision is always guaranteed under temperature increasing, where for an operation temperature of 51°C the maximum static error is of 0.4° for a rotation of 90°.

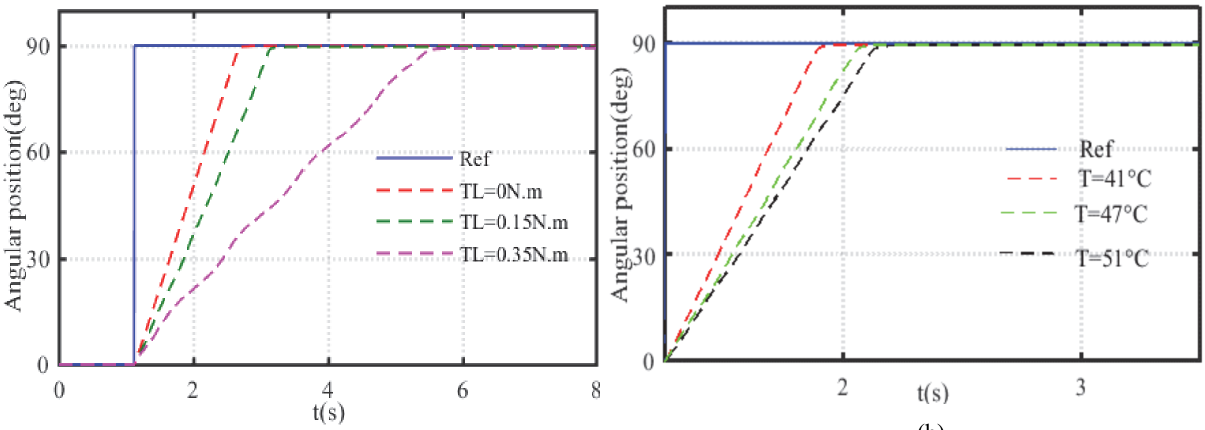

(a) (b)

Fig. III-38. Step responses of H_∞ position controller : (a) With different load torques, (b) Under different motor temperatures (T_L=0 Nm)

III.8.2RST test results

The RST position controller is synthesized in discrete time with a sampling period of 0.1 ms. The position step response and the control signal of the RST controller with a driving frequency of 35 kHz are presented in Fig. III-39.a. Similar to the other controller, there is no overshoot of the step response with a precision of 0.1%. The RST controller with auxiliary Diophantine equation shows high precision levels for polynomials position reference and especially for the sine-wave trajectory (Fig. III-39.b), where the reference signal frequency is taken into account in the synthesis procedure (Chapter II, sectionII.3). The loaded motor tests show that the static error increases significantly. One solution to ameliorate the precision is to use the polynomial $T(z^{-1})$ and with modifying the filter A_0 (II-28). The test with modified polynomials gives a static error between 0.1% and 1% (Fig. III-39.c)

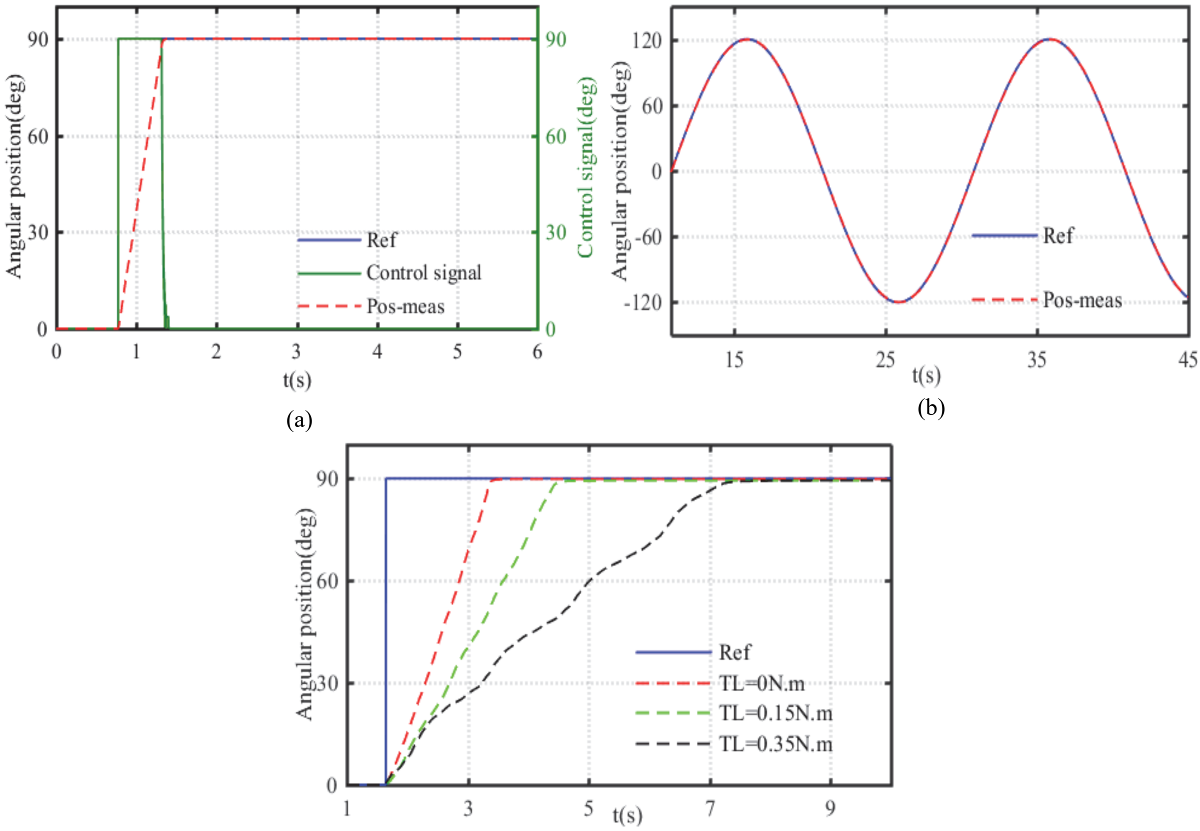

(a) (b)

(c)

Fig. III-39. RST responses: (a) Step motion (T_L=0 Nm),(b) Sine-wave motion (T_L=0 Nm),(c) With different load torques

III.8.3. Comparative study of controller performances

A comparative study between the H-infinity, RST, and a PID controllers will be presented in this section in order to prove the advantage of the proposed methods. The comparison criteria are the precision and time response, load torque (dead-zone) sensitivity, adaptation with polynomial reference signals, and the rejection of control signal or measurement disturbances. The controller parameters are the same used in the simulation study presented in section III.7. The proposed controllers show good performances in terms of time response and precision in case of no-load tests and without motor heating. However, when load torque is added, the H_∞ controller gives higher precision levels and faster response times as shown in Fig. III-40 for load torques of 0.1 Nm and 0.2 N m. The degradation of the precision levels is explained by the dead zone around zero phase values in the speed-phase shift characteristics with load torques (Fig. III-24).

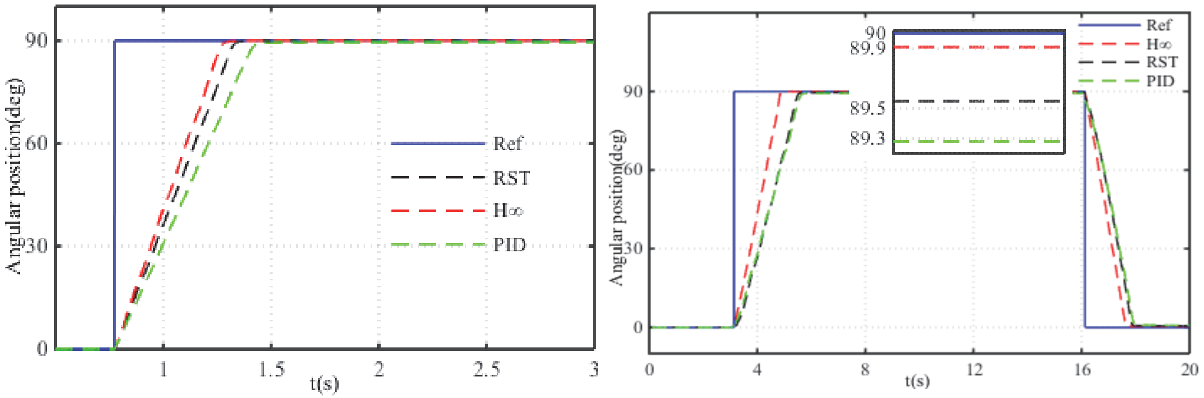

(a) (b)

Fig. III-40. Comparison of H_∞, RST and PID step position responses for loaded motor: (a) 0.1N.m, (b) 0.2N.m

The robustness of the H∞ controller can be easily distinguished in these cases, where the controller gives a static error less than 0.1° in case of 90° rotation under 0.2 Nm. The resulting static error ratios of the three controllers in the case of loaded motor step response (90°) are summarized in Table III-3. From this table, it is clear that the very high precision levels can be achieved with the H∞ controller when the motor operates under load conditions. Fig. III-41. shows the comparison test results for sinus position response (120°) with a load torque of 0.2 Nm, giving a maximum static error of 0.65% (0.8°) for H∞, 1% (1.2°) for RST, and 1.8% (2.2°) for PID controller. The steady state error in load conditions is caused by the quality of the control signal and the resulting dead zone (Fig. III-24). The better results of the H∞ controller due mainly to the weighting filter W2 which filters directly the control signal. The disturbances rejection capability of the three proposed controllers is also compared. Additional Gaussian random noises are injected to the closed loop system as a kind of system disturbances. Firstly, a high frequency noises is injected to the measured position data (encoder output) to anticipate the noises that can be generated by the position sensing and acquisition system. Secondly the control signal (φ) is perturbed by injecting additional oscillations. The proposed positioning system show high rejection capability of the control signal distortion as shown in Fig. III-42.a. Where for an injected perturbation of +/- 5° of the control signal, the maximum position distortion is 0.3°. However, when the measured position is perturbed by high frequency signal (10 kHz) and an amplitude of +/-5°, the robust H∞ position controller shows much better rejection capability than the RST and PID controllers as illustrated in Fig. III-42.b. In the zoomed area of this figure, the resulting static error is respectively 0.3, 1 and 1.6° for the H∞, RST, and PID controllers. The advantage of the H∞ controller in case of injected measurement noises is justified by the fact that the error signal between the measured and reference positions is directly filtered by the weighting filter W1.

Table III-3: Static error as function of load torques

T_L(N.m)	H_∞	RST	PID
0.1	0.1%	0.3%	0.4%
0.3	0.25%	0.6%	1%
0.5	0.4%	1%	1.65%

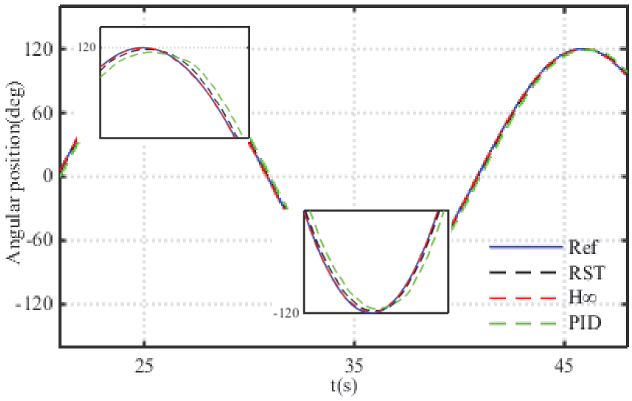

Fig. III-41. Comparison of controller performances for sine-wave motion tracking (TL=0.2 Nm)

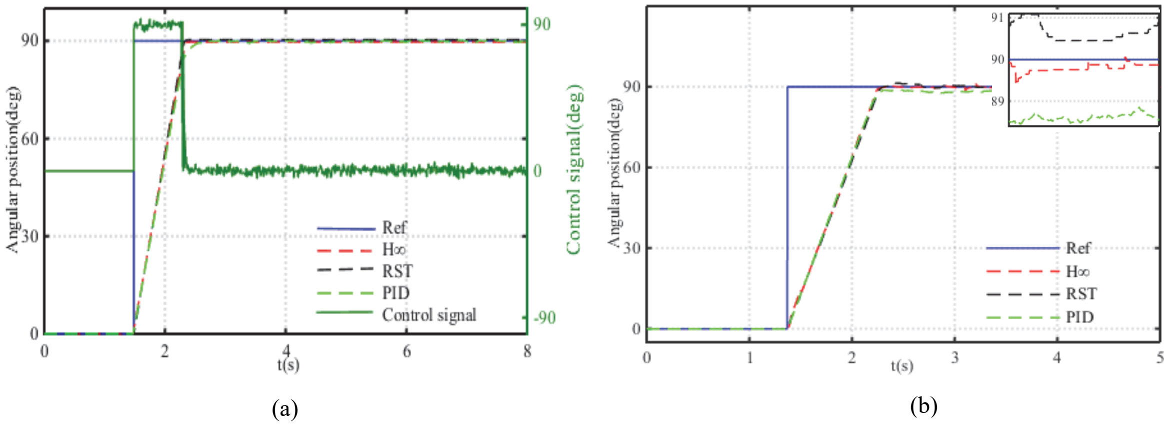

Fig. III-42. Comparison of controller rejection perturbations capability: (a) Control signal noises, (b) measurement noises

III.9 Conclusions

This chapter deals with a high precision positioning closed loop system based on traveling wave ultrasonic motor. In order to achieve this goal, we started with the description of the working principle of TWUSM type USR60. A survey about the developed models of TWUSM and the related position controllers was presented in order to highlight the contributions of the proposed research work.

The problem with the TWUSM models for control issues is that; the Equivalent Circuit Models (ECM) which are generally used for TWUSM control purposes [86, 87] for the sake of simplicity, lack of the ability to capture the dynamic behavior of the contact zone between the stator and rotor which is at the origin of the torque generation. In other hand the developed analytical and numerical models which describe the highly nonlinear behavior of the contact mechanism [97, 98, 100, 125] are very complex for control design and implementation. A simplification effort of a full hybrid model was reported in [133] for speed control implementation, but it leads to neglect the vertical motion of the rotor by imposing a constant length of the contact zone and a zero rotor vertical speed. Moreover, the proposed model can be controlled only via the driving frequency, and in consequence in only one motion direction.

The contribution of the designed model is that: Firstly, it is able to capture the dynamic of the motor including the traveling wave generation process at the stator surface, the contact mechanism leading to the torque generation, and the vertical and angular motions of the rotor. Secondly, it permits the implementation of motion control in the clock/counterclockwise directions via the supply voltages amplitude, frequency, and phase shift. Moreover, via the established USR60 model in the Matlab/Simulink environment, one can evaluate the effect of the stator (damping, stiffness, and coupling factor) and contact surface parameters on the output motor performances. The model simulation results reflect the behavior of the USR60 output characteristics variation published by the manufacturer. In second time it served to implement robust closed loop positioning controllers using the voltages phase shift as control signal.

Compact experimental positioning system based on USR60 is setup, and the motor characteristics are analyzed via the open loop tests. The experimental evaluation of the USR60 output characteristics shows that the frequency drive method is more suitable for speed control and not for position control. This is due principally to the "pull-out" phenomenon, where the motor shut-down immediately if the driving frequency decreases below the mechanical resonance frequency. Whereas, the resonance frequency is variable and depending on motor temperature and external loads. Moreover, the immediate switching between the on and off motion states of the USM is not feasible using the driving frequency, where a progressive increase of the frequency is needed to restart the motor.

The USR60 was also driven in open loop using supply voltage amplitudes, where a minimum voltage of 80 V_{rms} is needed to move the motor. The speed-V_{rms} characteristic has a quasi-linear behavior, but a large variation of supply voltage (40 V_{rms}) produces a small speed variation and in consequence reduced motion range. In addition, the bidirectional motion feature is missing using this method.

The USR60 drive using the voltages phase shift is more suitable to control the shaft position. The motor can move in bidirectional motion by inverting the sign of the phase shift, and the switching between the on and off motion states can be done immediately by imposing a zero phase shift. However, the speed-phase shift experimental characteristic shows dead zone when a load torque is added. The effect of this dead zone must be overcome to achieve high precision levels. In other hand, when the motor reaches the desired position, it has a high holding torque even without supply. The drawback of the drive technique using the voltages phase shift is that in “off” motion state, the motor continuous to consume power while the voltage amplitude is different to zero.

The voltage phase shift was chosen as position control signal in order to meet the specific requirements of the motor application. A Transfer Function (TF) between the control signal (phase shift) and the motor angular position is then experimentally identified. The H-infinity and RST position controllers are then synthesized on the basis of the TF model.

The advantage of the proposed control methods is that, they combine the precision performances and the robustness requirements in one simple design controller. The goals are to overcome the nonlinear behavior of the motor caused by the resonance structure, motor heating, and load torques leading to motor parameters variation, and to reject the external perturbation without supplementary compensation systems or complex adaptation methods.

The closed loop positioning systems based on H_∞ and RST controllers are simulated in closed loop using the designed electromechanical USR60 model. The simulation results confirm the accuracy of the proposed systems, and the robustness to model parameters uncertainties. The simulation comparison with PID control proves the advantage of the H_∞ in term of robustness to external disturbances. Afterwards, the positioning system is implemented in real time via a dSPACE microcontroller. A graphical interface is designed to configure the system parameters and test conditions in real time. The H_∞ and RST positioning accuracies in closed loop for the no-load conditions reached the maximum resolution of the position sensor (0.09°). While the motor temperature is a critical point for USM, the accuracy of the proposed system is also validated in case of motor heating. When load torques are applied to the motor shaft, the H_∞ and RST experimental positioning results show higher precision levels than the PID. This is because that in the synthesis approaches of the two first controllers the load torque is taken as disturbance and the related sensitivity functions are optimized in order to overcome the dead zone effect. To avoid the load torque effect on the PID positioning results, a supplementary dead zone compensation system is needed. Electrical noises are injected to the control signal (phase shift) and to the measured position data in order to evaluate the perturbation rejection capability of the tested controllers. The H_∞ control method shows higher robustness levels with respect to the external noises compared to the RST and PID controllers. This is due to the flexibility design of the H_∞ given by the three weighting filters, where one is selected to meet the precision and response time requirements, while the two others are designed to reject the external disturbances in a specific frequency range. The rejection capability of the RST controller can be improved by a rearrangement of the closed loop poles in discrete time, but at the expense of precision performances. For the PID controller, an on-line tuning parameters as function of the position and control signal quality is required to ameliorate the robustness to external disturbances.

Finally, rotary TWUSM positioning system based on H_∞ control method fulfills the requirements of high precision positioning applications including robotic engineering. The advantages of the proposed system are the accuracy, fast response, and robustness to system parameters uncertainties, load torques, and external perturbations without additional compensation systems or online parameters adaptation. These features make it suitable to be integrated into practical embedded system where the compact size, precision and robustness are important

Chapter IV

Modeling and Design of Robust Closed Loop Position Controllers for Piezoelectric Actuator Drive (PAD)

IV.1 Introduction

The Piezoelectric Drive Actuator (PAD) is a novel structure of non-resonant piezoelectric motor which was introduced by Kappel et al. [68] in 2006. The working principle of PAD is based on the conversion of the linear actuator elongations into a precise rotation. The high torque (up to 5 N.m) at very low speed, high accuracy, low inertia, and high holding torque without supply characteristics make the principle use of PAD in robotic applications.

A few works related to the modeling and closed loop position control of the PAD are reported in the literature. The proposed PAD models are used to characterize the motor in static and dynamic operation modes, and for parameters identification. In [134], an equivalent mechanical dynamic model of the stator combined with a Masson model are proposed in order to identify the motor parameters through the frequency analysis. A dynamic model of the PAD is also proposed in [135] to investigate the dynamical behavior of the motor with a special emphasis on the pull off. A generalized model is presented in [136] to analyze the PAD output characteristics as function of the load torque and the actuator damping factors. However, PAD models for control purposes are not discussed in the modeling related works.

Due to the special structure of the PAD, the motor has a good position resolution in open loop. Nevertheless, the nonlinear behavior of the used stack actuators [136], and the maladjustment between the stator ring and the rotor shaft (see section IV.3) which was widely discussed in [136-138], can affect the position accuracy of the motor in ultra-precision applications. Therefore a closed loop control is needed to overcome these problems.

In this chapter, the working principle and features of the PAD will be firstly introduced. Electromechanical model of PAD7220 motor is presented for control purposes. The proposed model includes the orthogonal piezoelectric actuators and the motion of the stator ring, the micro-teeth mechanical system, and the angular motion of the shaft. Afterwards, the experimental positioning system based on PAD7220 is discussed. This setup is used firstly to evaluate the output characteristics in open loop as function of the driving parameters. Secondly, to implement in real time the synthesized robust closed position controllers. An experimental comparative study between the H_∞, RST, and PID controllers will be presented at the end of this chapter to discuss the accuracy and robustness issues of the proposed strategies.

IV.2 PAD working principle and features

IV.2.1 PAD working principle

The working principle of the rotary PAD is mainly based on the conversion of periodic elongations of linear Piezoelectric Multilayer Actuators (PMAs) into continuous rotation of a motor shaft. The PAD is composed by four piezoelectric stack actuators orthogonally oriented and stiffly connected to a ring as shown in Fig. IV-1.a. The ring has a square exterior profile with a circular cutout in its center which houses the motor shaft [139]. The shaft is fixed to the motor housing through ball bearings and has a diameter d_{shaft} slightly smaller than the internal diameter of the ring d_{ring}. The inside surface of the ring and the circumference of the shaft are machined into micro-mechanical teeth with diametral pitch of 38 µm [71]. The ring and shaft have 313 and 312 teeth respectively.

Powerful piezoelectric stack actuators (2080 N blocked force) are used to create the linear elongation with a large displacement (free displacement of 50 µm). The four piezoelectric actuators are driven by two sinusoidal voltages with a phase shift of 90° between them. Thus, the actuators expand and contract linearly and thereby push and pull against the motor ring. Thereby, the motor ring moves in a circular trajectory defined by Cartesian coordinate pair (r_x, r_y) expressed by:

$$r_x = x_a \sin(2\pi f t + \varphi_1)$$
$$r_y = y_a \sin(2\pi f t + \varphi_2 \qquad \text{IV-1}$$

where x_a and y_a represent the elongations of orthogonal stacks (m) in the vertical and horizontal directions, f is the driving frequency (Hz), φ_1 and φ_2 are the driven voltages phase shift (rad) with the restriction that $\varphi_1 - \varphi_2 = +/-90°$.

The shaft rolls on the inner surface of the ring and thus putting it into rotation. Each full period of the applied sinusoidal voltage generates a full rotation of the ring around the shaft and this, in turn, will cause the shaft to step one tooth in the opposite direction Fig. IV-2 [139].

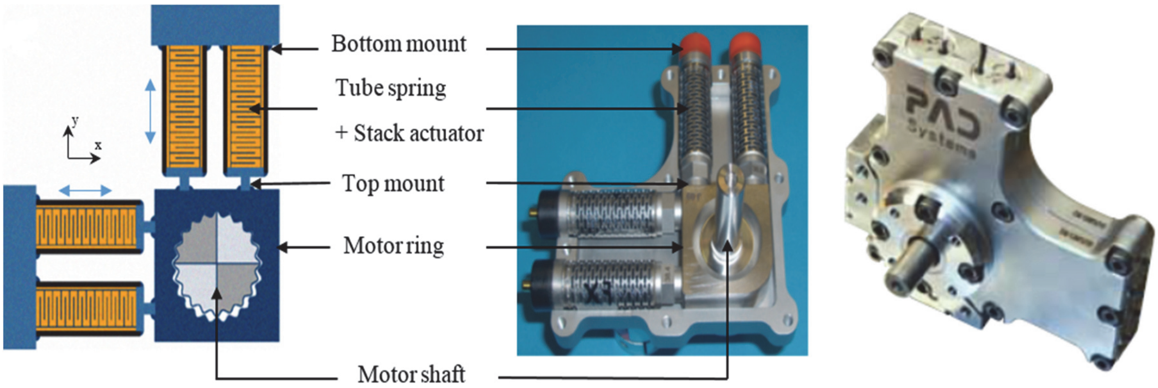

(a)

(b)

Fig. IV-1. (a) Working principle and assembled parts of PAD [138] , (b) PAD prototype [71]

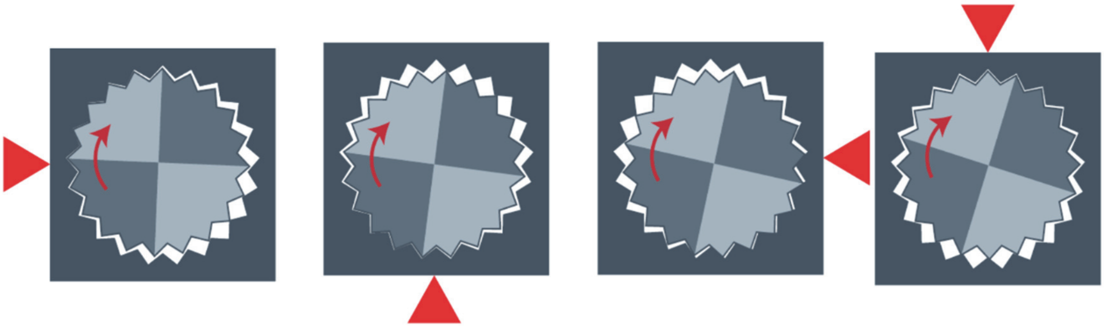

Fig. IV-2. The PAD rotation; The red arrow represents the direction of actuation. The shaft is fixed by a bearing while the ring is free to rotate around it. One revolution of the contact point will cause the motor shaft to step one tooth [139].

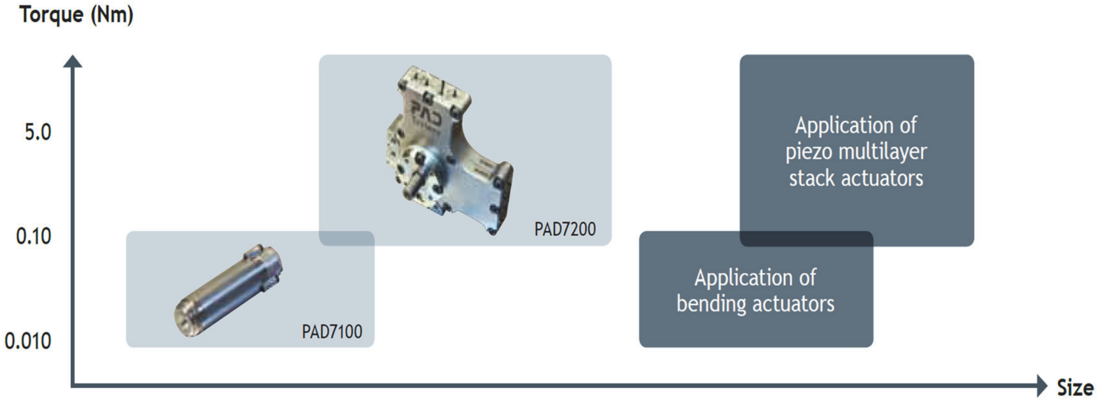

Fig. IV-3: Scalable technology of PAD [71]

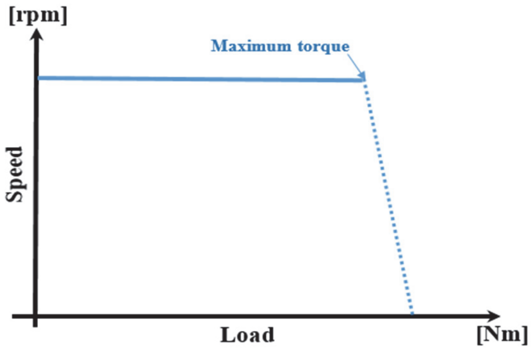

Fig. IV-4. PAD speed-load characteristics [68]

IV.2.2 PAD features

The PAD benefits from the conventional features of piezoelectric motors such as the high precision levels, high torque/weight ratio, high holding torque without supply, and no electromagnetic interferences. The combination of PMAs and rotary shaft using micro-teeth mechanical system offers the PAD additional interesting characteristics. The motor can easily be driven at very low speed (<1rpm) compared to other piezoelectric motors and up to 100 rpm. Moreover, this topology makes the PAD scalable in size and output power [68]. In fact, depending on the type, number, and size of the linear actuators, the dimension of the ring and the micro-teeth mechanical system can be readjusted. Therefore, the motor power and dimensions are adaptive as function of the application requirements. Fig. IV-3 gives an idea about the scalable technology of PAD proposed by Noliac [71]. In other hand, the special structure of the PAD enables a smart load sensing through the phase shift between the actuators charge and voltage as demonstrated in [140]. This phase shift is equal to zero in no-load conditions, and it is different to zero if a load torque is applied to the motor shaft. A relationship between the load torque and phase shift including the motor parameters is established in [140], and can be used for sensor-less torque control.

The PAD motor has also a special speed-load characteristic (Fig. IV-4). As the stack actuators permit a permanent contact between ring and shaft, the force transmission is independent of how fast the ring translates. Consequently, the rotational speed is not affected by the applied load [68].
The aforementioned features explain well the competitiveness of the PAD motor in compact and precise positioning systems, and especially the robotic applications.

IV.3 Modeling of Piezoelectric Actuator Drive (PAD7220)

The studied motor is a PAD7220 from Noliac [71] with rated speed and torque of 56.25 rpm and 4 Nm respectively (the motor datasheet is given in Annex B). In this section, Simulink model of the PAD7220 is proposed to evaluate the motor behavior as function of driving parameters, and in second time to simulate the proposed closed loop position controllers. The synoptic of the PAD model is given in Fig. IV-5. It consists of the supply part to generate the two phase shifted sinusoidal voltages (U_x, U_y). The orthogonal linear piezoelectric actuators will produce the linear mechanical elongations and forces in x and y directions. The last model part represents the micro-teeth mechanical system between the ring and the shaft.

The behavior of the piezoelectric actuators can be described by the linear piezoelectric equations:

$$\Delta x = d_{33}U - \frac{1}{K}F \tag{IV-2}$$

$$Q = CU - d_{33}F \tag{IV-3}$$

where; Δ x is the actuator elongation (m), d_{33} is a piezoelectric constant (m/v), U is the voltage (V), k is the actuator stiffness (N/m), C is the equivalent capacitance (F),Q is the actuator charge (C), and F is the generated force (N).

The elongations of linear actuators will create a circular motion of the motor ring, and due to the gear system, a rotation of the shaft will be generated. The dynamic model of the actuators and the kinematic of the ring-shaft system can be represented by the equivalent model [136] shown in Fig. IV-6.

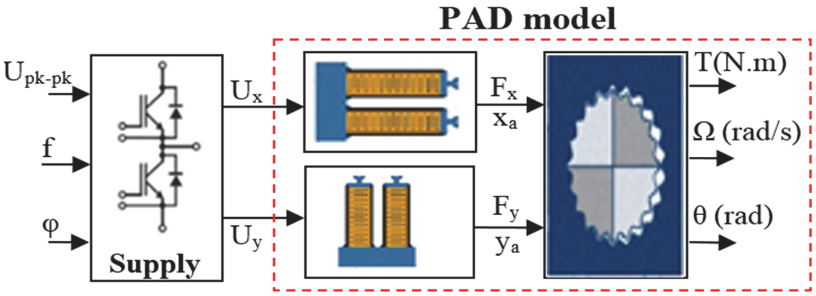

Fig. IV-5. Synoptic of PAD model

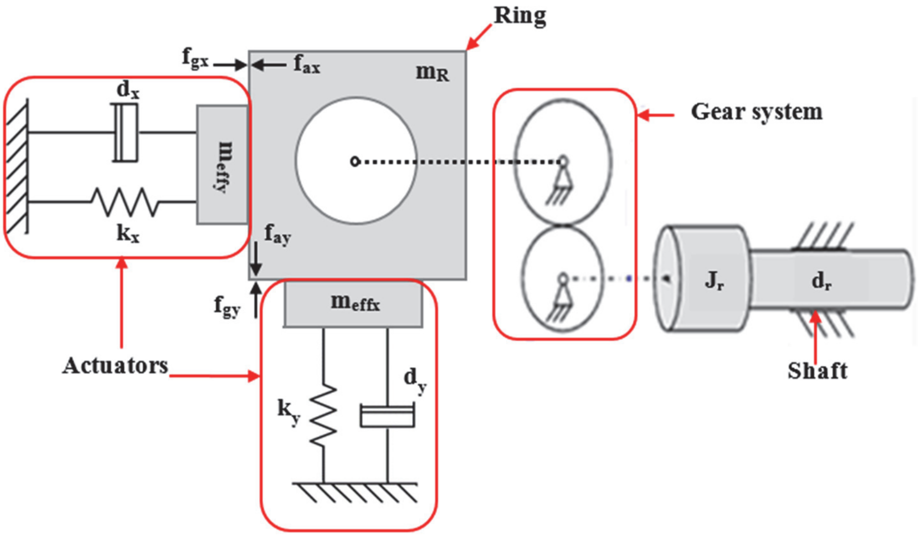

Fig. IV-6. Equivalent dynamic model of the actuators and the kinematic of ring-shaft system

As shown in Fig. IV-6, the linear actuators are modeled by equivalent spring-damper-mass systems and their motion equations can be written as:

$$\begin{aligned} m\ddot{x_s} + d_x\dot{x_s} + k_x x_s &= F_{gx} - F_{ax} \\ m\ddot{y_s} + d_y\dot{y_s} + k_y x_s &= F_{gy} - F_{ay} \end{aligned} \qquad \text{IV-4}$$

$$m = \sum_{k=1}^{n}\left(m_{effk} + m_{tk} + \frac{1}{3}m_{resk}\right) + m_R \quad ; n = 4 \qquad \text{IV-5}$$

where; $k_{x,y}$ are the actuators stiffness in x-y directions (N/m), $d_{x,y}$ are the actuators damping in x-y directions (Ns/m), $m_{effx,y}$ are the actuators effective mass in x-y directions (kg), m_R is the ring mass (kg), m_{tk} is the top cap mass (kg), m_{resk} is the tubular spring mass(kg), $F_{gx,y}$ and $F_{ax,y}$ are the generated and applied forces in x-y directions (N) respectively.

In order to build a simple PAD model for control purposes, some assumptions should be taken. Therefore, the damping and stiffness of the actuators in the two direction will be assumed to be equals

(d_x= d_y= d; k_x=k_y= k). The maladjustment between the ring and shaft position will be neglected (the shaft is in the centered position). In fact, the effect of the maladjustment on positioning performance must be compensated later by the closed loop control.

The center of the ring moves on a circular trajectory with a diameter of about a=19 µm [136] (Fig. IV-7).

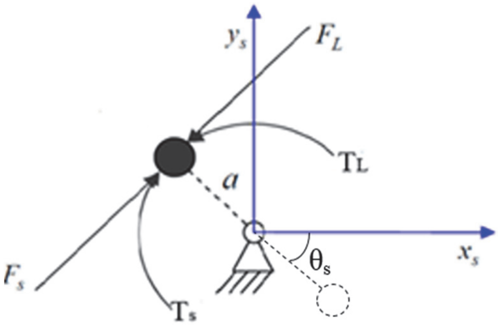

Fig. IV-7. Circular trajectory of the ring and forces on the ring

Its circular coordinates can be written as function of the angular position in x-y plane (θ_s):

$$x_s = \mathrm{acos}(\theta_s) \qquad \text{IV-6}$$
$$y_s = \mathrm{asin}(\theta_s)$$

The actuators generated torque is given by the dot product of the forces and displacement vectors of the PMAs as:

$$T_{act} = \mathrm{acos}(\theta_s)\, F_{gy} - \mathrm{asin}(\theta_s)\, F_{gx} \qquad \text{IV-7}$$

The fundamental dynamic equation of the actuator-ring contact can be also written as:

$$T_{act} - T_s = j_{trans}\ddot{\theta_s} + d\dot{\theta_s} \qquad \text{IV-8}$$

where, T_s is the ring torque (N.m), and j_{trans} is the transmission inertia (kg.m^2).

In fact, for ideal transmission system between the motor ring and shaft (T_r. Ω_r= T_s. Ω_s), the rotor generated torque (T_r) can be expressed by:

$$T_r = i_{trans}T_s = i_{trans}T_{act} - {i_{trans}}^2 j_{trans}\ddot{\theta_r} + {i_{trans}}^2 d\dot{\theta_r} \qquad \text{IV-9}$$

where; i_{trans} is the transmission ratio

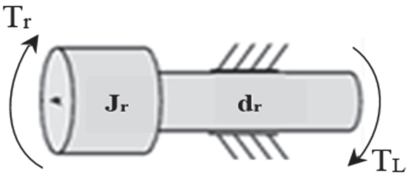

Fig. IV-8. Model of shaft angular motion

In other hand, the generated rotor torque can be written also as:

$$T_r = j_r\ddot{\theta_r} + d_r\dot{\theta_r} + T_L \qquad \text{IV-10}$$

where; T_L is the load torque (N.m), j_r is the shaft inertia (kg.m^2), and $d_r$is the shaft damping factor (Nms/rad).

From the equations IV-10, IV-9, and IV-7, the acceleration of the motor shaft can be formulated as following:

$$\ddot{\theta}_r = \frac{i_{trans}}{\left(j_r + {i_{trans}}^2 j_{trans}\right)} T_{act} - \frac{\left({i_{trans}}^2 . d . a^2 + d_r\right)}{\left(j_r + {i_{trans}}^2 j_{trans}\right)} \dot{\theta}_r - \frac{1}{\left(j_r + {i_{trans}}^2 j_{trans}\right)} T_L \qquad \text{IV-11}$$

The motor speed and position can then be deduced as function of the model parameters, which are given in details in the Annex B. It should be also mentioned that in case of maladjustment between the shaft and ring position (Fig. IV-9), the circular coordinates of the ring (Eq.IV-6) will be given as following:

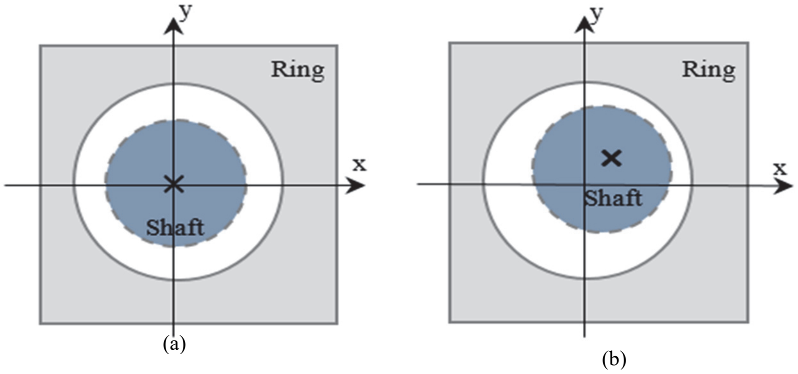

(a)

(b)

Fig. IV-9. Working area of the ring; (a) Centered position, (b) Maladjusted position

$$\begin{aligned} x_s &= \mathrm{a}\cos(\theta_s) + x_{adjust} \\ y_s &= \mathrm{a}\sin(\theta_s) + y_{adjust} \end{aligned} \qquad \text{IV-12}$$

where x_{adjust} and y_{adjust} correspond to the shaft deviations in x and y directions respectively.

Moreover, if the identical behavior condition of the orthogonally actuators (k_x=k_y= k, and d_x= d_y= d) is not considered, the rotor acceleration will be written as:

$$\begin{aligned} \ddot{\theta}_r = {} & \frac{i_{trans}}{\left(j_r + {i_{trans}}^2 j_{trans}\right)} T_{act} \\ & - \frac{\left({i_{trans}}^2 . a^2\left(d_y cos^2(i_{trans}\theta_r) + d_x sin^2(i_{trans}\theta_r) + d_r\right)\right)}{\left(j_r + {i_{trans}}^2 j_{trans}\right)} \dot{\theta}_r \\ & - \frac{i_{trans}}{\left(j_r + {i_{trans}}^2 j_{trans}\right)} \left(k_y cos(i_{trans}\theta_r)\left[\mathrm{a}\sin(i_{trans}\theta_r) - y_{adjust}\right]\right) \\ & - k_x sin(i_{trans}\theta_r)\left[\mathrm{a}\cos(i_{trans}\theta_r) - x_{adjust}\right]) - \frac{1}{\left(j_r + {i_{trans}}^2 j_{trans}\right)} T_L \end{aligned} \qquad \text{IV-13}$$

The model is implemented in the Matlab/Simulink environment, the driving voltage amplitudes are taken equal to 160 $V_{pk\text{-}pk}$ and the phase shift is fixed to 90°. The applied voltages to the PMAs and the equivalent charges at a frequency of 100 Hz are given in Fig. IV-10.a and b respectively. The linear displacements and the generated forces of the orthogonally piezoelectric actuators driven are shown in Fig. IV-11. The time evolution of the PAD angular speed at 100 Hz is given in Fig. IV-12.a, showing a steady state speed around 2rad/s which is very close to the values given by the motor manufacturer [71] . Due the special structure of the PAD, the motor speed can be only controlled through the driving frequency. The phase shift can be switched between +/-90° to inverse the motion direction. The simulation results of the PAD model under different driving frequencies are shown in Fig. IV-12.b.

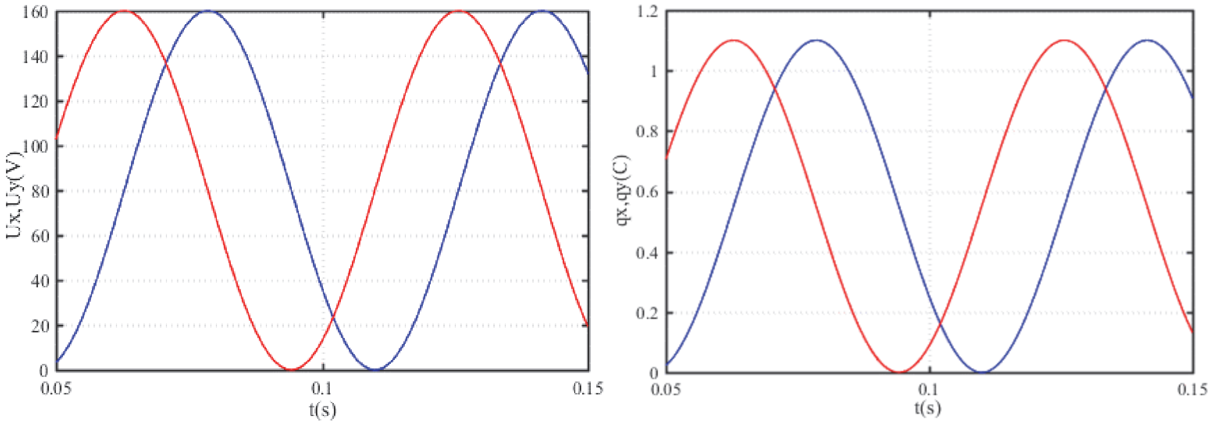

(a) (b)

Fig. IV-10. (a): Driving voltages, (b): Actuator charges

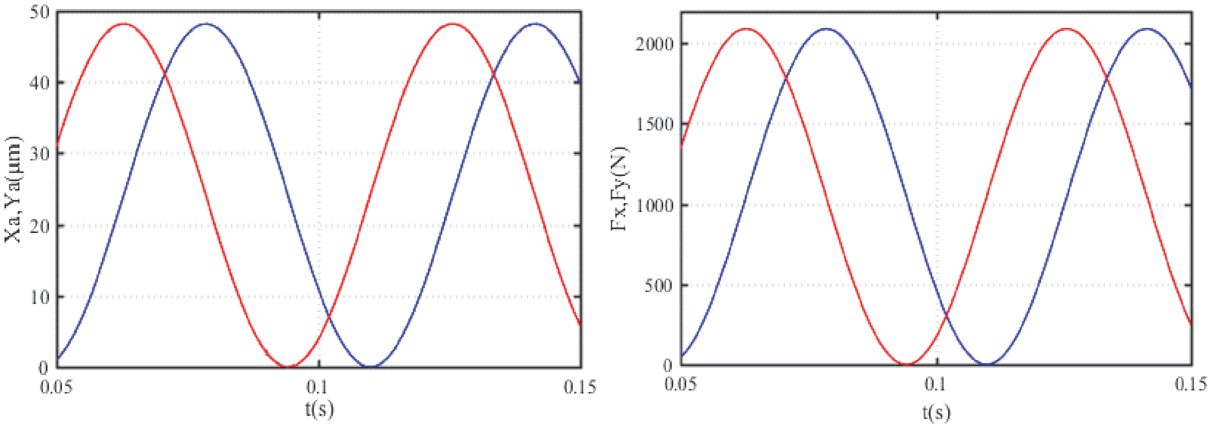

(a) (b)

Fig. IV-11. (a): Linear actuators displacement, (b): Linear actuators forces

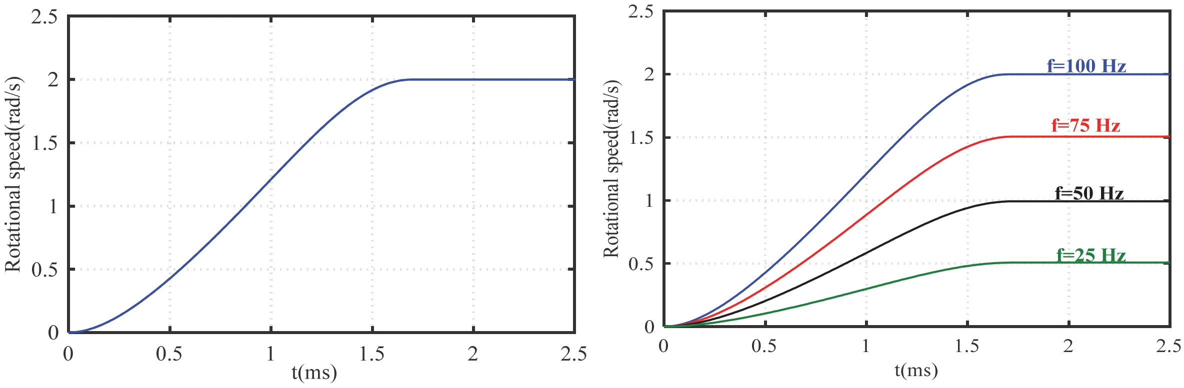

(a) (b)

Fig. IV-12. (a): Rotational speed at 100Hz, (b): Rotational speed at different frequencies

IV.4 Experimental test bench

Rotary experimental positioning system based on PAD7220 is setup in order to evaluate the open loop characteristics of the motor, experimentally identify the transfer function between the PAD angular position and the driving frequency, and to implement in real time the synthesized closed loop position controllers.

IV.4.1 Experimental platform description

The experimental platform (Fig. IV-14) consists of a PAD7220 from Noliac coupled to an optical encoder with a resolution of 10000 p/r (Baumer, Go356). High resolution sensor is used because with this motor topology, high precision levels can be achieved. The load torque is generated using a powder brake from Merobel (FAS21). The torque is measured and conditioned via a mini-smart torque sensor with a control/monitoring board from Kistler. A dSPACE controller board (dS1104) is used for the real time closed loop control.

In the open loop configuration, the driving analog voltages (+/-10V) are programmed in the Matlab/Simulink environment and sent to the power amplifiers via the DAC interface (Fig. IV-13). The voltages are amplified and an offset is also introduced in order to keep the output voltages between -20 and 200 V_{max}. The two quadratic voltages are then used to drive the PAD and the output characteristics can be evaluated. In closed loop operation mode, the motor position data are introduced to the control board via the incremental encoder interface of dSPACE microprocessor (Fig. IV-13). The measured position is compared to a reference signal, and a position control algorithm will be executed in dSPACE environment. The control signal parameter (frequency) is then calculated and used to generate the phase shifted voltages. Graphical interface is designed using control desk in order to configure the driving parameters and operation conditions (motion direction, open/closed loop, control type…) (See annex B)

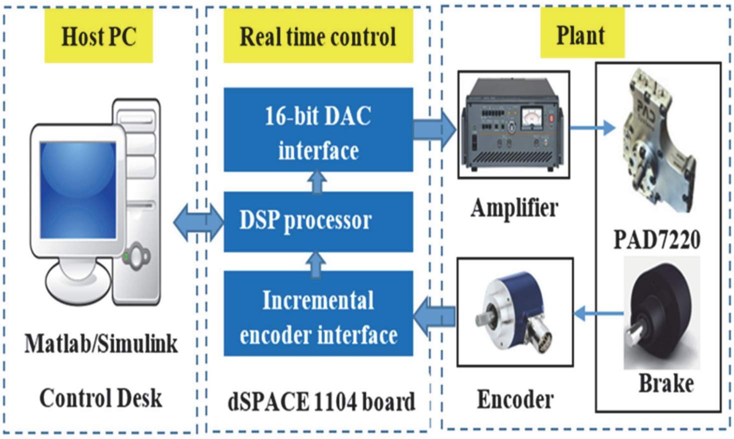

Fig. IV-13. Block diagram of experimental setup

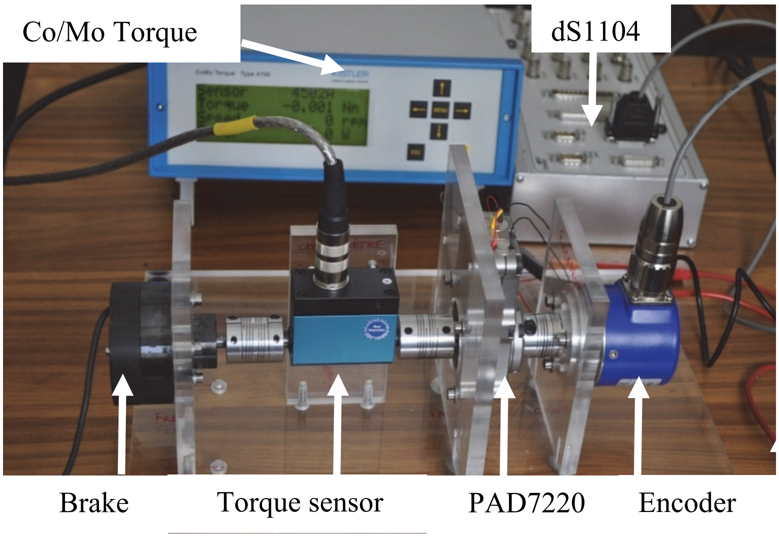

Fig. IV-14. Experimental setup

IV.4.2 Frequency-position relationship identification

To apply the position controller synthesis approaches (explained in Chap.II), a Transfer Function (TF) model between the control signal which is the voltage frequency in this case and the motor angular position is needed. The TF will be identified through the integration of the experimental frequency-speed relationship. Therefore, the motor is driven at different frequencies and the angular velocities are measured and collected. The nominal operation frequency of the PAD7220 is of 300Hz. With the tested prototype, the speed and position control signal (f) will be saturated in order to avoid high signal values. The saturation levels are variable (< 300Hz) to perform the operation at low and high rotation speeds. As mentioned above, the PAD speed is load independent, and to experimentally confirm this feature, the motor is tested in case of no-load condition and under a load torque of 2 Nm. The evolution of the motor speed in the two cases under different frequencies is shown in Fig. IV-15. The experimental results prove that the PAD angular speed is not affected by the external loads. Fig. IV-15.a and b show a linear relationship between the angular speed and the driving frequency. The position-frequency TF ($G_{PAD}(s)$) will be the integer of this relationship and is given by:

$$G_{PAD}(s) = \frac{\theta(rad)}{f(Hz)} = \frac{2\pi}{320}\frac{1}{s} \qquad \text{IV-14}$$

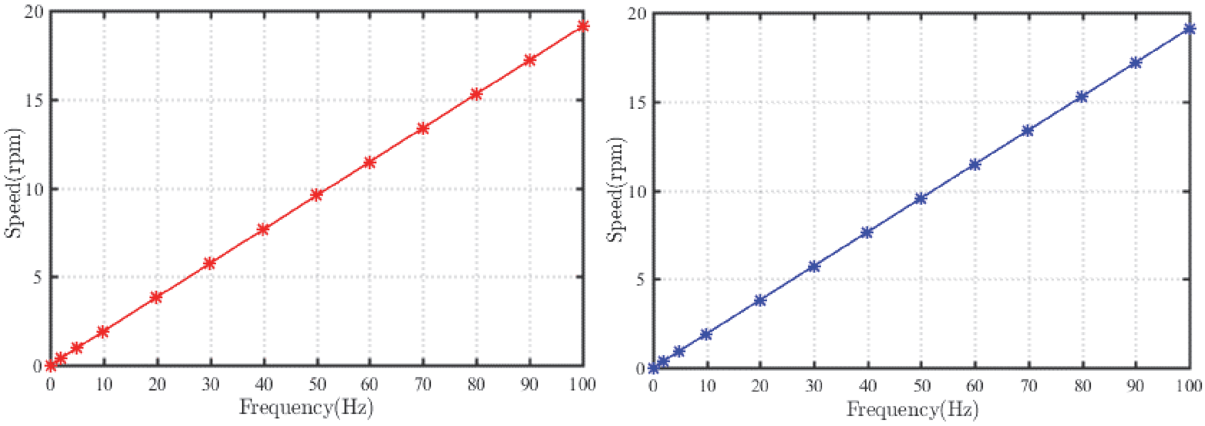

(a) (b)

Fig. IV-15. PAD speed-frequency characteristics in cases of : (a) no-load condition, (b) 2 Nm of load torque

IV.5 Synthesis of robust position controllers of PAD

The synthesis approach of robust H-infinity (H_∞) and discrete time RST position controllers will be applied here to the PAD case. The performances of the positioning system based on PAD7220 will be fixed, and using the motor TF $G_{PAD}(s)$, the controller parameters will be determined. A proportional, integral, and derivative (PID) controller will be designed and experimentally implemented and compared to the proposed robust position controllers to prove the advantage of the proposed techniques.

IV.5.1 H-infinity position controller of PAD

The feedback H_∞ control method is applied to control the position of the PAD plant represented by $G_{PAD}(s)$ as shown in Fig. IV-16.a, where the reference and measured position are represented by r and y respectively, and b is the input perturbation. In order to prove the accuracy and robustness of this method, and to satisfy the H_∞ proprieties, weighting filters are introduced as shown in Fig. IV-16.b. In Fig. IV-16.b, the error ε and the control signal u are filtered by W_1 and W_2 respectively. The input perturbation b is the output of the weighting filter W_3. The open loop experimental tests of the PAD7220 show that the motor can move at very low speed, which means it can be driven at very low frequency. Moreover, when the frequency signal is perturbed, the ring tooth vibrate inside two teeth of the shaft without passing to the next tooth. This phenomenon generates a lot of acoustic noises and decreases the motor precision. The frequency perturbation can be caused by the generation process of this signal inside Matlab Simulink with high sampling frequency and the DAC conversion stages, and by noises coming from the measured position data. Therefore, the weighting filters (W_2 and W3) of the closed loop positioning system must be carefully selected in order to avoid these problems. In other hand, the challenge is to achieve high bandwidth in closed loop with respect to the motor resonance frequency but without destabilizing the closed loop system. The stability criteria are performed via the weighting filter W_1.

To guarantee these performances, a closed loop bandwidth of 300 rad/s with minimum gain and phase margins of 10dB and 45° respectively are fixed.

Based on the aforementioned performances criteria, and after checking of the first closed loop results, the obtained parameters of the weighting filters are:

$$W_1 = \frac{s+270}{0.9(s+3.10^4)} \;;\; W_2 = \frac{s+10}{0.5(s+1.10^5)};\; W_3 = 0.01 \qquad \text{IV-15}$$

The resulting controller K(s) is a third order controller. This controller is reduced to simplify the implementation effort to a first order controller. Finamlly, the obtained H_∞ feedback controller and the optimal gamma value are then:

$$K_{red}(s) = \frac{2.17\,.10^6}{s+2.98\,.10^6} \;;\; \gamma = 1.09 \qquad \text{IV-16}$$

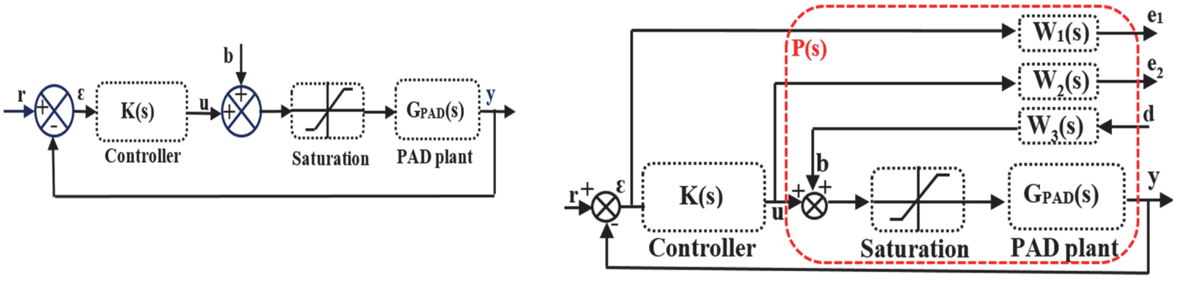

(a) (b)

Fig. IV-16. **(a)** PAD closed loop configuration, (b) PAD closed loop augmented by weighting filters

IV.5.2 RST position controller of PAD

The RST control method is applied based on robust pole placement method in discrete time domain. Thereby, zero order hold discretization method is applied to the continuous time model with a sampling time of 0.1 ms, to obtain the discrete time PAD model $G_{PAD}(z^{-1})$:

$$G_{PAD}(z^{-1}) = \frac{B(z^{-1})}{A(z^{-1})} = \frac{1.96.10^{-6}z^{-1}}{1-z^{-1}} \qquad \text{IV-17}$$

The PAD plant is designed to be controlled so that the closed loop will have a second order type with a damping factor of 0.6 and a bandwidth of 300 rad/s. Thus , a the reference denominator $A_m(z^{-1})$ is given by:

$$A_m = 1 - 1.94z^{-1} + 0.94z^{-2} \qquad \text{IV-18}$$

$$s(z^{-1}) = 1 + 0.94z^{-1} \;\;;\; R(z^{-1}) = 447 + 427z^{-1} \qquad \text{IV-19}$$

The polynomials $T(z^{-1})$ will be obtained by fixing an unity gain in steady state and by resolving the auxiliary Diophantine equations (II-28 and II-32):

$$T(z^{-1}) = 10^3(2.72 - 2.67z^{-1}) \qquad \text{IV-20}$$

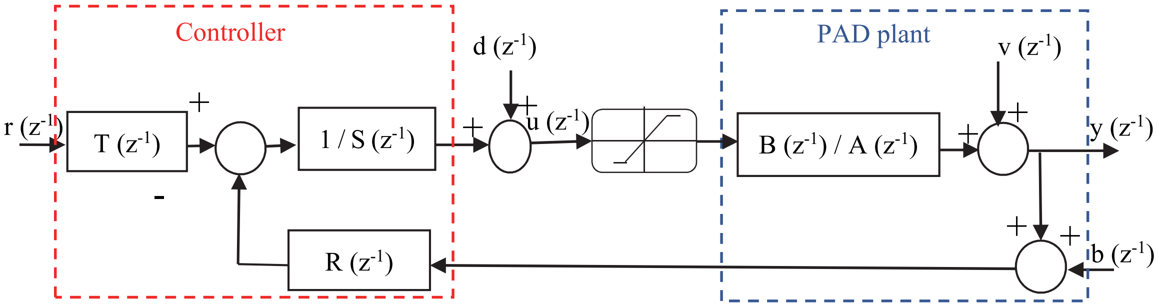

Fig. IV-17. Discrete time PAD plant controlled by RST regulator

IV.6 Simulation results

The stability of the closed loop system is guaranteed with both the H∞ and RST controllers (Fig. IV-18) with a large margin phases equal to 88° and 58° respectively. For practical uses, the PAD must operate with maximum driven frequency of 300Hz as recommended by the manufacturer. The step responses of the PAD positioning system based on the H∞ and RST controllers under frequency limitation show high accuracy without overshoots at different rotation speeds as can be seen in Fig. IV-19. The robustness of the closed loop system to external perturbations is also analyzed through the simulation study. External electrical noises are injected to the control signal and the measured position, and the rejection capability of such disturbances is evaluated. As shown in Fig. IV-20.a, when the noises are injected (t=0.4 s), the RST step response shows a position ripple of +/-0.5% and the H∞ control method rejects completely this perturbation. The two proposed controllers show high robustness to control signal noises. Where, the injected disturbance at the instant t=0.4 s, is rejected by both the RST and H∞ controllers as shown in Fig. IV-20.a.

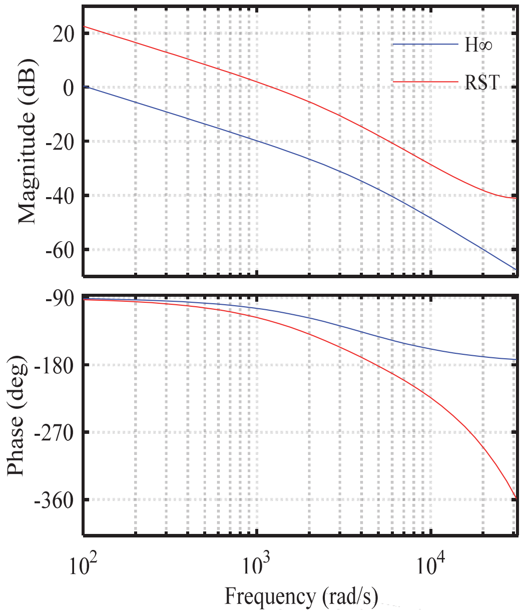

Fig. IV-18. Bode diagrams of PAD control systems

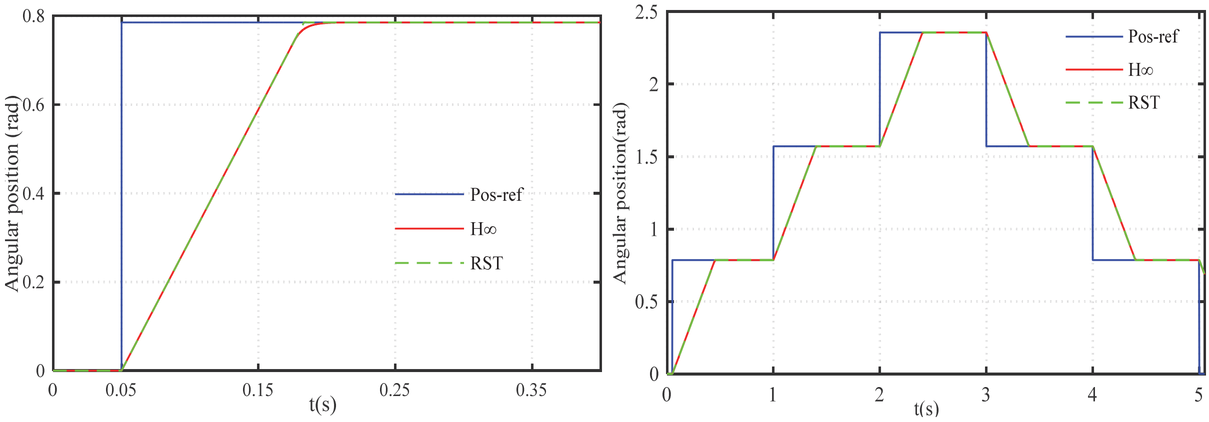

(a) (b)

Fig. IV-19. Comparison of step responses ; (a) High rotation speed, (b) low rotation speed

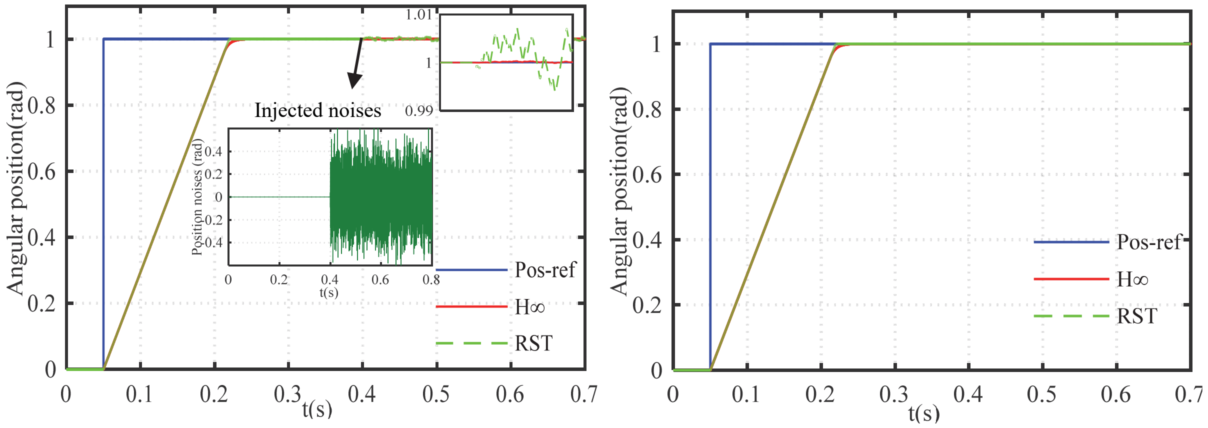

(a) (b)

Fig. IV-20. Comparison of perturbation rejection capability; (a) Sensor noises (t=0.4s), (b) Control signal noises (t=0.4s)

IV.7 Real-time implementation of PAD closed loop positioning system

The experimental platform presented in Fig. IV-14 is used to experimentally validate the synthesized PAD position controllers. The experimental results of H_∞ and RST control methods will be discussed respectively. A comparative study with a PID controller for robustness issues will be presented at the end of this section.

The proposed position controllers are implemented in the Matlab/Simulink environment and compiled via the dSPACE board with a sampling time of 0.1 ms. The three controllers are inserted together in the same Simulink file, which makes the switching between them easier through the graphical interface. The goals of the proposed system is to achieve fast and ultra-precise positioning performances in closed loop under different working conditions, and to confirm the robustness to external disturbances. In fact, the motor behavior depends on the motion speed, on-line control parameters adaptation is mostly addressed to deal with this problem. So, the idea is to propose a high performance positioning system without additional parameters adaptation or compensation systems.

IV.7.1 H-infinity test results

The PAD positioning system based on H_∞ control is implemented in real time and the experimental results will be discussed here. The motor speed is adjusted by the variation of the maximum value of the generated control frequency. The step response of the H_∞ controller at low speed shows high precision without overshoot (Fig. IV-21). The steady state accuracy of the unloaded motor is of 0.009° (which is the maximum resolution of the sensor) for a motion of 90°. The high precision level of the closed loop system is confirmed in the two motion direction of the PAD as shown in Fig. IV-22.a for a motion sequence of +/-45°. Due the special structure of the PAD, the PMAs vibration increases when the driving frequency increases. These vibrations can generate oscillations at the final position of the motor shaft. The robustness of the proposed method to reject these oscillations under different motor speed is validated as shown in Fig. IV-22.b. In order to evaluate the robustness of the positioning system to sensor disturbances and control signal perturbations, external Gaussian random noises are injected to the measured position and to the generated control signal (driving frequency) at the instant t=.7.8s. As can be seen in Fig. IV-23.a and b, the mixed sensitivity H_∞ controller shows high rejection capability of both control signal and measurement noises.

The robust mixed sensitivity H_∞ approach gives a high precision level in static operation mode (very low speed) and until the quasi-static operation zone. Moreover, it proves the robustness to reject the external injected noises to control signal and to the measured position.

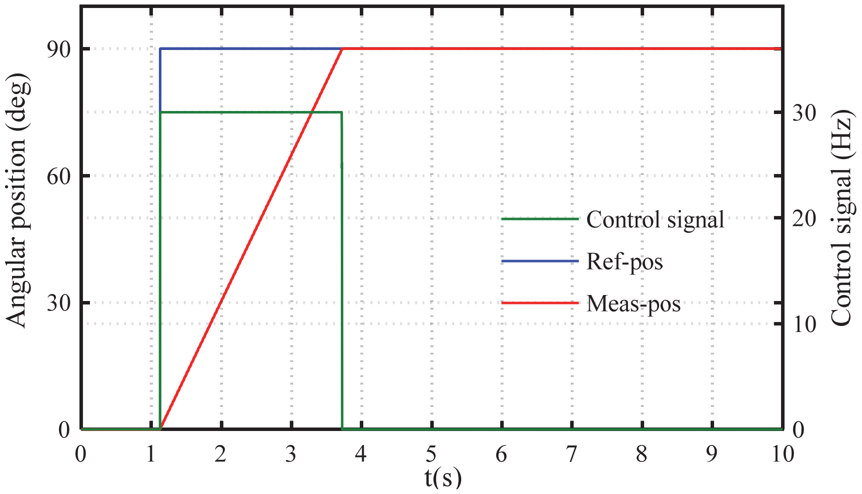

Fig. IV-21. Experimental H_∞ step response (Ω=6 rpm)

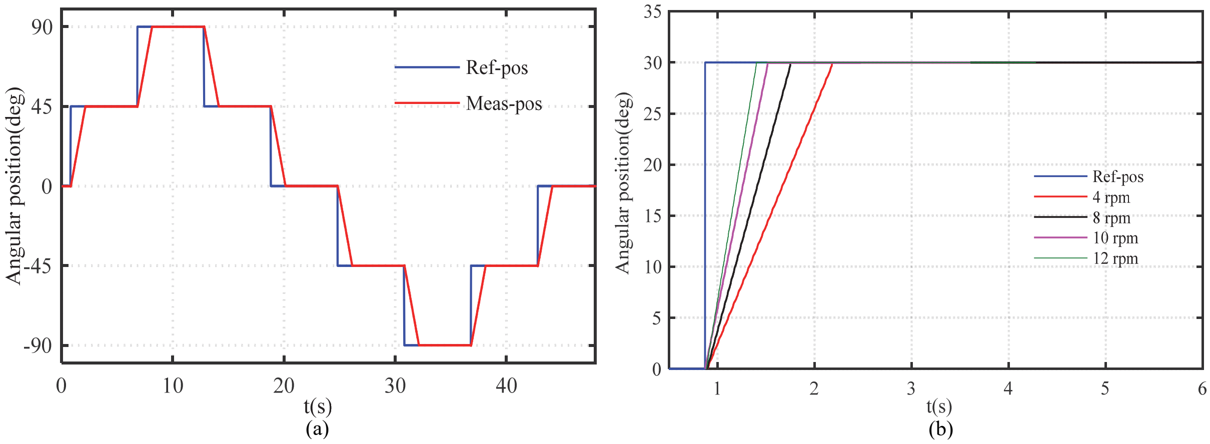

(a) (b)

Fig. IV-22. (a) H_∞ response for two motion directions (Ω=10 rpm), (b) H_∞ responses at different motor speeds

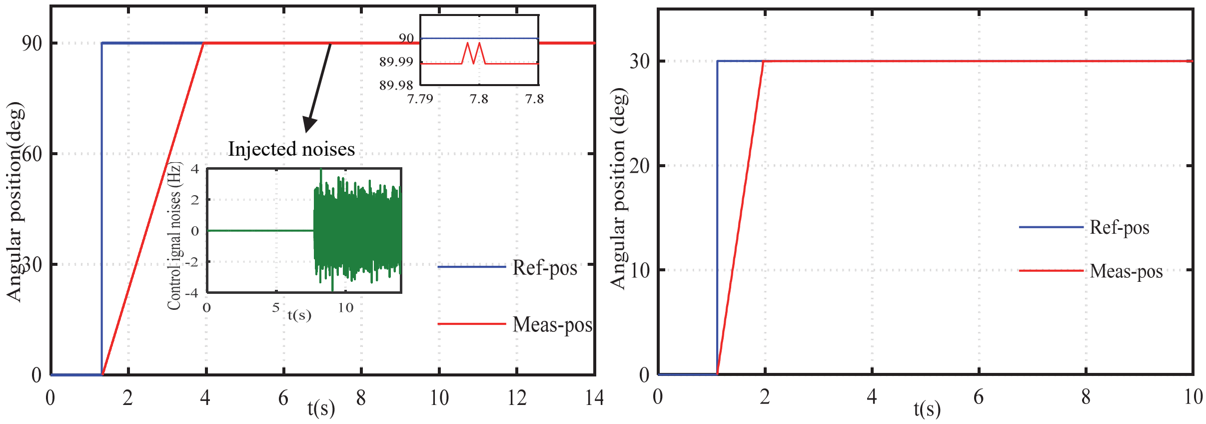

(a) (b)

Fig. IV-23: H∞ perturbation rejection capability, (a) Control signal noises (Ω=6 rpm), (b) Sensor noises (Ω=6 rpm)

IV.7.2 RST test results

The RST control approach based on discrete time pole placement method is also implemented in real time. The step responses of the PAD positioning system based on RST controller show high precision levels for very low speeds (≈1.5rpm) and also for relatively high rotational speeds as illustrated in Fig. IV-24. The perturbation rejection capability of the discrete time controller is also evaluated as done for the H∞.

As shown in Fig. IV-25.a, the electrical noises are injected to the driving frequency at the instant t=8 s. This perturbation generates a position distortion of about +/-0.08° illustrated in the zoomed area. Similarly, the noises are injected to the position sensor data at the instant t=7.2 s as shown in Fig. IV-25.b. The resulting positioning response shows an oscillation of about 0.4° when the position data are perturbed. The RST pole placement method achieves a high positioning performances as explained in the aforementioned paragraph. However, it shows a weak robustness to reject the external disturbances.

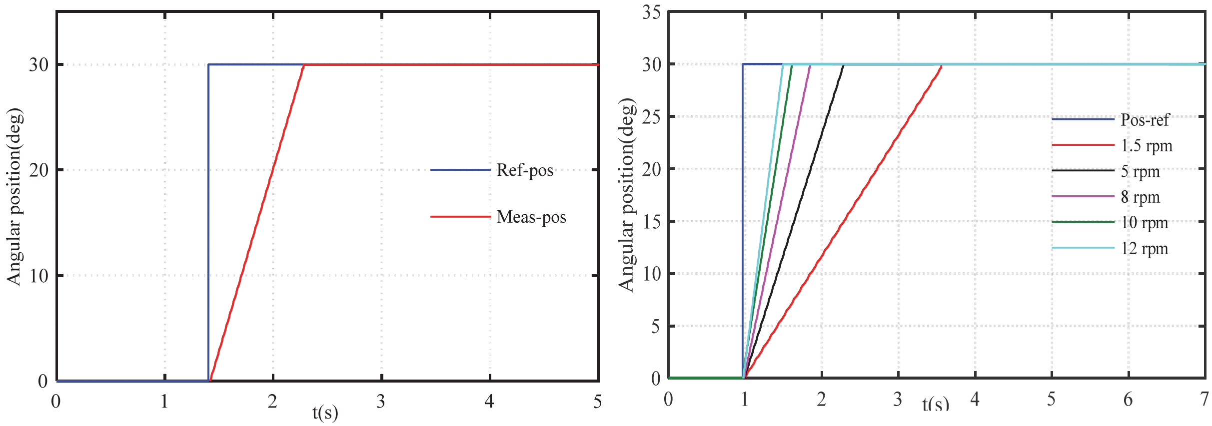

(a) (b)

Fig. IV-24: RST step responses, (a) Ω=6 rpm, (b) at different speeds

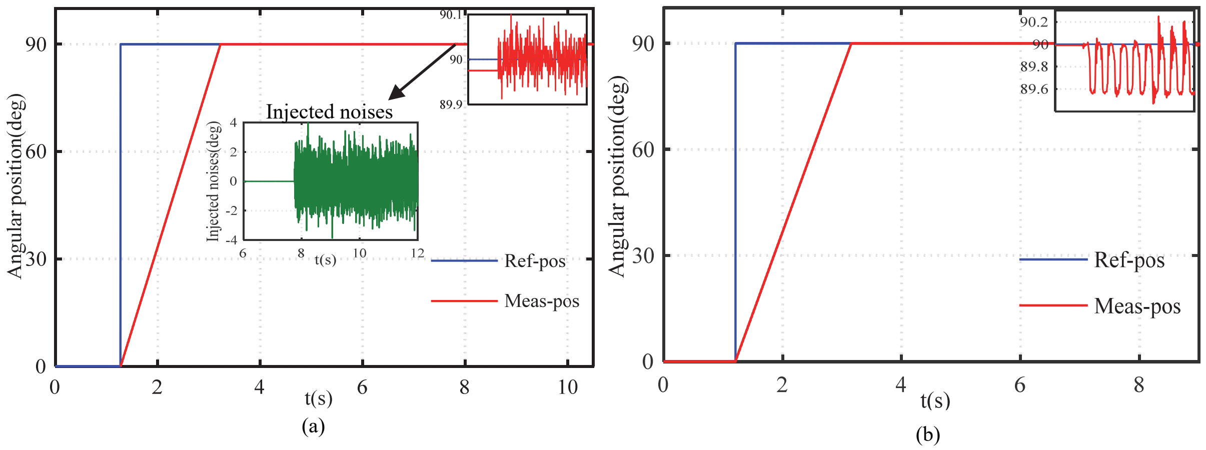

Fig. IV-25: RST perturbation rejection capability, (a) Control signal noises, (b) Sensor noises

IV.7.3 Comparative study

A comparative study between the H-infinity, RST, and a PID controllers is carried out in this section. The comparison criteria are the accuracy of the positioning system in static and quasi-static operation modes, and the rejection capability of external disturbances. The H_∞ and RST controller parameters are the same given in section IV.5, while the PID parameters are tuned by trial-and-error through intensive tests in order to achieve similar performances with the other controllers. The resulting PID parameters are K_p =2750, K_i=0.01, and K_D=0. The three controllers show high precision without overshoot for a rotation of 30° under a driving frequency of 30 Hz as shown in Fig. IV-26.a. However, when the motor operates close to the dynamic zone, the PID controller fails to prove the positioning performances in relatively high speed as shown in Fig. IV-26.b. The tracking errors and oscillations in the case of PID control, can be avoided by modifying the PID parameters (K_p =3000). Thus an adaptive PID method as function of the operation mode is needed to achieve the required performances. The robustness of the positioning system to control signal and sensor perturbations is also evaluated.

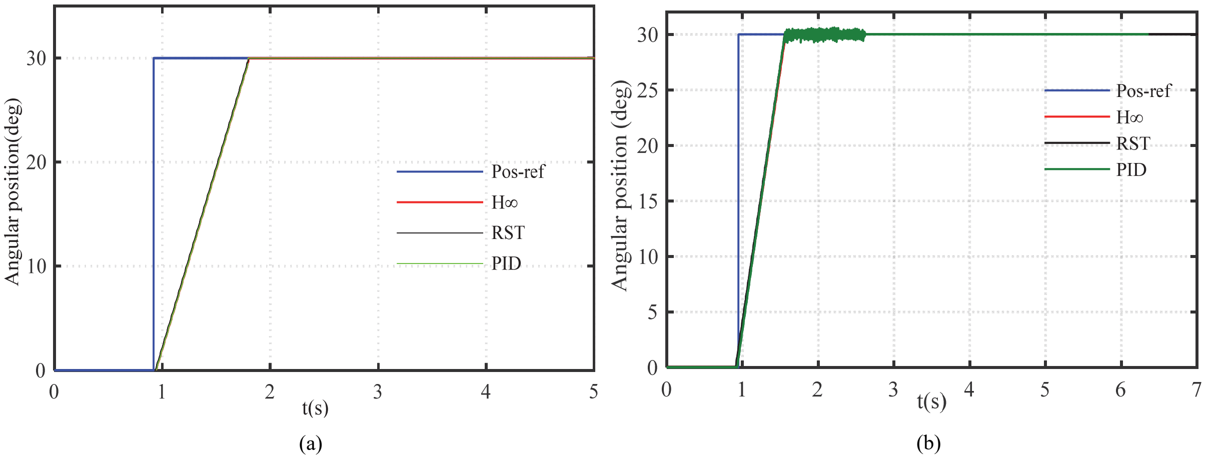

Fig. IV-26. Comparison of controller step responses (a) Under 30Hz, (b) Under 50Hz

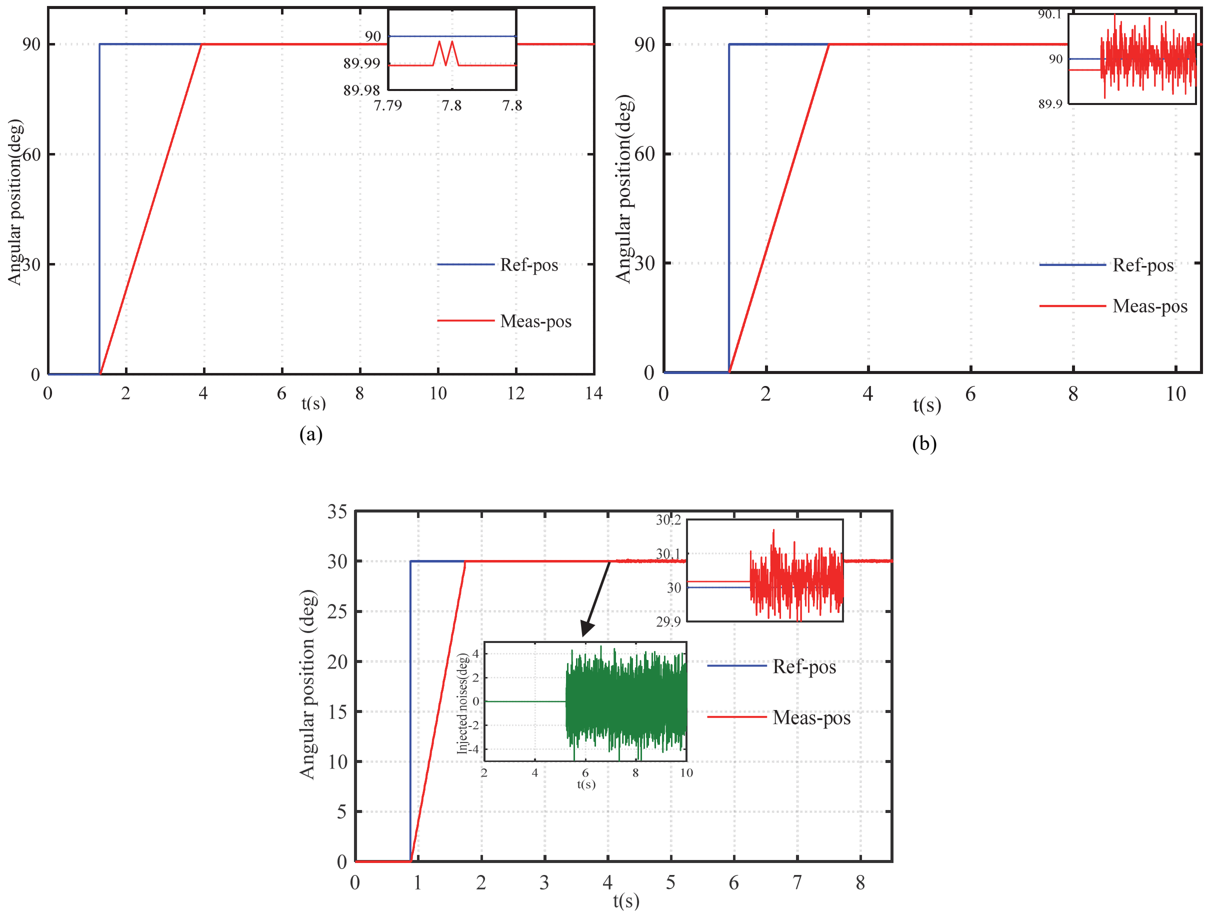

(a)

(b)

(c)

Fig. IV-27. Comparison of rejection capability of control signal perturbations (Ω=6 rpm): (a) H_∞, (b) RST,(c) PID

The electrical noises injected to the control signal are rapidly rejected by the H_∞ control method as can be seen in the zoomed area of Fig. IV-27.a. In the cases of RST and PID control techniques, the injected noises cause a position distortion of +/-0.08° and +/-0.15° respectively as shown in Fig. IV-27.b. The sensor perturbations injected at the instant t=5.8 s, are completely rejected by the H_∞ controller as can be seen in Fig. IV-28.a. However, the measurement disturbances generate oscillations in steady state of +/- 0.5° in the cases of RST and PID controllers as shown in Fig. IV-28.b and c. The comparative study confirms the advantages of the H_∞ position control of PAD system in terms of accuracy, stability, and robustness. The ultra-precision of the positioning system based on H_∞ control is confirmed at very low speed (low driving frequency) and at relatively high speeds. The weighting selection approach gives to this method high robustness levels to reject the external noises.

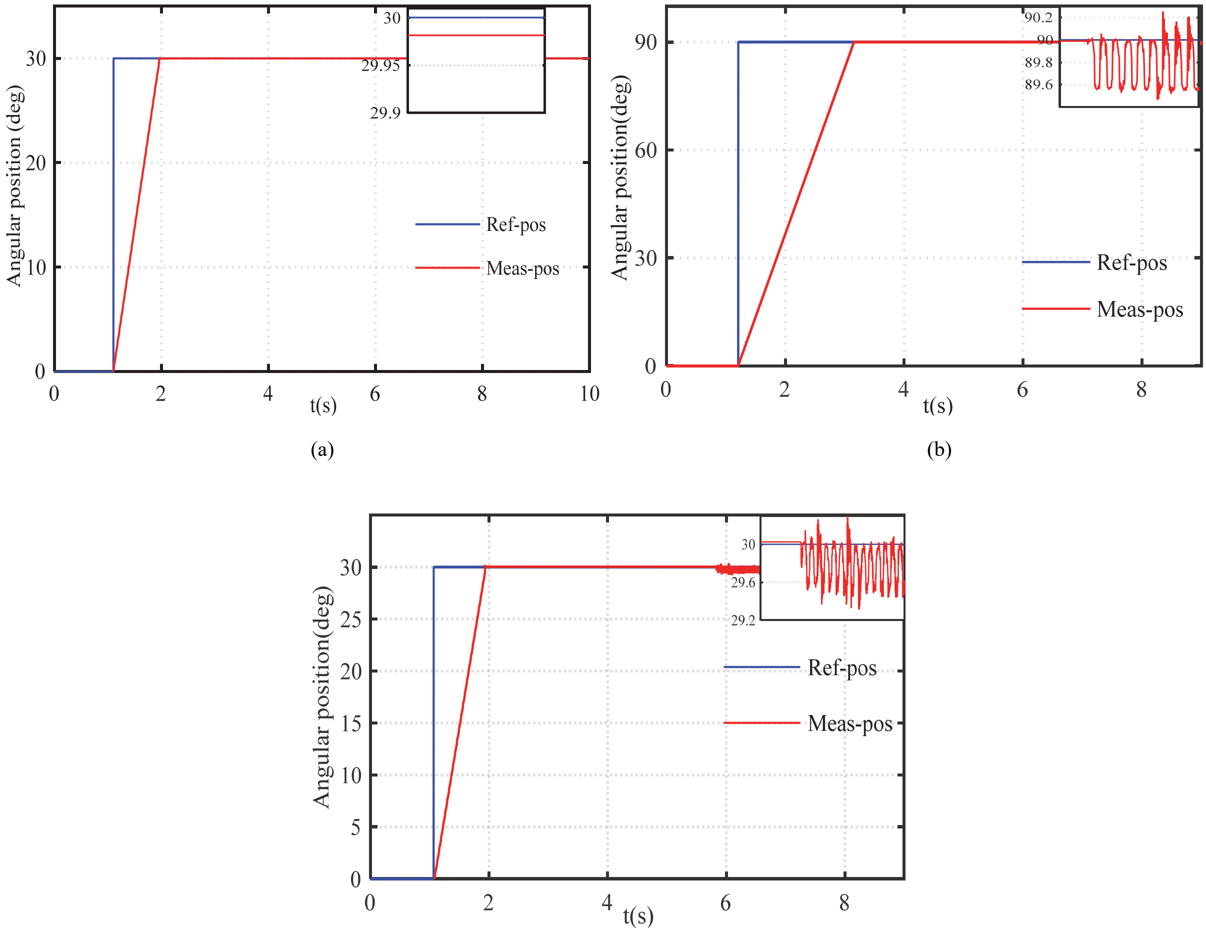

(a)

(b)

(c)

Fig. IV-28. Comparison of rejection capability of measurement perturbations injected at t=5.8s (Ω=6 rpm): (a) H_∞, (b) RST,(c) PID

IV.8 Conclusions

This chapter deals with a high precision positioning closed loop system based on Piezoelectric Actuator Drive (PAD). The working principle and features of the novel piezoelectric motor structure are firstly introduced.

An overview of the proposed models of PAD was presented to highlight the contribution of the proposed model. In fact, the developed PAD models are addressed to capture the motor behaviors in static and dynamic operation modes, and to simulate the effect of the multilayer actuator parameters on the output motor characteristics. The contribution of the proposed PAD7220 model is that it describes the motor dynamic including the elongation of the multilayer stack actuators, the actuators/stator ring contact mechanism, and the motion transmission to the rotor via the micro-teeth system. Moreover, it permits a control techniques implementation in closed loop through the driving signals (voltage amplitude, frequency, and phase shift).

Compact rotary positioning system based on PAD7220 is designed. The experimental platform is used firstly to drive the PAD7220 in open loop to determine the output characteristics variation as function of the driving signals and external loads. The open loop test results show that the motor speed is constant whatever the load torque until the maximum torque. The independent speed-load characteristic gives it a success in industrial fields.

Due to the working principle of the PAD, it can be controlled in speed and position only via the driving frequency. In fact, the phase shift between the supply voltages must be equal to +/-90° in order to keep the synchronization of the orthogonal piezo-actuators and to generate the circular trajectory of the stator ring. The amplitude of the driving voltages must be minimum equal to 160 $V_{pk\text{-}pk}$, otherwise the stator ring tooth will stay blocked between two rotor teeth which generates an acoustic noise.

The control method using the driving frequency permits the smooth motion of the motor from very low speed (<1 rpm) and until 56.25 rpm, and an easy and fast switching between the on and off motion states of the motor. The two listed features are very important for pickup and place automation missions of industrial robots. In other hand, when reaching the desired position, the motor has a high holding torque even without supply. One demerit of the frequency-drive method, is that in “off” motor motion state, it continuous to consume power while the voltage amplitudes are different to zero.

The maladjustment between the stator ring and the rotor shaft positions is one of the open loop drive inconvenient. In fact, the stator ring position depends directly on the state of the multilayer actuators after operating cycles (contracted or expanded), and the rotor shaft will not be necessarily at the center of the ring. The solution was often an auto-adjustment technique for the stator/rotor position.

The speed-frequency characteristics are then used to identify the transfer function ($G_{PAD}(s)$) between the angular position (θ) and the control frequency signal (f). The transfer function serves to synthesis the robust H_∞ and the RST control approaches based on the desired closed loop performance.

The advantage of the proposed controllers of the piezo-motor is that, it combines the high precision performance for a large bandwidth, and the robustness requirements to the uncertain motor parameters and external disturbances, in one simple design controller. The goal is to perform a high resolution in closed loop both in static and dynamic mode (high rotational speed), to overcome the maladjustment between the stator and rotor, and to show a high robustness with respect to the uncertain motor parameters and external electrical noises.

The precision, stability, and robustness of the proposed methods is firstly discussed through the simulation results of the closed loop system. Where the stability of the closed loop system was guaranteed for a large bandwidth. Afterwards, the position control techniques are implemented in real time via the experimental positioning platform. A PID controller is also experimentally implemented in order to establish a comparative study between the three controllers and to prove the advantages of the proposed methods. The three controllers show high precision levels in static mode (very low speed), however, when the rotational speed increases, the PID control fails to quickly track the reference position while the two other controllers keep the high precision levels reaching the maximum resolution of the sensor (0.009°) whatever the speed. The degrees of freedom of the H_∞ and the RST given by the weighting filters and the poles placement technique respectively, are at the origin of the high precision levels in a wide frequency band. Where, the controllers design in the frequency domains permits the adjustment of the amplification gains regarding to the frequency operation range, leading to tracking errors reduction. The precision and response time of the closed loop system can be improved using a PID controller, but a tuning parameters method as function of the operation conditions is mandatory. This online-learning and parameters adaptation complicates the real time implementation of this controller.

The robustness of the positioning system with respect to the control signal and measurement noises is evaluated. Electrical noises are injected respectively to the driving frequency and to the position sensor data. The advantages of the H_∞ in term of perturbations rejection can be clearly distinguished compared to the RST and PID controllers. The superiority of the H_∞ in term of perturbation rejection capability is explained by the design flexibility of the weighting filters (W_i). Where, the parameters of the filter W_1 are fixed to mainly improve the precision and response time performances. Whereas, the parameters of W_2 and W_3 are principally selected to reject the additional perturbations in a specific frequency range. The robustness of the RST controllers to external disturbances can be ameliorated by a rearrangement of the pole locations in the discrete time domain, but it is at the expense of precision and response time performances.

Finally, rotary positioning system based on quasi-static PAD positioning system can fulfill the performance requirements of robust ultra-precision applications using mixed sensitivity H_∞ control method. The accuracy and robustness of this system are guaranteed in the static operation mode and in relatively high PAD rotation speeds and under uncertain operation conditions.

Chapter V

Modeling and Design of Robust Closed Loop Position Controllers for Linear Walking Piezoelectric Motor

V.1 Introduction

The Walking Piezoelectric Motor (WPZM) is a quasi-static piezoelectric motor. It consists of two or more sets of drive piezoelectric legs alternately in friction contact with a movable rod in order to enable the motion steps or walks (the working principle will be detailed in section II). It was the subject of many patents [141-143], where the motor's principle of operation and construction methods are detailed. The WPZM can generate a translational or rotational motion depending on the mechanical configuration and it overcomes the very low speed of inchworm motors. The high force and high stiffness of the WPZM with high resolution (<1nm in open loop), small size, high holding force without supply, and non-electromagnetic interferences [26], make this motor useful in ultra-positioning system including zooming and optical image stabilization, microscopy and biotechnology research such as cell manipulation, actuation of robot arms, guiding of surgical MRI robots, microscopy and biotechnology research such as cell manipulation, semiconductor processing, actuation of hexapod robots, and many other applications [26]. The positioning performances of WPZM are proved in open loop and in closed loop for reduced motion range (nano/micro scales). Nevertheless, the high precision level for large motor stroke in closed loop and under load conditions is not yet confirmed.

V.2 Literature Review of WPZM position controllers

Positioning in macro and micro scales requires an accurate and robust position control techniques. Since the PZMs have non-linear behavior and inherit hysteresis, creep, and vibration, a closed loop operation mode is often mandatory. In [144], a WPZM is used to drive a single DOF position stage. The system was PID feedback- controlled by prescribing the driving voltages frequency from the measured position. The voltages amplitude and phase are controlled based on reference velocity and using feed-forward control strategy. The presented experimental results show significant overshoot and steady state error when changing the amplitude and phase of the voltage waveforms with overlapping trajectories. Similarly, for the same motor, relations between the motor step size and the voltage amplitude and phase are derived in [145], and by applying a cascaded type adaptive controller of step size, the positioning precision and overshoots are improved. Feedback control with Gain Scheduling (GS) of PiezoLEGS [62] motor is proposed in [146]. The overshoot and oscillations problems still exist in the proposed PID control based on Hadamard transform of the applied voltages for a WPZM working in bending mode [145, 147]. Based on the x-y elongations of the piezo legs, coordinate transformation of driving voltages is presented in [148]. A called virtual time controller is then designed for the modulation of the step frequency as function of the error amount. The motor behavior under load conditions was considered in positioning systems, and force controllers should be applied to handle loading tasks. In [149], force-motor speed relations are identified for PiezoLEGS motor. Based on this knowledge, motor is linearized by dynamic compensation, and PI control is applied. Therefore, an additional force sensor is needed and the speed variation as function of the applied force must be approximated to a linear relationship. Polynomial control technique for adaptive positioning was proposed in [150]. It is implemented by changing speed and motor step size to decrease overshoot and achieve desired position. The speed-overshoot dependence characteristics are determined through experimental tests under three different step positions. Therefore, the polynomial control feasibility is limited to the relationships established in the range of the tested nano-step position. Repetitive Control (RC) to compensate disturbances that are independent of time are also used in [151, 152]. The RC is designed based on a periodic and repetitive disturbance. However, it is not always the case for a piezoelectric motor. In [153], position control with parameter adaptation of XYZ nano-robotic cell is discussed. The position stage is actuated by PiezoLEGS and the control strategy uses a simple bang-bang control with step size modulation to achieve very precise positioning without overshoot. However, for the last two methods, the positioning accuracy is not improved for the full motion range of the motor but only for the nano-metric scale.

V.3 Contributions and outlines

In this chapter, the effectiveness and reliability of long travel (up to 50 mm) positioning system based on linear walking piezoelectric motor (WPZM) are studied. The contribution is to prove the high accuracy of WPZM in closed loop at low and high speeds (up to 10 mm/s) and under external applied loads (up to 10 N). This is in order to prove the feasibility of using such motor for robotic applications demanding high precision levels with relatively high generated forces. Experimental single DOF positioning system is designed and the motor position is controlled in real-time via dSPACE board. A laser position sensor is used to ensure high position resolution. For the synthesis approach of position controllers, a Transfer Function (TF) between the control signal and the motor position is experimentally identified in open loop. Then, robust H-infinity (H_∞) and discrete time RST position controllers are synthesized based on the identified TF. The proposed controllers are implemented in real time and the positioning accuracy and robustness are evaluated and compared with conventional PID controller.

This chapter is organized as follows. First, the working principle of the WPZM is explained in section II. In section III, the experimental test bench of the single DOF positioning system, and the motor transfer function identification are detailed. The synthesis approach and the simulation results of H-infinity and RST position controllers are illustrated in section IV. The real time implementation of the proposed controllers, the evaluation of motor positioning performances, and comparison of accuracy and robustness results are discussed in section V. Finally, conclusions and discussions will be drawn in section VI.

V.4 Working Principle of Walking Piezoelectric Motor

The motor under consideration in this study is a commercially available linear WPZM (N-310.13) from Physik Instrumente (PI) GmbH [62], (Fig. V-1.a). The travel range of the N-310.13 motor is of 50mm with a maximum generated force of 10 N and a linear velocity of 10 mm/s. The motor can perform stepping or analog operation mode (for micrometer stroke). To achieve a long travel, the motor must operate in stepping mode which will be on the focus of this work. The WPZM has four Piezoelectric drive Legs (PZL) (Fig. V-1.b), each leg consists of two electrically separated piezoelectric stacks. These stacks consist of shear piezoelectric actuators (acting in x-direction) that are responsible of micro-stepping attached at the tip of longitudinal actuators (acting in y-direction) responsible of clamping [26]. The four legs are supplied by four separated voltage signals. The motor drive voltages can be written as shown in Eq. V-1 and the leg states in each step are described in Fig. V-1.c.

$$\begin{aligned} U_1 &= A\sin(\omega t) \\ U_2 &= A\sin(\omega t + \frac{\pi}{2} + \varphi) \\ U_3 &= A\sin(\omega t + \pi) \\ U_4 &= A\sin(\omega t + \frac{3\pi}{2} + \varphi) \end{aligned} \qquad \text{V-1}$$

The legs elongate in y-direction when equal voltages are applied to the two piezo stacks of one leg. Applying different voltages on the two piezo stacks of one leg causes the leg to bend. According to the applied voltages, a leg will perform a periodic movement in the plane (Fig. V-1.b). During the operation, the legs will drive a preloaded rod due to the friction force formed at the contact surface. The PZLs are driven in pair of two and perform a stepping motion that causes a forwards and backwards feed of the rod. As can be seen in Fig. V-1.b, the first pair of legs p_1 consisting of legs A and C is driven by the voltages $U_1(t)$ and $U_2(t)$. The second pair p_2, consisting of legs B and D is driven by the voltages $U_3(t)$ and $U_4(t)$. In the stepping mode, the voltage waveforms are chosen such that at all times only one pair of legs is in contact with the drive surface (phase shift of π rad) and such that the pairs of legs perform a movement in x-direction for the rod. Each pair of legs will perform the clamping or fed of the rod depending on the applied voltages as explained in Eq.V-2.

$$Leg - pair\ 1: \begin{matrix} U_{clamping} = \frac{U_1+U_2}{2} \\ U_{feed} = U_1 - U_2 \end{matrix} \qquad Leg - pair\ 2: \begin{matrix} U_{clamping} = \frac{U_3+U_4}{2} \\ U_{feed} = U_3 - U_4 \end{matrix} \qquad \text{V-2}$$

The shape of the elliptical trajectory performed by each leg is determined mainly by the voltage amplitude A and phase φ [16]. The effects of A and φ on the elliptical motion of legs are explained in Fig. V-2. The elliptical shape variation will then change the motor step size.

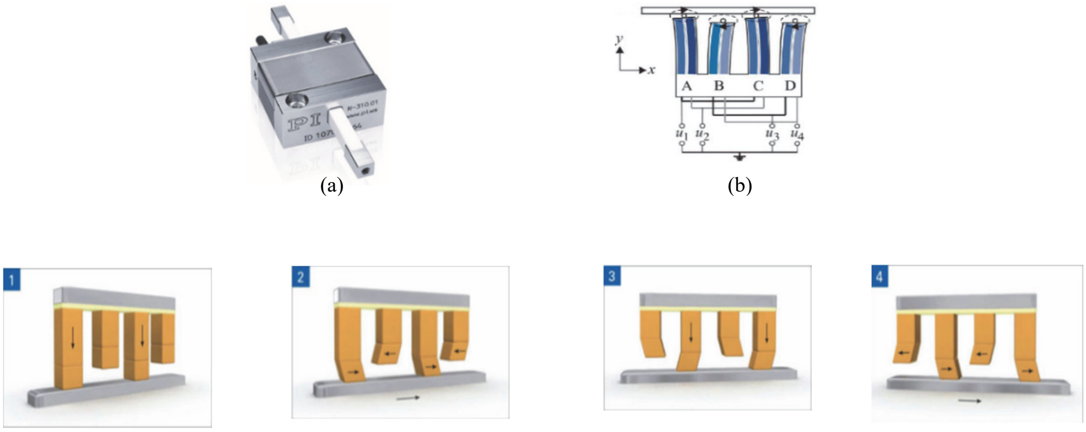

(a) (b)

1: One pair is in contact the rod, the second is lifted off

2: the first pair of the legs is lifted and bent in the right direction, keeping contact with the rod while the other pair retracts and moves in the left direction

3: The leg pair that was initially retracted now extends to push against the rod while the first pair retracts

4: The cycle is completed with the second pair bending to the right while the first pair is moved left

(c)

Fig. V-1. (a) N-310 motor series, (b) Elliptical motion of legs, (c) Working principle of WPZM

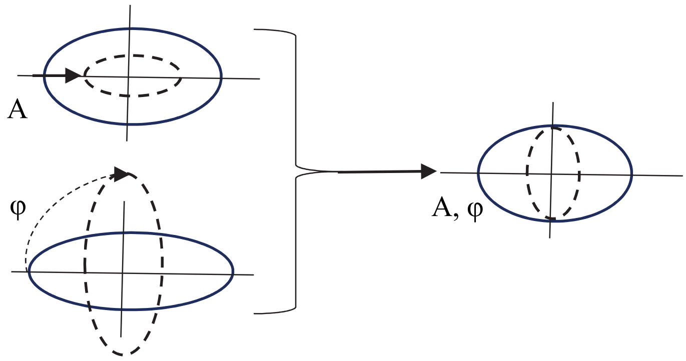

Fig. V-2. Influence of the voltage amplitude A (V), and phase φ (rad) on the elliptical trajectory of the drive leg tip

The N-310.13 step size can be varied between 5 nm and 5 µm and it depends also on the applied external forces [67]. Whereas, the drive frequency determines the number of elliptical trajectories per second and therefore the motor velocity. The latter depends on the step size and the drive frequency i.e. Speed (m/s) = step size (m) ×frequency (Hz). The studied motor has a maximum input voltage of 45 V and a maximum driven frequency of 1.5 kHz.

V.5 Experimental test bench and motor transfer function identification

V.5.1 Experimental test bench

A single DOF experimental platform based on linear WPZM is setup (at the laboratory of actuation technology "LAT") as shown in Fig. V-4. The experimental test bench will be used in first time for the open loop tests and transfer function identification. Afterwards, it will be used for the real time implementation of closed loop position controllers. The experimental platform consists of the linear WPZM (N-310.13) from Physik Instrumente (PI) GmbH. The motor is driven by for phase shifted voltage waveforms (0-45V) generated by the E-862 driver. The electronic driver is powered by 24V DC power supply. A weight set is attached to the bottom side of the motor rod in order to evaluate the performances in load conditions. The motor rod position is measured via a laser position sensor (G-152) from Keyence, with measurement range of 80 mm around 150 mm

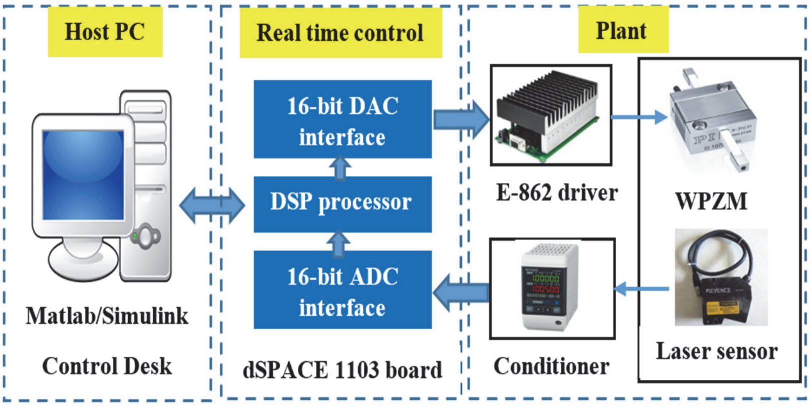

Fig. V-3. Block diagram of the closed loop experimental setup

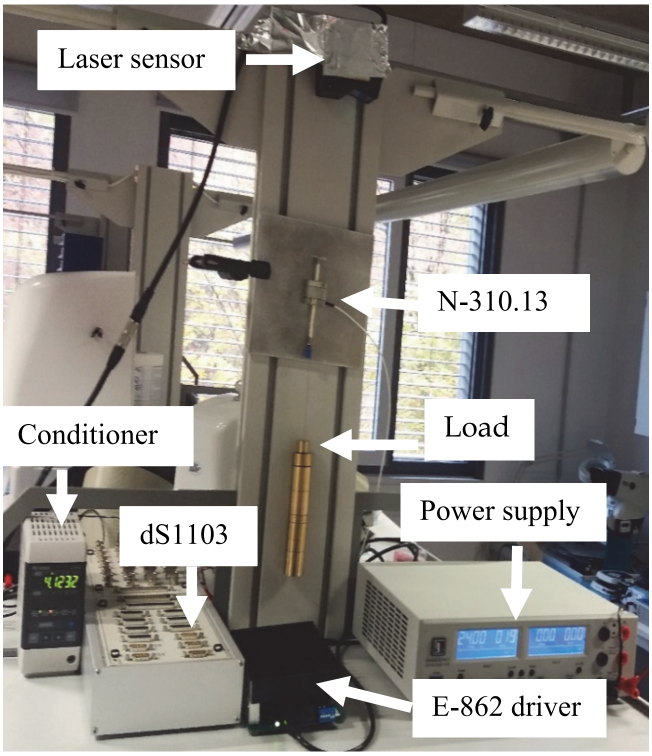

Fig. V-4. Experimental platform

A dSPACE board 1103 is used for the real time position control of the WPZM. The position sensor data are processed by a G3001PV conditioner that will generate analog voltage (+/-10 Vmax) as function of the measured position. The position data is introduced to the control program via the ADC interface. Three output signals are sent from the dSPACE DAC interface to the E-862 driver: one of 5 V as supply of the electronic circuit, 0/5 V signal to enable/disable the motor motion (0: enable, 5: disable), and the analog control signal of +/- 10 V. The synoptic of the closed loop diagram of the experimental setup is illustrated in Fig. V-3.

V.5.2 Motor transfer function identification

The transfer function (TF) identification approach consists on applying a control signal (Vc (V)) step change and measuring the corresponding motor velocity (dY/dt (mm/s) in open loop. Therefore, the TF between the motor position and Vc will be the integrator of the identified TF between dY/dt and Vc. A control signal step change is then applied, the motor velocity is derived from the position sensor data as illustrated in Fig. V-5. The analog control signal of the linear WPZM is between +10 and -10V, i.e. the maximum speed is for +/-10 V (in the two motion directions) and for 0V there is no motion. The motor velocity depends on the drive frequency and on the phase shift (for motion direction).Therefore, the control signal will act on the step frequency and the voltage phase shift (+/-90°). The experimental open loop tests show that the motor velocity is not always the same for the right and left motion direction under the identical drive voltage waveforms. This nonlinearity is also mentioned by the motor manufacturer (PI). Fig. V-6 shows two different open loop responses for two different control signal steps. As mentioned above, the main applications of such motors is for precise positioning at low speed. Therefore, the transfer function for the low motor speed (Fig. V-6.a) will be taken as motor TF reference model. It will be approximated to a first order function to reduce the complexity of the controller and the implementation effort. The model uncertainty should be compensated by the robustness of the applied closed loop controllers.

The control signal (Vc)-Position (Y) transfer function is then deduced as:

$$G_{WPZM}(s) = \frac{Y}{V_c} = \frac{k_w}{s(1+\tau_w s)} \qquad \text{V-3}$$

where the gain constant k_w and the time constant τ_w are respectively equals to 1.2 mm/v and 0.15 s.

The TF parameters can significantly change as function of control signal values and external forces. For example the time and gain constants are respectively of 30 ms and 0.79 mm/v when the motor is moving with speed of 8 mm/s.

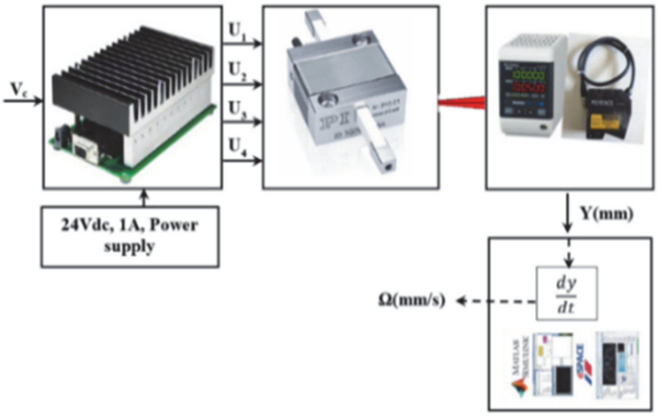

Fig. V-5. Block diagram of experimental open loop setup

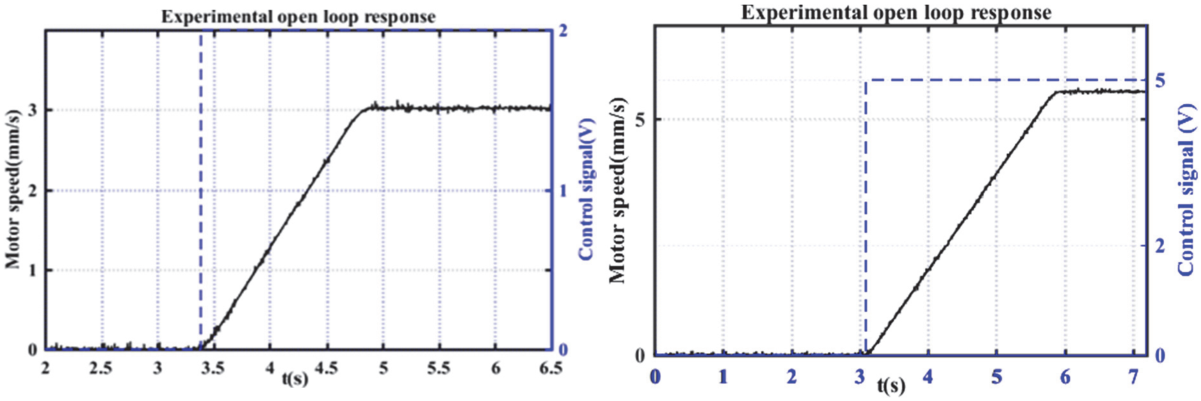

(a) (b)

Fig. V-6. Open loop motor responses: (a) 2V control signal step, (b) 5V control signal step

The controller parameters will be determined using only the given TF (V-3), and we will rely on the robustness of the proposed controllers to ensure the high precision levels in the case of uncertain motor parameter uncertainties (due to speed variation or applied load).

V.6 Synthesis of robust position controllers of WPZM

The synthesis approach of robust H-infinity (H_∞) and discrete time RST position controllers will be applied here to the WPZM case. The performances criteria of the positioning system based on WPZM will be fixed, and using the motor TF $G_{WPZM}(s)$ (Eq.V-3), the controller parameters will be determined. The control signal (u) which is the analog voltage V_c in this case is limited between +/-10 Vmax (V.5.1) . The motion speed of the linear motor is performed via the value of the control signal, therefore, V_c will be saturated at different levels to change the motor speed.

V.6.1 H-infinity position controller of WPZM

The classical closed loop system configuration (Fig. V-7.a) is used to synthesis the robust feedback H_∞ controller for the WPZM plant. Afterwards, the weighting filters are introduced to apply the mixed sensitivity H_∞ optimization method as shown in Fig. V-7.b. The first closed loop tests of the N-310.13 motor show that the rod positioning accuracy is very sensitive to the control signal quality, i.e. the least control signal perturbation generates a lot of oscillations at the final rod position with acoustic noises. The control signal distortion is caused by the motor parameters variation under different test conditions, and from the position sensor with analog output signal (+/-10 V of laser sensor conditioner) and the conversion stages. Therefore, the filter (W_i) parameters of the H_∞ controller must be carefully chosen in order to reject the introduced disturbances and to internally stabilize the closed loop system. As the synthesis method is explained in chapter II, the performances of the positioning system based on the N310.10 motor will be introduced to deal with the WPZM case. The first challenge of the designed controller is to achieve a fast response without instability with respect to the maximum operating frequency of the motor, the closed loop bandwidth is fixed to 100rad/s with a minimum phase and gain margins respectively of 15 dB and 50°. The motor will guarantee high precision levels in closed loop with a steady state error ratio lower than 0.1%. Based on the listed performances and after checking of the first closed loop test results, the obtained weighting filters for the N-310.10 plant are:

$$W_1 = \frac{s+90}{0.9(s+10^4)} \; ; \; W_2 = \frac{s+5.10^6}{10(s+5.10^2)} \; ; \; W_3 = \frac{s+10}{0.5(s+1)} \qquad \text{V-4}$$

Based on the filter parameters, the optimal controller and gamma constant satisfying the H_∞ norm can be found using the MATLAB function "hinfsyn". Otherwise, the obtained fifth order controller contains zeros and poles outside the system operation frequency range. The useless zeros and poles can be reduced via the "reduce" MATLAB function. Finally, a second order controller and optimal gamma gain are obtained:

$$K(s) = \frac{4,15\,.\,10^5 s + 3,75\,.\,10^6}{s^2 + 631.5\,s + 1.02\,.\,10^6} \quad ; \quad \gamma = 1.09 \tag{V-5}$$

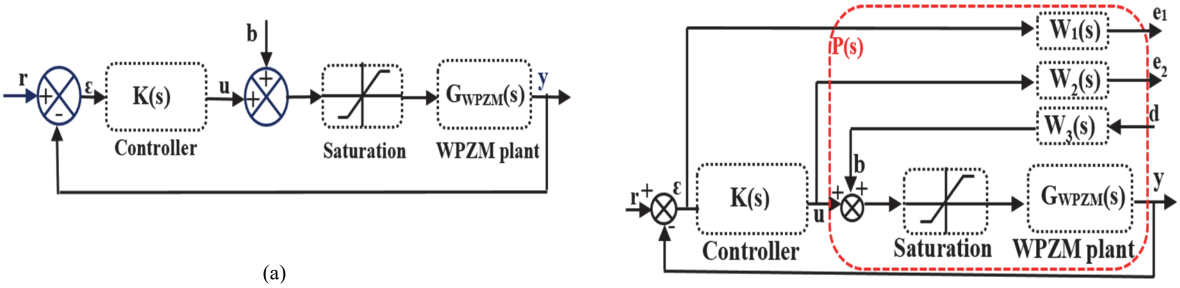

(a)

(b)

Fig. V-7. (a) Closed loop configuration, (b) closed loop augmented by weighting filter

The filters and system transfer function behaviors are verified through the frequency analysis as shown in Fig. V-8. The criteria of the H∞ in the frequency domain are satisfied, the accuracy and robustness of the proposed method will be evaluated via the simulation and experimental results.

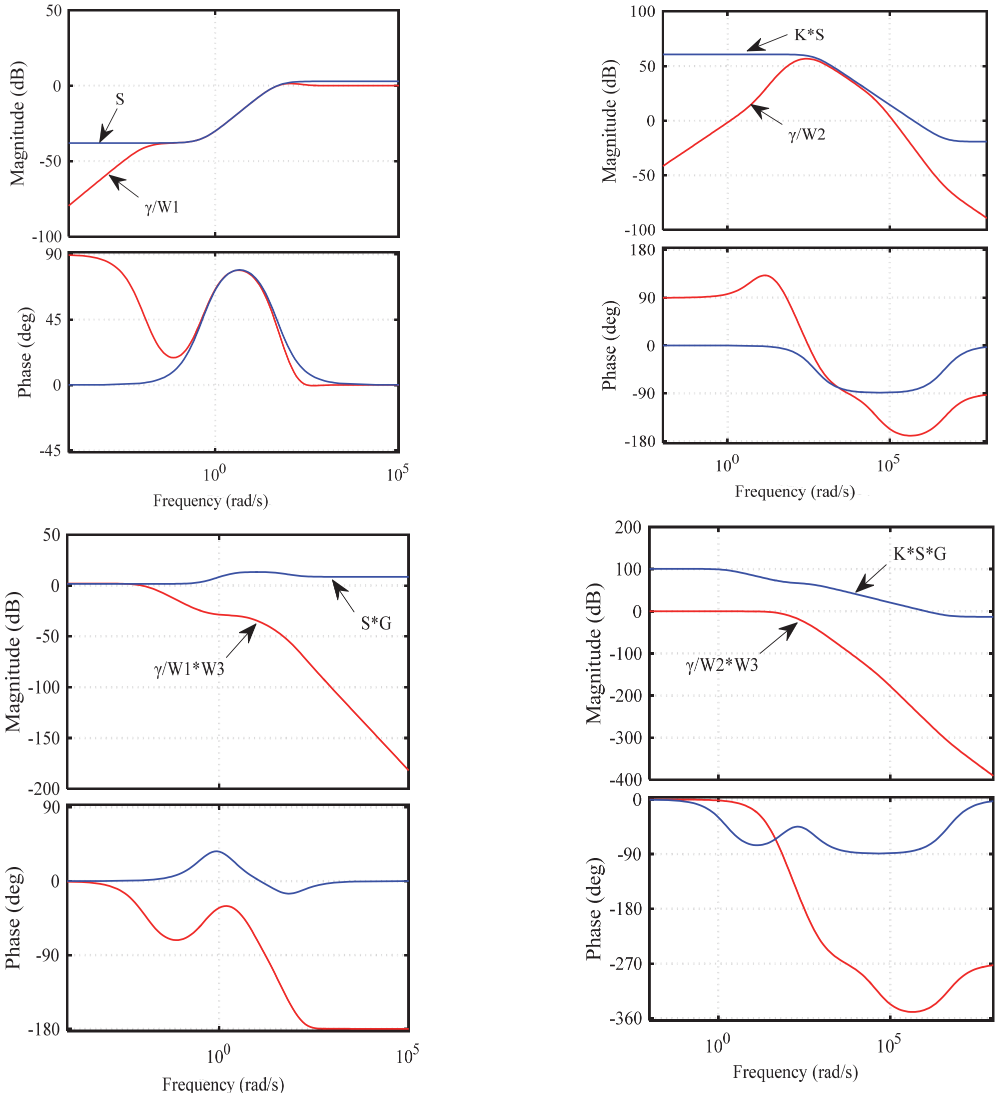

Fig. V-8. Frequency analysis of Filters and transfer functions behavior

V.6.2 RST position controller of WPZM

The RST position control for the N-310.13 motor is synthesized in dicrete time based on pole placement method. Therefore, a discrete time motor plant ($G(z^{-1})=B(z^{-1})/A(z^{-1})$) is needed to synthesis the controller. It can be obtained by the discretization of the continuous model $G_{WPZM}(s)$ (Eq.V-3). A zero-order hold method is used for the discretization aproach and a discrete WPZM plant is obtained:

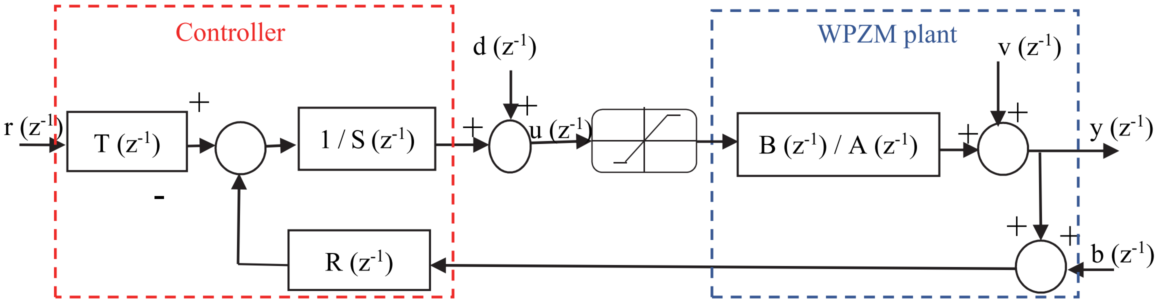

Fig. V-9. Discrete time WPZM plant controlled by RST regulator

$$G_{WPZM}(z^{-1}) = \frac{B(z^{-1})}{A(z^{-1})} = \frac{4.10^{-6}(z^{-1}+1)}{z^{-2}-2z^{-1}+1} \qquad \text{V-6}$$

This plant is designed to be controlled so that the closed loop will have a second order type with a damping factor of 0.7 and a bandwidth of 100 rad/s. Thus, a discrete characteristic polynomial $A_m(z^{-1})$ is given by:

$$A_m = 1 - 1.96z^{-1} + 0.96z^{-2} \qquad \text{V-7}$$

By the resolution of the primary Diophantine equation (II-19), the polynomials $S(z^{-1})$ and $R(z^{-1})$ can be obtained:

$$s(z^{-1}) = 1 + 3.9.10^{-2}z^{-1} \quad ; R(z^{-1}) = (9.68 - 9.45z^{-1}).10^3 \qquad \text{V-8}$$

The polynomials $T(z^{-1})$ will be obtained by fixing an unity gain in steady state and by resolving the auxiliary Diophantine equations (II-28 and II-32):

$$T(z^{-1}) = (1.054 - 1.032z^{-1}).10^4 \qquad \text{V-9}$$

V.7 Simulation of WPZM closed loop system

The simulation results of the WPZM closed loop system are presented in this section in order to prove the performances of the proposed methods. The robustness of the positioning system to motor parameters variation and injected disturbances are evaluated and compared to a PID control method. The stability of the closed loop system is always guaranteed with the H_∞ and RST controllers as illustrated in Fig. V-10 and Table V-1. The fixed phase and gain margins are achieved with the two proposed controllers (Table V-1)

Table V-1: Comparison of stability margins

	Gain margins (dB)	Phase margins (deg)
H_∞	25.6	74.5
RST	47.8	78.5

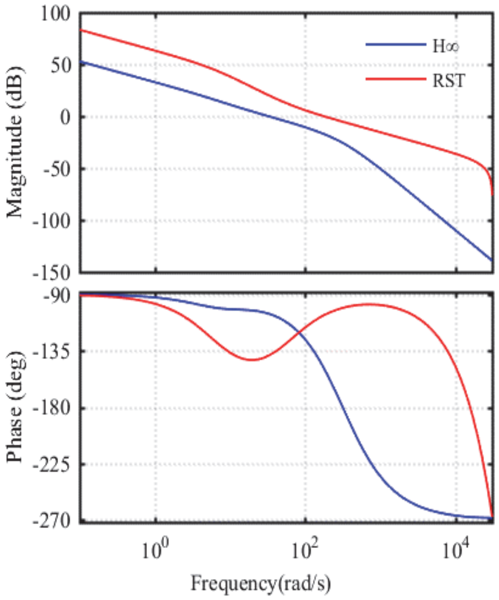

Fig. V-10. Bode diagrams of WPZM positioning system

The time analysis of the position response shows high precision levels without overshoot for the two proposed controllers and in case of low and high motor velocities as illustrated in Fig. V-11. It should be mentioned that the motor velocity is adjusted by the selected maximum value of the generated control voltage. To simulate the effect of model parameters uncertainties, the identified model parameters (k_w,τ_w) are changed with a ratio of 50%. The H_∞ is not affected by the gain constant (k_w) variation, while with the RST method an overshoot of 1% appears (Fig. V-12.a). In case of time constant increase (τ_w) by a ratio of 50% (which is the case when the motor speed equals to 6mm/s), the RST generates an overshoot of 4% and of 0.4% for the H_∞ control as shown in Fig. V-12.b. The perturbation rejection capability of the positioning system is also analyzed through the simulation results. In Fig. V-13.a, random Gaussian noises are injected to the control signal at t=2s, the closed loop system shows high rejection capability of such perturbations. When the noises are injected to the measured position, the H_∞ shows higher robustness levels than the RST control method as shown in the zoomed area of Fig. V-13.b.

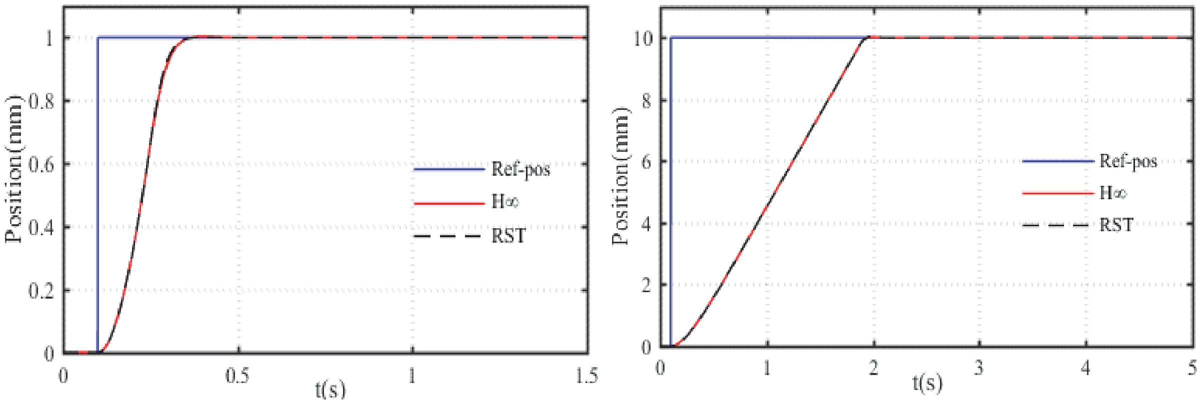

(a)

(b)

Fig. V-11. Comparison of simulation step responses at different velocities: (a) 1 mm, (b) 10 mm

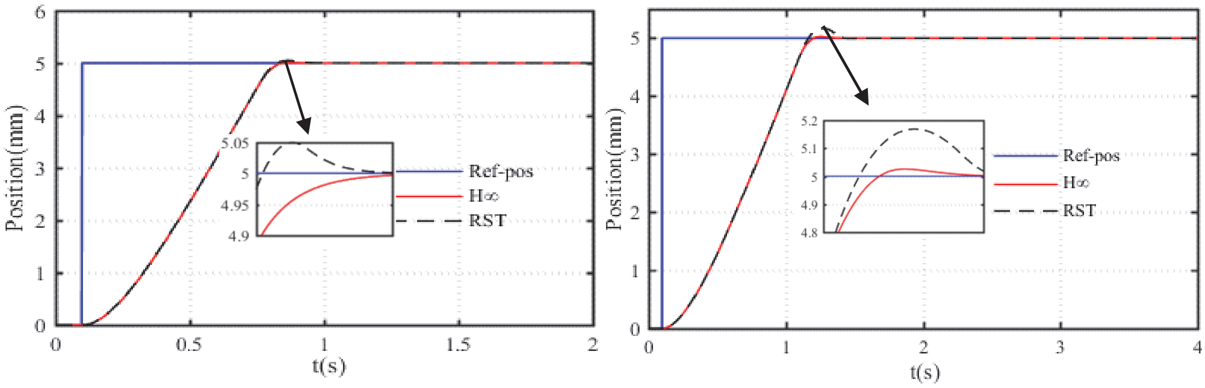

(a) (b)

Fig. V-12. Comparison of simulation step responses under model parameters variation: (a) 50% of gain variation (k_w), (b) 50% of constant time variation (τ_w)

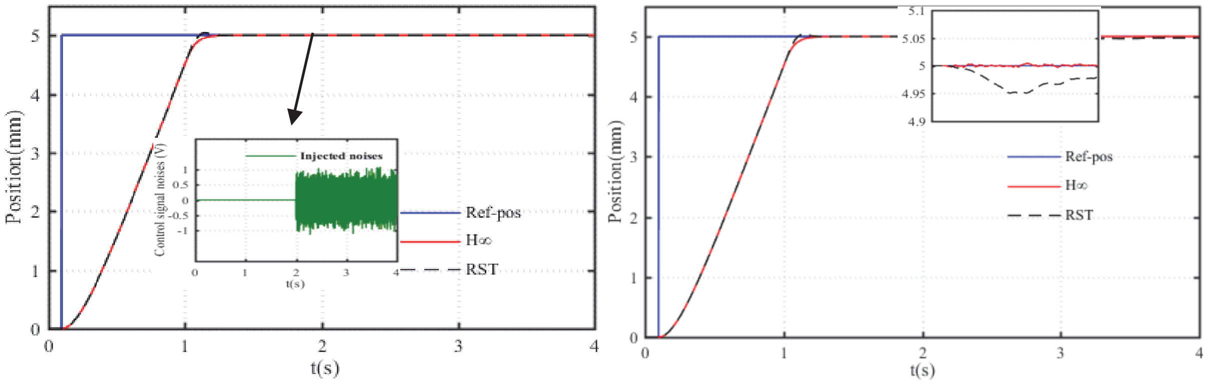

(a) (b)

Fig. V-13. Comparison of simulation step responses under disturbances: (a) Control signal noises, (b) Measurement noises

V.8 Real-time implementation of WPZM closed loop positioning system

The experimental platform shown in Fig. V-4 is used to experimentally validate the performance of the positioning system. The experimental results of the H_∞ and RST control methods are discussed respectively. A comparative study with a PID controller for robustness issues will be presented at the end of this section. The proposed position controllers are implemented in the Matlab/Simulink environment and compiled via the dSPACE board. The three controllers are inserted together in the same Simulink file, which makes the switching between them easier. A graphical interface is also built to configure the motor operation mode, and to change the system parameters in order to evaluate the performances of the closed loop system. Via the graphical interface one can also switch between the open and closed loop operation mode, and choose the motor trajectory and the rod full stroke. In order to verify the robustness of the proposed controllers in case of low and high motor speeds, the velocity of the motor in closed loop can be also selected and changed in real time via the graphical interface. The purposes of the proposed system is to design an ultra-precision positioning system based on WPZM for micro and macro-scales (up to 40 mm). The accuracy and robustness of the closed loop under the system parameter variation due to the motor speed variation and external applied forces must be validated.

V.8.1 H-infinity test results

The mixed sensitivity H_∞ controller is tested with the parameters given in section V.6.1 which are determined based on the motor TF model ($G_{WPZM}(s)$). Fig. V-14 shows the experimental and simulation results of the positioning system for a rod stroke of 100 µm (Fig. V-14.a) and up to 40 mm (Fig. V-14.d). From these figures, one can see clearly the quasi-identical responses of the experimental and simulation systems. The proposed H_∞ control system gives high precision levels with respect to the prefixed static error ratio (0.1%) for the micro scale (Fig. V-14.a). Moreover, the proposed system keeps the accuracy without overshoot for a long travel range up to 40 mm with a resolution of 10 µm as shown in Fig. V-14.d

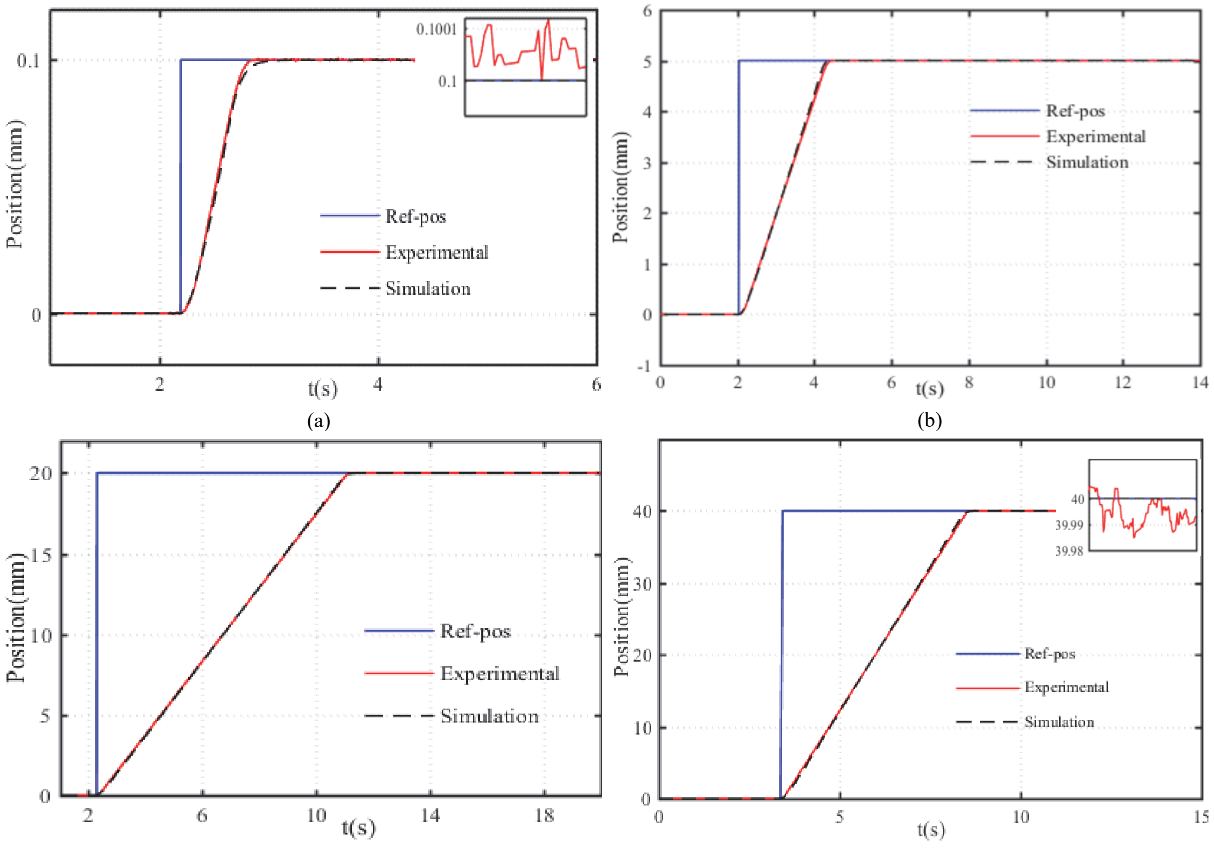

(a) (b) (c) (d)

Fig. V-14. H∞ experimental and simulation step responses: (a) 0.1mm,(b) 5 mm, (c) 20 mm,(d) 40 mm

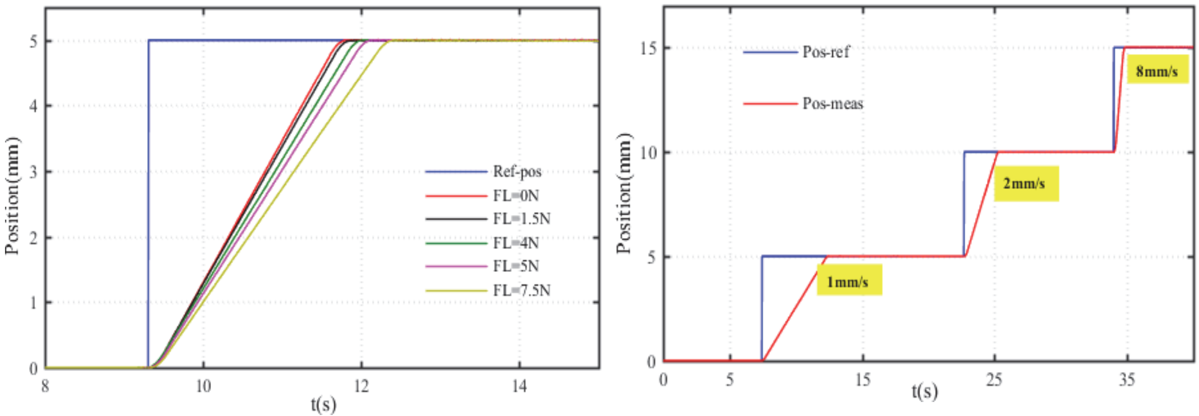

(a) (b)

Fig. V-15. H∞ experimental results under: (a) Different load forces, (b) Real rime speed variation

.The speed response of the WPZM changes when an external force is applied against the motion direction of the rod. Therefore the TF (V-3) parameters change, for a load force of 7.5 N, the time constant τ is of 0.23 s (instead of 0.15 s). The robustness of the H∞ controller under TF parameters variation due to the applied load is also validated. The N-310.13 is tested under different load forces up to 7.5 N, and the positioning system shows high precision as shown in Fig. V-15.a. In Fig. V-15.b, the performances of the loaded motor (2 N) under real time motor speed variation is illustrated. As can be seen, the system precision without overshoot is always guaranteed until a motor speed of 8 mm/s, where the maximum static error is of 5 µm for a displacement of 15 mm. The closed loop test results confirm the high precision levels of the proposed H_∞ at low and high motor speeds. The robustness of the controller in case of model uncertainties due to the nonlinear behavior of the motor or to the applied force is also confirmed.

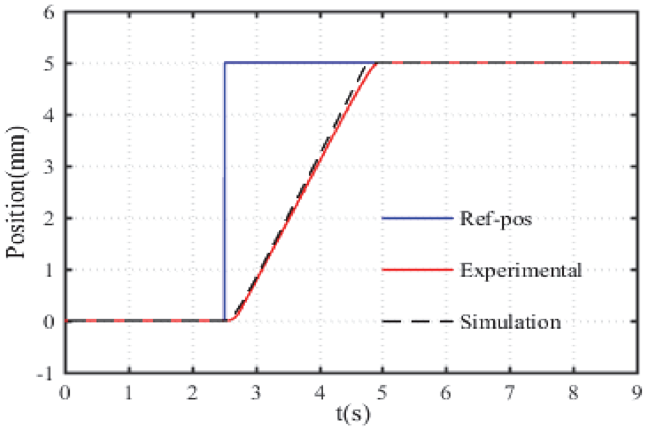

Fig. V-16. Experimental and simulation RST step responses

V.8.2 RST test results

The discrete time pole placement method based on RST controller is also implemented and evaluated. The experimental and simulation results given in Fig. V-16 validate the model conformity and the high precision levels when the motor moves with 2 mm/s of speed with a static error of 5 µm. From motor speed of 5 mm/s and higher, the closed loop response of the RST position controller presents a lot of overshoot up to 0.2 mm for a position step of 5 mm as shown in Fig. V-17.a. The overshoot and oscillation in steady state are critical points for the motor positioning applications. The performances of the closed loop system based on RST controller under load forces are also evaluated as illustrated in Fig. V-17.b, the system time response and precision are acceptable for external forces until 4 N.

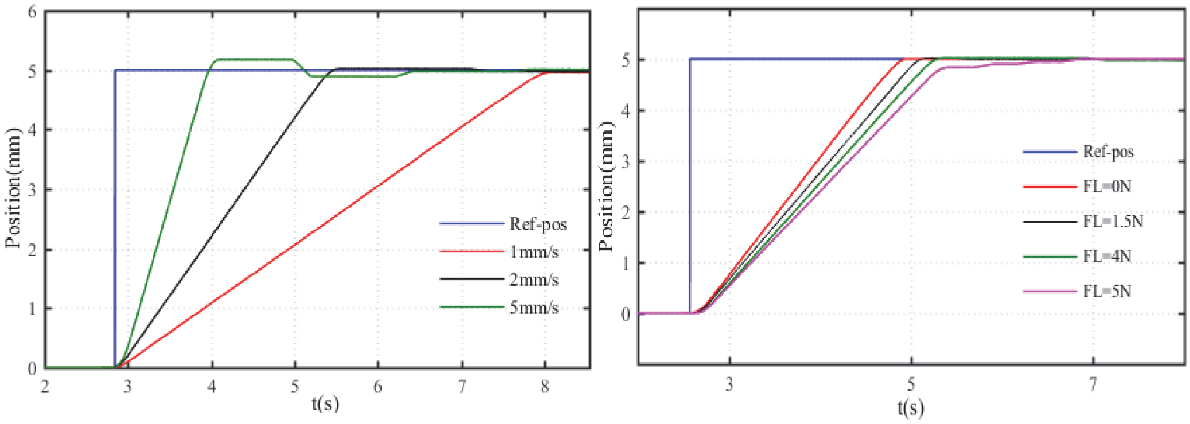

(a)

(b)

Fig. V-17. RST experimental results: (a) at different speeds, (b) under different load forces

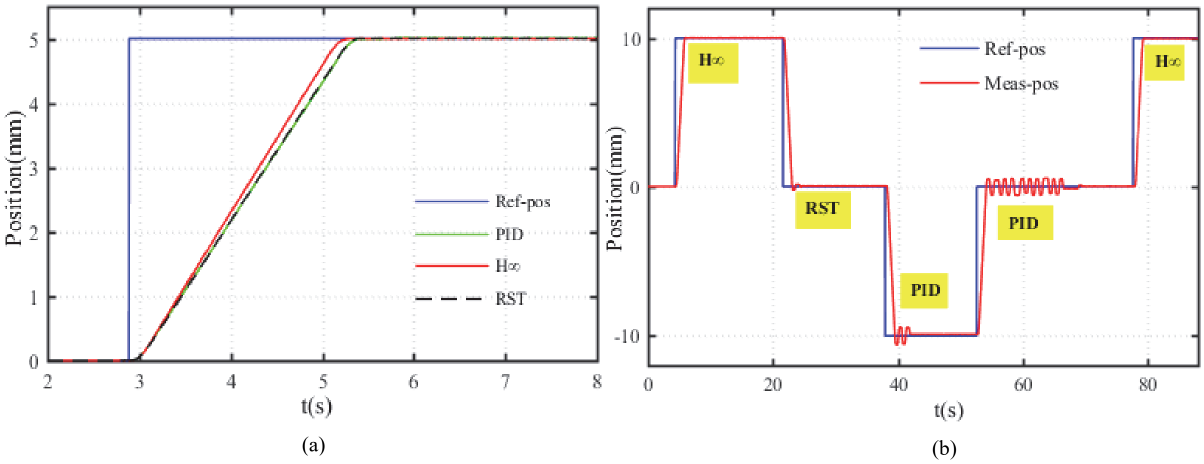

Fig. V-18. Comparison of controller experimental step responses: (a) at 2 mm/s speed,(b) at 8 mm/s speed

However, from a load of 5 N, the response time is higher than the expected values with an oscillation in steady state, which complicates the tests with higher load forces.

The experimental test results show that the proposed discrete time position control based on RST method is not robust in case of motor parameter uncertainties due to the speed variation or the applied external forces.

V.8.3 Comparative study

In this section, the H_∞ and RST techniques are compared to a PID controller. The synthesis approach of the H_∞ and RST parameters was already detailed. The PID controller parameters are determined based in the motor TF (V-3) and tuned by trial –and-error through intensive tests in order to achieve similar performances with the other controllers in normal conditions. The resulting proportional, integrator, and derivative gains are respectively equals to 48, 0.01, and 1.4. The comparison criteria are the positioning accuracy at low and high motor speeds, and the robustness in case of model uncertainties due to the nonlinear behavior of the motor or to an external forces. The experimental results of the three proposed controllers in no-load condition and with a velocity of 2 mm/s is given in Fig. V-18.a. As can be seen, all controllers present fast responses without overshoot in normal operation mode. In order to evaluate the performances of the positioning system at higher motor velocity, the motor is driven with 8 mm/s speed, and the tracking capability of 10 mm position steps sequence is tested. Using the graphical interface, we switch in real time between the three controllers as shown in Fig. V-18.b. The H_∞ presents better performances since there is no overshoot and oscillation can be distinguished easily. In fact, as shown in Fig. V-18.b, the RST has an overshoot of 100 µm and the PID gives an oscillation of +/-250 µm, while the H_∞ present a static error of 8µm without overshoot.

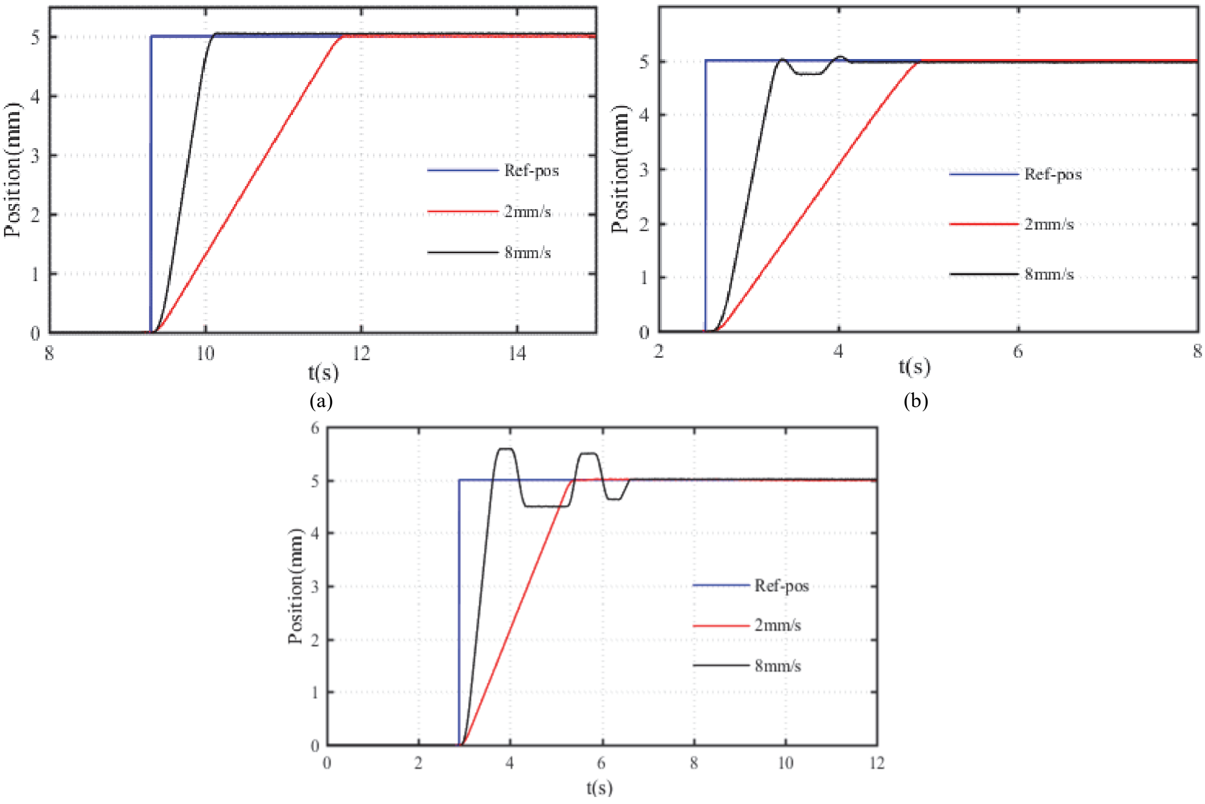

(a)

(b)

(c)

Fig. V-19. Comparison of controller experimental step responses at different velocities: (a) H∞, (b) RST, (c) PID

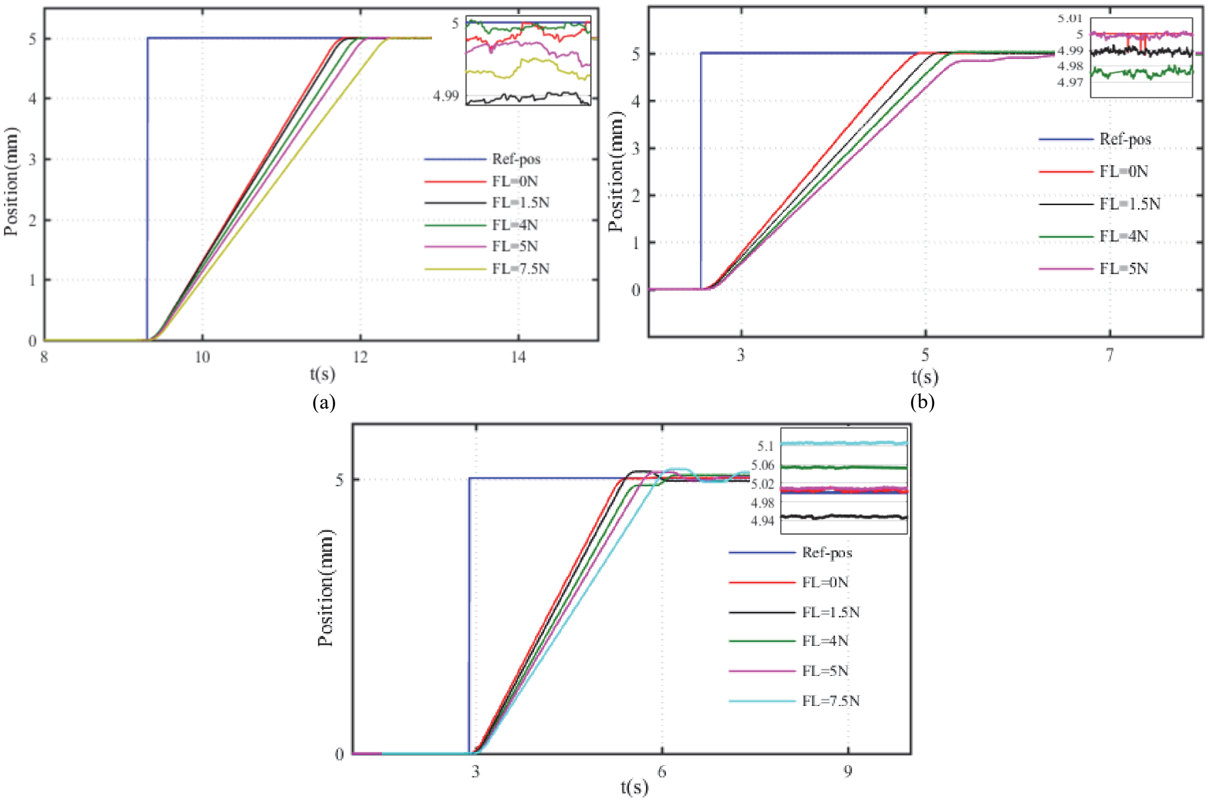

(a)

(b)

(c)

Fig. V-20. Comparison of controller experimental step responses under different loads: (a) H∞, (b) RST, (c) PID

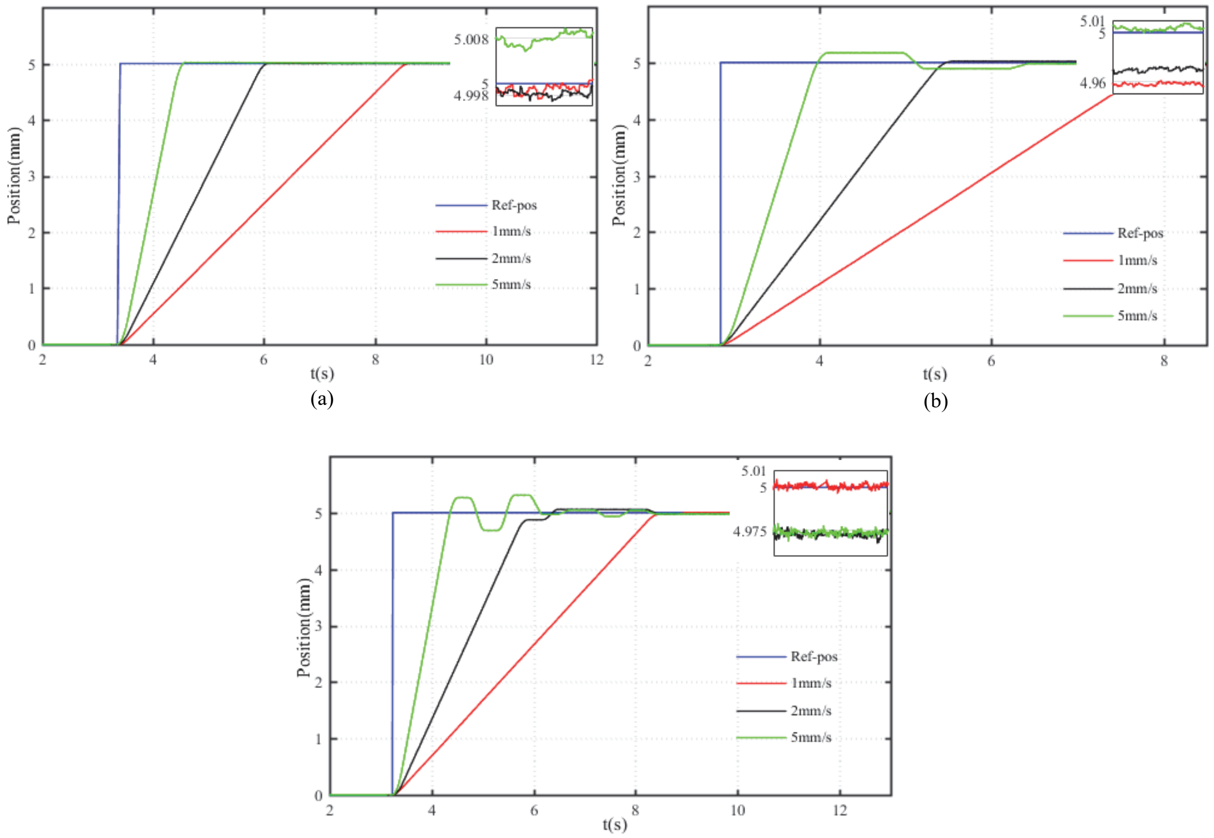

(a) (b)

(c)

Fig. V-21. Comparison of controller experimental responses under a load of 4 N at different velocities: (a) H∞, (b) RST, (c) PID

The closed loop step responses at low and high motor speeds of the proposed controllers are compared as shown in Fig. V-19. Up to 8 mm/s of speed, the H∞ gives a high resolution (5 µm) for a stroke of 5mm. The RST and PID results show a lot of overshoot up to 500 µm for the later. The accuracy and the stability of the closed loop system under applied external forces are also evaluated as detailed in Fig. V-20. For a load force up to 7.5 N, the steady state error of the H∞ controller is always less than 10µm. However, the response time of the RST controller is much affected by the applied load, and the PID method shows a weak precision (150 µm of static error for 7.5 N) with overshoot. The effect of both load force and speed variation is tested when an external force of 4 N is applied to the motor rod and moving at different speeds as shown in Fig. V-21. In terms of overshoot and oscillation, the H∞ controller shows high robustness levels compared to the RST and PID controllers. Similarly, for the steady state errors, as can be seen in the zoomed areas that the maximum static error is of 8 µm for the H∞, and of 40 µm and 25 µm for the RST and the PID controllers respectively.

From the briefly comparative study between the three proposed position controllers, it is clear that the precision and robustness of the H-infinity controller are very high compared to the RST and PID controllers. With the H∞ controller, the motor model uncertainties and the effect of the speed variation are completely compensated. The high precision levels under load conditions is also guaranteed. Moreover, with this robust controller, the stability of the closed loop system with large bandwidth is guaranteed.

V.9 Conclusions

High precise closed loop positioning system based on linear WPZM is presented in this chapter. The studied motor (N-310.13) has a full stroke of 50 mm and generates force up to 10 N. The motor structure and working principle are explained in details.

An overview of the proposed positioning systems based on WPZM and the corresponding position control methods was presented at the beginning of this chapter to highlight the contributions of our proposed system. The reported position controllers of WPZMs are limited to the nano/micrometric scales which are useful for cells manipulation and microscopy applications. Furthermore, depending on the application requirements, the accuracy of the closed loop system was performed for slow motion to avoid the nonlinear behaviors when operating close to the dynamic operation range.

The contributions of our closed loop WPZM positioning system are; the high precision level is proved for the total motor stroke (50 mm) and whatever the motion speed (until the maximum speed), the robustness to uncertain motor parameters caused by the external forces and the nonlinear behavior in dynamic mode is confirmed. The advantage of the proposed method is that, the position control method combines the precision and robustness requirements in one simple design control.

The motor is driven firstly in open loop in order to evaluate the output characteristics as function of the control signal (V_c) and external forces, and to experimentally identify the equivalent second order Transfer Function (TF) model between the slider position (Y) and V_c. Robust mixed sensitivity H_∞ and discrete time RST controllers are then synthesized based on the identified TF.

The experimental tests prove that the WPZM is an accurate actuator for high precise positioning (nanometer resolution) with relatively high generated forces, provided that the position control signal be carefully selected. In fact, the least perturbation of the control signal (electrical noise) generates acoustic noises and a lot of oscillations around the final position of the slider. The vibration of the slider is a critical point when the motor is used to guide a needle in surgery robot [61] .

The experimental positioning platform is used also to validate the closed loop position control methods. The H_∞ and RST are compared to a PID controller in order to confirm the advantage of the proposed method. The motor position is measured with a laser sensor and the controllers are executed in real time via a dSPACE microcontroller. The output signal of the position sensor and the motor control signal are both analog voltages, therefore two ADC/DAC conversion stages are mandatory. These conversion stages in addition to the high sampling frequency of the real time control block into Matlab/Simulink affect the control signal quality. Thus, the weighting filters of the H_∞ and the pole locations of the RST control must be carefully selected in order to overcome these perturbations.

Due to the special structure of the motor and the nonlinear behavior of the used piezoelectric actuators to create motion, the motor TF is uncertain and depending on operation conditions. Therefore, the closed loop positioning system is simulated in case of motor parameter uncertainties. The proposed position controllers show high robustness to the motor gain and constant time variation with an amount up to 50%. The rejection capability of injected electrical noises of the proposed system was also discussed. The results prove that the H_∞ is more robust to external perturbations, especially when they are injected to the measured position.

The experimental results prove the ultra-precision of the positioning system for the micro and macro-scales motion. The high precision of the closed loop system is validated for a large motor stroke (40 mm) with a steady state error ratio lower than 0.1%. The H_∞ control technique shows high robustness to motor parameters uncertainties due to the speed variation. Where, the H_∞ closed loop system keeps a high precision level without overshoot for low motor speed (1 mm/s) and up to the maximum speed (10 mm/s). The RST and PID controllers present a robustness weakness to motor parameters variation. In fact, the WPZM is identified at low motor speed (2 mm/s), and when the motor moves with higher speeds, the positioning system based on RST and PID controllers generate overshoots with oscillations in steady state. The robustness of the closed loop system to load torque is also evaluated. External forces are applied in the opposite direction of the motor motion, and the positioning responses are compared. The H_∞ control method gives high position resolution (<0.1%) also in load conditions (up to 7.5 N). However, it is not the case with the two other controllers, where the position static error increases significantly (3% for the PID with a force of 7.5 N).

The mixed sensitivity design approach of the H_∞ gives it the precision and robustness performances simultaneously, where one weighting filter was selected to perform the accuracy and stability requirements, while the two others are adjusted to improve the sensitivity function and consequently to reject the effect of additional perturbations (loads, noises, etc.).

Finally, an ultra-precision WPZM positioning system based on H_∞ control can perform high closed loop resolution for micro scale even using the total motor motion. The robustness of the proposed method to system parameters variation, motor nonlinear behavior, and external forces is confirmed without additional compensation system or online parameters adaptation. These features make it suitable to be integrated into practical embedded system where the compact size, precision and robustness are important. In order to confirm this, an embedded control board prototype (65*50 mm) based on dSpic microcontroller is designed, which can replace the dSPACE platform. The topology and architecture of this board are given in annex C.

Chapter VI

Suggestions, recommendations, and general conclusions

This chapter provides an overview of the content of this thesis dealing with the piezoelectric motors for robotic applications: modeling and robust closed loop position control issues. The proposed control models of PZMs, synthesis of robust position controllers, and simulation and experimental investigations are summarized. The drive technique, positioning performance, and behaviors in open and closed loop of each studied motor will be discussed. Recommendations about the selection and drive methods of PZMs as function of the application requirements will be carried out. Finally, suggestions for future works will be presented.

VI.1 Summary and contributions of this thesis

VI.1.1 Summary

This thesis deals with the study of three PZMs with different topologies and operating principles for modeling and robust position control purposes. The nano/micro piezo-motors are not in the interest of this research, the concerned motors are in the range of 0.1-20W as output mechanical power and with a linear motion up to 100 mm.

The first studied motor is a bidirectional Traveling Wave Ultrasonic Motor (TWUSM) type USR60 with a nominal output torque of 0.5 Nm and rated speed of 100 rpm. The second is a bidirectional quasi-static rotary motor type Piezoelectric Actuator Drive (PAD) with an output torque of 4 Nm and rated speed of 56 rpm. The last one is a linear quasi-static motor type N-310.13, working with walking drive method, and has a total stroke of 50 mm with a maximum speed of 10 mm/s and 10 N as generated force.

This manuscript begins with an initiation to the piezoelectric field by introducing the principle of the piezoelectric actuators and motors, a kind of piezo-motors classification, and a description of the nonlinear behaviors of these devices. An overview of the industrial applications of PZMs was also presented. The thesis contributions and outlines are mentioned at the end of this chapter.

For the control purposes, H-infinity and RST position controllers are synthesized for a generalized plant. Afterwards, it will be applied to each motor plant regarding to the motor parameters and the desired closed loop performances.

The three chapters focusing on the modeling and design of robust closed position control of the three piezo-motors are addressed in a similar way. An illustration of the motor structure and working principle is given at the beginning of each chapter in order to make the reader familiar with this. Literature review of the modeling and position control research works is presented in second step to highlight the advantages of the proposed systems. Thereafter, the development approach consists of three main parts:

- Design of accurate Simulink model which describes the motor topology, reflects the dynamic behavior of the motor, and permits the closed loop controls implementation.

- Design of experimental positioning platform based on the corresponding motor, evaluation of the experimental output characteristics, and identification of the Transfer Function (TF) model between the control signal and the motor position.

- Synthesis of position control parameters, simulation validation, and real time implementation via the experimental positioning system: the precision and robustness results are discussed and compared to conventional PID controller.

VI.1.2 Contributions

The contributions of this thesis can be divided into three main parts; the modeling approaches, position controllers, and performance of real time positioning systems.

- **Modeling approaches:** The reported models of TWUSM employed for control purposes are Equivalent Circuit Model (ECM). The parameters of the ECM are generally identified through experimental tests. These models lack to capture the dynamic of the contact mechanism which is at the origin of torque generation. The second category of TWUSM models are of type analytical models which use numerical and mathematical methods to describe the highly nonlinear motor behaviors. These models are not suitable for control techniques implementation due to the time execution and so no adapted to fast prototyping systems. In our modeling approach, some assumptions which not affect the motor dynamic and motion are taken. The geometry and parameters of the stator (stiffness, damping, coupling factor…), the contact surface leading to the torque generation, and the vertical and angular motions of the rotor are integrated in the proposed Simulink USR60 model. This model serves for speed and position control implementation in the two directions via the supply voltages amplitude, frequency, and phase shift. The output characteristics of the USR60 model are similar to those given by the motor manufacturer. Moreover, it permits to evaluate the effect of the stator and contact surface parameters variation on the output motion and the generated torque.

  The Piezoelectric Actuators Drives (PAD) models focused only on the motor characterization, parameters identification, and sensing of load torque. The motor behavior in static and dynamic operation modes are analyzed through equivalent circuit models. The electromechanical models served to evaluate the effect of the parameters variation of the employed multilayer actuators on the output characteristics. In this thesis, hybrid model of PAD7220 motor is proposed for position control purposes. This model includes equivalent spring-mass-damper systems which describe the motion of the orthogonal piezoelectric actuators, the contact model between the actuators and the stator ring, and the micro-teeth mechanical system used to transmit the motion to the rotor. The Simulink model of PAD7220 motor permits both, the simulation of closed loop position controllers through the driving signals, the evaluation of motor parameters effect on the actuator displacements and the motor angular speed.

- **Position control design:** The construction, topology, and motion generation process of the PZMs (ultrasonic, inertia, stepping…) are widely different. In addition, the behavior of the piezoelectric ceramics is not the same when operating in quasi-static (low frequencies) and ultrasonic (>20 kHz) modes. In consequence, the solution to perform the precision of such actuators in closed loop, is to propose different control methods regarding to the motor topology specifications.

  - The first contribution of the position control part is that the proposed H-infinity and RST robust controllers are synthesized for a generalized plant and can be used similarly for the three types of PZMs by introducing the specified motor requirements through a flexible design concept.

The position accuracy of PZMs is much affected by the nonlinearities between the deformations of the employed actuators (stators) and the driving signals, caused principally by the hysteresis, creep, and dynamical vibrations. The parameters of PZMs (stiffness, damping, and coupling factor) depend also on the materials wear and operation conditions of the motor. Furthermore, the USM output characteristics present a highly nonlinear behavior when operating very close to the mechanical resonance frequency, and are affected by the motor heating. To overcome the parameters uncertainty problems, complex control techniques with on-line parameters adaptation are proposed. The nonlinearity problems are often addressed by the applying of neural networks and fuzzy logic compensation based models. The accuracy of these models and the feasibility of such techniques for practical engineering applications are the common locks of this methodology.

- The second contribution of the proposed controllers is that, they combine the precision and the stability performances, and the robustness again nonlinear behaviors and motor parameter uncertainties, in one simple design controller without additional parameters adaptation or compensation systems.

- **Real time positioning systems:** This thesis deals also with the development of three compact positioning platforms based on PZMs. The two rotational positioning systems based on the USR60 and PAD7220 are installed and validated in the Group of electrical engineering of Paris (GeePs), while the linear one based on the N-310.13 motor was installed and validated in the Laboratory of Actuation Technology (LAT) in Saarbrucken (Germany). Theses platforms permit a rapid and flexible real time implementation of closed loop position controllers through dSPACE microcontroller board. The positioning platforms are equipped with graphical interfaces which serves to configure the operation conditions in real time (switching between open/closed loop, selection of control method, motion trajectory, etc.). The positioning performances of the PZMs under load condition can be also evaluated, where a smart torque sensor is installed.
  The features of the drive techniques and the flexible design of the robust position controllers make the proposed control suitable for integration into embedded systems. In fact, compact control board prototype (65*50 mm) for the linear piezo-motor is designed (Fig. VI-1), where the controllers are executed via a dSPIC microcontroller.

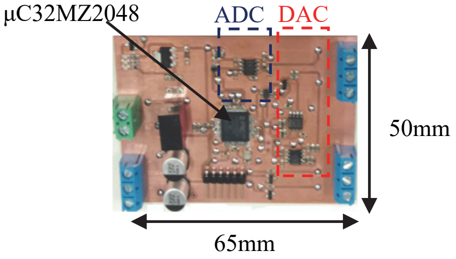

Fig. VI-1. Prototype of walking motor control board

VI.2 General conclusions

In this thesis, modeling, simulation, and experimental achievements had been presented. General conclusions and recommendations related to each studied PZM can be drawn as following:

VI.2.1 Traveling wave ultrasonic motor (USR60)

- **Modeling:** In the modeling approach of the TWUSM, the USR60 model complexities related especially to the contact mechanism are simplified, without neglecting the principal parameters allowing the torque generation (location of the half-contact and stick points), or the vertical motion of the rotor. This is in order to capture the dynamic of the motor and to implement closed loop control techniques. The evolution of the output characteristics (speed, torque) as function of the driving signals are similar to those given by the manufacturer. The model is used to simulate robust closed loop position controllers in the two motion directions. Moreover, the synthesized controller simulations parameters are very close to those used in the experimental USR60 platform, which confirms the accuracy of the proposed model.

- **Experimental investigations:** From the experimental results of the USR60 positioning system, it could be concluded that:

  - ✓ The USM can be controlled using the voltages amplitude, frequency, and phase shift. The drive signal should be selected regarding to aims of the control. In fact, the speed-frequency characteristic of the USR60 presents an asymmetrical and nonlinear behavior around the mechanical resonance frequency (f_r), where the motor shutdown immediately when the driving frequency decreases bellow f_r. Moreover, the resonance frequency depends on many factors like the temperature and the load torque. To restart the motor motion, the driving frequency must be increased progressively exceeding the resonance frequency range. Therefore, many precautions should be taken if the position of the USR60 is controlled via the driving frequency. Reminder also, the motor operation in the two motion directions is not possible using only the frequency. Based on these features, the driving frequency is recommended for speed control and not for position control.

  - ✓ The amplitude of the supply voltages of USR60 must be higher than 80 Vrms to create motion, and recommended to be lower than 130 Vrms. The speed-voltage characteristic presents a quasi-linear behavior in the frequency range above the resonance. However, the voltage amplitude increase of 40 Vrms produces a speed increase of about 20 rpm in the best case (resonance). Thus, this technique permits only a slow motor motion in one direction.

  - ✓ To create ideal traveling wave, the phase shift between the excitation voltages (φ) should be equal to +/-90°. Nevertheless, this phase shift can be used as speed and position control signal when variating between +90° and -90°, the no motion state corresponds theoretically to 0°. In addition, this is the unique variable permitting the motor operation in two motion directions by inverting the sign of the phase shift. The driving method using φ permits also rapid and easy switching between the on and off motion states of the motor. In the other hand, the speed (Ω) variation function of φ is not nicely linear, and the Ω-φ characteristic presents a dead zone when a load torque is applied. These features make the phase shift more suitable for position control than speed control, and it is the selected variable for our closed loop positioning application.

  - ✓ The feedback voltage generated by the actuation electrodes placed in the stator gives information about amplitude of the traveling wave and can be used to estimate the resonance frequency which corresponds to the maximum traveling wave amplitude.

  - ✓ The Transfer Function (TF) between the motor angular position (θ) and φ was experimentally identified in open loop, and used to synthesize the position controllers.

- ✓ The USR60 motor has a high holding torque even without supply, i.e. the motor can maintain its final position in off power condition. One demerit of the phase shift drive method (and also frequency drive method) is that in "off" motion state, the motor continuous to consume power while the voltage amplitude is different to zero.

- ✓ The efficiency of the USR60 can be improved if a resonance frequency tracking is added, in order to keep the motor frequency very close to this resonance one.

- ❖ **Real time positioning results:** The simulation and experimental results of the USR60 closed positioning system show that the listed challenges in terms of precision and robustness are achieved with the H_∞ and RST control methods:

  - ✓ The closed loop positioning system achieves the maximum resolution of the position sensor (0.09°).

  - ✓ The uncertain motor parameters and the dead zone effects caused respectively by the nonlinear behaviors of the motor and the load torques are overcome without parameters adaptation or compensation techniques.

  - ✓ The H_∞ present higher robustness to the load torque variation and the electrical noise effect than the RST, justified by the design flexibility of the H_∞ given by the weighting filters.

  - ✓ The comparison of the two controllers with conventional PID controller highlights their advantages.

VI.2.2 Rotary quasi-static motor (PAD7220)

- ❖ **Modeling:** An accurate model of PAD7220 was designed. It describes the motor dynamic including the elongation of the multilayer stack actuators, the actuators/stator ring contact mechanism, and the motion transmission to the rotor via the micro-teeth system, and it permits a control techniques implementation in closed loop through the driving signals (voltage amplitude, frequency, and phase shift).
- ❖ **Experimental investigations:** from the experimental investigations related to the PAD motor, it could be concluded that:

  - ✓ The speed and position of the PAD can be controlled only via the driving voltage frequency, while the phase shift can be used to change the motion direction but it must be kept to +/-90°.
  - ✓ The structure of the motor makes it capable to operate at very low speed (<1rpm) by imposing low drive frequencies, and able to generate high torque. This is an advantage compared to the TWUSM.

  - ✓ The quality of the driving frequency must be monitored, because the least electrical noise injected to this signal (which can occur in closed loop) generate acoustic noise at the output motion.

- ✓ The driving voltages amplitude must be minimum equal to 160 $V_{pk\text{-}pk}$ (and maximum 200 $V_{pk\text{-}pk}$), because with lower voltage values the stator tooth still blocked between two rotor teeth leading also to acoustic noise without moving the shaft.

- ✓ Load torques are applied to the motor shaft without affecting the rotation speed, which confirm the speed-load independent feature of the PAD.

- ✓ The transfer function between the control signal (f) and the motor angular position is experimentally identified through the open loop experimental tests.

- ✓ As the case of the other PZMs, the PAD has a high holding torque without supply, but by stopping the motor using the driving frequency, it continuous to consume power in no motion state.

- ❖ **Real time positioning results:** In the PAD positioning platform, the employed position sensor has a resolution of 0.009°. With the implemented position closed loop controllers, the maximum resolution is achieved:

    - ✓ The closed loop system shows high stability margins for large bandwidth with respect to the resonance frequency.

    - ✓ The precision of the closed loop system is guaranteed at very low and relatively high speeds without overshoot and oscillation.

    - ✓ The electrical noises generated by the ADC/DAC conversion stages of the control board reflected on the measurement and control signals are completely rejected by the mixed sensitivity H_∞ approach. In fact, the cut-off frequency and amplification gains of the weighting filters are adjusted in order to prove the robustness of the controller to these perturbations.

    - ✓ The comparison of the two controllers with PID control method highlights their advantages in term of precision under different operation conditions. Where, in the case of high rotation speed, the PID control lacks to quickly track the reference position and generates overshoot in steady state. This problem can be avoided by introducing parameters adaptation technique function of the operation conditions, at the expense of real time execution.

VI.2.3 Linear walking piezoelectric motor (N-310.13)

- ❖ **Modeling:** In the case of linear walking motor, only motor model based on Transfer Function (TF) is developed. The control signal of the motor is an analog voltage (+/-10 V) sent to the input of the voltage amplifier. The TF between the control signal (V_c) and the slider position (Y) is experimentally identified in open loop by introducing a step change of V_c and measuring the corresponding speed variation. Afterwards, the TF is identified using the experimental data and the identification toolbox of MATLAB. The TF parameters change regarding to the moving speed. Therefore, the motor TF model for low speed (2 mm/s) was taken to synthesize the position controllers, and we rely on the robustness of the position controllers to overcome the model uncertain parameters problem.

- **Experimental investigations:** The walking motor is composed by four piezo-legs guiding a linear rod by friction contact. From the experimental results, it could be concluded:

  - ✓ The N-310.13 motor can operate in analog or stepping mode depending on the configuration of the legs. In the analog mode, all piezo-legs are always in contact with the rod and the maximum feed is of 10 µm and corresponding to the deflection of the piezo-actuators. In stepping mode only one pair of legs is in contact with the rod, and the motor is moving for long distances by a succession of clamping and unclamping movements.

  - ✓ The motor speed depends on the step size and the driving frequency. The phase shift between the driving voltages of the two pairs of legs must be equal to 180° in order to keep always one leg in contact with the slider. The phase shift between the driving voltages of one leg can be switched between +/-90° in order to reverse the motion direction.

  - ✓ The step size of the N-310-13 motor version varies between 5 nm and 5 µm, and it depends on the applied external load

  - ✓ The rod position is affected by the quality of the control signal, where noised signal generates vibration of the rod at the final position and positioning error. The quality of the control signal depends of the output signal of the position sensor (laser sensor) which is an analog voltage +/-10 V, and is automatically perturbed by the ADC/DAC conversion stages of the dSPACE control board.

- **Real time positioning results:** The designed N-310-13 positioning system based on H_∞ and RST controllers has reached the fixed precision with static error of 0.1% for a displacement range between 100 µm and 40 mm.

  - ✓ The H_∞ experimental results show high accuracy without overshoot whatever the moving speed, overcoming the model parameters variation problem. This is due to the large closed loop bandwidth introduced via the first weighting filter independently of the frequency of the injected noises.
  - ✓ The precision of the H_∞ control method was also tested under load conditions (up to 7.5 N) keeping high resolution (error of 5 µm for a displacement of 10 mm).

  - ✓ The experimental test results using the RST and PID controllers presents overshoots with oscillations in steady state when the motor moves with speeds higher than 5 mm/s.

  - ✓ The static errors in case of load conditions are relatively high with the RST and PID controllers, exceeding the permissible tolerances for high precision applications.

VI.2.4 Recommendations for future works

This work opens new perspectives which are related to the studied PZMs in terms of modeling, drive techniques, and control:

TWUSM (USR60): The USM achieves its maximum effectiveness when operating at the resonance frequency. Therefore, a resonance frequency tracking technique can be implemented in parallel to the position controller to improve the effectiveness of the USM, and to increase its response time at a fixed voltage phase shift. This can be done through a dual control method, the motor position will be controlled via the voltages phase shift, and the resonance frequency will be tracked using the driving voltage frequency.

The experimental results of the TWUSM show that the resonance frequency (and in consequence the rotational speed) drifts function of the motor temperature. To perform the effectiveness and the time response of the TWUSM under heating, one solution is to insert coiling system **to** the motor plant. Alternative solution is to identify the relationship between the motor temperature and the resonance frequency, and adjust the driving frequency regarding to the motor temperature through dual control (phase shift and frequency).

Linear walking piezoelectric motor (N-310.13): For the walking motor, electromechanical model can be designed to take into account the dynamic of the four piezo-legs, and the contact mechanism between the legs and the rod. This model can be used to evaluate the effect of piezo-leg and contact surface parameters in the output motor characteristics.

The drive of the walking motor can be also realized through four output voltage amplifiers which make possible the evaluation of control results using the voltages amplitude, frequency, and phase shift as was done with TWUSM.

Linear encoder with high resolution (5 nm) can be installed with the walking motor for higher precision requirement and to avoid the generated noise by the ADC conversion stage of the analog output signal of the laser sensor.

The designed H_∞ and RST controllers can be implemented using dSPIC microcontroller for embedded systems. Control card based dSpic microcontroller was designed for the walking motor (Fig. VI-1), this card has a dimension of 65*50 mm and replaces the dSPACE board. The same concept of control board can be realized for the two other motors.

As demonstration of the robotic application, prototype of robotic arm is designed to be actuated by the three studied motors (Fig. VI-2). As shown in Fig. VI-2, the base joint will be articulated by the PAD7220 motor and the second joint is articulated by the USR60. The gripper of the prototype will be actuated by the linear walking motor N-310.13. Mini-control cards based on dSPIC microcontroller will be designed to control the arm in closed loop.

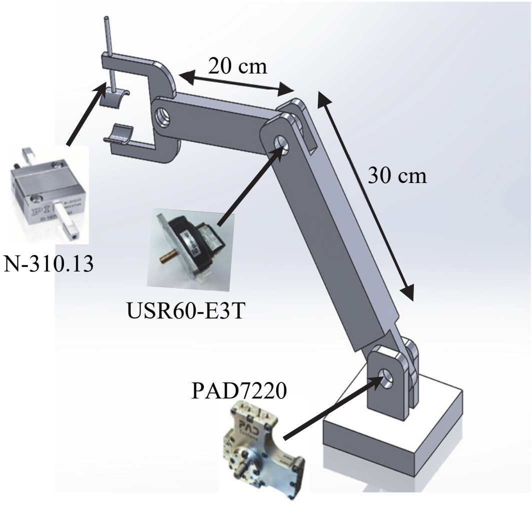

Fig. VI-2. Prototype of robotic arm actuated by PZMs

References

[1] T. Ikeda, *Fundamentals of Piezoelectricity*: Oxford University Press 1990.

[2] F. Claeyssen, R. L. Letty, F. Barillot, and O. Sosnicki, "Amplified piezoelectric actuators: Static & dynamic applications," *Ferroelectrics,* vol. 351, pp. 3-14, 2007.

[3] R. G. Ballas, *Piezoelectric multilayer beam bending actuators: Static and dynamic behavior and aspects of sensor integration*: Springer Science & Business Media, 2007.

[4] M. Hunstig, "Piezoelectric Inertia Motors—A Critical Review of History, Concepts, Design, Applications, and Perspectives," in *Actuators*, 2017, p. 7.

[5] D. Jiles and D. Atherton, "Theory of ferromagnetic hysteresis," *Journal of magnetism and magnetic materials,* vol. 61, pp. 48-60, 1986.

[6] G.-Y. Gu, L.-M. Zhu, C.-Y. Su, H. Ding, and S. Fatikow, "Modeling and control of piezo-actuated nanopositioning stages: a survey," *IEEE Transactions on Automation Science and Engineering,* vol. 13, pp. 313-332, 2016.

[7] A. J. Fleming and K. K. Leang, *Design, modeling and control of nanopositioning systems*: Springer, 2014.

[8] C. Ru, X. Liu, and Y. Sun, *Nanopositioning Technologies: Fundamentals and Applications*: Springer, 2015.

[9] A. Visintin, *Differential models of hysteresis* vol. 111: Springer Science & Business Media, 2013.

[10] P. Ge and M. Jouaneh, "Tracking control of a piezoceramic actuator," *IEEE Transactions on control systems technology,* vol. 4, pp. 209-216, 1996.

[11] A. J. Fleming, "Charge drive with active dc stabilization for linearization of piezoelectric hysteresis," *IEEE transactions on ultrasonics, ferroelectrics, and frequency control,* vol. 60, pp. 1630-1637, 2013.

[12] A. J. Fleming, "Quantitative scanning probe microscope topographies by charge linearization of the vertical actuator," *Review of Scientific Instruments,* vol. 81, p. 103701, 2010.

[13] G. Schitter, P. Menold, H. Knapp, F. Allgöwer, and A. Stemmer, "High performance feedback for fast scanning atomic force microscopes," *Review of Scientific Instruments,* vol. 72, pp. 3320-3327, 2001.

[14] K. K. Leang and S. Devasia, "Feedback-linearized inverse feedforward for creep, hysteresis, and vibration compensation in AFM piezoactuators," *IEEE Transactions on Control Systems Technology,* vol. 15, pp. 927-935, 2007.

[15] G.-Y. Gu and L.-M. Zhu, "Motion control of piezoceramic actuators with creep, hysteresis and vibration compensation," *Sensors and Actuators A: Physical,* vol. 197, pp. 76-87, 2013.

[16] H. Jung, J. Y. Shim, and D. Gweon, "Tracking control of piezoelectric actuators," *Nanotechnology,* vol. 12, p. 14, 2001.

[17] M. Rakotondrabe, C. Clévy, and P. Lutz, "Complete open loop control of hysteretic, creeped, and oscillating piezoelectric cantilevers," *IEEE Transactions on Automation Science and Engineering,* vol. 7, pp. 440-450, 2010.

[18] G. M. Clayton, S. Tien, K. K. Leang, Q. Zou, and S. Devasia, "A review of feedforward control approaches in nanopositioning for high-speed SPM," *Journal of dynamic systems, measurement, and control,* vol. 131, p. 061101, 2009.

[19] G.-Y. Gu, L.-M. Zhu, C.-Y. Su, and H. Ding, "Motion control of piezoelectric positioning stages: modeling, controller design, and experimental evaluation," *IEEE/ASME Transactions on Mechatronics,* vol. 18, pp. 1459-1471, 2013.

[20] D. Croft, G. Shedd, and S. Devasia, "Creep, hysteresis, and vibration compensation for piezoactuators: atomic force microscopy application," in *American Control Conference, 2000. Proceedings of the 2000*, 2000, pp. 2123-2128.

[21] D. Croft and S. Devasia, "Vibration compensation for high speed scanning tunneling microscopy," *Review of Scientific Instruments,* vol. 70, pp. 4600-4605, 1999.

[22] G. Schitter, P. J. Thurner, and P. K. Hansma, "Design and input-shaping control of a novel scanner for high-speed atomic force microscopy," *Mechatronics,* vol. 18, pp. 282-288, 2008.

[23] T. Chang and X. Sun, "Analysis and control of monolithic piezoelectric nano-actuator," *IEEE Transactions on control systems technology,* vol. 9, pp. 69-75, 2001.

[24] G.-Y. Gu, L.-M. Zhu, and C.-Y. Su, "Integral resonant damping for high-bandwidth control of piezoceramic stack actuators with asymmetric hysteresis nonlinearity," *Mechatronics,* vol. 24, pp. 367-375, 2014.

[25] I. Mahmood and S. R. Moheimani, "Making a commercial atomic force microscope more accurate and faster using positive position feedback control," *Review of Scientific Instruments,* vol. 80, p. 063705, 2009.

[26] K. Spanner and B. Koc, "Piezoelectric motors, an overview," in *Actuators*, 2016, p. 6.

[27] I. Prisacariu and C. C. Filipiuc, "A general view on the classification and operating principle of piezoelectric ultrasonic motors," in *Electrical and Power Engineering (EPE), 2012 International Conference and Exposition on*, 2012, pp. 409-414.

[28] K. Uchino, "Piezoelectric ultrasonic motors: overview," *Smart materials and structures,* vol. 7, p. 273, 1998.

[29] D. W. Pohl, "Dynamic piezoelectric translation devices," *Review of scientific instruments,* vol. 58, pp. 54-57, 1987.

[30] T. Higuchi and M. Watanabe, "Apparatus for effecting fine movement by impact force produced by piezoelectric or electrostrictive element," ed: Google Patents, 1990.

[31] K. Spanner, "Survey of the various operating principles of ultrasonic piezomotors," in *Proc. of the international conference Actuator*, 2006.

[32] J. W. G. May, "Piezoelectric electromechanical translation apparatus," ed: Google Patents, 1975.

[33] S. P. Salisbury, R. B. Mrad, D. F. Waechter, and S. E. Prasad, "Design, modeling, and closed-loop control of a complementary clamp piezoworm stage," *IEEE/ASME Transactions on Mechatronics,* vol. 14, pp. 724-732, 2009.

[34] P. E. Tenzer and R. B. Mrad, "A systematic procedure for the design of piezoelectric inchworm precision positioners," *IEEE/ASME Transactions on Mechatronics,* vol. 9, pp. 427-435, 2004.

[35] J. Li, R. Sedaghati, J. Dargahi, and D. Waechter, "Design and development of a new piezoelectric linear Inchworm actuator," *Mechatronics,* vol. 15, pp. 651-681, 2005.

[36] J. E. Frank, G. H. Koopmann, W. Chen, and G. A. Lesieutre, "Design and performance of a high-force piezoelectric inchworm motor," in *1999 Symposium on Smart Structures and Materials*, 1999, pp. 717-723.

[37] A. D. Brisbane, "Position control device," ed: US Patent 3377489,, 9 April 1965.

[38] G. V. Galutva, J. K. Modestov, G. S. Presnyakov, and A. I. Ryazantsev, "Device for precision displacement of a solid body," ed: Google Patents, 1972.

[39] V. Lavrinenko and M. Nekrasov, "Electrical Motor," ed: USSR Patent 217509, 10 May 1965.

[40] V. S. Vishnevsky, V. L. Kavertsev, I. A. Kartashev, V. V. Lavrinenko, M. M. Nekrasov, and A. A. Prez, "Piezoelectric motor structures," ed: US Patents 4019073, 1977.

[41] H. Barth, "IBM Tech," *Disclosure Bull,* vol. 16, 1973.

[42] C. Zhao, *Ultrasonic Motors: Technologies and Applications*: Springer Berlin Heidelberg, 2011.

[43] T. Sashida, "Trial construction and operation of an ultrasonic vibration driven motor," *Oyo Butsiuri,* vol. 6, pp. 713-718, 1982.

[44] A. Endo, N. Sasaki, and Y. Tomikawa, "Linear type ultrasonic motor using two-dimensionally positioned piezoelectric elements," *Ferroelectrics,* vol. 112, pp. 165-170, 1990.

[45] B. Koc, S. Cagatay, and K. Uchino, "A piezoelectric motor using two orthogonal bending modes of a hollow cylinder," *IEEE transactions on ultrasonics, ferroelectrics, and frequency control,* vol. 49, pp. 495-500, 2002.

[46] *http://www.newscaletech.com/*.

[47] *http://www.nanomotion.com/product-type/nanomotion-motors/*.

[48] W. Wischnewskiy, S. Kovalev, and O. Vyshnevskyy, "New ultrasonic piezoelectric actuator for nanopositioning," in *Proceedings of the 9th International Conference on New Actuators, Bremen, Germany*, 2004, pp. 118-122.

[49] T. Sashida, "Motor device utilizing ultrasonic oscillation," ed: US Patent 4562374, 1984.

[50] *http://www.shinsei-motor.com/English/techno/ultrasonic_motor.html*.

[51] T. Sashida and T. Kenjo, "Introduction to ultrasonic motors," 1993.

[52] M. Hermann and W. Schinköthe, "Piezoelectric travelling wave motors generating direct linear motion," in *Conference Proceedings, S*, 1999, p. 203.

[53] T. Takano and Y. Tomikawa, "Characteristics of the ultrasonic linear motor using radial and nonaxisymmetric vibration modes of an annular plate," *Japanese journal of applied physics,* vol. 34, p. 5288, 1995.

[54] M. Tominaga, R. Kaminaga, J. R. Friend, K. Nakamura, and S. Ueha, "An ultrasonic linear motor using ridge-mode traveling waves," *IEEE transactions on ultrasonics, ferroelectrics, and frequency control,* vol. 52, pp. 1735-1742, 2005.

[55] K. Spanner and B. Koc, "Piezoelectric Motors and Their Industrial Applications," in *Proc. of the international conference Actuator*, 2014.

[56] (01/06/2017). *http://www.canon.com/technology/now/element/cp.html*.

[57] K. Uchino, "Piezoelectric motors for camera modules," in *ACTUATOR 2008 Conference Proceedings, Bremen*, 2008, pp. 157-160.

[58] D. Henderson, Q. Xu, and D. Piazza, "Continuous Auto Focus for Next Generation Phone Cameras," *ACTUATOR 2010,* 2010.

[59] (01/06/2017). *https://www.konicaminolta.com/about/research/index.html*.

[60] (01/06/2017). *http://aimlab.wpi.edu/research/*.

[61] H. Su, G. A. Cole, and G. S. Fischer, "High-field MRI-compatible needle placement robots for prostate interventions: pneumatic and piezoelectric approaches," in *Advances in robotics and virtual reality*, ed: Springer, 2012, pp. 3-32.

[62] (02/06/2017). *http://www.piezomotor.com/products/linear/*.

[63] "http://www.neuroarm.org/," 02/06/2017.

[64] (02/06/2017). *https://www.keio.ac.jp/en/research/index.html*.

[65] R. Clavel, "A fast robot with parallel geometry," in *Proc. Int. Symposium on Industrial Robots*, 1988, pp. 91-100.

[66] R. Zeichfüßl, B. Gottlieb, C. Wallenhauer, A. Kappel, M. Vogl, T. Kraus*, et al.*, "Synchronously controlled piezoelectric actuator drives (PAD) as motors of a Delta-3 robot," in *Proceedings of the 11th international conference on new actuators, Bremen, Germany*, 2008, pp. 125-8.

[67] (02/06/2017). *https://www.physikinstrumente.com/en/products/linear-stages-and-actuators/compact-stages-with-piezowalk-stepping-drive/n-310-nexact-oem-miniature-linear-motor-actuator-1000700/*.

[68] A. Kappel, B. Gottlieb, T. Schwebel, C. Wallenhauer, and H. Liess, "PAD-Piezoelectric Actuator Drive," in *Proc. 10th Int. Conf. New Actuators*, 2006, pp. 457-460.

[69] (02/06/2017). *http://www.cedrat-technologies.com/en/applications/*.

[70] J. N. Kudva, C. A. Martin, L. B. Scherer, A. P. Jardine, A. R. McGowan, R. C. Lake*, et al.*, "Overview of the DARPA/AFRL/NASA smart wing program," in *Proc of 6th Ann Int Symp Smart Struct Mat, Newport Beach, USA, 1*, 1999.

[71] *http://www.noliac.com/products/motors/pad7220/*.

[72] S. Skogestad and I. Postlethwaite, *Multivariable feedback control: analysis and design* vol. 2: Wiley New York, 2007.

[73] J. W. Helton, "Operator theory and broadband matching," in *Proceedings of the 11th Annual Allerton Conference on Communications, Control and Computing*, 1976.

[74] G. Zames, "Feedback and optimal sensitivity: Model reference transformations, multiplicative seminorms, and approximate inverses," *IEEE Transactions on automatic control,* vol. 26, pp. 301-320, 1981.

[75] X.-H. Chang, *Robust output feedback H-infinity control and filtering for uncertain linear systems* vol. 7: Springer Science & Business, 2014.

[76] J. W. Helton and O. Merino, *Classical control using H∞ methods: theory, optimization, and design*: SIAM, 1998.

[77] G. Duc, "Commande H∞ et μ-Analysis, des outils pour la robustesse," 1999.

[78] J. C. Doyle, K. Glover, P. P. Khargonekar, and B. A. Francis, "State-space solutions to standard H/sub 2/and H/sub infinity/control problems," *IEEE Transactions on Automatic control,* vol. 34, pp. 831-847, 1989.

[79] M. G. Ortega, M. Vargas, F. Castaño, and F. R. Rubio, "Improved design of the weighting matrices for the S/KS/T mixed sensitivity problem-application to a multivariable thermodynamic system," *IEEE Transactions on control systems technology,* vol. 14, pp. 82-90, 2006.

[80] I. D. Landau and G. Zito, *Digital control systems: design, identification and implementation*: Springer Science & Business Media, 2005.

[81] E. Ostertag and E. Godoy, "RST-Controller design for sinewave references by means of an auxiliary Diophantine equation," in *Decision and Control, 2005 and 2005 European Control Conference. CDC-ECC'05. 44th IEEE Conference on*, 2005, pp. 6905-6910.

[82] T. Sashida and T. Kenjo, *An Introduction to Ultrasonic Motors*: Clarendon Press, 1993.

[83] H. Hirata and S. Ueha, "Characteristics estimation of a traveling wave type ultrasonic motor," *IEEE Transactions on Ultrasonics, Ferroelectrics, and Frequency Control,* vol. 40, pp. 402-406, 1993.

[84] N. Elghouti and J. Helbo, "Equivalent circuit modeling of a rotary piezoelectric motor," *Modelling and Simulation, Pittsburgh, USA,* 2000.

[85] V. Bolborici, "Modeling of the stator of piezoelectric traveling wave rotary ultrasonic motors," University of Toronto, 2009.

[86] H. Mojallali, R. Amini, R. I. Zamanabadi, and A. A. Jalali, "Systematic modeling for free stators of rotary piezoelectric ultrasonic motors," *IEEE/ASME Transactions on Mechatronics,* vol. 12, pp. 219-223, 2007.

[87] H. Mojallali, R. Amini, R. Izadi-Zamanabadi, and A. Jalali, "A new scheme for experimental-based modeling of a traveling wave ultrasonic motor," 2005.

[88] T. Maeno, T. Tsukimoto, and A. Miyake, "Finite-element analysis of the rotor/stator contact in a ring-type ultrasonic motor," *IEEE Transactions on Ultrasonics, Ferroelectrics, and Frequency Control,* vol. 39, pp. 668-674, 1992.

[89] J. Krome and J. Wallaschek, "Finite element models for the piezoelectric actuation in ultrasonic traveling wave motors," *Journal of intelligent material systems and structures,* vol. 7, pp. 157-161, 1996.

[90] Y. Kagawa, T. Tsuchiya, T. Kataoka, T. Yamabuchi, and T. Furukawa, "Finite element simulation of dynamic responses of piezoelectric actuators," *Journal of Sound and Vibration,* vol. 191, pp. 519-538, 1996.

[91] A. Frangi, A. Corigliano, M. Binci, and P. Faure, "Finite element modelling of a rotating piezoelectric ultrasonic motor," *Ultrasonics,* vol. 43, pp. 747-755, 2005.

[92] S. Shen, H. Li, F. Cui, G. Zhang, and X. Dai, "Contact Modeling of Traveling Wave Ultrasonic Motors," in *ASME 2014 Conference on Information Storage and Processing Systems*, 2014, pp. V001T01A020-V001T01A020.

[93] A. Iula and M. Pappalardo, "A high-power traveling wave ultrasonic motor," *IEEE transactions on ultrasonics, ferroelectrics, and frequency control,* vol. 53, pp. 1344-1351, 2006.

[94] P. Hagedorn and J. Wallaschek, "Travelling wave ultrasonic motors, Part I: Working principle and mathematical modelling of the stator," *Journal of Sound and Vibration,* vol. 155, pp. 31-46, 1992.

[95] N. W. Hagood and A. J. McFarland, "Modeling of a piezoelectric rotary ultrasonic motor," *IEEE Transactions on Ultrasonics, Ferroelectrics, and Frequency Control,* vol. 42, pp. 210-224, 1995.

[96] J. Wallaschek, "Contact mechanics of piezoelectric ultrasonic motors," *Smart materials and Structures,* vol. 7, p. 369, 1998.

[97] A. Morega, G. Robello, M. Morega, and L. Pîslaru-Dănescu, "Numerical study of the stator motion in a piezoelectric ultrasonic motor," in *Advanced Topics in Electrical Engineering (ATEE), 2015 9th International Symposium on*, 2015, pp. 609-613.

[98] T. Senjyu, M. Nakamura, N. Urasaki, H. Sekine, and T. Funabashi, "Mathematical model of ultrasonic motors for speed control," *Electric Power Components and Systems,* vol. 36, pp. 637-648, 2008.

[99] R. García-Rochín, M. Kühne, R. Santiesteban-Cos, G. J. Rubio-Astorga, and A. Peer, "Second-order model for rotary traveling wave ultrasonic motors," in *Humanoid Robots (Humanoids), 2015 IEEE-RAS 15th International Conference on*, 2015, pp. 991-996.

[100] N. El Ghouti, "Hybrid modeling of a traveling wave piezoelectric motor," *Diss. Department of Control Engineering, Aalborg University,* 2000.

[101] A. Gencer, "A new speed/position control technique for travelling wave ultrasonic motor under different load conditions," in *Power Electronics and Motion Control Conference and Exposition (PEMC), 2014 16th International*, 2014, pp. 65-70.

[102] Z. Sun, H. Li, and W. Huang, "Control of multiple ultrasonic motors with robust parameter design," in *Ultrasonics Symposium, 2008. IUS 2008. IEEE*, 2008, pp. 1827-1830.

[103] A. Djoewahir, K. Tanaka, and S. Nakashima, "Adaptive PSO-based self-tuning PID controller for ultrasonic motor," *International Journal of Innovative Computing, Information and Control,* vol. 9, pp. 3903-3914, 2013.

[104] T. Senjyu, S. Yokoda, Y. Gushiken, and K. Uezato, "Position control of ultrasonic motors with adaptive dead-zone compensation," in *Industry Applications Conference, 1998. Thirty-Third IAS Annual Meeting. The 1998 IEEE*, 1998, pp. 506-512.

[105] T. Senjyu, T. Kashiwagi, and K. Uezato, "Position control of ultrasonic motors using MRAC and dead-zone compensation with fuzzy inference," in *Power Electronics Specialists Conference, 2001. PESC. 2001 IEEE 32nd Annual*, 2001, pp. 2031-2036.

[106] T. Senjyu, H. Miyazato, and K. Uezato, "Quick and precise position control of ultrasonic motor using hybrid control," *Electrical engineering in Japan,* vol. 116, pp. 83-95, 1996.

[107] F. Bazrafshan, B. Rasti, and H. Mojallali, "Fuzzy modeling and position control of a traveling wave ultrasonic motor," in *Computer and Automation Engineering (ICCAE), 2010 The 2nd International Conference on*, 2010, pp. 457-461.

[108] G. Bal, E. Bekiroğlu, Ş. Demirbaş, and I. Colak, "Fuzzy logic based DSP controlled servo position control for ultrasonic motor," *Energy Conversion and management,* vol. 45, pp. 3139-3153, 2004.

[109] Y. Izuno, R. Takeda, and M. Nakaoka, "New fuzzy reasoning-based high-performance speed/position servo control schemes incorporating ultrasonic motor," *IEEE Transactions on Industry applications,* vol. 28, pp. 613-618, 1992.

[110] A. Gencer, "A comparative speed/position control technique based Fuzzy Logic control for travelling wave ultrasonic motor," in *Electronics, Computers and Artificial Intelligence (ECAI), 2015 7th International Conference on*, 2015, pp. SG-7-SG-12.

[111] T. Senjyu, H. Miyazato, S. Yokoda, and K. Uezato, "Position control of ultrasonic motors using neural network," in *Industrial Electronics, 1996. ISIE'96., Proceedings of the IEEE International Symposium on*, 1996, pp. 368-373.

[112] F.-J. Lin, R.-J. Wai, and C.-M. Hong, "Identification and control of rotary traveling-wave type ultrasonic motor using neural networks," *IEEE Transactions on Control Systems Technology,* vol. 9, pp. 672-680, 2001.

[113] S. Yildirim, "Design of adaptive robot control system using recurrent neural network," *Journal of Intelligent & Robotic Systems,* vol. 44, pp. 247-261, 2005.

[114] M. Ahmadi, H. Mojallali, and M. H. Fotovvati, "Predictive Control of Traveling Wave Ultrasonic Motors using neural network," in *Power Electronics, Drive Systems and Technologies Conference (PEDSTC), 2011 2nd*, 2011, pp. 256-261.

[115] F.-J. Lin, R.-J. Wai, and C.-C. Lee, "Fuzzy neural network position controller for ultrasonic motor drive using push–pull DC–DC converter," *IEE Proceedings-Control Theory and Applications,* vol. 146, pp. 99-107, 1999.

[116] T. Yoshida, T. Senjyu, M. Nakamura, N. Urasaki, H. Sekine, and T. Funabashi, "Position control of ultrasonic motors using dead-zone compensation with fuzzy neural network," *Electric Power Components and Systems,* vol. 34, pp. 1253-1266, 2006.

[117] F.-J. Lin, R.-J. Wai, and H.-H. Lin, "An adaptive fuzzy-neural-network controller for ultrasonic motor drive using the LLCC resonant technique," *IEEE transactions on ultrasonics, ferroelectrics, and frequency control,* vol. 46, pp. 715-727, 1999.

[118] J. Shi, J. Zhao, Z. Cao, Y. Liang, L. Yuan, and B. Sun, "SELF-TUNING FUZZY SPEED CONTROLLER OF TRAVELLING WAVE ULTRASONIC MOTOR," *International Journal on Smart Sensing & Intelligent Systems,* vol. 7, 2014.

[119] S. Mu, K. Tanaka, S. Nakashima, H. Tomimoto, and S. Aramaki, "Intelligent control of USM using a modified NN with PSO," in *Consumer Electronics (GCCE), 2015 IEEE 4th Global Conference on*, 2015, pp. 507-510.

[120] K. Tanaka, M. Oka, A. Uchibori, Y. Iwata, and H. Morioka, "Precise position control of an ultrasonic motor using the PID controller combined with NN," *Electrical Engineering in Japan,* vol. 146, pp. 46-54, 2004.

[121] X. Leng, S. Wu, Y. Du, and Y. Cheng, "Fuzzy sliding mode control for pan-tilt-zoom system driven by ultrasonic motor," in *Automation Science and Engineering (CASE), 2015 IEEE International Conference on*, 2015, pp. 868-873.

[122] F. Giraud, B. Lemaire-Semail, J. Aragones, J. P. Robineau, and J.-T. Audren, "Precise position control of a traveling-wave ultrasonic motor," *IEEE Transactions on Industry Applications,* vol. 43, pp. 934-941, 2007.

[123] M. Jahani and H. Mojallali, "GA-neural network based position control of Traveling Wave Ultrasonic Motor," in *Computer Engineering and Technology (ICCET), 2010 2nd International Conference on*, 2010, pp. V6-369-V6-373.

[124] D. P. Murphy, "Analysis of a Rotary Ultrasonic Motor for Application in Force-Feel Systems," Virginia Tech, 2008.

[125] J. Maas, P. Ide, N. Frohleke, and H. Grotstollen, "Simulation model for ultrasonic motors powered by resonant converters," in *Industry Applications Conference, 1995. Thirtieth IAS Annual Meeting, IAS'95., Conference Record of the 1995 IEEE*, 1995, pp. 111-120.

[126] J. Maas, T. Schulte, and N. Frohleke, "Model-based control for ultrasonic motors," *IEEE/ASME Transactions on mechatronics,* vol. 5, pp. 165-180, 2000.

[127] *http://rikind.com/wp-content/uploads/2015/03/FAS-FRAS-21.pdf*.

[128] T.-C. Chen and C.-H. Yu, "Motion control with deadzone estimation and compensation using GRNN for TWUSM drive system," *Expert Systems with Applications,* vol. 36, pp. 10931-10941, 2009.

[129] L. H. G. Chenglin, "QUICK AND PRECISE POSITION CONTROL OF ULTRASONIC MOTORS USING ADAPTIVE CONTROLLER WITH DEAD–ZONE COMPENSATION," *Journal of ELECTRICAL ENGINEERING,* vol. 53, pp. 197-201, 2002.

[130] M. A. Tavallaei, S. F. Atashzar, and M. Drangova, "Robust motion control of ultrasonic motors under temperature disturbance," *IEEE Transactions on Industrial Electronics,* vol. 63, pp. 2360-2368, 2016.

[131] X. Lu, J. Hu, and C. Zhao, "Analyses of the temperature field of traveling-wave rotary ultrasonic motors," *IEEE transactions on ultrasonics, ferroelectrics, and frequency control,* vol. 58, 2011.

[132] S. Li, W. Ou, M. Yang, C. Guo, C. Lu, and J. Hu, "Temperature evaluation of traveling-wave ultrasonic motor considering interaction between temperature rise and motor parameters," *Ultrasonics,* vol. 57, pp. 159-166, 2015.

[133] S. A. Alsabbah, "Mise en oeuvre de techniques issues de l'intelligence artificielle pour le contrôle de moteurs ultrasoniques à onde progressive," Paris 11, 2005.

[134] C. Mangeot, "Operation of a quasi-static piezomotor in transitory frequency range up to resonance," *ACTUATOR proceedings,* 2014.

[135] C. Giraud, M. Amberg, F. Giraud, C. Mangeot, and B. Lemaire, "Dynamic model of a PAD actuator: dynamic operations and pull-off at high speed," in *ACTUATOR 2016*, 2016.

[136] H. Sven, "Aufbau und Verifikation eines dynamischen Modells für einen piezoelektrischen Stellantrieb (PAD)," Disseration FH Kaiserslautern, 2008.

[137] C. Wallenhauer, "Effiziente Ansteuerung und Nutzung des Sensoreffekts piezoelektrischer Aktoren," Dissertation, Technischen Universität München, 2011.

[138] R. Zeichfussl, B. Gottlieb, C. Wallenhauer, S. Herzig, A. Kappel, and T. Luth, "A method for auto-adjustment of a new piezoelectric drive," in *Mechatronics, 2009. ICM 2009. IEEE International Conference on*, 2009, pp. 1-6.

[139] G. T. Zsurzsan, Z. Zhang, M. M. Andersen, and N. A. Andersen, "Control and sensor techniques for PAD servo motor drive," in *Power Engineering Conference (UPEC), 2015 50th International Universities*, 2015, pp. 1-5.

[140] C. Wallenhauer, B. Gottlieb, A. Kappel, T. Schwebel, J. Rucha, and T. Luth, "Accurate load detection based on a new piezoelectric drive principle employing phase-shift measurement," *Journal of microelectromechanical systems,* vol. 16, pp. 344-350, 2007.

[141] S. Johansson, M. Bexell, and P. O. Lithell, "Fine walking actuator," ed: Google Patents, 2002.

[142] S. Johansson, M. Bexell, and P. O. Lithell, "Switched actuator control," ed: Google Patents, 2002.

[143] S. Johansson, M. Bexell, and A. Jansson, "Fine control of electromechanical motors," ed: Google Patents, 2004.

[144] R. J. Merry, N. C. De Kleijn, M. J. Van De Molengraft, and M. Steinbuch, "Using a walking piezo actuator to drive and control a high-precision stage," *IEEE/ASME Transactions on mechatronics,* vol. 14, pp. 21-31, 2009.

[145] E. Golubovic, T. Uzunovic, Z. Zhakypov, and A. Sabanovic, "Adaptive control of piezoelectric walker actuator," in *Mechatronics (ICM), 2013 IEEE International Conference on*, 2013, pp. 132-137.

[146] R. J. Merry, J. L. Holierhoek, M. J. van de Molengraft, and M. Steinbuch, "Gain scheduling control of a walking piezo actuator," *IEEE/ASME Transactions on Mechatronics,* vol. 19, pp. 954-962, 2014.

[147] Z. Zhakypov, E. Golubovic, T. Uzunovic, and A. Sabanovic, "High precision control of a walking piezoelectric motor in bending mode," in *Control Conference (ASCC), 2013 9th Asian*, 2013, pp. 1-6.

[148] T. Uzunovic, E. Golubovic, and A. Sabanovic, "Piezo LEGS driving principle based on coordinate transformation," *IEEE/ASME Transactions on Mechatronics,* vol. 20, pp. 1395-1405, 2015.

[149] F. Szufnarowski and A. Schneider, "Compliant piezo-flexdrives for muscle-like, antagonistic actuation of robot joints," in *Biomedical Robotics and Biomechatronics (BioRob), 2010 3rd IEEE RAS and EMBS International Conference on*, 2010, pp. 381-388.

[150] G. Škorc, R. Šafaric, and A. Rojko, "Polynomial control technique for adaptive positioning within sub-micrometer scale," in *Robotics in Alpe-Adria-Danube Region (RAAD), 2010 IEEE 19th International Workshop on*, 2010, pp. 131-136.

[151] R. Merry, D. Kessels, R. van de Molengraft, and M. Steinbuch, "Repetitive control applied to a walking piezo actuator," in *Control and Automation, 2009. ICCA 2009. IEEE International Conference on*, 2009, pp. 854-859.

[152] R. J. Merry, D. Kessels, W. Heemels, M. Van De Molengraft, and M. Steinbuch, "Delay-varying repetitive control with application to a walking piezo actuator," *Automatica,* vol. 47, pp. 1737-1743, 2011.

[153] G. Škorc, J. Čas, S. Brezovnik, and R. Šafarič, "Position control with parameter adaptation for a nano-robotic cell," *Strojniški vestnik-Journal of Mechanical Engineering,* vol. 57, pp. 313-322, 2011.

Appendix A: Shinsei motor USR60-E3T

A.1. Datasheet parameters of USR60-E3T

Driven frequency	40 kHz
Driven voltage	130 Vrms
Rated torque	0.5 Nm
Rated output power	5 W
Rated speed	100 rpm
Maximum torque	1 Nm
Endurance time	1000 Hrs
Temperature range	-10°C, +55°C
Weight	275 g

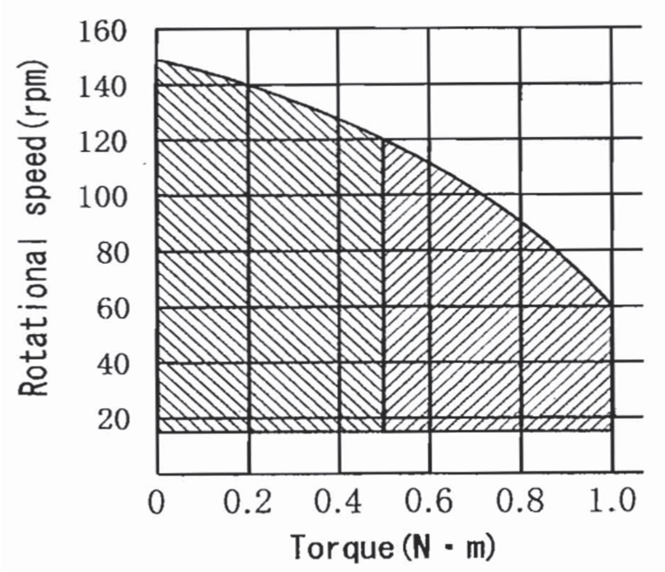

Speed-torque characteristic of USR60

A.2. Simulation parameters of USR60

Vrms	130 V
f	40 kHz
φ	+/-90 °
η	0.2263 N/V
M_{eff}	10.1 g
$Cs_{1,2}$	15.4 Ns/m
$Ks_{1,2}$	$5.95.10^{8}$ N/m
Rr	0.7
Ro	26.75 mm
b	4.41 mm
k	9
h	1.5 mm
M_r	30 g
J_r	$7.2\ 10^{-6}$ Kg/m^2
x_r	$5.4\ 10^{11}$ N/m^3
F_{ext}	160 N

A.3. Real time implementation of position control for USR60 (Simulink file)

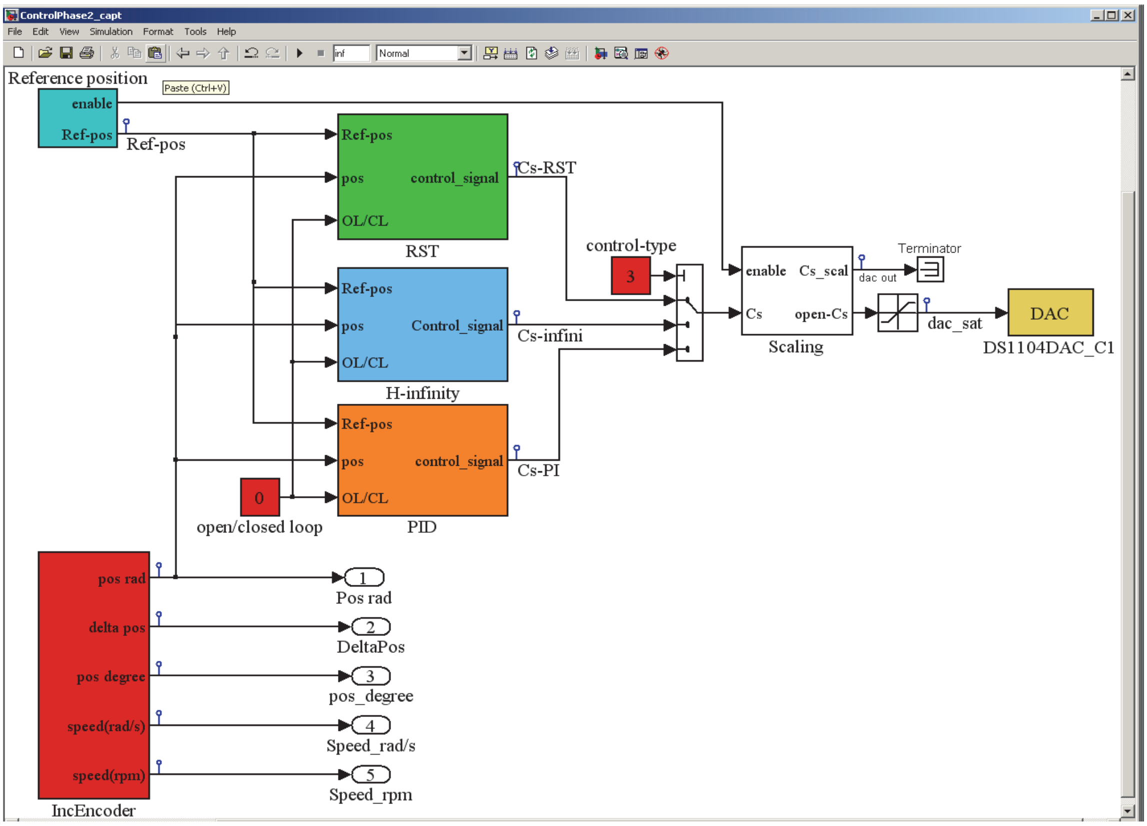

Appendix B: Noliac motor PAD7220

B.1. Datasheet parameters of PAD7220

Mechanical interface	
Shaft diameter	10 mm
Max axial load	10 N
Max radial load	450 N
Mass	865 g
Inertia	0.423 Kg.mm^2
Operating conditions	
V_{max}	200 V
V_{min}	-20 V
Rated frequency	300 Hz
Maximum frequency	1800 Hz
Rated speed	56.25 rpm
Rated torque	4 Nm
Temperature range	0-60°C

B.2. Simulation parameters of PAD7220

$V_{pk\text{-}pk}$	160 V
f	100 Hz
φ	+/-90 °
d_{33}	325.75.10^{-9} m/v
C	7.2 µF
n	350
$k_{x,y}$	40.12.10^{6} N/m
$d_{x,\, y}$	200 Ns/m
a	19 µm
$m_{eff\ x,y}$	14 g
m_R	85 g
m_{tk}	9 g
m_{res}	3 g
i_{trans}	-312
J_r	2.28 .10^{-6} kg/m^2

d_r	0.5 Nms/rad
J_{trans}	52.10^{-12} kg/m^2
n_{shaft}	312
n_{ring}	313
d_{shaft}	10 mm

B.3. Real time implementation of position control for PAD7220 (Simulink file)

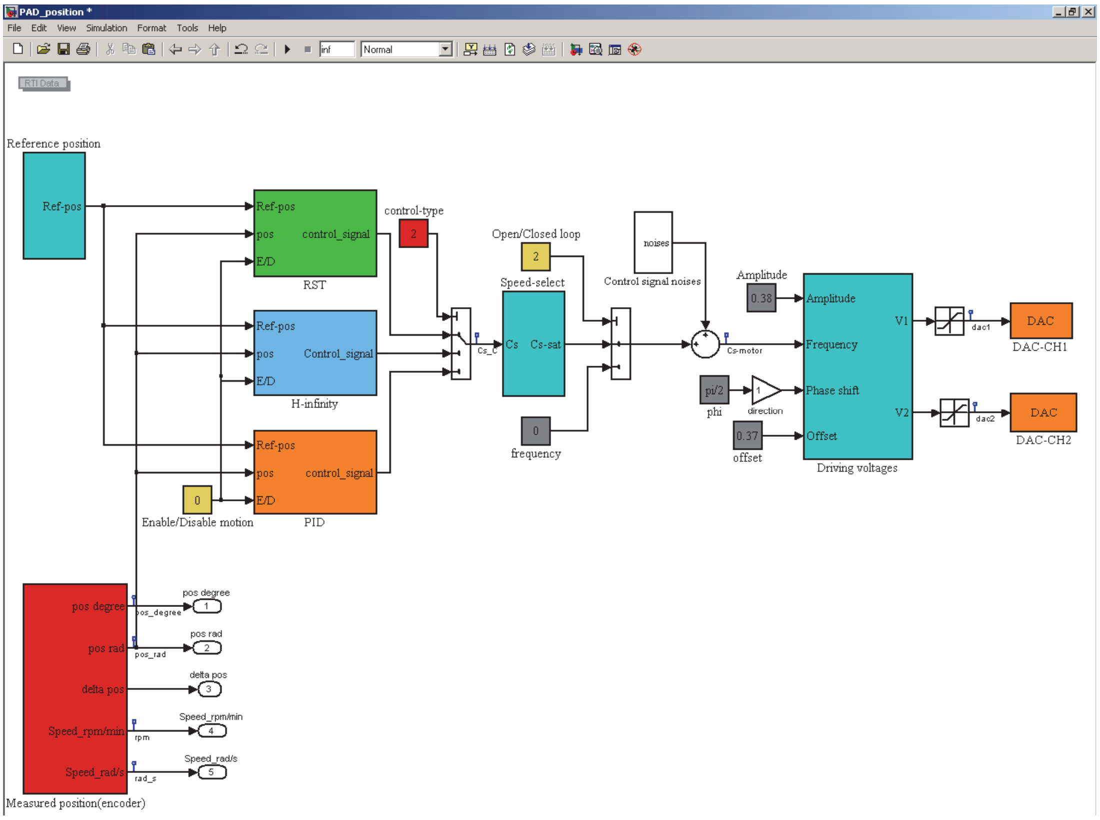

B.4. Real time graphical interface for PAD7220 (ControlDesk)

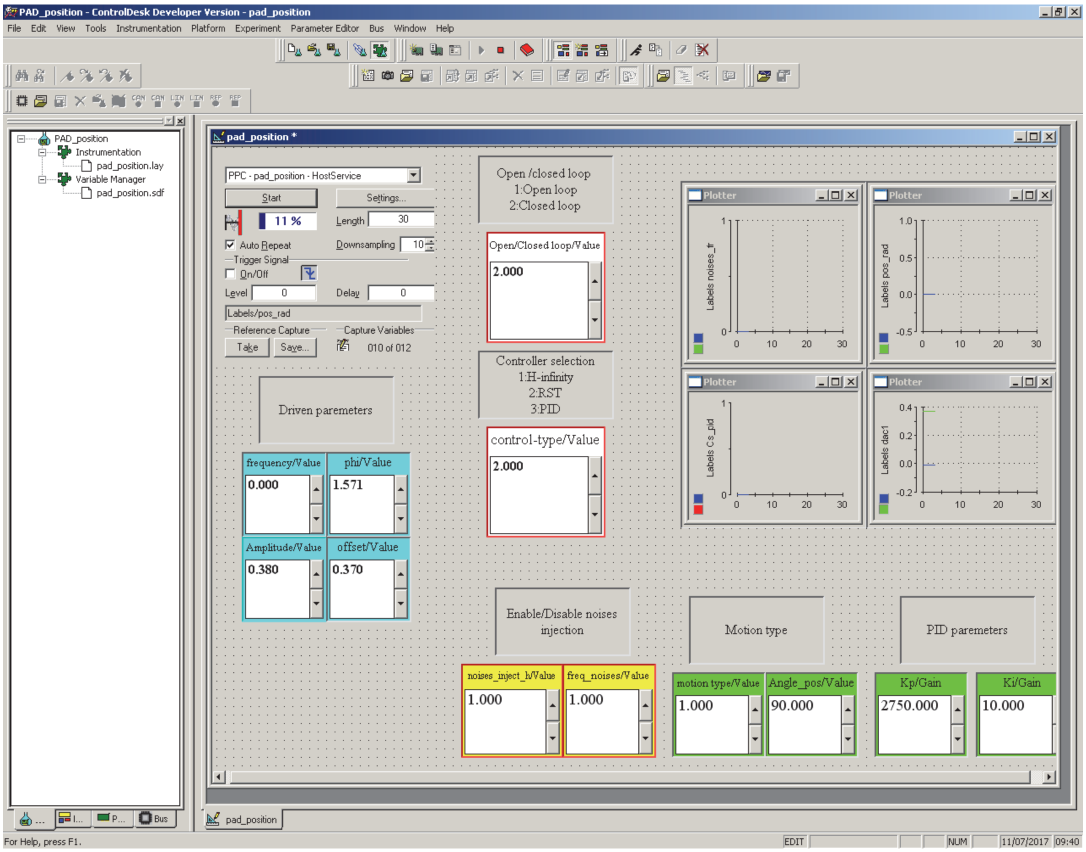

PPC - pad_position - HostService

11 %

Length 30

☑ Auto Repeat

Downsampling 10

Trigger Signal

☐ On/Off

Level 0

Delay 0

Labels/pos_rad

Reference Capture

Capture Variables 010 of 012

Open /closed loop
1:Open loop
2:Closed loop

Open/Closed loop/Value: 2.000

Controller selection
1:H-infinity
2:RST
3:PID

control-type/Value: 2.000

Driven paremeters

frequency/Value: 0.000

phi/Value: 1.571

Amplitude/Value: 0.380

offset/Value: 0.370

Enable/Disable noises injection

noises_inject_h/Value: 1.000

freq_noises/Value: 1.000

Motion type

motion type/Value: 1.000

Angle_pos/Value: 90.000

PID paremeters

Kp/Gain: 2750.000

Ki/Gain: 10.000

Appendix C: Physik Instrumente motor N-310.13

C.1. Datasheet parameters of N-310.13

Operating voltages	-10 to +45 V
Operating frequency	1.5 kHz max
Travel range	50 mm
Velocity	10 mm/s
Step size	5 nm to 5 µm
Force	10 N
Size	25*25*12 mm
Rod length	90 mm
Weight	50 g

C.2. Real time implementation of position control for N-310.13 (Simulink file)

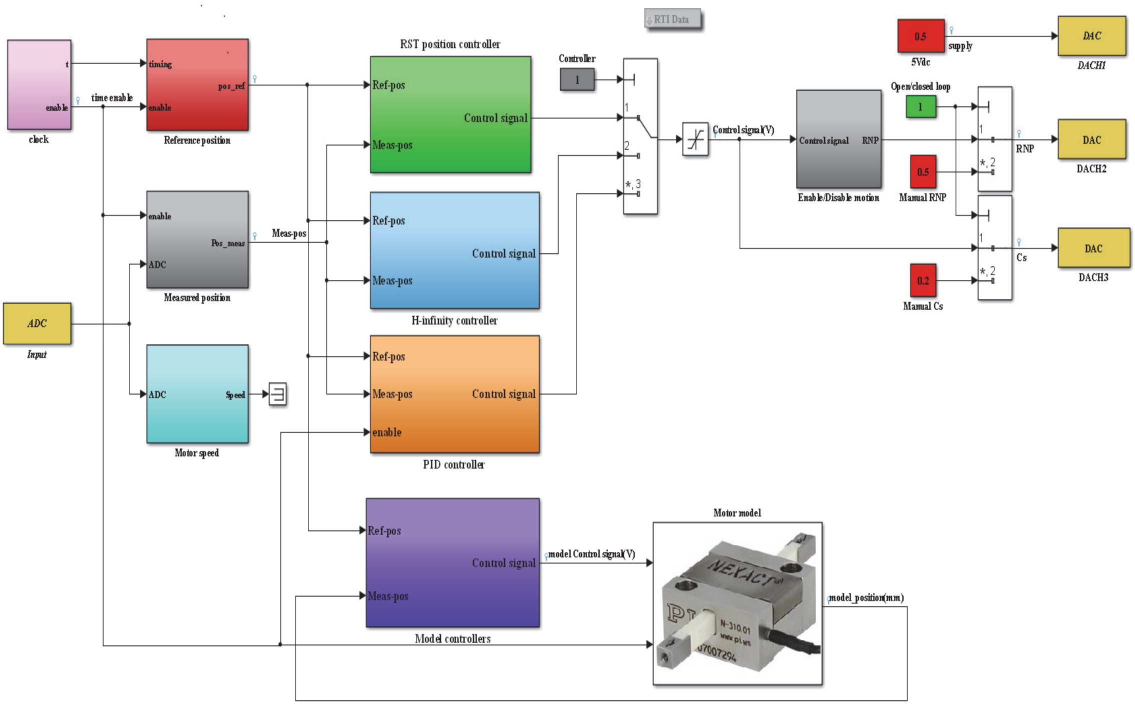

C.3. Real time graphical interface for N-310.13 (ControlDesk)

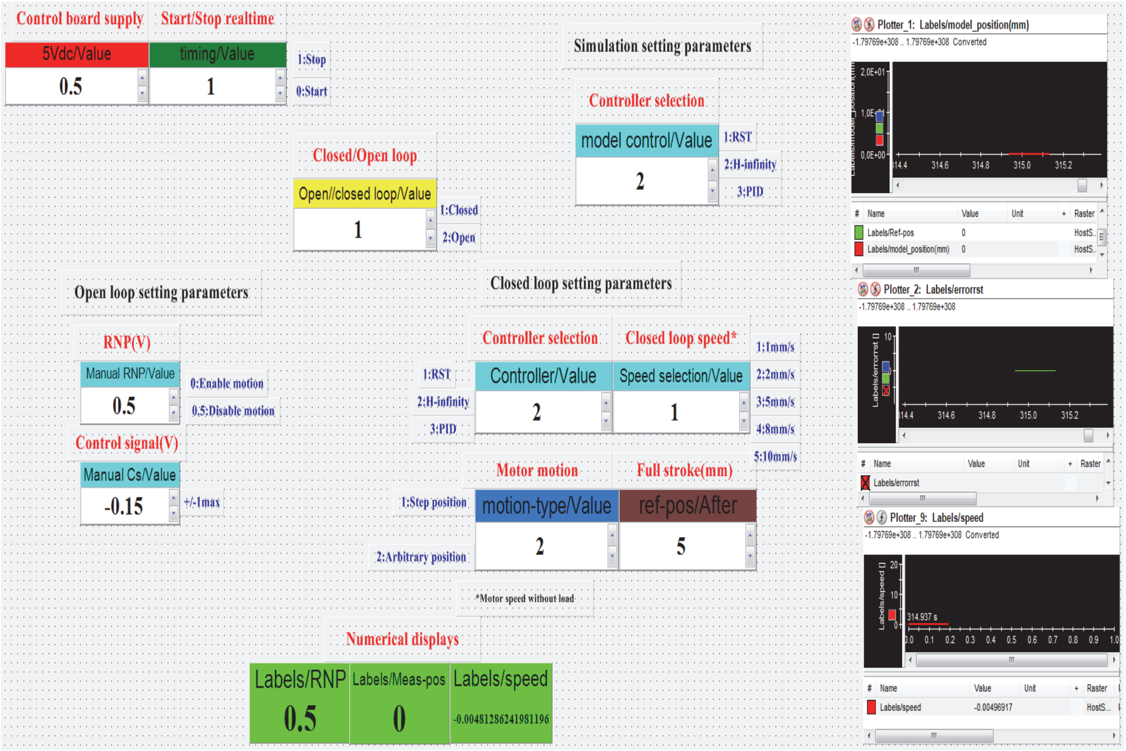

Control board supply
5Vdc/Value: 0.5

Start/Stop realtime
timing/Value: 1
1:Stop
0:Start

Simulation setting parameters

Controller selection
model control/Value: 2
1:RST
2:H-infinity
3:PID

Closed/Open loop
Open//closed loop/Value: 1
1:Closed
2:Open

Open loop setting parameters

RNP(V)
Manual RNP/Value: 0.5
0:Enable motion
0.5:Disable motion

Control signal(V)
Manual Cs/Value: -0.15
+/-1max

Closed loop setting parameters

Controller selection
Controller/Value: 2
1:RST
2:H-infinity
3:PID

Closed loop speed*
Speed selection/Value: 1
1:1mm/s
2:2mm/s
3:5mm/s
4:8mm/s
5:10mm/s

Motor motion
motion-type/Value: 2
1:Step position
2:Arbitrary position

Full stroke(mm)
ref-pos/After: 5

*Motor speed without load

Numerical displays
Labels/RNP: 0.5
Labels/Meas-pos: 0
Labels/speed: -0.00481286241981196

Plotter_1: Labels/model_position(mm)
Labels/Ref-pos: 0
Labels/model_position(mm): 0

Plotter_2: Labels/errorrst

Plotter_9: Labels/speed
Labels/speed: -0.00496917

C.4. Schematic files for the control board of N-310.13 based on dSPIC microcontroller

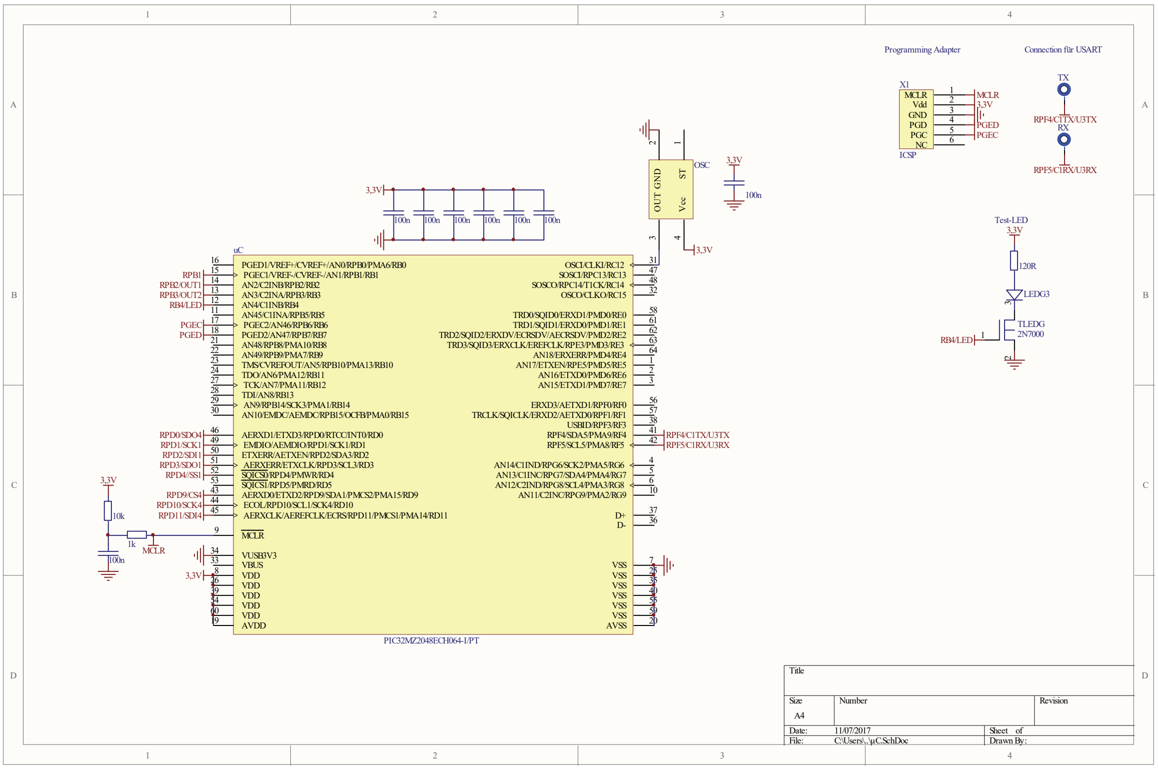

μC schematic document

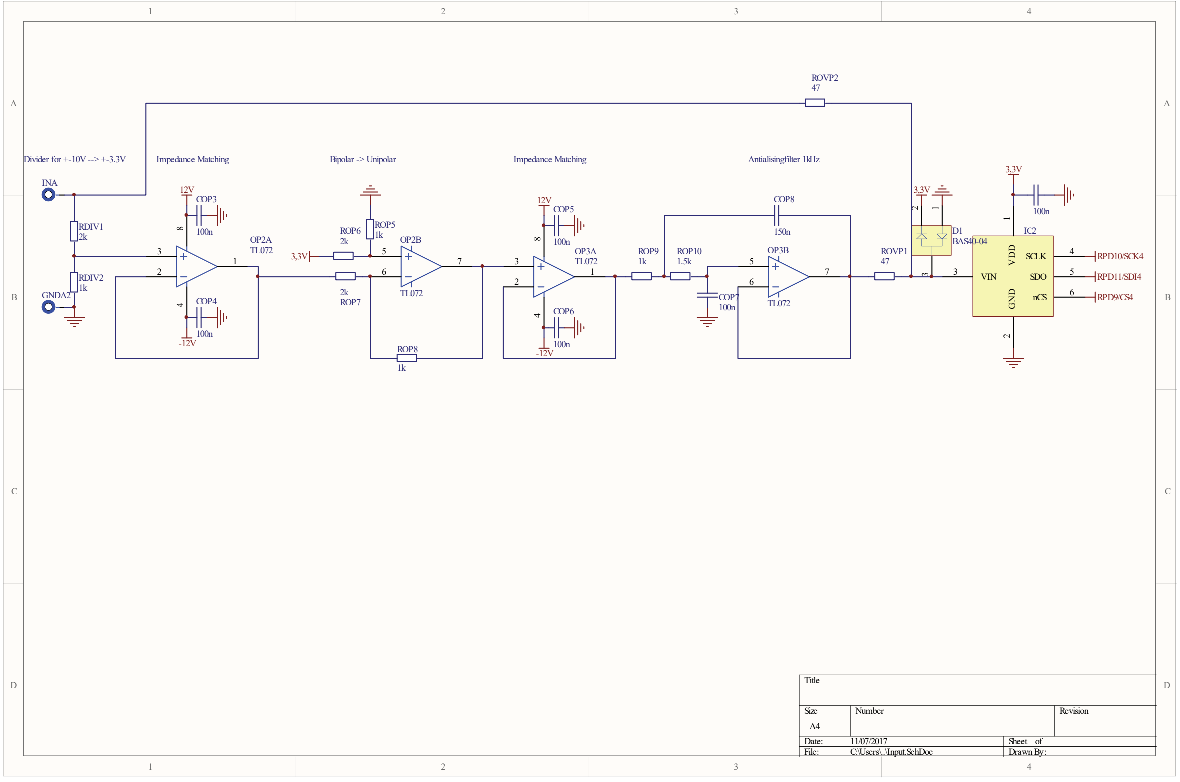

Input stage schematic document

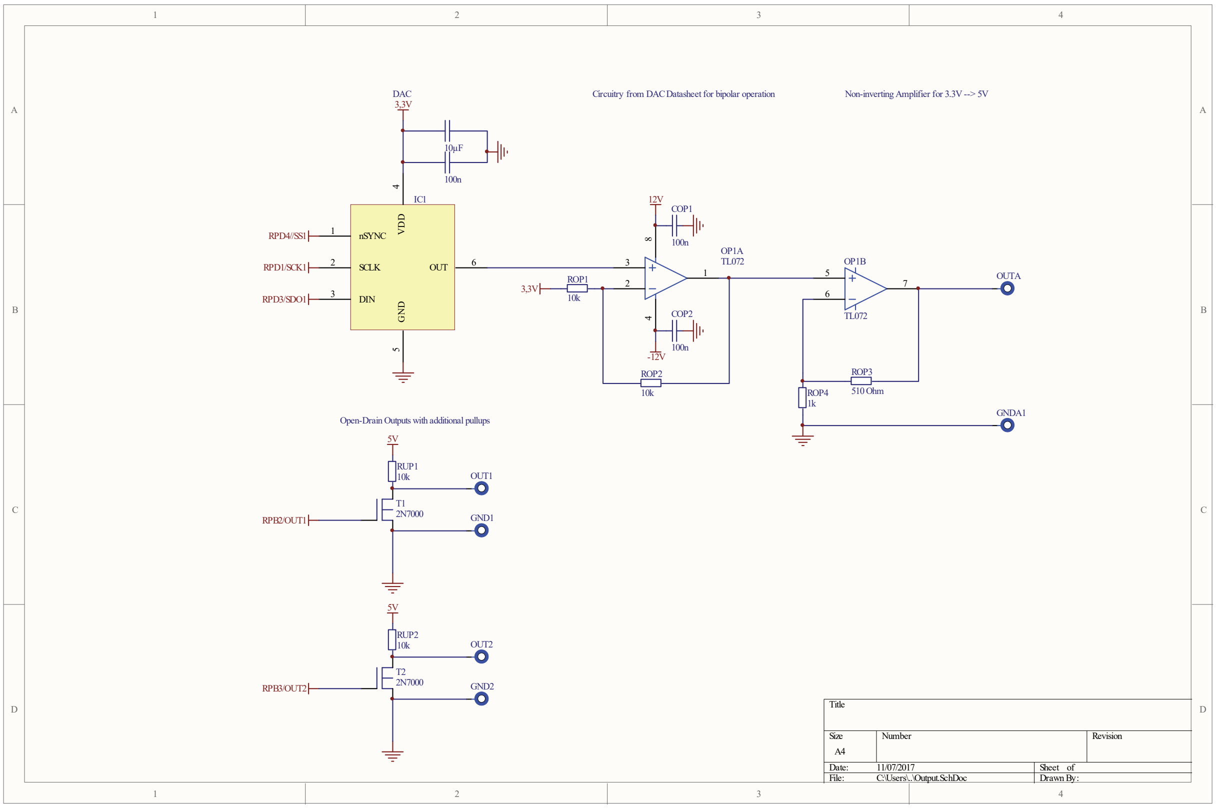

Output stage schematic document

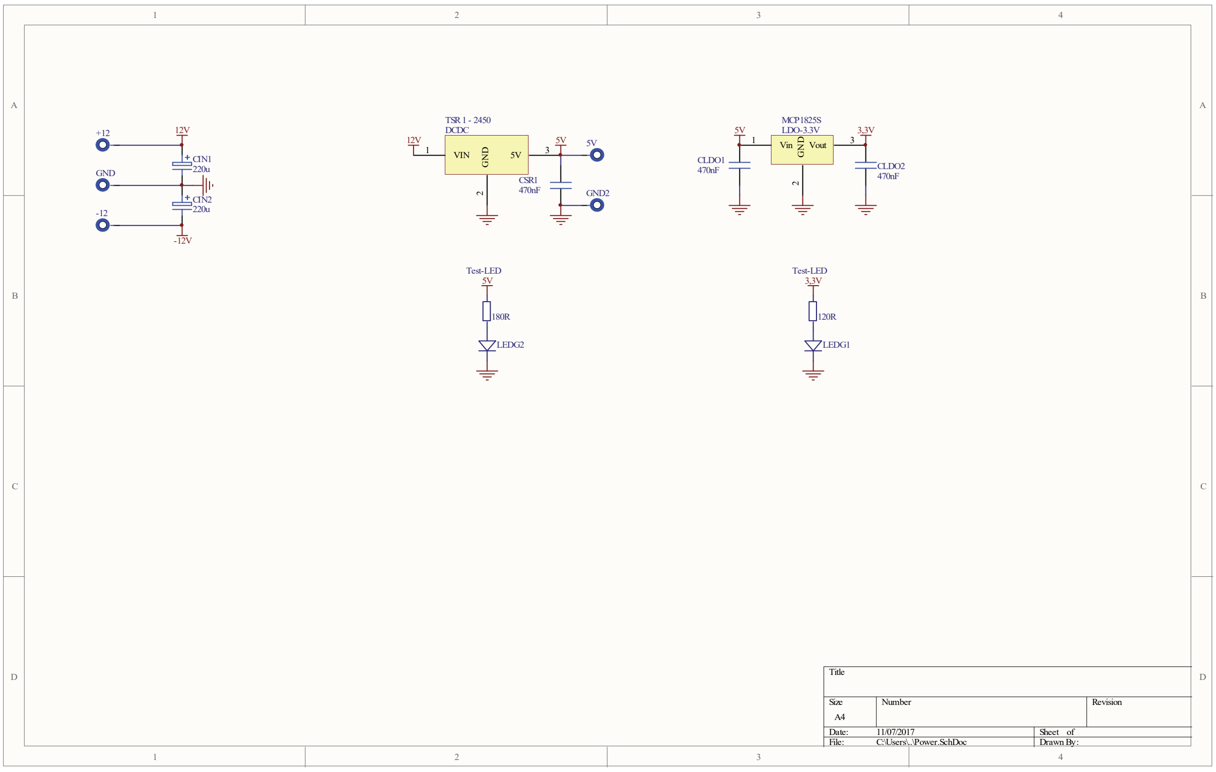

Power stage schematic document

université
PARIS-SACLAY

ÉCOLE DOCTORALE
Physique et ingénierie : électrons, photons, sciences du vivant (EOBE)

Titre : Modélisation et Contrôle en Position des Moteurs Piézoélectriques

Mots clés : Moteurs piézoélectriques, Modélisation, Contrôle en position, H-infini, RST, Robustesse.

Résumé : Pour des applications de positionnement, les moteurs piézoélectriques présentent aujourd'hui une alternative intéressante aux moteurs électromagnétiques classiques en raison de leur forte précision de l'ordre de quelques nanomètres ainsi que de leur faible niveau de bruit électromagnétique. Dans ce contexte, les travaux de cette thèse portent sur la modélisation, la conception, et l'implantation en temps réel de contrôleurs en position pour des moteurs piézoélectriques. L'objectif est de proposer un système de contrôle en position robuste pour des applications robotiques avec un cahier des charges prédéfini. Trois moteurs piézoélectriques avec des principes de fonctionnement différents (USR60, PAD7220, N-310.13) ont été choisis. Leurs modèles électromécaniques ont été développés afin de valider leurs principes de fonctionnement et d'analyser leurs comportements dynamiques face à des perturbations (variation de couple de charge, de température, etc…). Ensuite, ces modèles sont utilisés pour simuler et valider les performances des algorithmes de contrôle en boucle fermée notamment en termes de précision, de robustesse et de stabilité. Des bancs de test expérimentaux ont été mis en œuvre pour les trois moteurs, et des modèles réduits reliant les positions des moteurs aux signaux de commande correspondants ont été identifiés expérimentalement. Deux contrôleurs de position de type H-infini (H_∞) et RST sont ensuite synthétisés et simulés. Ces contrôleurs sont implantés en temps réel sur les bancs de tests expérimentaux via un système dSPACE. Les performances de chaque moteur associé à sa commande sont évaluées. Une étude comparative entre les résultats expérimentaux de ces deux contrôleurs et ceux d'un contrôleur PID classique est aussi présentée.

Title : Modeling and Position Control of Piezoelectric Motors

Keywords: Piezoelectric motors, Modeling, Position control, H-infinity, RST, Robustness.

Abstract: The Piezoelectric motors present an interesting alternative to electromagnetics motors for precise positioning systems. This is mainly due to their high accuracy in the nanometer scale, and to their very low electromagnetic noise levels. In this context, the work presented in this thesis deals with the modeling, design, and real time implementation of position controllers for piezoelectric motors. The objective is to propose robust closed loop position controller of piezoelectric motors for robotic applications. Based on the application specification requirements, three motors with different topologies (USR60, PAD7220, N-310.10) are selected. Their electro mechanic models are developed in order to validate their operating principle and to analyze their dynamics. These models are also used to simulate the controller algorithms in closed loop. Experimental platforms based on the three motors are designed, and the reduced models linking the motor positions to the corresponding control signals are experimentally identified. Afterwards, two position controllers of type H-infinity (H_∞) and RST are synthesized and simulated. These controllers are implemented in real time via the experimental platforms equipped by dSPACE boards. The performances of each motor in closed loop associated to the position controllers are evaluated using the experimental results. Comparative study between the experimental results of two proposed controllers and conventional PID controller is also presented.

Université Paris-Saclay
Espace Technologique / Immeuble Discovery
Route de l'Orme aux Merisiers RD 128 / 91190 Saint-Aubin, France